eman ta zabal zazu

UPV EHU

INNOVATIVE MIXED IONIC-ELECTRONIC CONDUCTORS FOR ENERGY STORAGE SYSTEMS

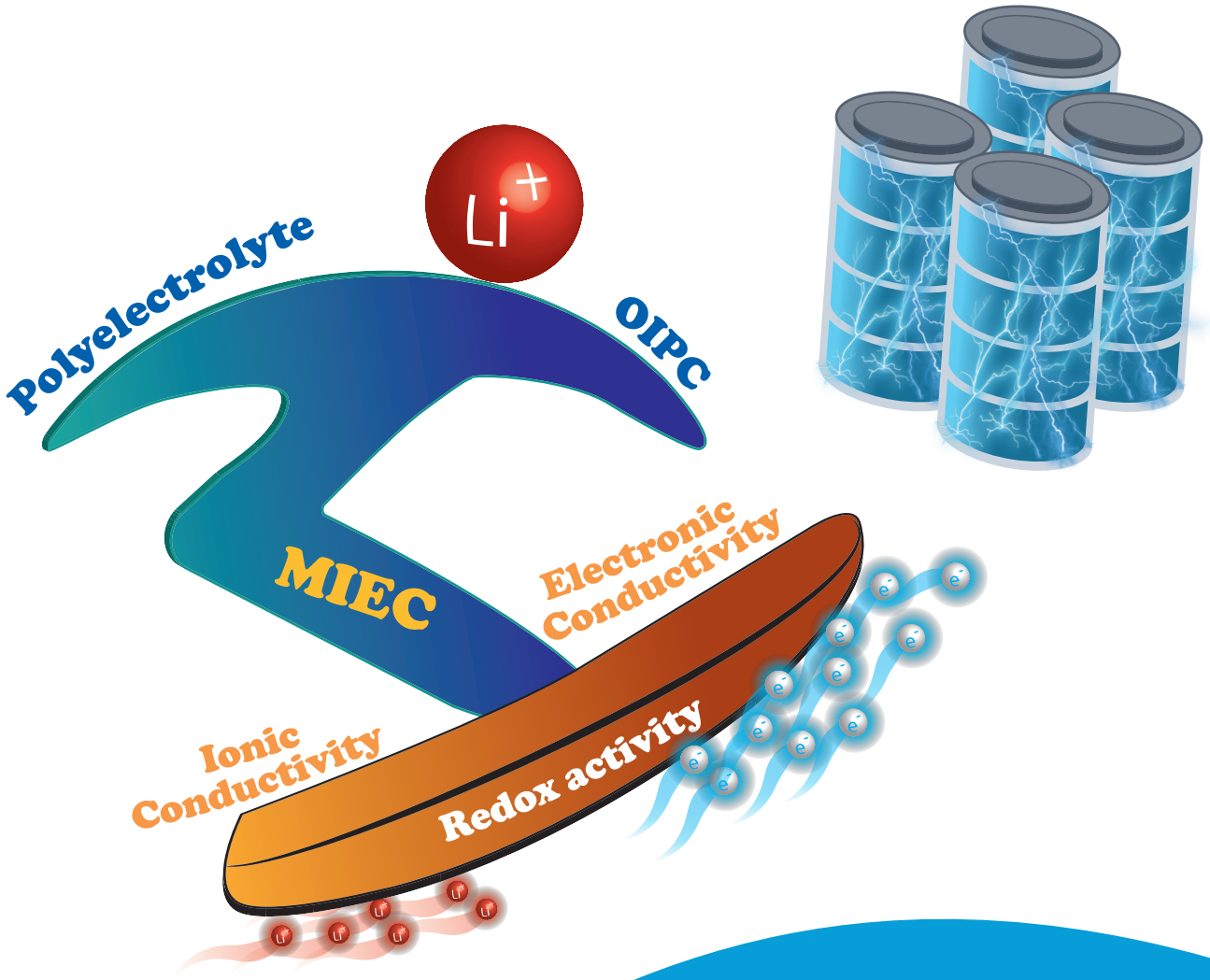

RAFAEL DEL OLMO MARTINEZ

Ph.D. Thesis 2022

Innovative Mixed Ionic-Electronic Conductors for Energy Storage Systems

Rafael Del Olmo Martínez

University of the Basque Country UPV/EHU

Donostia-San Sebastián

Contents

Chapter 1. Introduction

Chapter 1. Introduction

1.1. Electrochemical energy storage

Nowadays, most of the energy demand is satisfied by the use of the combustion of fossil fuels, which on top of the well-recognized adverse effects on the environment, are produced by a non-renewable source. However, due to these environmental concerns, there is a trend for obtaining energy from wind, solar, hydro, and geothermal power plants that necessarily need to be stored.[1,2] Among the technologies used as energy storage systems (ESSs) to handle the harvested energy, batteries, supercapacitors, and pseudo-capacitors stand out, particularly lithium batteries.

The evolution of the energy density that lithium-ion batteries (LIB) can store has been continuously increasing since its development in 1991 by Sony (see Figure 1.1a) through new materials development and optimized conditions. Despite the enhanced energy that LIB can store, society's energy demand has also increased exponentially during the last two decades (Figure 1.1.b). The main sectors of application are electronic devices and the transport sector, which lead to sales of more than 75,000 MWh supplied by this technology in 2016.[3]

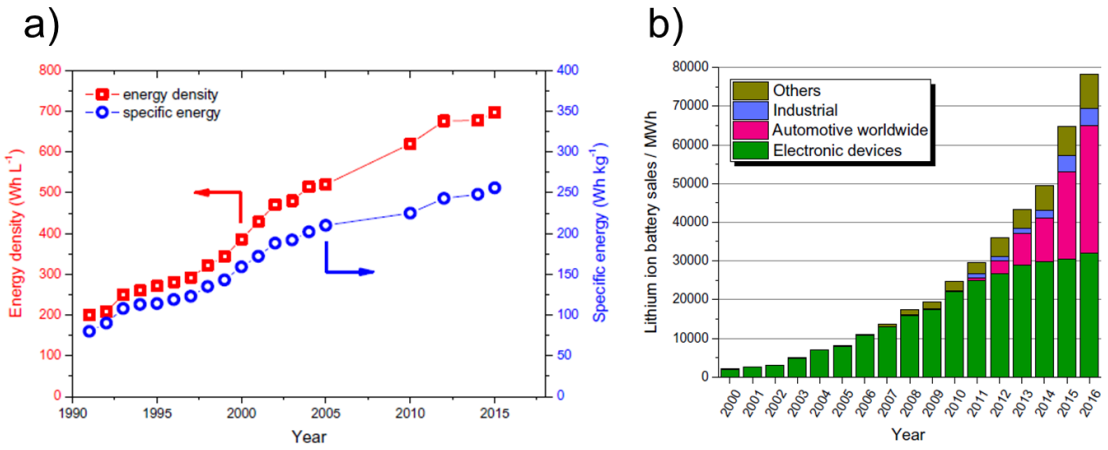

Figure 1.1. a) Evolution of the specific energy and energy density of LIBs from 1991 to 2017. b) Lithium-ion battery sales worldwide from 2000 to 2016. Others: power tools, gardening tools, e-bikes, medical devices, etc. Reprinted with permission from [3]. Copyright 2017, Springer Nature.

However, even if LIBs have become one of the most famous technologies in the ESSs field because of their high specific capacity density (Q, mAh Kg^{-1}) and light-weight, some other technologies have emerged or are still needed. Figure 1.2 shows a classification of most extended ESSs depending on their specific power and energy. In the x-axis the specific energy (E, Wh kg^{-1}) is depicted, which accounts for the energy that a specific device offers, while the y-axis represents the specific power (P, W kg^{-1}), which is a measure of how fast energy can be delivered. Capacity, energy and power are related between them according to the following equations, being the capacity calculated in a faradaic system as:

$$Q = \frac{z \times F}{M} \quad \text{(Eq. 1.1)}$$

$$E = Q \times V \quad \text{(Eq. 1.2)}$$

$$P = \frac{E}{\Delta t} \quad \text{(Eq. 1.3)}$$

where z is the number of electrons transferring, F is the Faraday constant, V is the battery voltage, Δt time required to discharge a battery at a certain rate.

Once these parameters have been defined we can describe more in detail the available technologies to store energy. The ideal technology should be therefore in the top right corner of Figure 1.2 delivering large amounts of energy as fast as required. Leaving combustion processes outside due to environmental issues and restricted application, we can distinguish that devices EDLC (electric double layer capacitor) or pseudocapacitors can deliver very fast small to medium energies, respectively. In contrast, batteries can store larger amounts of energy, but their release is not as fast as (pseudo)capacitors. Those properties are given by their different working mechanisms, further explained in the next section, and make them suitable for a certain application type.

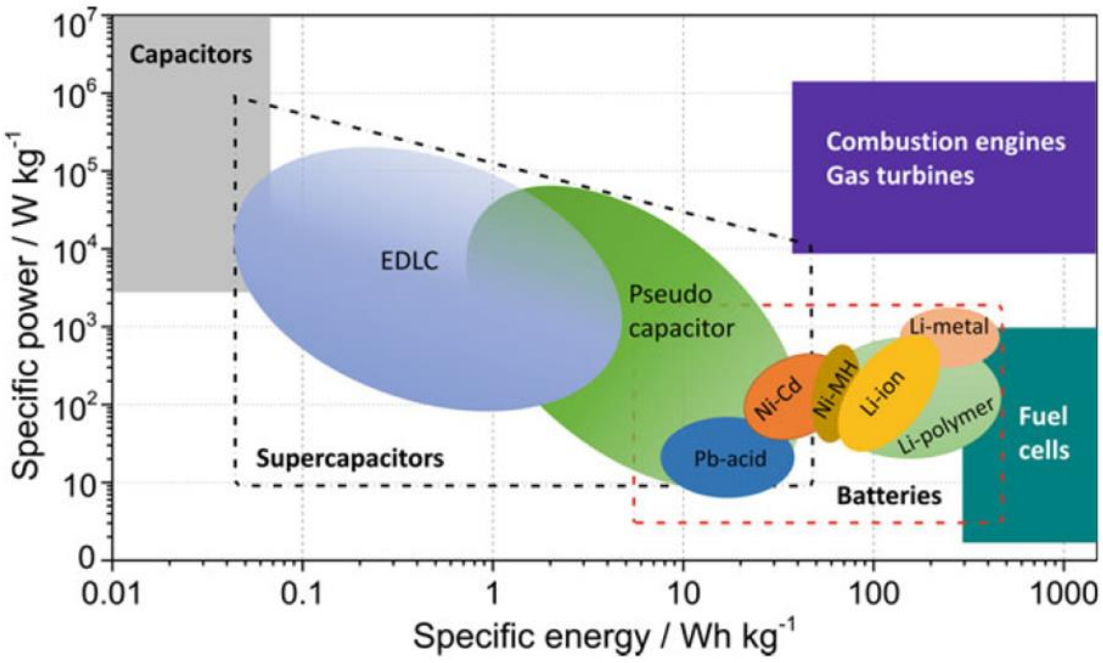

Figure 1.2. Ragone plot of the current electrochemical energy storage systems with conventional capacitors and internal engines and turbines. Reprinted with permission from [4]. Copyright 2019, Springer Nature.

1.1.1. Batteries, supercapacitors and pseudocapacitors

The main difference between batteries and capacitors is that the first ones are governed principally by faradaic processes, where redox reactions (reduction

and oxidation) occur in the electrodes (Figure 1.3d, deeply explained below); whereas in the second ones, the energy is stored in the electrode/electrolyte interface electrostatically along all the surface of the electrode. After, different approaches have been considered to increment the energy density of capacitors forming what is called supercapacitors: EDLC (through porous nanostructures, Figure 1.3a) and pseudocapacitors (with faradaic additives, Figure 1.3b). As a result of the combination of faradaic and non-faradaic architectures, devices offer performances between EDLC and batteries with medium energy and power densities. Hybrid architectures can be also assembled looking for synergistic performance between non-faradaic and faradaic electrodes (see Figure 1.3c)

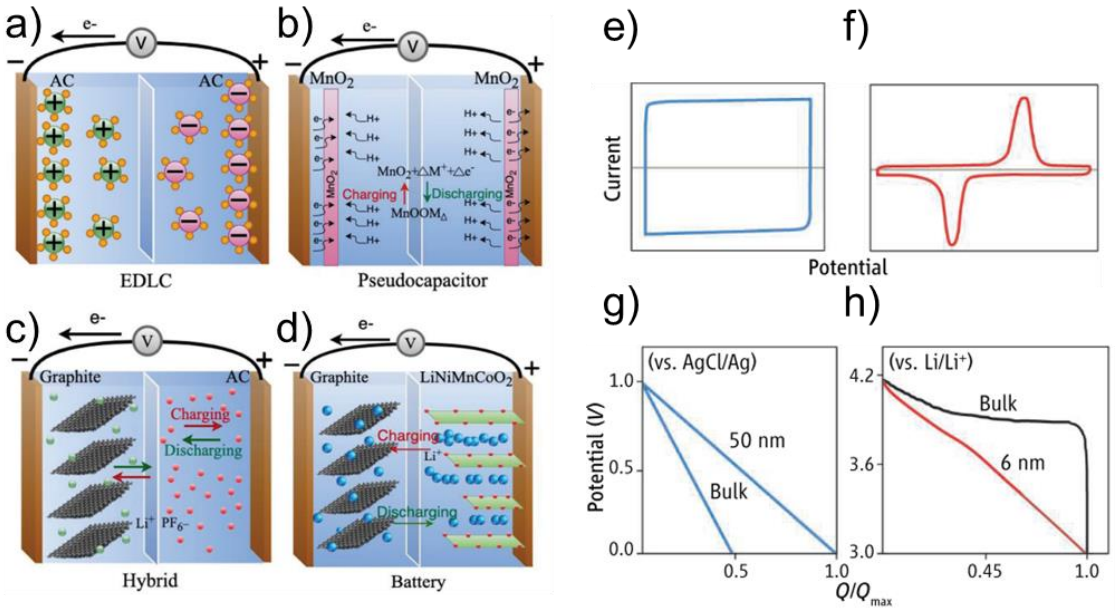

Figure 1.3. a-d Different storage mechanisms: a) carbon-based EDLC, b) pseudocapacitor, c) hybrid capacitor, and d) battery. Reprinted with permission from [5]. Copyright 2020, John Wiley & Sons. e-h Electrochemical response of different based devices: cyclic voltammetry of e) EDLC and f) battery; galvanostatic discharge of g) EDLC and h) battery. Reprinted with permission from [6]. Copyright 2014, American Association for the Advancement of Science.

Therefore, those different mechanisms give distinct electrochemical responses. Classic rectangular shapes are obtained for supercapacitors in cyclic voltammetries (Figure 1.3e) as they follow Eq. 1.4.

$$I_C = C \times \frac{dV}{dt} \quad \text{(Eq 1.4)}$$

where I_C is the capacitive current, C is the capacitance (F) and dV/dt the scan rate. Since the capacitance is an intrinsic material constant property, at a constant scan rate, the current given must be also constant. In contrast, in battery-like behavior, redox peaks occurs at a specific voltage (Figure 1.3f), being the current of the peak (i_p) proportional to the square root of the scan rate (ν) exhibiting a classic semi-infinite diffusion. Besides, even if the voltage position of oxidation and reduction of battery-like materials may displace to higher and lower voltages as the scan rate is increasing, the potential difference (ΔE) must remain constant. When these devices are cycled galvanostatically, the capacitor-like behavior shows a linear-time dependent change in potential at a constant current (Figure 1.3g), while batteries show constant voltage values since the current is employed in the redox reaction that occurs at that potential and will not change until the active material is all oxidized or reduced (Figure 1.3h).

Both technologies have some similarities in a sense, they are composed of two electrodes divided by an ionic conducting material, as is observed in all the architectures of Figure 1.3. Each electrode is composed of an active material (AM), which stores the energy; an electronic conducting additive, to create an electronic pathway from the redox AM to the current collector; and a polymeric binder to tight everything together. In the case of LIB, the anode is usually made of carbon-based active materials such as graphite; and the cathode is normally

composed of lithium metal oxides such as $LiFePO_4$ (LFP), $LiNi_xMn_yCo_zO_2$ (NMC) or $LiNiCoAlO_2$ (NCA).

In a LIB, when the device is charging, in the positive electrode (cathode) the AM is oxidizing, releasing Li^+ to the electrolyte and electrons to the current collector that will be delivered to the negative electrode (anode), which will use them to reduce the AM. After, when we discharge the battery, the anode gets oxidized releasing Li^+ and electrons that will be used back to reduce the cathode. See below the half-reactions for a graphite|LFP system.

	Charging:	**Discharging:**
Anode:	$C_6 + Li^+ + e^- \rightarrow LiC_6$	$LiC_6 \rightarrow C_6 + Li^+ + e^-$
Cathode:	$LiFePO_4 \rightarrow FePO_4 + Li^+ + e^-$	$FePO_4 + Li^+ + e^- \rightarrow LiFePO_4$
Overall:	$C_6 + LiFePO_4 \rightarrow LiC_6 + FePO_4$	$LiC_6 + FePO_4 \rightarrow C_6 + LiFePO_4$

Figure 1.4. Half-reactions of a graphite|LFP cell.

By replacing the active materials of the battery electrodes, enhanced performances can be obtained. For instance, lithium metal (Li^0) and silicon anodes are proposed for the next generation of batteries since they show much higher volumetric capacities than carbon-based anodes (see Figure 1.5). On the positive side, LFP is the most widely used active material for cathodes thanks mainly to its long cycle life and stability, but some other active materials that offer higher voltages and capacities (and hence, energy) are employed such as NMC, despite is not as stable as LFP. Some other architectures are proposed for the advanced ESSs such as lithium-sulfur and lithium-air batteries which offer high capacity and avoid the use of rare elements like cobalt. However, among the

advanced generation of batteries, the only one that is being commercialized is lithium metal batteries (LMB) in combination with LFP by Blue Solutions.

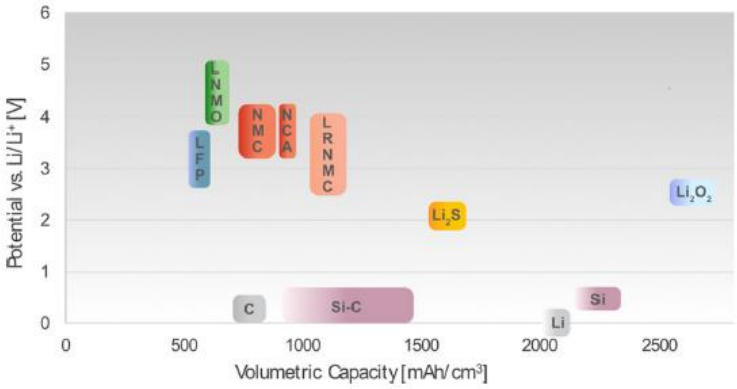

Figure 1.5. Redox potential of positive and negative active materials for rechargeable lithium batteries versus their volumetric capacities (mAh cm^{-3}). Reprinted with permission from [3]. Copyright 2017, Springer Nature.

Nonetheless, the development of LMB brings some issues that need to be fixed for their implementation. The main reason for the failure of these devices is the short circuit by the dendritic growth of lithium from the anode to the cathode, closing the circuit electronically. Those dendrites are initiated by heterogeneous plating of Li^+ onto Li^0 during the charge as can be seen from Figure 1.6. This phenomenon occurs when Li^+ cannot reach the anode as fast as required either by too fast charge or Li^+ slowing-down movement by interaction with other species in the electrolyte. Therefore, to mitigate this process among other strategies to promote homogenous Li^+ deposition, the battery community agree with the use of solid-state electrolytes with high shear modulus, particularly at least twice that of Li metal (Monroe's criterion). Moreover, electrolytes with a high Li^+ transference number, meaning most of the ionic conductivity is given by this ion, are also proposed to avoid the Li^+ slowing down.

a) b)

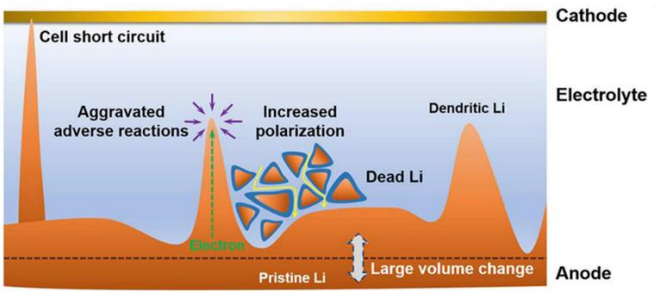

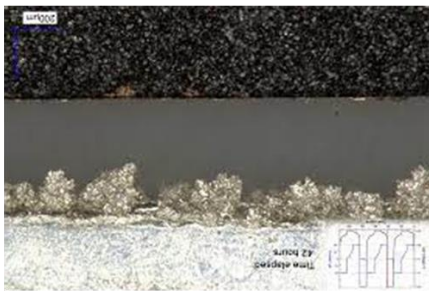

Figure 1.6. a) Scheme of dilemma for lithium metal anode. Reprinted with permission from [7]. Copyright 2017, American Chemical Society. b) The light-grey crystalline structures (dendrites) are forming on a lithium metal electrode. Image by El-Cell.

Once liquid electrolytes, which are normally volatile, toxic and flammable, are removed from the scheme; some other issues need to be fixed when using a solid electrolyte. In liquid-based devices, the Li^+ diffusion to the active material is ensured by the penetration of the electrolyte into the porous electrode. However, this diffusion is not going to occur when solid electrolyte is used. Then, part of the electrolyte needs to be included in the electrode formulation to have an extra source of mobile Li^+ close enough to the active material. Besides, solid-solid interfaces become significant and may have a negative impact in terms of impedances, efficiency of electron and ion transference, voids, cracks, etc. (depicted in Figure 1.7); in comparison with wet batteries and need to be optimized to have a practical application.

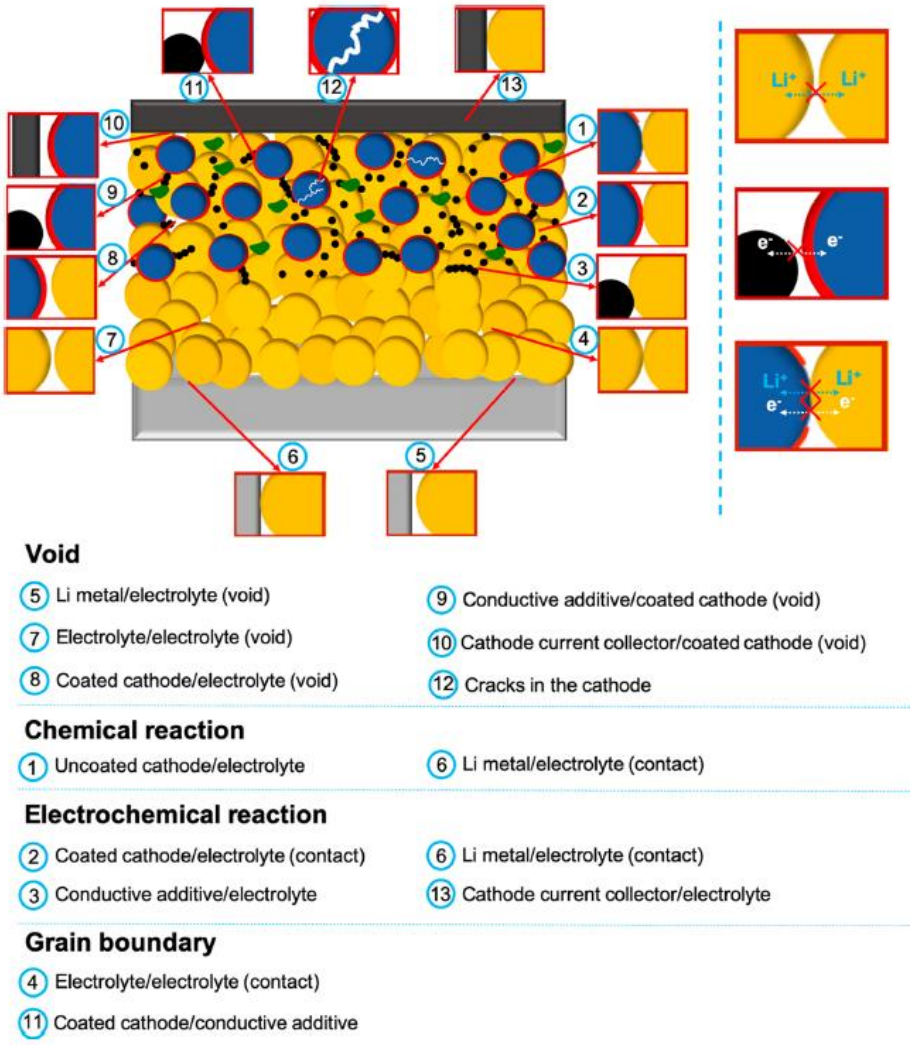

Figure 1.7. Scheme of interfacial phenomena experienced in All-Solid-State Batteries. Reprinted with permission from [8]. Copyright 2020, American Chemical Society.

1.2. Organic Mixed Ionic and Electronic Conducting materials

Organic mixed ionic-electronic conductors (OMIECs) are entirely dominated by radical polymers and mainly π-conjugated polymers.

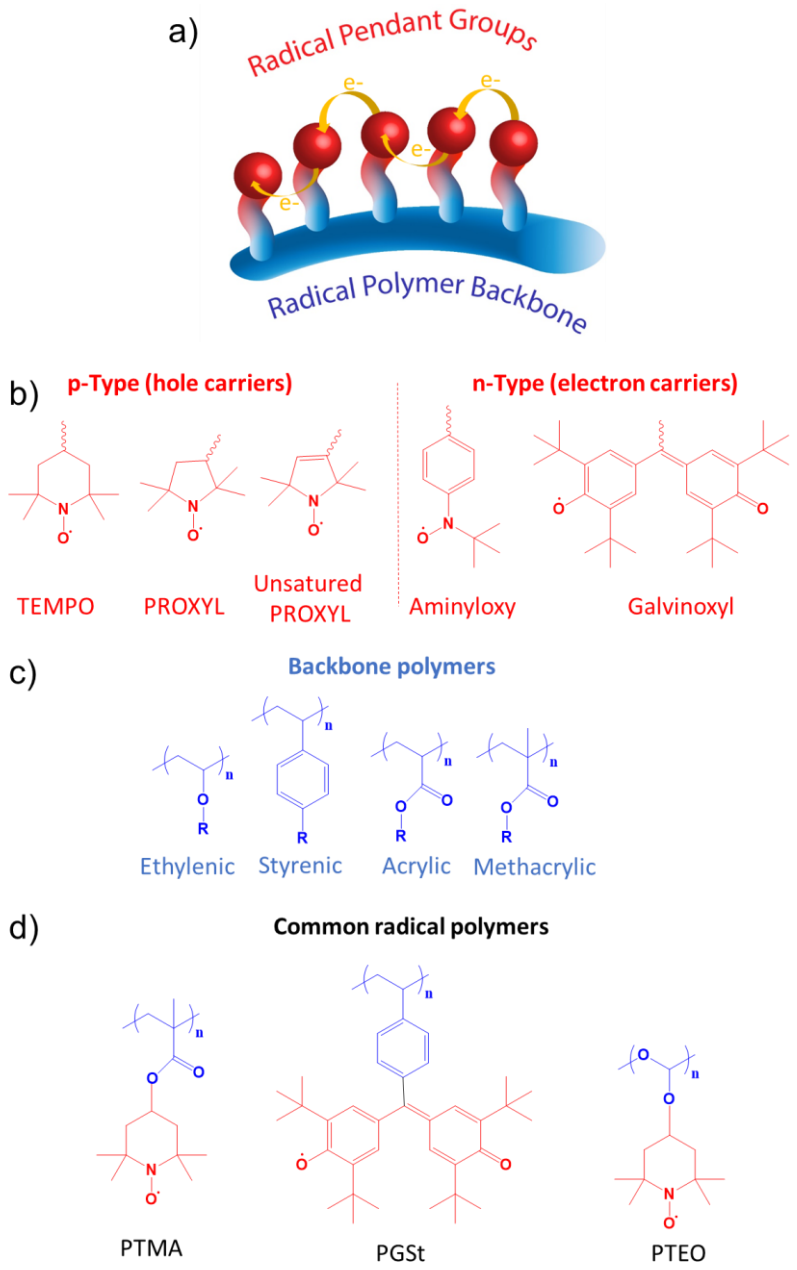

Figure 1.8. a) Typical structure of radical polymers and common examples, b) radicals commonly used, c) backbone polymers normally used and d) examples of radical polymers. TEMPO: (2,2,6,6-tetramethylpiperidin-1-yl)oxidanyl, PROXYL: 1-pyrrolidnyloxy,2,2,5,5-tetramethyl, PTMA: poly (2,2,6,6-tetramethyl-1-piperidinyloxy-4-yl methacrylate, PGSt: poly(4-(2,6-di-tert-butyl-α-(3,5-di-tert-butyl-4-oxo-2,5-cyclohexadien-1-ylidene)-p-tolyloxy)styrene) and PTEO: poly(4-glycidyloxy-2,2,6,6-tetramethylpiperidine-1-oxyl).

Radical polymers are macromolecules containing a stable radical group that is usually pending from the polymeric backbone, as shown in Figure 1.8a-d. Conjugation doesn't necessarily exist in this kind of polymers, where the electron

charge transfer occurs through hops facilitated by the dynamics of the redox-active pendant groups. Basically, the electron charges are transported by redox self-exchange reactions being able to transport charge across interfaces (e.g. at current-collecting electrodes) and also through heterogeneous redox reactions.[9] Depending on the choice of the pendant group chemistry, radicals can act as n-type (electron carriers) or p-type (hole carriers) (Figure 1.8b), which enables the design and customization for a large variety of applications.[10–12] For instance, a nitronyl nitroxide-based system has been demonstrated to have three redox states: p-doped state, neutral and an n-doped state, as depicted in Figure 1.9, which is of special interest for rechargeable devices.[13] The electronic conductivity of radical polymers is around 10^{-3}-10^{-5} S cm^{-1},[9,14] but values of 0.3 S cm^{-1} has been also obtained for PTEO samples.[15]

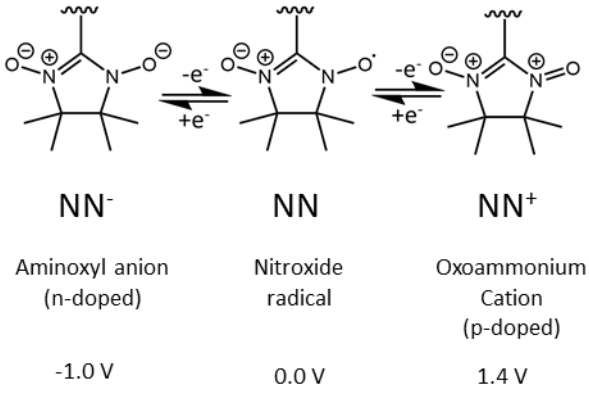

Figure 1.9. Doping states of nitronyl nitroxide.

Since 2002, when Nakahara et al. [16] reported the first radical polymer-based battery, radical polymers have been of great interest in the field of superfast charging-discharging batteries[17–20] and solar cells coupled with perovskites.[21,22]

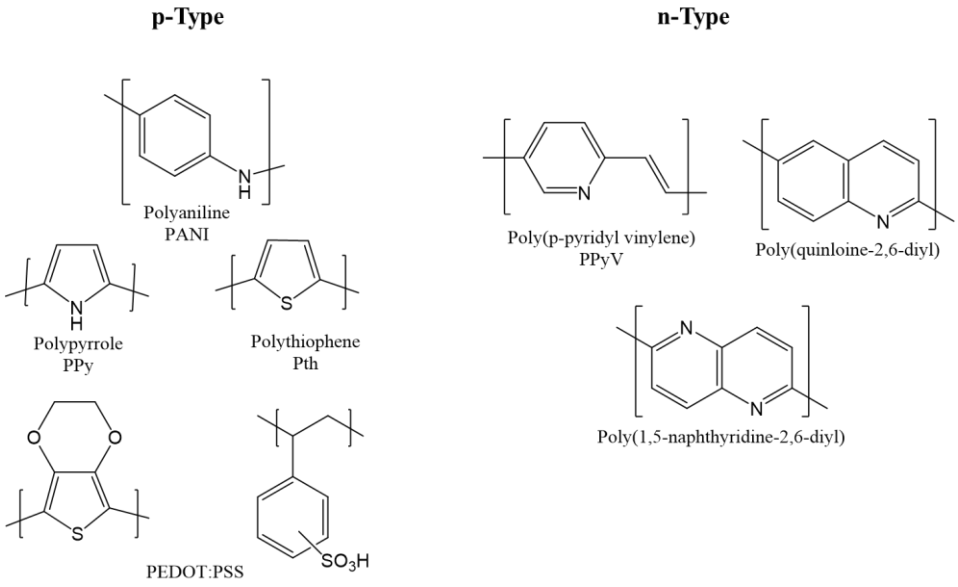

Figure 1.10. Common p-type and n-type conducting polymers.

Differently, conducting polymers (CPs) necessarily must have a π-conjugated polymer backbone, which enables the electronic conductivity. Conducting polymers have been widely studied and their structure, electronic transport mechanisms and applications have been reported in several books and reviews [23,24]. The most common conducing polymers are listed in Figure 1.10. All the carbon atoms in a fully π-conjugated molecule are sp^2 hybridized, forming localized σ bonds that determine the geometrical structure of the molecule. The remaining $2p_z$ orbitals, which are perpendicular to the chain plane, overlap forming π orbitals through which the electrons are delocalized. The number of π and π^* formed orbitals is proportional to the number of carbon atoms, exhibiting a splitting of the energy levels as the number of carbons is doubled. Figure 1.11 represents an example of the simplest conjugated molecule based on trans-acetylene. For long conjugated chains (trans-polyacetylene), the difference of energy between levels becomes negligible and can be considered as continuous

bands along with the electrons that can flow better. The filled π band is named the valence band and the empty π^* band, is the conduction band.

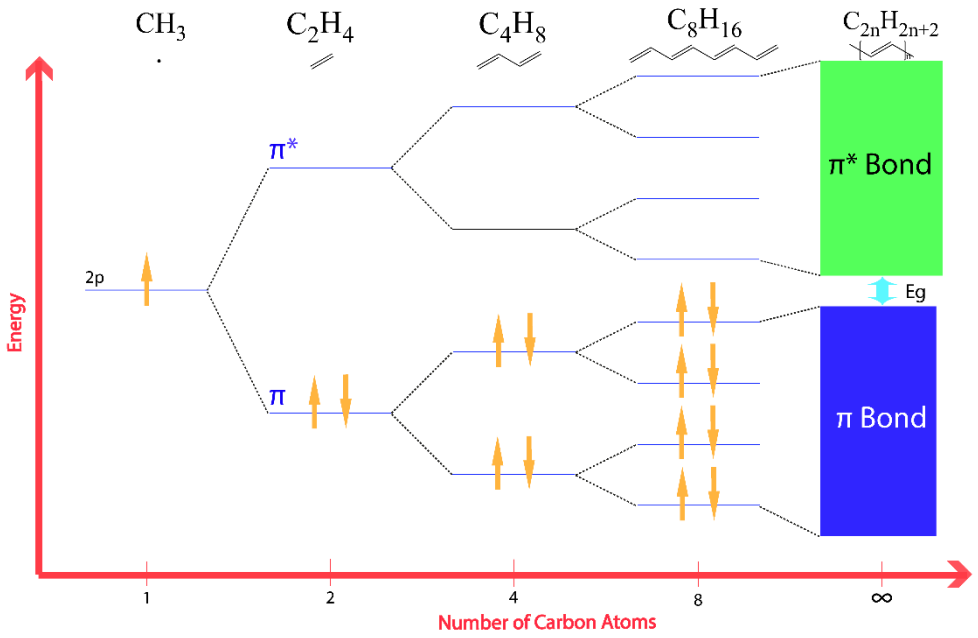

Figure 1.11. Energy levels of π and π^* as a function of the number of carbon atoms.

Nonetheless, the conduction of the most famous polymers is facilitated by the induction of charge defects in the polymer, which reduces the energy gap between π band (HOMO) and π^* band (LUMO) levels, forming so-called polarons and bipolarons (two polarons close to each other) to create conjugated pathways (Figure 1.12). A polaron can be described as a charged quasi-particle localized along the polymer chains, stabilized by other ions acting as dopants in a mechanism that receives the name of primary doping. Basically, the more doped the polymer is, the better the electronic conductivity, showing higher charge defects and hence also creating more electronic and ionic pathways. In Section 1.2.2, the most important dopants that have been studied to date are introduced. Those who are interested in the understanding and prediction of polaronic density state by DFT (density functional theory) and pre-DFT approaches would do well

by reading the article published by Zozoulenko et al.[25] Until now, the progress and conductivity of n-type conducting polymers (electron transporting) are limited compared to p-type (hole transport).

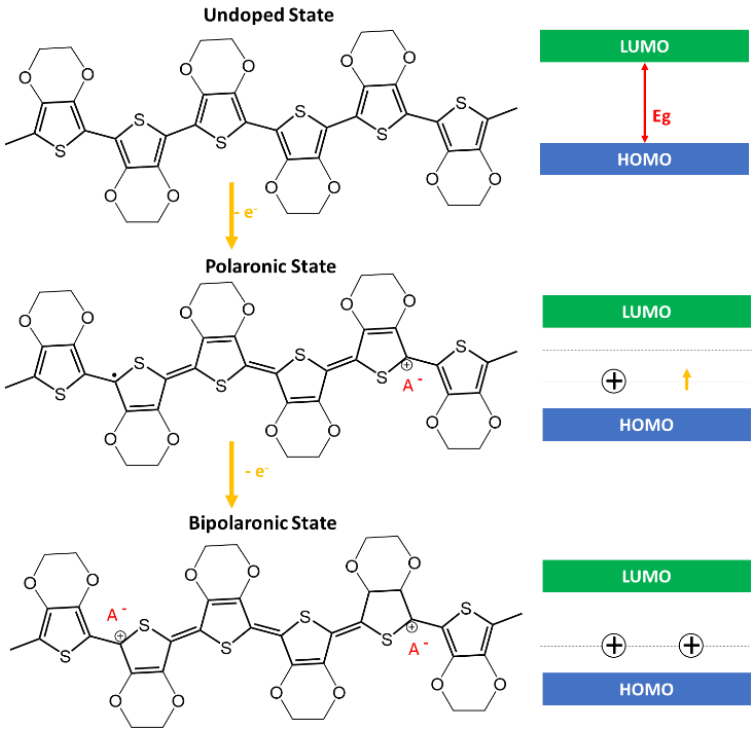

Figure 1.12. Undoped, polaronic and bipolaronic states of PEDOT (poly(3,4-ethylenedioxythiophene)) with a representation of their HOMO and LUMO levels. A^- refers to a dopant that stabilizes the charge.

Since the research conducted in the 1960s on the synthesis and electronic properties of π-conjugated trans-polyacetylene,[26–28] considerable efforts have been paid to the characterization, improvement of electronic transport, design and application of π-conjugated polymers. Conducting polymers have attracted much attention in terms of mass production, due to their ease of manufacturing and low-temperature processability relative to ceramic materials, as well as their semi-metallic electronic conductivity at room temperature, flexibility and binding effect. These features enable the design of wearable, light and versatile devices

such as transistors,[29] ion pumps,[30] sensors [31] electrochromic displays[32] and energy storage systems.[33]

Conducting polymers are typically brittle, so one effective way to produce them is to create a layer on a surface by vapor phase polymerization (VPP). This method results in materials with high electronic conductivities due to the good distribution of the material in a really thin film, which is less affected by internal mechanical stress and other kinds of physical defects. Many studies have focused on creating really thin layers revealing a huge impact on the final electronic conductivity, obtaining values above 6000 S cm^{-1}.[34] Another way to synthesize them is by oxidative chemical polymerization, which is more attractive in terms of scale-up and has resulted in high and air-stable electronic conductivities in bulky films. Among these conducting polymers, poly(3,4-ethylenedioxythiophene):poly(styrene sulfonate) (PEDOT:PSS) is one of the most ubiquitous ones. As shown in Figure 1.10, the conducting agent, PEDOT, is accompanied by the polyelectrolyte polystyrene sulfonate (PSS), which acts not only as a dopant with its SO^{3-} groups but also influences the water solubility of the final compound, the ability to create self-standing films and certain extra ion conduction.

There has been a fundamental development in the design of new functionalized OMIEC systems that can be sorted into different categories, as reported by Paulsen et al.[35] The stabilizer that accompanies the conducting polymer can be split into those that intrinsically have an ionic charge such as PSS (Figure 1.13 I, III, V) and those whose ionic conduction mechanism is based on the solvation of external ions (salts into a polymer electrolyte) (Figure 1.13 II, IV, VI), where the ionic species need to be incorporated. This stabilizer can be

attached to the conducting polymer, forming block copolymers or just mixed to obtain blends, showing in both cases regions that are predominantly ion conductors and other areas that are predominantly electron conductors. This leads to different types of OMIECs according to Paulsen et al.[35]: blends with either ionic polymers (Type I),[36] or ion solvating polymer electrolytes (Type II),[37,38] and block copolymers with ionic polymers (Type III)[39] or ion solvating polymer electrolytes (Type IV).[40,41] Finally, the conducting polymer can exhibit the ionic and electronic conduction simultaneously throughout a single material, without segregation of the charge transfers, by functionalization of the conducting polymer. Two further types appear regarding this variable: conjugated polymer with ionic charge bearing compound (Type V)[42] (counterbalanced by either ions, or forming a self-balanced zwitterion); and conjugated polymer with ion solvating side-chains (Type VI).[43] Other classifications can be also found in literature with redox-active moieties, more biocompatible stabilizers or even radical polymers, which could be considered for another classification.[20]

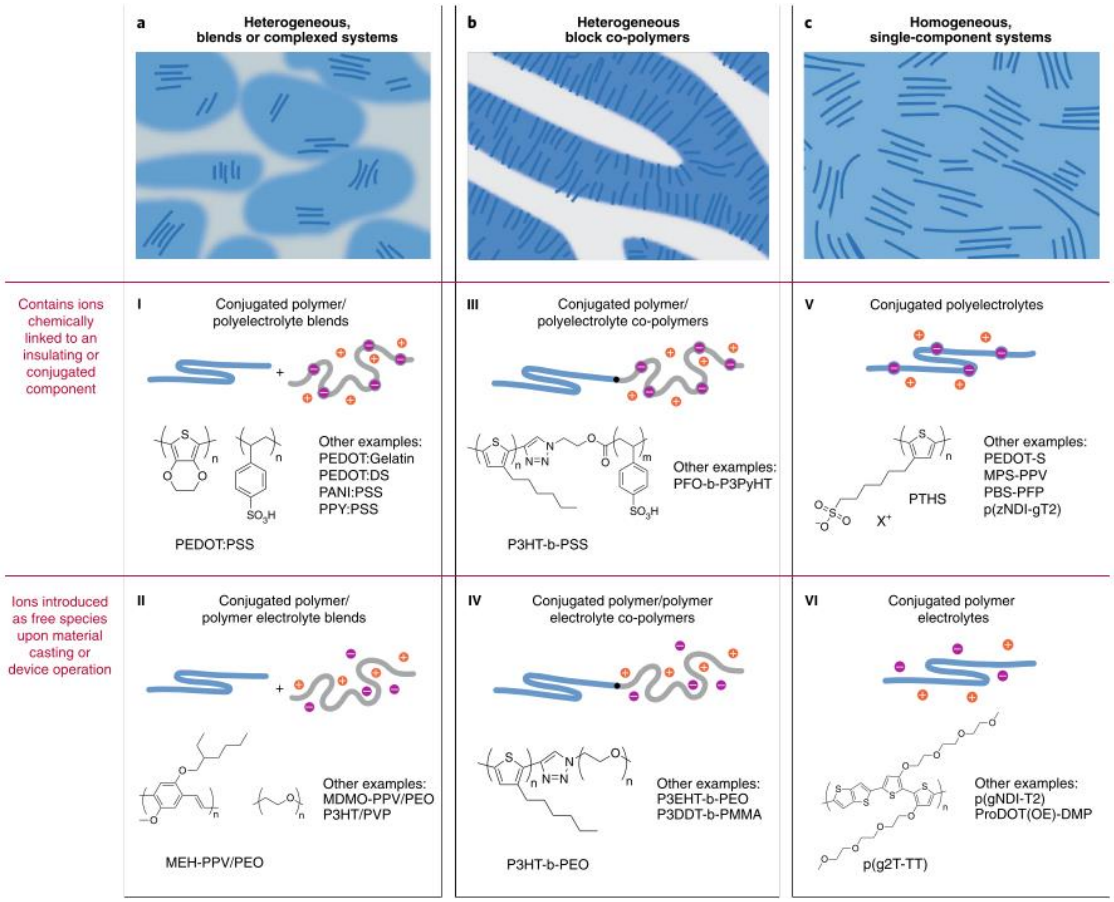

Figure 1.13. Material classes of OMIECs: a) Heterogeneous blends of an electronically conducting conjugated polymer with (I) an ionic charge bearing polyelectrolyte or (II) an ion solvating polymer electrolyte. b) Heterogeneous block copolymers of an electronically conducting conjugated polymer with (III) an ionic charge bearing polyelectrolyte or (IV) an ion solvating polymer electrolyte. c) Fully conjugated (V) ionic charge bearing polyelectrolytes and (VI) ion solvating polymer electrolytes. Reprinted with permission from [35]. Copyright 2019, Springer Nature.

The extensive range of OMIECs that can be designed reflects the large array of target applications and optimization variables. The use of one OMIEC over another for a specific application is usually due to the compatibility with other parts of the device, physic-chemical or electrochemical stability, processability or conductivity values. For this reason, a more thorough characterization is required for the improvement of a wide variety of gadgets whose performances are completely affected by the features of OMIECs and specifically where the ionic transfer is crucial. Even though there are some reports of the ionic and electronic

characterization of OMIECs, there is still a gap in the full understanding of ionic transport and especially the ionic-electronic coupling due to their ion carrier properties being overlooked and unnoticed until quite recently.

To have an idea of the values of conductivity involved in this kind of materials and have a comparison with inorganic mixed ionic and electronic conductors, Figure 1.14 summarizes the reported works so far. Normally, inorganic MIECs stand out for their ionic conductivity remaining their electronic conduction quite low in contrast to OMIECs. In Section 1.2.2. a deeper discussion about the highest values reported until now will take place.

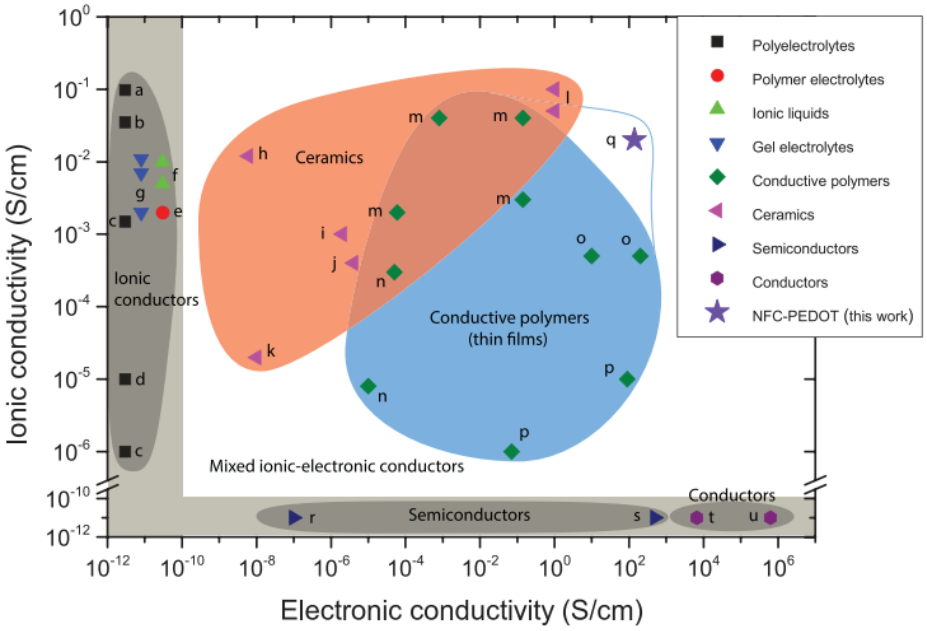

Figure 1.14. Electronic and ionic conductivity values of different materials. a: Nafion; b: poly(diallyldimethyl ammonium chloride)/poly(2,6-dimethyl1,4-phenylene oxide); c: poly(4-styrenesulfonic acid); d: poly(ethylene oxide)/poly(acrylic) acid/multiwalled carbon nanotubes); e: polyvinylidene fluoride/polyethylene oxide/propylene carbonate/ $LiClO_4$; f: (lithium bis(oxlate)borate and lithium tetrafluoroborate)/1-ethyl-3-methyl-imidazolium tetrafluoroborate; g: $LiCF_3SO_3$/poly(methyl methacrylate), $LiClO_4$/poly(methyl methacrylate), and $LiClO_4$/propylene carbonate/ethylene carbonate/dimethylformamide/poly(acrylonitrile); h: $Li_{10}GeP_{22}S_{12}$; i: Ag_2HfS_3; j: Ag_2S; k: $Li_{3.5}V_{0.5}Ge_{0.5}O_4$; l: $Ce_{0.8}Gd_{0.2}O_{2-d}$ –$CoFe_2O_4$; m: poly(3,4-ethylenedioxythiophene):polystyrene sulfonate; n: poly-[1-methyl-3-(pyrrol-l-ylmethyl)pyridinium perchlorate]; o: Polyaniline p: Polypyrrole; q: poly(3,4-

ethylenedioxythiophene):polystyrene sulfonate/ nanofi brillated cellulose/dimethyl sulfoxide/polyethylene glycol; r/s: GaAs; t: Nichrome; u: Ag. Reprinted with permission from [44]. Copyright 2015, John Wiley & Sons.

1.2.1. Poly(3,4-ethylenedioxithiophene)

Amon all the conducting polymers available, PEDOT (introduced in Figure 1.10) has attracted the attention of the researchers for practical applications due to its good stability, easy processing and high conductivity. It was chemically prepared for the first time in the 1980s by Bayer AG.[45] Nowadays, it is commonly prepared by VPP or electrochemically when it is required for the application but low amounts of material are produced by these techniques. It is considered more practical the oxidative chemical polymerization for the synthesis of large amounts of material. EDOT monomer can be polymerized using different oxidants: $FeCl_3$, $Fe(OTs)_3$, $Na_2S_2O_8$ $(NH_4)_2S_2O_8$. The overall polymerization can be divided into two major steps (Figure 1.15). First, monomers are polymerized through oxidative polymerization, resulting in the undoped neutral polymer (Figure 1.15a-d). After, the neutral polymer chain is doped with the excess of oxidant, being stabilized with the presence of anions, yielding a conducting polymer (Figure 1.15e). Going more in detail into the oxidative polymerization, the reaction can be divided into three steps: (1) oxidation of EDOT monomer into a radical cation (Figure 1.15a) followed by (2) its coupling with another radical cation and re-aromatization forming dimers (Figure 1.15b) and (3) final chain propagation through oxidation and recombination of oligomers (Figure 1.15c-d). This procedure yields a dark blue precipitated PEDOT polymer that can be easily filtered unless it is combined with some other additives such as polystyrene sulfonate (PSS) to give a water-processable material.

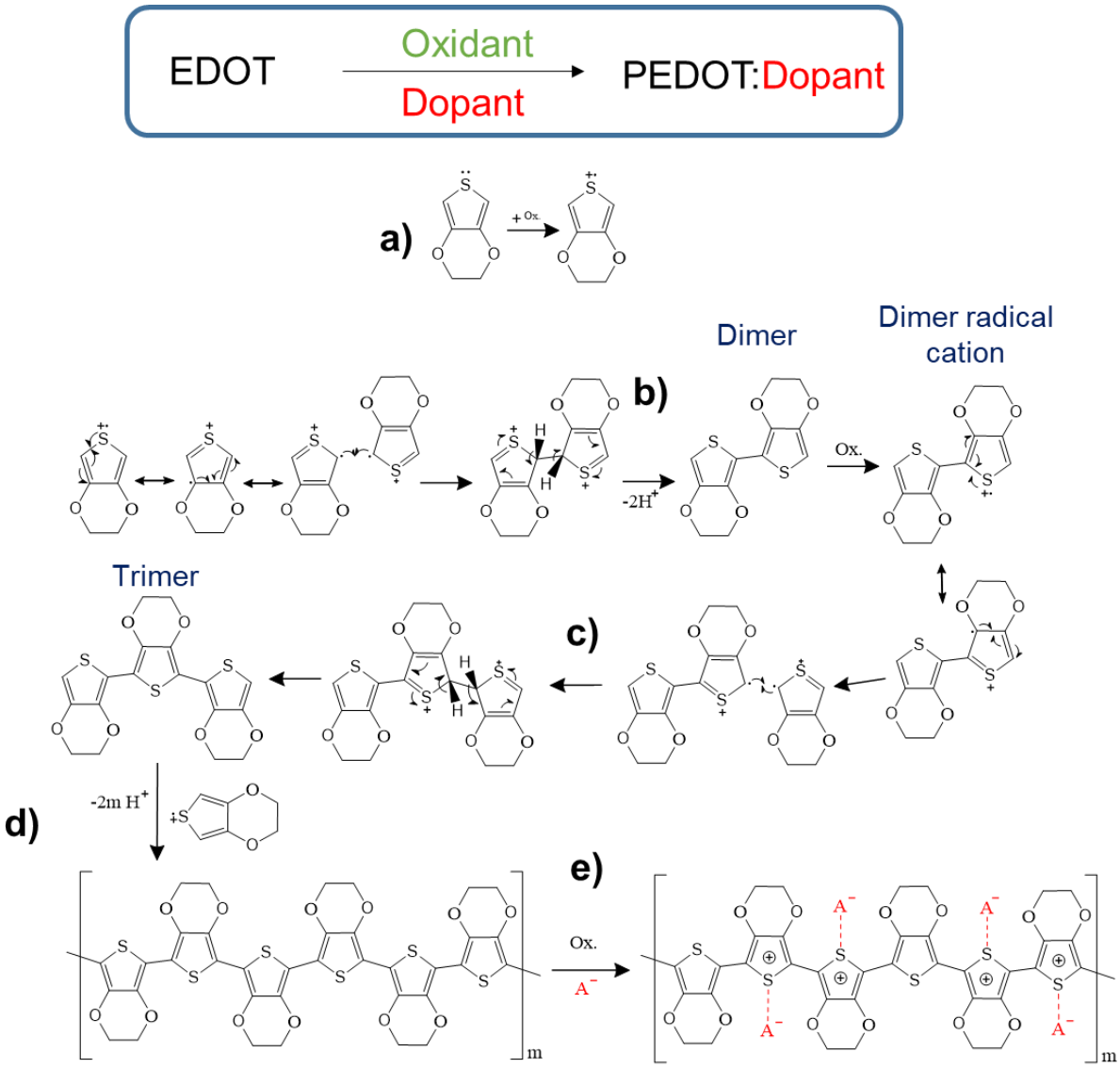

Figure 1.15. Scheme of oxidative polymerization of PEDOT. Ox.: oxidant; A^-: anion.

It is worth mentioning that PEDOT is normally a very fragile material s a consequence of its rigid structure and short polymeric chains. It is believed that the molecular weight of PEDOT does not exceed 1,000 to 2,500 Da (6-18 repeating units).[46] Therefore, it is usually accompanied by stabilizers such as PSS, being commercialized (i.e. Clevios) for a large variety of applications.

1.2.2. Dopants and additives

As explained in the previous section, conducting polymers in their oxidized state form positive charges that need to be counterbalanced by anions to stabilize this doped state. These counter ions are called dopants. Acidic compounds have been commonly used to dope PEDOT, PANI and PPy, such as hydrochloric acid (HCl), sulfuric acid (H_2SO_4), triflic acid (CF_3SO_3H), p-toluene sulphonic acid (PTSA) and dodecyl benzene sulfonic acid (DBSA).[47–51] Besides, DFT calculations have shown that protons also dope PEDOT predominantly by the most favorable interaction with the α-position of thiophene in a doping/de-doping fully reversible mechanism.[52] Other ways to boost the electronic conductivity of these polymers are through electrochemical doping[53] or by the addition of polar solvents (methanol, dimethylsulfoxide, ethylene glycol)[54] to PEDOT:PSS to promote phase segregation between PEDOT and PSS, namely secondary doping, as depicted in Figure 1.16. Rich cores of PEDOT are normally surrounded by isolating PSS, which after secondary doping, detach from PEDOT creating more continuous and conducting particles of PEDOT. In addition to all of these techniques to improve the electrical transport, organic-based additives can be incorporated (see Section 1.2.2.1) or hybrid systems (more focused on thermoelectric applications) can be designed as supplementary approaches. In this way, electronic conductivity values ranging from 10^{-1} S cm^{-1} to semimetallic values have been reported.[44,50,55]

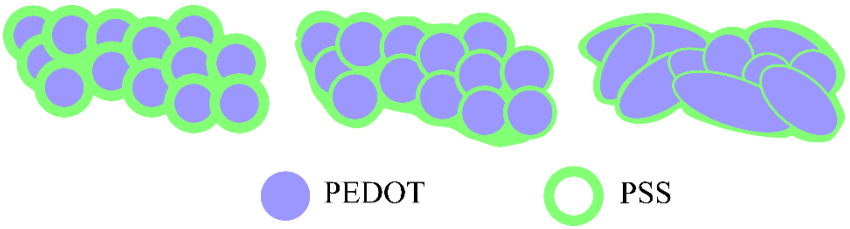

Figure 1.16. Phase segregation between PEDOT and PSS.

1.2.2.1. Organic based additives

Ionic liquids (ILs) emerged highlighting their electrochemical stability, high ionic conductivity and safer properties versus the flammable and volatile conventional electrolytes.[56,57] The addition of ILs to conducting polymers has improved ionic-electronic conductivities and Seebeck coefficient (induced thermoelectric voltage in response to a temperature difference) without losing mechanical properties.[55,58] Although the mechanism is not fully clear, a secondary doping is believed to be coming from an ion exchange as depicted in Figure 1.17, followed by the below-described phase segregation, where PEDOT incorporates IL anions and PSS the cations. Through free energy calculations using DFT, Izarra et al. showed that among various ILs the most efficient pairs were the ones with the lowest binding energies, meaning the least tightly bound, which lead to more favorable and spontaneous ion exchange, and also with p-doping power.[59] The extra Seebeck coefficient has been explained by several authors by an ionic Seebeck effect.[60]

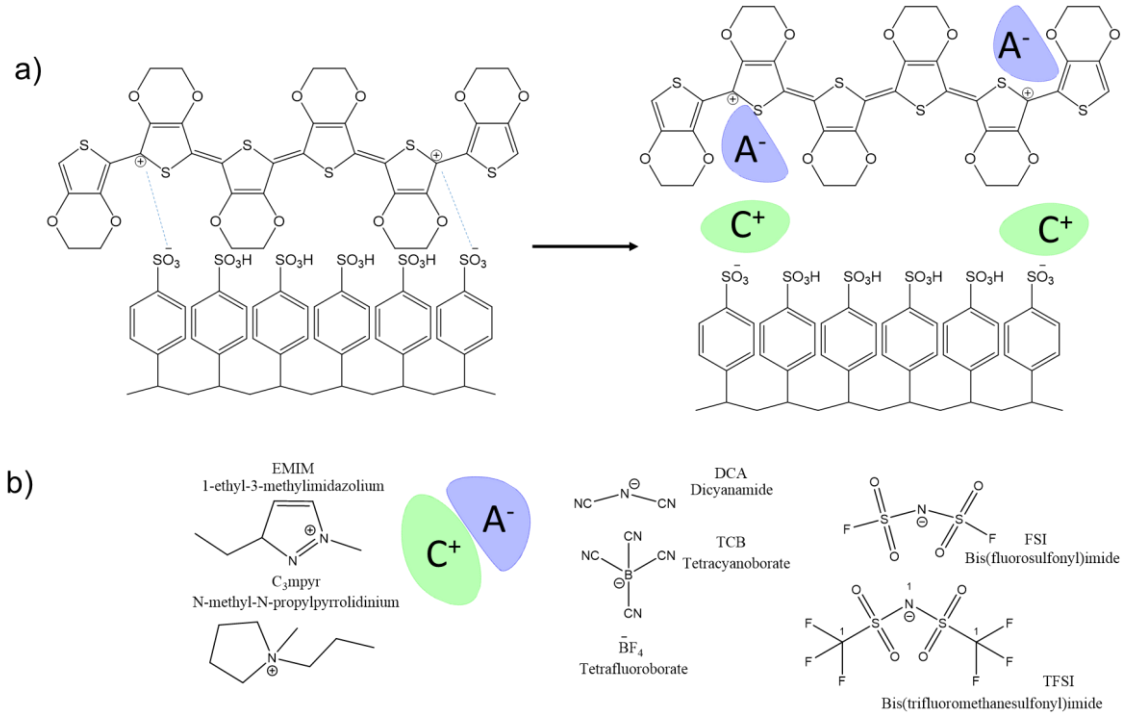

Figure 1.17. a) Ion exchange of PEDOT:PSS with ionic liquids and b) commonly used ionic liquids.

Untreated, commercially available PEDOT:PSS (Clevios PH1000) typically presents an electronic conductivity lower than 1 S cm^{-1} at room temperature,[61] while the incorporation of an IL can successfully achieve values of 1000-2000 S cm^{-1}.[36,62,63] The enhancement in the electronic conductivity typically comes accompanied by a higher electrochemical response as well.

1.2.3. Organic Ionic Plastic Crystals (OIPCs)

OIPCs are considered the solid-state version of ILs. Ionic liquids are usually composed of such big ions that do not let the structure crystallize remaining amorphous. OIPC trend to contain smaller ions than ILs enabling crystallization. Therefore, OIPCs are basically crystalline salts at room temperature which still have dynamics in the structure as depicted by Yoshizawa-Fujita et al. (see Figure 1.18).[64] To distinguish an OIPC from an ordinal salt

Timmerman's criterion is used, which defines that the entropy of fusion (ΔS_f) must be < 20 J K mol^{-1} as a consequence of their rotation and diffusion in the solid state. As a matter of these dynamics, it is also common to observe different solid-solid phase transitions at certain temperatures (T_{S-S}) meaning different orderings of these complex salts.

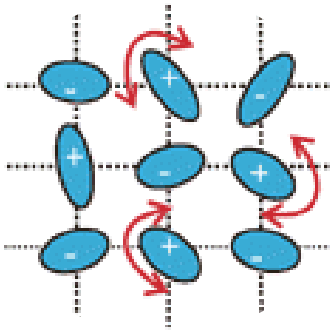

Figure 1.18. General structure representation of OIPCs. Reprinted with permission from [64]. Copyright 2022, The Chemical Society of Japan.

Figure 1.19 collects common ions (with their abbreviations) whose combinations can be found in literature satisfying Timmerman's criterion. In the field of electrolytes, it is clear that amorphous structures lead to higher ionic conductivities than crystalline ones. Nonetheless, OIPCs have shown quite high ionic conductivity to be considered for ESSs.

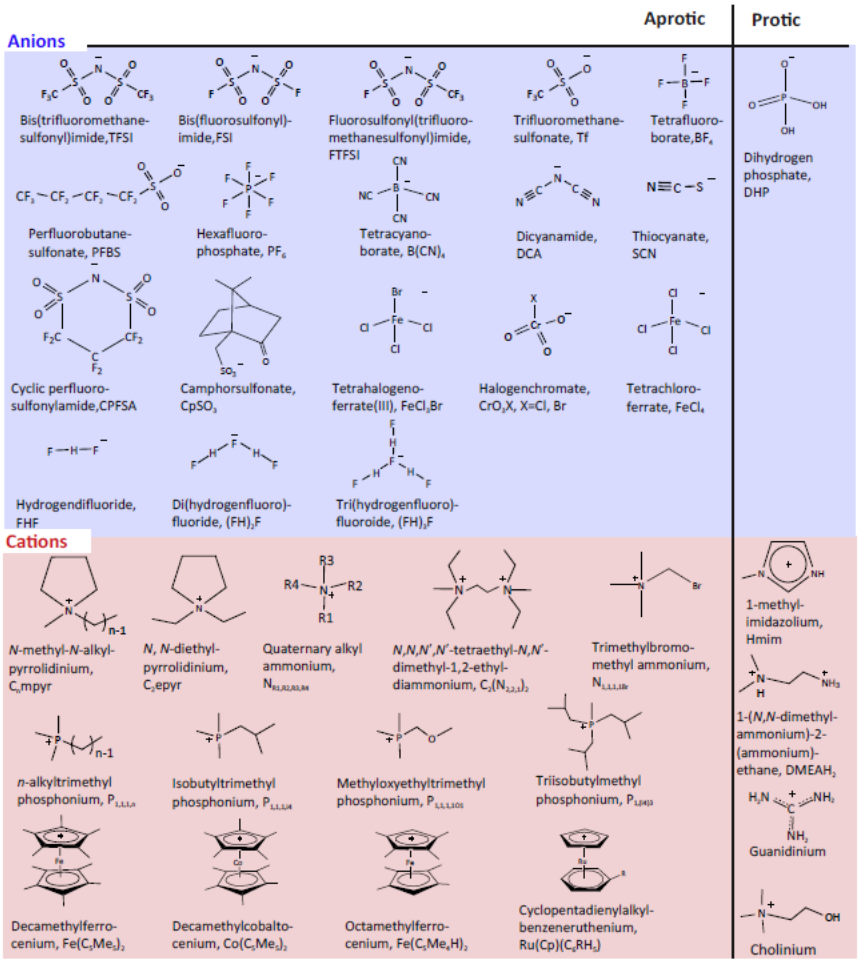

Figure 1.19. Typical OIPC ions are categorized into protic and aprotic depending on the availability of labile proton(s). Reprinted with permission from [65]. Copyright 2019, Elsevier.

OIPCs have shown good interactions with the surrounding species involved in the final device and have been used as electrolytes in different type of devices. For example, the cation C_2mpyr^+ has been combined with FSI anion and blended with LiFSI and a solid polymer electrolyte (SPE) for LIB showing conductivities around 10^{-4} S cm^{-1} at room temperature and good performance in Li|LFP cell (150 mAh g^{-1} at 0.2C).[66] Same cation has been also combined with TFSI anion for sodium-ion batteries (incorporating NaTFSI) reaching 10^{-4} S cm^{-1} at 60 ºC.[67] They have been also employed in EDLCs such as $C_1mpyr(FH)_2F$ with activated carbon reaching values above 220 F g^{-1} for 300 cycles.[68]

1.2.4. Charge transport

Electronic conduction has been investigated for many years in π-conjugated polymers as well as the ionic transport in polymer electrolytes and polyelectrolytes. In the following Sections 1.2.4.1-1.2.4.4 their mechanisms of transport and coupling in MIECs will be expounded with the latest models and techniques of characterization.

1.2.4.1. Electronic transport

In non-conjugated radical polymers, the electronic conduction occurs via electron hopping (Figure 1.20a), which is thermally activated between pendant radical sites by self-exchange reactions. They can also transfer charge through heterogeneous redox reactions and across interfaces (e.g. at current-collecting electrodes).[9] The distance between radical sites has been demonstrated to play a key role in efficient charge transfer to occur.[12] An electron transport assisted via the segmental motion of the pendant groups has been proposed by Yu et al., (Figure 1.20f), which implies a disorder dependence.[9] The addition of lithium salt to a TEMPO-based polymer (PTEO), increases the chain dynamics, promoting an improvement of the electronic conductivity across long channel lengths in a synergistic step where the ionic conductivity is enhanced as well.

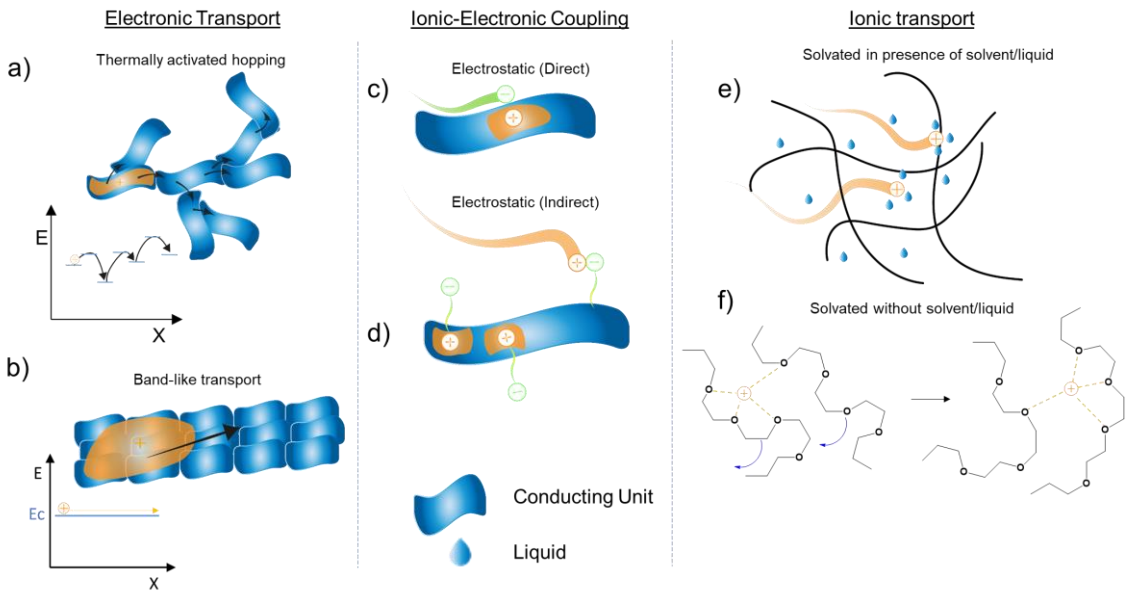

Figure 1.20. Mechanisms of electronic and ionic transports and ionic-electronic coupling. Electronic conduction given by a) thermally activated hopping and b) band-like transport. Ionic-electronic coupling given by c) directly electrostatic and d) indirectly electrostatic. Ionic conduction e) through liquid and f) facilitated by the segmental motion of the polymer.

In conducting polymers, in addition to the degree of doping, the ordering of the chains, which is directly influenced by the surrounding environment, also plays a key role in the efficiency of the charge transport. The movement of the electrons can take part along the backbone of the conducting polymer or across π-stacked backbones (Figure 1.20b). A high degree of π-conjugation allows the electrons to move along less-interrupted pathways through delocalized π-orbitals and between molecules where there is sufficient π–π overlapping. DFT calculations on neat and crystallites of doped PEDOT have demonstrated that the intra-chain ordering is considerably more efficient than the inter-chain transfer.[69] The disorder of the conducting polymer normally limits the delocalization of charge carriers and overlap, which leads to charge transport occurring as a series of thermally activated jumps between states with a favorable distance and energy that can be described by different models.[70] In contrast,

when the ordering is good enough, the conducting polymer can display diffuse band-like electron transport. Electronic conductivity values of 8800 S cm^{-1} have been obtained for single-crystal PEDOT nanowires where highly ordered diffraction spots were observed.[71] Several works have reported the electronic conduction behavior versus temperature resulting in a typical semi-metallic behavior with a thermally activated mechanism.[72,73]

Several characterization techniques have been employed to explain electronic transport. UV measurements are typically used to qualitatively quantify the amount of neutral, polaronic and bipolaronic states of a conducting polymer, which is directly related to the doping degree. Figure 1.21a shows an example of electrochemically doped poly(3-hexylthiophene-2,5-diyl) (P3HT), where the more oxidized compound shows no neutral states (below 600 nm), just polaronic (600-1200 nm) and bipolaronic states (>1200 nm).[53] X-ray based systems, such as X-ray diffraction (XRD), wide-angle X-ray scattering (WAXS) and small-angle X-ray scattering (SAXS) have been extensively employed to measure the degree of ordering of lamella interchain stacking and interchain π-π stacking, which is given by the intensity of the peaks related to the [1 0 0], [2 0 0] and [0 1 0], [0 2 0] signals respectively. In Figure 1.21b, grazing incidence WAXS spectra are shown which demonstrate the ordering of PEDOT:PSS blends with different loads of 4-(3-Butyl-1-imidazolio)-1-butanesulfonic acid triflate, exhibiting a much better stacking of PEDOT chains with 45.5 % loading.[74] Finally, in addition to FTIR (Fourier transform infrared) and X-ray photoelectron spectroscopy (XPS), which are commonly used to analyze structural changes and the interaction with different additives by the appearance of peaks or the shifting or intensity changes in the peaks, AFM is a useful technique to observe the PEDOT-PSS phase

segregation, where an example is presented in Figure 1.21c for a PEDOT:PSS LiTFSI system.[62]

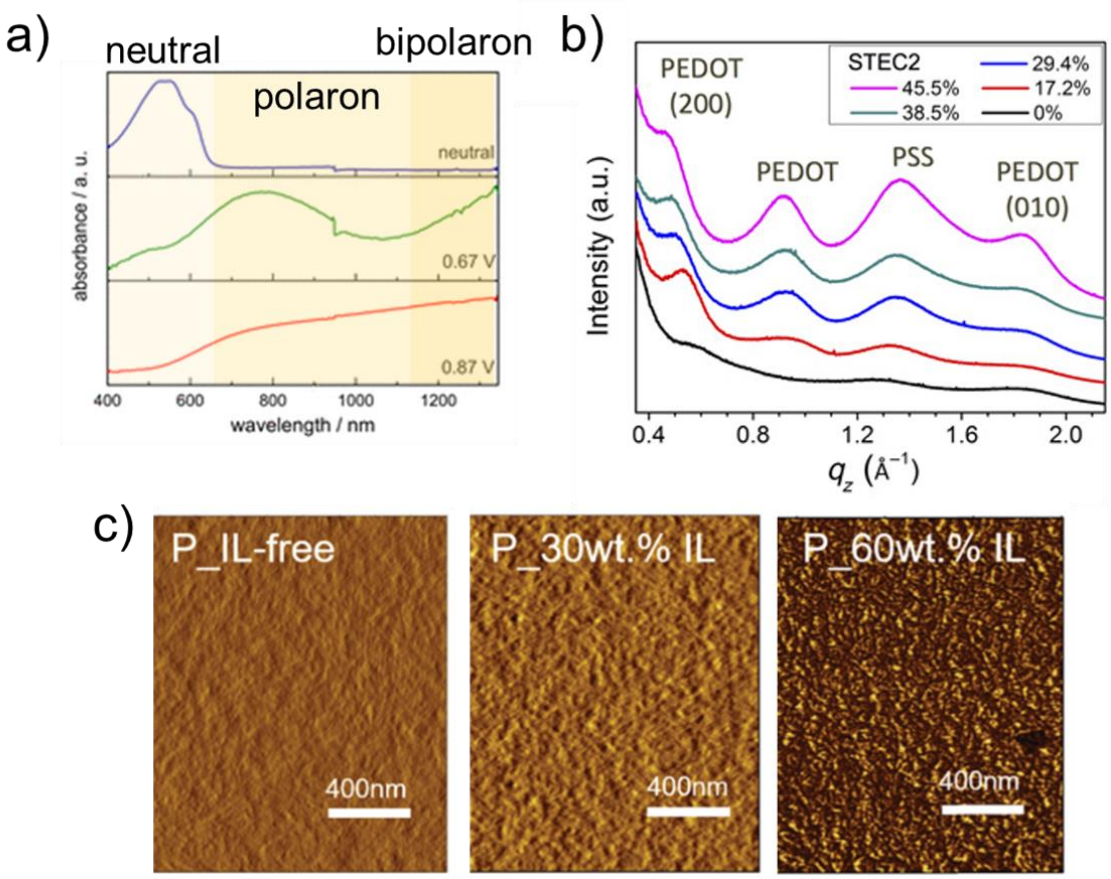

Figure 1.21. a) UV spectra of electrochemically doped P3HT. Reprinted with permission from [53]. Copyright 2020, American Chemical Society. b) GIWAX measurements of PEDOT:PSS with different loadings of 4-(3-Butyl-1-imidazolio)-1-butanesulfonic acid triflate ionic liquid. Reprinted with permission from [74]. Copyright 2017. c) AFM images of the phase segregation created by doping PEDOT-PSS with LiTFSI. Reprinted with permission from [62]. Copyright 2017, Royal Society of Chemistry.

1.2.4.2. Ionic transport

The ionic conduction can introduce new and diverse variables to a system that can sometimes result in a system being too complex to analyze. Ions can be multivalent, exist in multiple species and induce ion exchange, form pairs and larger clusters, be solvated and interact with traces of solvent. The ionic transference in a certain material is quantified as ionic conductivity (σ_{ionic}), which

represents the sum of the different ionic conductivity values of each mobile ionic specie, i. The contribution of each ion to the total conductivity is given by the transfer number (t_i). These parameters are mathematically related by Eq. 1.5.

$$\sigma_{ionic} = \sum_i t_i \sigma_{ionic,i} \quad \text{(Eq. 1.5)}$$

The ionic conductivity of an ion, i, is a function of the ion charge (z_i), number density (n_i), elementary charge (e) and mobility (μ_i) as follows the next equation:

$$\sigma_{ionic,i} = |z_i| n_i e \mu_i \quad \text{(Eq. 1.6)}$$

And finally, the ion mobility and diffusivity (D) are related by the Einstein equation (Eq. 1.7):

$$D_i = \frac{\mu_i k_B T}{e} \quad \text{(Eq. 1.7)}$$

where k_B is Boltzmann's constant and T is temperature.

When one of the ions is a polymer, the mobility of such an ion can be considered negligible versus small molecules. This effect has a particular interest for some applications when only the movement of a specific ion is required or desirable for a good performance. For instance, lithium-ion batteries where a high transfer number of lithium is required for the electrolytes, to prevent polarization of the system which typically ends up with the growth of lithium dendrites, causing a short circuit, or in ion pumps that deliver specific analytes.

The measurement of this parameter is quite sensitive to moisture and all the characterization related to it needs to be performed in a glovebox, under inert

atmosphere. The presence of liquid electrolyte or solvent wets and swells OMIECs, causing ion transfer to occur more rapidly through solvated ion vehicle transport (Figure 1.20e), making other contributions negligible. In dried films, the ion motion proceeds through ion hopping coupled with the segmental motion of the polymer side chains or backbone (Figure 1.20f). Ions can be solvated by either carbonates or ethers, radicals, polyelectrolytes or any moiety that could interact with them adding more degrees of freedom to flow through.

The ionic conductivity is typically obtained by measuring the ionic resistance and taking into account the geometry of the sample as described in Eq. 1.8.

$$\sigma_{ionic} = \frac{t}{R_{ionic}\, A} \qquad \text{(Eq. 1.8)}$$

where t is the thickness and A is the area of the sample. Electrochemical impedance spectroscopy (EIS) has been widely used, not only to measure the ionic conductivity but also the number of transference in the field of electrolytes, showing a totally different behavior than mixed conductors, and this will be explained in Section 1.2.4.4. Plots of log (σ_{ionic}) versus $1000/T$ following the Arrhenius equation (Eq. 1.9) are typically presented in studies of ionic conductivity to evaluate the conductivity dependence with temperature.

$$\sigma_{ionic} = \sigma_0 \exp\left(\frac{-Ea}{RT}\right) \qquad \text{(Eq. 1.9)}$$

where σ_{ionic} is the ionic conductivity, σ_0 is the pre-exponential factor, E_a is the activation energy, R the universal gas constant and T the absolute temperature. It is desirable to have high ionic conductivities with low activation energies that

enable the conduction at room temperature, avoiding the need for activation by temperature.[75]

Despite the unnoticed and underestimated ionic contribution of CP, ionic conductivities of 0.02 S cm^{-1} have been reached for high relative humidity systems (PEDOT:PSS – nanofibrillated cellulose (NFC) at 80 % relative humidity (RH)).[44] Nonetheless, the bottleneck for dried systems is around the values of solid polyelectrolytes/polymer electrolytes, 10^{-3}-10^{-4} S cm^{-1}.

1.2.4.3. Ionic-Electronic coupling

Overall, while a high crystallization of the conducting polymer results in high electronic conductivity, it limits the ionic dynamics. In fact, many works have used the suppression of crystallinity for the improvement of the ionic conductivity.[76,77] The addition of lithium salts to polymers that can solvate it, such as PEO; a common electrolyte, used since the 1980s thanks to Professor M. Armand, diminishes the crystallinity of the polymer (PEO) enabling the ion conduction.[78] However, there are studies reported that have included lithium salts to polymer electrolyte (e.g. polyvinylpyridine or PEO) based OMIECs resulting in an enhancement of both conductivities.[9,37,38,41,79] The mechanism of this controversial behavior is not fully understood. In any case, the coupling between electronic and ionic species is fundamental for batteries, solid-state electronics and energy devices, though its study is in a steady state.

The addition of ionic dopants allows for strategic ionic−electronic coupling that could lead to electronic structural modifications and consequently modulate the electronic conduction in these materials. Due to the intrinsic demand of

charge balance in all systems, for there to be a presence of an electronic charge, a stabilizing excess ionic charge with the net opposite sign is required. Conducting polymers combined with just polymer electrolytes need the inclusion of mobile ions to stabilize the doping state, while OMIECs stabilized by polyelectrolytes do not need extra ions. The ionic-electronic coupling can proceed directly (Figure 1.20c), via electrostatically charge transference (for instance the protonation of PANI)[35] or is facilitated by a self-exchange reaction (radical polymers),[9] and the subsequent dragging of ions. But also can proceed indirectly as it is represented in Figure 1.20d.[35]

EIS has been used to deconvolute the electronic and ionic conductivities, which is explained in Section 1.2.4.4, and also the ionic-electronic coupling by measuring the volumetric capacitance or the electrochemical density of states.[80–82]

The geometry, size, as well as intended application govern the direction, speed and dimension along which the ions and electrons flow. The reason why conducting polymers are often employed as thin films (from nm to µm) is because the ionic/electron transport is always more favorable along the surface than across the defects and layers of thickness. For instance, in applications such as batteries, where the ionic and electronic transport take place across the film (see Figure 1.22a), the best performances are reached for really thin films that show highly active cyclic voltammograms, while in thick films, that activity drops. Not only do the theoretical transport mechanisms matter, but also the dimension and geometry of the designed devices play key roles in the electronic transport, which should also be considered in their scalability and understanding.

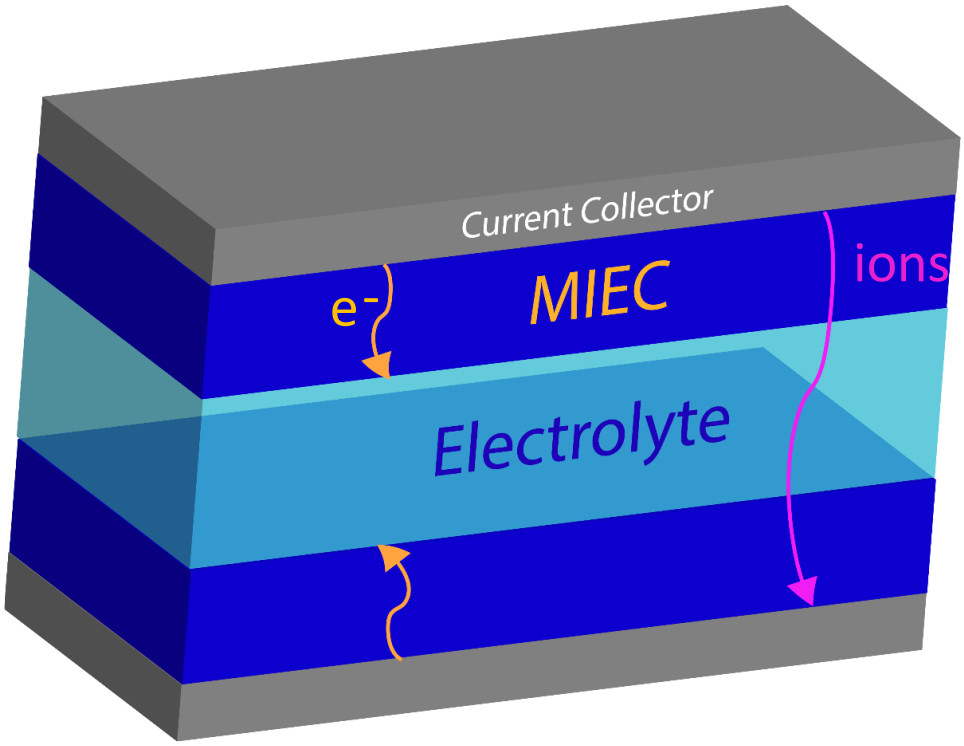

Figure 1.22. Electronic and ionic transport in batteries depicted with yellow and pink arrows, respectively. Current collectors, electrodes and electrolyte are represented with grey, dark and light blue colours, respectively.

1.2.4.4. Charge transport analysis

Electrochemical Impedance Spectroscopy (EIS) is a powerful characterization technique that applies a small AC voltage to an electrochemical cell and then measures the frequency-dependent complex impedance through the cell. This kind of measurement results in real and imaginary components that are typically represented in Nyquist plots, providing information about the ionic resistance and store charge respectively, in different processes occurring in the sample. EIS has been largely used to extract the mobility and conductivities of ionic[44] and electronic transport.[83] Even though some systems are satisfactorily modeled with simple circuits, mixed conductors generally have some more complex impedance spectra.

These Nyquist plots must be interpreted by fitting an equivalent circuit that is a representation of what is happening electronically in a sample. That equivalent circuit must have a physical meaning, considering the involved processes in a certain material, and taking into account that complex equivalent circuits can fit any Nyquist plot, but might not have a comprehensive sense. Different elements can be used such as resistances (R), capacitors (C), constant phase elements (Q), Warburg impedances (W), or inductors (L), that can be combined in serial or in parallel depending on the material and can have completely different meanings. Whereas serial connections are related to layer-by-layer materials or sequential elements, parallel ones refer to different pathways along which species can flow simultaneously. Although many systems are suitably modeled with simple circuits, OMIECs sometimes present some complications in finding the perfect equivalent circuit.

In ionic conductors, the common shape of graphs is a single semicircle followed by a tail at low frequencies, as represented in Figure 1.23a with a common equivalent circuit for electrolytes. Contrarily, in OMIECs, when the order of the ionic and electronic conductivity values are similar to each other, two semicircles appear (see Figure 1.23b). Nonetheless, ionic conductivity is usually much lower in conductive polymers than the electronic conduction and for this reason, only one semicircle attributed to the ionic conduction appears because the electronic resistance is negligible and not possible to measure with this technique, as demonstrated in Figure 1.23c.[84] Another difference between ionic conducting polymers and mixed conductors worth mentioning is the absence of tails in MIECs, because the interfacial capacitance is shunted by the electronic current at low frequencies. As can be observe from the shape of the Nyquist plots

and the usual equivalent circuits depicted in Figure 1.23, the measurement of the electronic conductivity can be measured for one MIEC but not for the other depending on the MIEC and system properties.

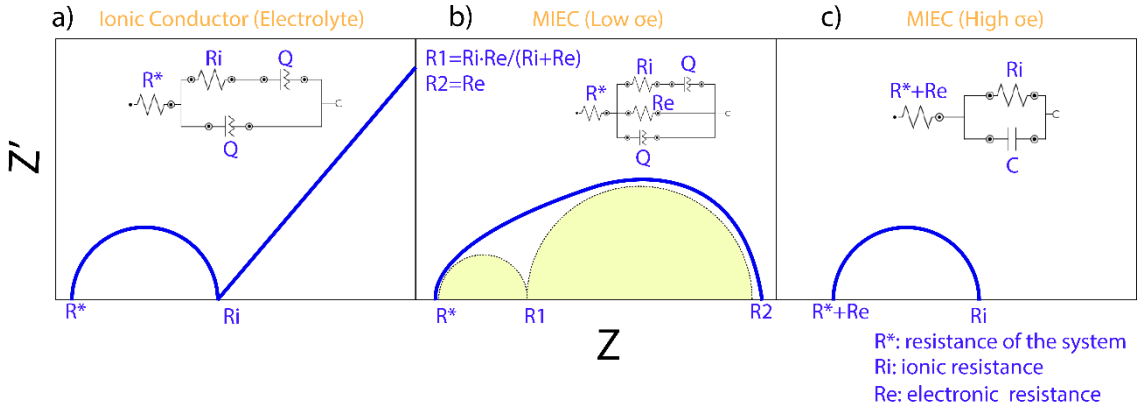

Figure 1.23. Typical Nyquist plots obtained by EIS for a) electrolytes, b) MIECs with low σ_e and c) MIECs with high σ_e, as well as their respective common equivalent circuits used.

To quantify electronic transport, several systems have been developed. The 4-point probe (4PP) and van der Pauw methods (see Figure 1.24 a and b, respectively) enable the measurement of the electronic conduction along with different directions of a film by applying a potential between two points of the sample and recovering a current in another two different points. The electronic conductivity is then calculated according to Eq. 10, by taking into account the electronic resistance (R_e) and film thickness (t).

$$\sigma_e = \frac{1}{R_e \cdot t} \qquad \text{(Eq. 10)}$$

In these techniques, an electron diffusion across the thickness occurs making the electronic resistance higher in thick films than in thin ones. Several works have developed physical models as well as corrections factors to account for this which are included in current 4PP devices and their software, which

should not be forgotten.[85,86] Despite those corrections, it should be acknowledged that the resulting values are estimations and even nowadays thin films always show higher electronic conductivity.

In contrast, DC polarization has been utilized to measure the electronic conductivity across a sample covered by ion-blocking Ag electrodes on both sides.[87] After applying a DC polarization, the steady-state current is recorded and plotted versus the applied potential, obtaining linear graphs as shown in Figure 1.24c. Interestingly, this last technique also permits the decoupling of the ionic conduction once the current is stabilized. However, equally to the EIS measurements, it also depends on the material, not being possible to decouple very low ionic conductivities (since the current will be given mostly by electrons and no drop in current will be observed).

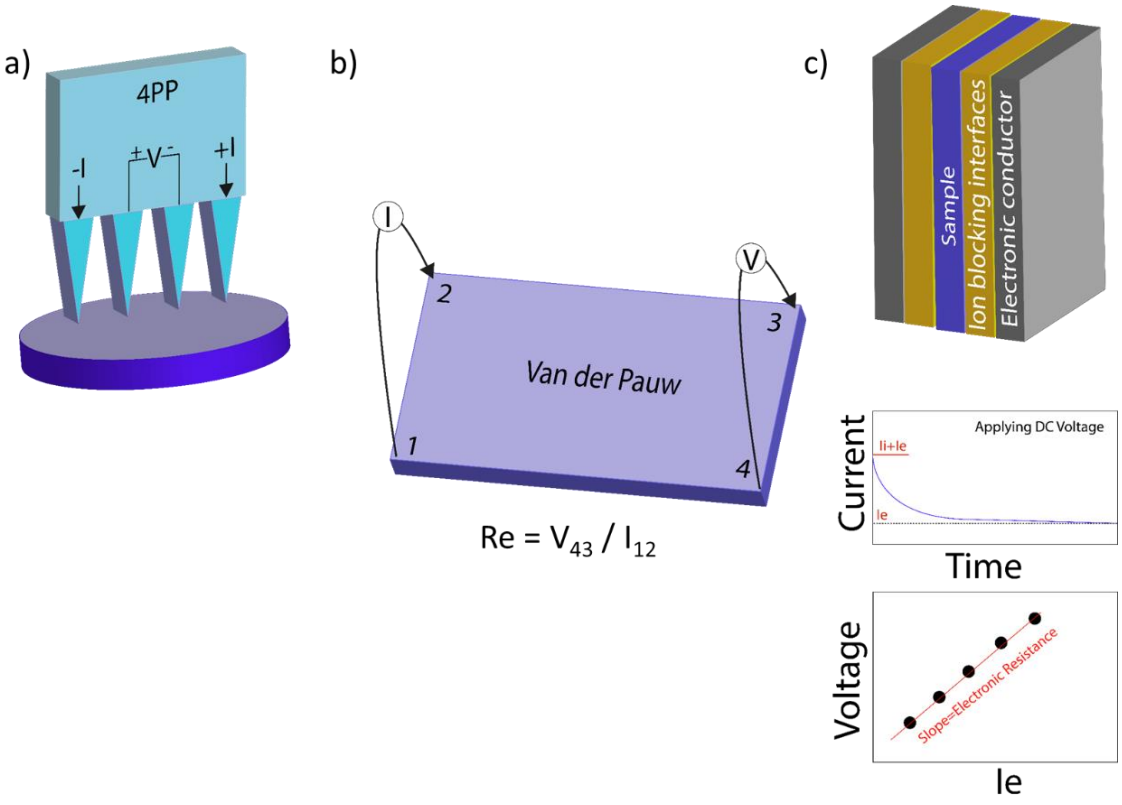

Figure 1.24. Common approaches for the quantification of electronic transport include a) the 4PP, b) the Van der Pauw method and c) via DC polarization.

1.3. Applications of OMIECs in Energy Storage Systems

The use of conductive polymers in batteries dates back to the 1980s when Yoshino et al. assembled a $LiCoO_2$ cathode with a polyacetylene (PA) anode to form $LiCoO_2$/PA full cell Li-ion batteries.[88] However, it had some deficiencies such as chemical instability and low density. In an attempt to overcome these performance issues, the same author replaced PA with carbonaceous materials, producing a new family of batteries with a huge impact, due to their high power density, low weight and versatile design.

CPs exhibit a pseudocapacitive behavior showing a rectangular shape during CVs despite being based on a faradaic mechanism. Specifically in the case of PEDOT:PSS, thiophene rings get oxidized and reduced reversibly in the range of -0.5 – 1 V vs Ag/AgCl. This faradaic contribution is largely improved with the electronic conductivity of the polymer. Besides, they also benefit from its fast redox kinetics showing values above 150 F g^{-1} for bulk materials[89] and 300 F g^{-1} in very thin layers of deposited material by VPP in the field of supercapacitors.[90]

Immense efforts have been dedicated to devise more efficient active materials as introduced in Section 1.1.1. On the anode side, graphite competitors have grown, with materials such as silicon, tin and titanium-based nanostructures that possess higher theoretical capacity.[91–94] Nonetheless, the enhanced capacity means more lithium can be stored, which comes accompanied by larger volume changes during cycling that induce cracking of the anode. This

phenomenon results in side reactions, contact loss and finally capacity fading.[91,95] On the other hand, others cathode active materials have been developed such as LFP,[2] NMC[96] and NCA,[97] satisfying the demands of cost and capacity.

To sustain those active materials, binders are required; polyvinylidene fluoride (PVDF) is the typically used binder material in conventional batteries. However, PVDF is isolating and presents drawbacks including the requirement of carbon additives to electronically connect all the active material, while the use of N-Methyl-2-pyrrolidone (NMP) solvent in the electrode fabrication is toxic.[98] An ideal binder should create strong interactions with the active material but also stick to the current collector to prevent electrode delamination. Additionally, the binder should form a continuous electronically connected electrode, accommodate volume changes during cycling, remain chemically and electrochemically stable, or show reversible processes in the application's conditions. Finally, the binder material should be easily processed both in its synthesis and electrode fabrication. Several studies have suggested that the cyclability problems of some of the most promising active materials could be overcome by selecting a more adequate binder.[1,99,100]

Many materials have been investigated for their potential as binders, such as sodium carboxymethyl cellulose (CMC),[100] sodium alginate (SA),[101] carboxymethyl chitosan (CCTS)[102] and nanofibrillated cellulose (NFC).[103] Generally, these showed strong polar interactions and polar-solvent dispersibility, making them processable from an aqueous system, but all of them still remain electronically isolating. The conventional quantities of each material in an electrode are at least 10 wt.% of carbon, 5-10 wt.% of binder and the rest is active material for cathodes in liquid state devices. Conducting polymers can play a dual

role as both the binder and conductive additive, opening the possibility of even using carbon-free electrodes and hence, increasing the amount of active material used. In this regard, PEDOT:PSS has been successfully applied as the binder in carbon-free systems, including Li-ion[104] and Li-S,[105] and it has also shown good electrochemical stability and performance as an additive in high voltage systems, including Lithium-ion batteries with NMC-111.[106]

Recent works have reported a new class of binders that combines conducting polymers such as PANI, Ppy or Pth (polythiophene) with the previously listed carboxylate-containing polymers (CMC, SA, CCTS, NFC), which form different morphologies including nanospheres[107,108] and nanofibers.[109] This strategy offers continuous ionic and electronic transport doped by carboxylate polymers with stronger binder properties. For instance, the interactions between Si and CMC carboxyl-silanol; covalent and hydrogen bonding might mitigate the volume changes of Si-based advanced anodes.[110]

Each kind of battery has intrinsic drawbacks that need to be solved. Although lithium-sulfur batteries offer superior energy storage capacity thanks to the high theoretical specific capacity of the sulfur cathode, they are still at a low technology readiness level. The growth of polysulfides and consequent cathode deformation makes it impossibly difficult to reach a reasonable lifespan. Several studies point out the use of alternative binders like CP, whose interactions with sulfur and polysulfide species (Li_2S and Li_2S_2) can suppress shuttle effects, maintaining the electronic pathways at the same time.[105,111,112]

Modified multifunctional conductive binders have also been synthesized and successfully applied in carbon-free electrodes, where processability and

enhanced binding affinity are required. For instance, sodium alginate poly(3,4-propylenedioxythiophene) (SA-PProDOT), exhibited stronger adhesion versus CMC, SA or PVDF binders even though the mechanism for the improved mechanical properties is not yet elucidated.[113] It is also worth mentioning that more redox activity has also been incorporated into conducting polymers either using redox polymers (PEDOT-TEMPO)[20] or biopolymers (PEDOT-lignin),[33] which can be used as direct electrodes or adding an extra capacity.

The porosity of electrodes is also known to impact performance and needs to be controlled. Das et al., observed that the higher the amount of CP in cathode formulation, the lower is the porosity and hence, limited electrolyte diffusion into the electrode is generated in a carbon-free system.[104] CPs have also been in situ polymerized in the presence of active materials,[114] and formed hydrogels with active materials by the use of crosslinkers and dopants.[115,116]

All the previously listed batteries are in liquid state, where the ionic conductivity is given by the liquid electrolyte and it is not intrinsically necessary in the electrode as it is going to be wet. Therefore, the commented previous works have benefited only from the better electronic interconnection between redox-active particles. In all-solid-state batteries, the mechanism is totally different. Solid-state batteries were designed to be safer devices than liquid state batteries, which traditionally use volatile, flammable and leakable electrolytes. Solid electrolytes prevent the growth of metal dendrites that can result in fires and explosions as explained in Section 1.1.1. The development of optimum, dense and scalable devices passes directly through the development of mixed conductors, which are considered to play a key role by enabling ion transfer to occur throughout the entire electrode.

Besides, the industry is requiring compact electrodes for solid state devices to minimize the contact resistances given by porosity voids, now counterproductive. Therefore, the use of electronic conducting carbon, despite its mature and low cost, needs to be optimized. Some strategies to compact the electrodes, apart from calendaring, are the removal of porous conducting carbon and its replacement for conducting polymers. However, it has not been reported yet any device for solid-state with promising cycling.

The energy stored in MIEC-based batteries is dependent on the ionic-electronic coupling, but the adequate charging rates and the available power are limited by the ionic conductivity[35] being much more important in all-solid-state batteries where there is no liquid wetting the system, providing an all-over ionic connection. Therefore, the progress in all-solid-state batteries passes directly through that of MIECs.

1.4. Motivation and objectives

Nowadays, energy storage systems play a key role in our future as a society by enabling the handling of clean energy resources and employment in electronic devices and the transport sector. During the last decades, multiple accessories dependent on batteries have been developed increasing the energy consumption with the facilities they offer. Besides, there is a global concern about environmental problems such as pollution and the use of non-renewable resources like fossil fuel. Consequently, it is being pursued high-performance technologies that enable large storage capacities at versatile rates keeping balanced safety, cost-effectiveness and processability.

In this area, organic mixed ionic-electronic conductors are considered promising candidates to be employed in the next generation of energy storage devices due to their superior conductivities, easy processing, low density and electrochemical stability. Their properties make them functional materials to be tunned depending on the application for batteries and supercapacitors. OIPCs are proposed as ideal allies of conducting polymers allowing a synergistic effect of ionic and electronic conductivity improvement. Accordingly, the main goal of this PhD thesis is to develop new OMIEC materials with light-weight, good electrochemical properties and sustainable processability. The nature of the targeted OMIECs is based on the innovative approach of combining for first time conducting polymer (PEDOT) and OIPCs for the improvement of energy storage systems. Within this scope, the specific objectives of this thesis are the following:

- ✓ Synthesis and characterization of conducting polymers based on PEDOT, ionic polymers and OIPCs with different counter-ions.
- ✓ Development of MIEC composites combining conducting polymers and OIPCs with enhanced ionic and electronic conductivities, as well as mechanical properties.
- ✓ Structural, thermal, morphological and electrochemical characterization of the developed MIEC composites to understand their structure-property relationships.
- ✓ Application of the developed MIEC composites as cathode binders in lithium-ion batteries, with liquid and solid-state electrolytes.
- ✓ Optimization of electrode formulations to improve the capacity of energy delivered, cycle life and rate capability.

1.5. Outline of the thesis

In Chapter 1, a brief introduction to energy storage systems is given, followed by an overview of mixed ionic and electronic conductors, more in detail PEDOT based; organic ionic plastic crystals, as well as their charge transport mechanisms, common analysis techniques and most important application in energy storage devices. The motivation and goals of this thesis are also presented in this chapter.

In Chapter 2, we show the characterization of the commercially available conducting polymer PEDOT:PSS in combination with two of the most successfully applied OIPCs: C_2mpyrFSI and C_2mpyrTFSI. The composites exhibited a synergistic effect combining high electronic but also ionic conductivity. The materials were employed an in all-solid-state Li|LFP device replacing the catholyte and conducting carbon, being the first carbon-free cathode in this sector, with promising results

In Chapter 3, a new family of OMIEC is presented combining PEDOT and poly(diallyldimetrhylammonium) (PolyDADMA$^+$), which is one of the most successful polyelectrolytes employed in batteries and enables the study of different anions of study. The selected anions to combine PEDOT:PolyDADMA were bis(fluorosulfonyl)amide (FSI), bis(trifluoromethane)sulfonimide (TFSI), triflate and tosylate. Then, they were combined with the respective OIPC based on C_2mpyr$^+$ and the homolog anion to further improve their conductivities as well as their electrochemical response.

In Chapter 4, we present a detailed study about the effect of single ion-conducting polymers as binders for LIBs to address the effect that PolyDADMA-TFSI may have when applying PEDOT:PolyDADMA TFSI. For this reason, poly(lithium 1-[3-(methacryloyloxy) propylsulfonyl]-1-(trifluoromethanesulfonyl) imide) (PMTFSI-Li) and PolyDADMA-TFSI were selected as Li^+ and $TFSI^-$ single ion-conducting polymers. The assessment is mainly based on the electrochemical response, battery testing and EIS.

In Chapter 5, the best OMEICs developed in Chapters 2-3: PEDOT:PSS and PEDOT:PolyDADMA TFSI composites; are employed in LIBs as additives due to their superior conductivities to improve the current delivery for high-performance devices. The materials were used as binders for cathodes to evaluate the effect of polymer nature, OIPC and C65 presence.

In Chapter 6, the most relevant conclusions of this thesis are summarized

1.6. References

1. H. Chen, M. Ling, L. Hencz, H. Y. Ling, G. Li, Z. Lin, G. Liu and S. Zhang. Exploring Chemical, Mechanical, and Electrical Functionalities of Binders for Advanced Energy-Storage Devices. *Chem. Rev.* **2018**;118:8936–8982.

2. C. Liu, Z. G. Neale and G. Cao. Understanding electrochemical potentials of cathode materials in rechargeable batteries. *Mater. Today* **2016**;19:109–123.

3. T. Placke, R. Kloepsch, S. Dühnen and M. Winter. Lithium ion, lithium

metal, and alternative rechargeable battery technologies: the odyssey for high energy density. *J. Solid State Electrochem.* **2017**;21:1939–1964.

4. Q. Zhen, S. Bashir and J. L. Liu. *Nanostructured Materials for Next-Generation Energy Storage and Conversion: Advanced Battery and SupercapacitorsNanostructured Materials for Next-Generation Energy Storage and Conversion: Advanced Battery and Supercapacitors*, **2019**.

5. J. Zhao and A. F. Burke. Electrochemical Capacitors: Performance Metrics and Evaluation by Testing and Analysis. *Adv. Energy Mater.* **2021**;11:1–29.

6. P. Simon, Y. Gogotsi and B. Dunn. Where do Batteries and Supercapacitors Begin? *Science (80-.).* **2014**;343:1210–1211.

7. X. B. Cheng, R. Zhang, C. Z. Zhao and Q. Zhang. Toward Safe Lithium Metal Anode in Rechargeable Batteries: A Review. *Chem. Rev.* **2017**;117:10403–10473.

8. A. Banerjee, X. Wang, C. Fang, E. A. Wu and Y. S. Meng. Interfaces and Interphases in All-Solid-State Batteries with Inorganic Solid Electrolytes. *Chem. Rev.* **2020**;120:6878–6933.

9. I. Yu, D. Jeon, B. Boudouris and Y. Joo. Mixed Ionic and Electronic Conduction in Radical Polymers. *Macromolecules* **2020**;53:4435–4441.

10. T. Suga, Y. J. Pu, S. Kasatori and H. Nishide. Cathode- and anode-active poly(nitroxylstyrene)s for rechargeable batteries: p- and n-type redox switching via substituent effects. *Macromolecules* **2007**;40:3167.

11. H. Nishide and T. Suga. Organic Radical Battery. *Electrochem. Soc. Interface* **2005**;14:32–38.

12. E. P. Tomlinson, M. E. Hay and B. W. Boudouris. Radical Polymers and Their Application to Organic Electronic Devices. *Macromolecules* **2014**;47:6145–6158.

13. T. Suga, S. Sugita, H. Ohshiro, K. Oyaizu and H. Nishide. p- and n-Type Bipolar Redox-Active Radical Polymer : Toward Totally Organic Polymer-Based Rechargeable Devices with Variable Confi guration. *Adv. Mater.* **2011**;23:751–754.

14. L. Rostro, S. H. Wong and B. W. Boudouris. Solid State Electrical Conductivity of Radical Polymers as a Function of Pendant Group Oxidation State. *Macromolecules* **2014**;47:3713.

15. Y. Joo, V. Agarkar and S. H. Sung. A nonconjugated radical polymer glass with high electrical conductivity. *Science (80-.).* **2018**;359:1391–1395.

16. K. Nakahara, S. Iwasa, M. Satoh, Y. Morioka, J. Iriyama, M. Suguro and E. Hasegawa. Rechargeable batteries with organic radical cathodes. *Chem. Phys. Lett.* **2002**;359:351.

17. Z. Song and H. Zhoue. Towards sustainable and versatile energy storage devices: an overview of organic electrode materials. *Energy Environ. Sci.* **2013**;6:2280.

18. S. Wang, F. Li, A. D. Easley and J. L. Lutkenhaus. Real-time insight into the doping mechanism of redox-active organic radical polymers. *Nat. Mater.* **2019**;18:69–76.

19. H. Tokue, T. Murata, H. Agatsuma, H. Nishide and K. Oyaizu. Charge − Discharge with Rocking-Chair-Type Li+ Migration Characteristics in a Zwitterionic Radical Copolymer Composed of TEMPO and Tri fl uoromethanesulfonylimide with Carbonate Electrolytes for a High-Rate Li-Ion Battery. *Macromolecules* **2017**;50:1950–1958.

20. N. Casado, G. Hernandez, A. Veloso, S. Devaraj, M. David and M. Armand. PEDOT Radical Polymer with Synergetic Redox and Electrical Properties. *ACS Macro Lett.* **2016**;5:59–64.

21. K. Suwa, K. Oyaizu, H. Segawa and H. Nishide. Anti-Oxidizing Radical Polymer-Incorporated Perovskite Layers and their Photovoltaic Characteristics in Solar Cells. *ChemSusChem* **2019**;12:5207–5212.

22. L. Zheng, S. Mukherjee, K. Wang, M. E. Hay, B. W. Boudouris and X. Gong. Radical polymers as interfacial layers in inverted hybrid perovskite solar cells †. *J. Mater. Chem. A Mater. energy Sustain.* **2017**;5:23831–23839.

23. A. Dey, A. Singh, D. Das and P. K. Iyer. Organic Semiconductors: A New Future of Nanodevices and Applications. in *Thin Film Structures in Energy Applications*, ed. S. Babu Krishna Moorthy, Springer International Publishing, Cham, **2015**., pp. 97–128.

24. J. Moon, N. Thapliyal, K. Khadim and R. N. Goyal. Conducting polymer-based electrochemical biosensors for neurotransmitters : A review. *Biosens. Bioelectron.* **2018**;102:540–552.

25. I. Zozoulenko, A. Singh, S. K. Singh, V. Gueskine, X. Crispin and M. Berggren. Polarons, Bipolarons, And Absorption Spectroscopy of PEDOT. *ACS Appl. Polym. Mater.* **2018**;1:83–94.

26. E. Tsuchida, C. Shih and I. Shinohara. Synthesis of a Polymer Chain Having Conjugated Unsaturated Bonds by Dehydrohalogenation of Polyhalogen-Containing Polymers. *J. Polym. Sci.* **1964**;2:3347–3354.

27. D. J. Berets and D. S. Smith. Electrical Properties of Linear Polyacetylene. *Trans. Faraday Soc.* **1967**;64:823–828.

28. A. S. Macpherson, R. Siudak, D. E. Weiss and D. Willis. Electronic Conduction in Polymers. *Aust. J. Chem.* **1965**;18:493–505.

29. J. Fan, S. S. Rezaie, M. Facchini-rakovich, D. Gudi, C. Montemagno and M. Gupta. Tuning PEDOT:PSS conductivity to obtain complementary organic electrochemical transistor. *Org. Electron.* **2019**;66:148–155.

30. I. Uguz, C. M. Proctor, V. F. Curto, A. Pappa, M. J. Donahue, M. Ferro, R. M. Owens, D. Khodagholy, S. Inal and G. G. Malliaras. A Microfluidic Ion Pump for In Vivo Drug Delivery. *Adv. Mater.* **2017**;29:1701217.

31. I. Gualandi, D. Tonelli, F. Mariani, E. Scavetta, M. Marzocchi and B. Fraboni. Selective detection of dopamine with an all PEDOT:PSS Organic Electrochemical Transistor. *Nat. Publ. Gr.* **2016**;6:35419.

32. L. Gomes, A. Branco, T. Moreira, F. Feliciano, C. Pinheiro and C. Costa. Increasing the electrical conductivity of electrochromic PEDOT:PSS films – A comparative study. *Sol. Energy Mater. Sol. Cells* **2016**;144:631–640.

33. N. Casado, M. Hilder, C. Pozo-gonzalo and M. Forsyth. Electrochemical Behavior of PEDOT/Lignin in Ionic Liquid Electrolytes: Suitable Cathode/Electrolyte System for Sodium Batteries. *ChemSusChem* **2017**;10:1783–1791.

34. X. Wang, X. Zhang, L. Sun, D. Lee, S. Lee, M. Wang, J. Zhao, Y. Shao-horn, M. Dinc, T. Palacios and K. K. Gleason. High electrical conductivity and carrier mobility in oCVD PEDOT thin films by engineered crystallization and acid treatment. *Sci. Adv.* **2018**;4:5780.

35. B. D. Paulsen, K. Tybrandt, E. Stavrinidou and J. Rivnay. *Organic mixed ionic – electronic conductorsOrganic mixed ionic – electronic conductors*, Springer US.

36. M. Y. Teo, N. Ravichandran, N. Kim, S. Kee, L. Stuart, K. C. Aw and J. Stringer. Direct Patterning of Highly Conductive PEDOT:PSS/Ionic Liquid Hydrogel via Microreactive Inkjet Printing. *ACS Appl. Mater. Interfaces* **2019**;11:37069–37076.

37. L. A. Renna, J. D. Lenef, M. Bag and D. Venkataraman. Mixed Ionic – Electronic Conduction in Binary Polymer Nanoparticle Assemblies. *Adv. Mater. Interfaces* **2017**;4:1700397.

38. S. Van Reenen, T. Akatsuka, D. Tordera, M. Kemerink and H. J. Bolink. Universal Transients in Polymer and Ionic Transition Metal Complex Light-Emitting Electrocemical Cells. *J. Am. Chem. Soc.* **2013**;135:886–891.

39. H. Erothu, J. Kolomanska, P. Johnston, S. Schumann, D. Deribew, D. T. W. Toolan, A. Gregori, C. Dagron-lartigau, G. Portale, W. Bras, T. Arnold, A. Distler, R. C. Hiorns, P. Mokarian-tabari, T. W. Collins, J. R. Howse and P. D. Topham. Synthesis, Thermal Processing, and Thin Film Morphology of Poly(3- hexylthiophene) − Poly(styrenesulfonate) Block Copolymers. *Macromolecules* **2015**;48:2107–2117.

40. S. N. Patel, A. E. Javier, K. M. Beers, J. A. Pople, V. Ho, R. A. Segalman and N. P. Balsara. Morphology and thermodynamic properties of a copolymer with an electronically conducting block: poly(3-ethylhexylthiophene)-block-poly(ethylene oxide). *Nano Lett.* **2012**;12:4901–4906.

41. S. N. Patel, A. E. Javier, G. M. Stone, S. A. Mullin and N. P. Balsara. Simultaneous conduction of electronic charge and lithium ions in block copolymers. *ACS Nano* **2012**;6:1589–1600.

42. S. Inal, J. Rivnay, P. Leleux, M. Ferro, M. Ramuz, J. C. Brendel, M. M. Schmidt, M. Thelakkat and G. G. Malliaras. A High Transconductance Accumulation Mode Electrochemical Transistor. *Adv. Mater.* **2014**;26:7450–7455.

43. A. Giovannitti, D. Sbircea, S. Inal, C. B. Nielsen and E. Bandiello. Controlling the mode of operation of organic transistors through side-chain engineering. *Proc. Natl Acad. Sci. USA* **2016**;113:12017–12022.

44. A. Malti, J. Edberg, H. Granberg, Z. U. Khan, J. W. Andreasen, X. Liu, D. Zhao, H. Zhang, Y. Yao, J. W. Brill and I. Engquist. An Organic Mixed Ion – Electron Conductor for Power Electronics. *Adv. Sci.* **2016**;3:1–9.

45. F. Jonas, G. Heywang and W. Schmidtberg. German patent DE 38 13 589 A1 (Bayer AG). **1988**.

46. S. Kirchmeyer and K. Reuter. Scientific importance, properties and growing applications of poly(3,4-ethylenedioxythiophene). *J. Mater. Chem.* **2005**;15:2077–2088.

47. K. S. Jang, H. Lee and B. Moon. Synthesis and characterization of water soluble polypyrrole doped with functional dopants. *Synth. Met.*

2004;143:289–294.

48. S. Sinha, S. Bhadra and D. Khastgir. Effect of Dopant Type on the Properties of Polyaniline. *J. Appl. Polym. Sci.* **2009**;112:3135–3140.

49. B. J. Polk, K. Potje-kamloth and M. Josowicz. Role of Protonic and Charge Transfer Doping in Solid-State Polyaniline. *J. Phys. Chem. B* **2002**;106:11457–11462.

50. H. Yano, K. Kudo, K. Marumo and H. Okuzaki. Fully soluble self-doped an electrical conductivity greater than 1000 S cm-1. *Sci. Adv.* **2019**;5:1–10.

51. X. Wang, K. Ko, C. Yin, F. Wang, Q. Zhu and T. Tang. Enhancement of thermoelectric performance of PEDOT:PSS films by post-treatment with a superacid. *RSC Adv.* **2018**;8:18334–18340.

52. H. Shuzhong, M. Masakazu, K. Kazuhiro, L. Lingyun and W. Qingshuo. Reversible Protonic Doping in Poly(3,4-Ethylenedioxythiophene). *Polymers (Basel).* **2018**;10:1065.

53. D. Neusser, C. Malacrida, M. Kern, Y. M. Gross, J. Van Slageren and S. Ludwigs. High Conductivities of Disordered P3HT Films by an Electrochemical Doping Strategy. *Chem. Mater.* **2020**;32:6003–6013.

54. M. J. Ikei, T. Y. Amaya, S. U. Ramoto and K. M. Atsumoto. Conductivity Enhancement of PEDOT/PSS Films by Solvent Vapor Treatment. *Int. J.*

Soc. Mater. Eng. Resour. **2014**;20:158–162.

55. A. Mazaheripour, S. Majumdar, D. Hanemann-rawlings, E. M. Thomas, C. Mcguiness, L. Alencon, M. L. Chabinyc and R. A. Segalman. Tailoring the Seebeck Coefficient of PEDOT:PSS by Controlling Ion Stoichiometry in Ionic Liquid Additives. *Chem. Mater.* **2018**;30:4816–4822.

56. J. M. Pringle, P. C. Howlett, D. R. Macfarlane and M. Forsyth. Organic ionic plastic crystals : recent advances. *J. Mater. Chem.* **2010**;20:2056–2062.

57. A. Basile, M. Hilder, F. Makhlooghiazad, C. Pozo-gonzalo, D. R. Macfarlane, P. C. Howlett and M. Forsyth. Ionic Liquids and Organic Ionic Plastic Crystals: Advanced Electrolytes for Safer High Performance Sodium Energy Storage Technologies. *Adv. Energy Mater.* **2018**;8:1703491.

58. S. Kee, H. Kim, S. Harish, K. Paleti, A. El Labban, M. Neophytou, A. Emwas, H. N. Alshareef and D. Baran. Highly Stretchable and Air-Stable PEDOT:PSS/Ionic Liquid Composites for Effi cient Organic Thermoelectrics. *Chem. Mater.* **2019**;31:3519–3526.

59. A. De Izarra, S. Park, J. Lee, Y. Lansac and Y. H. Jang. Ionic Liquid Designed for PEDOT:PSS Conductivity Enhancement. *J. Am. Chem. Soc.* **2018**;140:5375–5384.

60. H. Wang, U. Ail, R. Gabrielsson, M. Berggren and X. Crispin. Ionic Seebeck

effect in conducting polymers. *Adv. Energy Mater.* **2015**;5:1–6.

61. J. Xiong, C. Liu and J. Xu. Highly electrical and thermoelectric properties of a PEDOT:PSS thin- film via direct dilution – filtration †. *RSC Adv.* **2015**;5:60708–60712.

62. Q. Li, M. Deng, S. Zhang, D. Zhao, Q. Jiang, C. Guo, Q. Zhou and W. Liu. Synergistic enhancement of thermoelectric and modulated PEDOT flexible films †. *J. Mater. Chem. C* **2019**;7:4374.

63. S. Kee, N. Kim, B. S. Kim, S. Park, Y. H. Jang, S. H. Lee, J. Kim, J. Kim, S. Kwon and K. Lee. Controlling Molecular Ordering in Aqueous Conducting Polymers Using Ionic Liquids. *Adv. Mater.* **2016**;28:8625–8631.

64. M. Yoshizawa-Fujita, E. Kishi, M. Suematsu, T. Takekawa and M. Rikukawa. A Plastic Electrolyte Material in a Highly Desirable Temperature Range: N-Ethyl-N-methylpyrrolidinium Bis(fluorosu lfonyl)amide. *Chem. Lett.* **2014**.1909–1911.

65. H. Zhu, D. R. MacFarlane, J. M. Pringle and M. Forsyth. Organic Ionic Plastic Crystals as Solid-State Electrolytes. *Trends Chem.* **2019**;1:126–140.

66. X. Li, Z. Zhang, S. Li, K. Yang and L. Yang. Polymeric ionic liquid-ionic plastic crystal all-solid-state electrolytes for wide operating temperature

range lithium metal batteries. *J. Mater. Chem. A* **2017**;5:21362–21369.

67. M. Forsyth, T. Chimdi, A. Seeber, D. Gunzelmann and P. Howlett. Structure and dynamics in an organic ionic plastic crystal, N-ethyl-N-methyl pyrrolidinium bis(trifluoromethanesulfonyl) amide, mixed with a sodium salt. *J. Mater. Chem. A* **2014**;2:3993–4003.

68. R. Taniki, K. Matsumoto, T. Nohira and R. Hagiwara. All solid-state electrochemical capacitors using N,N-dimethylpyrrolidinium fluorohydrogenate as ionic plastic crystal electrolyte. *J. Power Sources* **2014**;245:758–763.

69. J. F. Franco-Gonzalez and I. V Zozoulenko. Molecular Dynamics Study of Morphology of Doped PEDOT: From Solution to Dry Phase. *J. Phys. Chem. B* **2017**;121:4299–4307.

70. N. Tessler, Y. Preezant, N. Rappaport and Y. Roichman. Charge Transport in Disordered Organic Materials and Its Relevance to Thin-Film Devices: A Tutorial Review. *Adv. Mater.* **2009**;21:2741–2761.

71. B. Cho, K. S. Park, J. Baek, H. S. Oh, Y. K. Lee and M. M. Sung. Single-Crystal Poly(3,4-ethylenedioxythiophene) Nanowires with Ultrahigh Conductivity. *Nano Lett.* **2014**;14:3321–3327.

72. J. Y. Kim, J. H. Jung, D. E. Lee and J. Joo. Enhancement of electrical conductivity of poly(3,4-ethylenedioxythiophene)/poly(4-styrenesulfonate)

by a change of solvents. *Synth. Met.* **2002**;126:311–316.

73. A. B. Kaisera and C. K. Subramaniama. Electronic transport properties of conducting polymers and polymer blends *. *Synth. Met.* **1995**;69:197–200.

74. Y. Wang, C. Zhu, R. Pfattner, H. Yan, L. Jin, S. Chen, F. Molina-lopez, F. Lissel, J. Liu, N. I. Rabiah, Z. Chen, J. W. Chung, C. Linder, M. F. Toney, B. Murmann and Z. Bao. A highly stretchable, transparent, and conductive polymer. *Sci. Adv.* **2017**;3:1–10.

75. D. W. Kang, K. A. Lee, M. Kang, J. M. Kim, M. Moon, J. H. Choe, H. Kim, D. W. Kim, J. Y. Kim and C. S. Hong. Cost-effective porous-organic-polymer-based electrolyte membranes with superprotonic conductivity and low activation energy. *J. Mater. Chem. A* **2020**;8:1147–1153.

76. J. L. Olmedo-Martinez, L. Meabe, A. Basterretxea, D. Mecerreyes and A. J. Müller. Effect of Chemical Structure and Salt Concentration on the Crystallization and Ionic Conductivity of Aliphatic Polyethers. *Polymers (Basel).* **2019**;11:452.

77. J. L. Olmedo-Martinez, L. Porcarelli, A. Alegria, D. Mecerreyes and A. J. Mu. High Lithium Conductivity of Miscible Poly (ethylene oxide)/ Methacrylic Sulfonamide Anionic Polyelectrolyte Polymer Blends. *Macromolecules* **2020**;53:4442–4453.

78. M. Armand. Polymer Solid Electrolytes - An Overview. *Solid State Ionics*

1983;9:745–754.

79. S. Van Reenen and M. Kemerink. Correcting for contact geometry in Seebeck coefficient. *Org. Electron.* **2014**;15:2250–2255.

80. H.-D. Wiemhöfer. Coupling Between Electron and Ion Transport in Mixed Conductors. *Solid State Ionics* **1990**;41:530–534.

81. E. M. Barea and E. Palomares. A review of recent results on electrochemical determination of the density of electronic states of nanostructured metal-oxide semiconductors and organic hole conductors. *Inorganica Chim. Acta* **2008**;361:684–698.

82. A. Savva, S. Wustoni and S. Inal. Ionic-to-electronic coupling efficiency in PEDOT:PSS films operated in aqueous electrolytes. *J. Mater. Chem. C* **2018**;6:12023–12030.

83. G. Garcia-Belmonte, J. Bisquert and G. S. Popkirov. Determination of the electronic conductivity of polybithiophene films at different doping levels using in situ electrochemical impedance measurements. *Appl. Phys. Lett.* **2003**;83:2178–2180.

84. M. B. Mcdonald and P. T. Hammond. Efficient Transport Networks in a Dual Electron/Lithium-Conducting Polymeric Composite for Electrochemical Applications. *ACS Appl. Mater. Interfaces* **2018**;10:15681–15690.

85. R. S. Waremra and P. Betaubun. Analysis of Electrical Properties Using the four point Probe Method. *E3S Web Conf.* **2018**;73:13019.

86. S. B. Catalano. Correction Factor Curves for Square-Array and Rectangular-Array Four-Point Probes Near Conducting or Nonconducting Boundaries *. *IEEE Trans. Electron Devices* **1963**;10:185–188.

87. S. Wang, M. Yan, Y. Li, C. Vinado and J. Yang. Separating electronic and ionic conductivity in mix-conducting layered lithium transition-metal oxides. *J. Power Sources* **2018**;393:75–82.

88. A. Yoshino. The birth of the lithium-ion battery. *Angew. Chem., Int. Ed.* **2012**;51:5798.

89. G. P. Pandey, A. C. Rastogi and C. R. Westgate. All-solid-state supercapacitors with poly(3,4-ethylenedioxythiophene)- coated carbon fiber paper electrodes and ionic liquid gel polymer electrolyte. *J. Power Sources* **2014**;245:857–865.

90. C. Karlsson, J. Nicholas, D. Evans, M. Forsyth, M. Strømme, M. Sjödin, P. C. Howlett and C. Pozo-Gonzalo. Stable deep doping of vapor-phase polymerized poly(3,4-ethylenedioxythiophene)/ionic liquid supercapacitors. *ChemSusChem* **2016**;9:2112–2121.

91. X. Su, Q. Wu, J. Li, X. Xiao, A. Lott, W. Lu, B. W. Sheldon and J. Wu. Silicon-Based Nanomaterials for Lithium-Ion Batteries: A Review. *Adv.*

Energy Mater. **2014**;4:1300882.

92. È. O. Besenhard, M. Winter and M. Wachtler. Tin and tin-based intermetallics as new anode materials for lithium-ion cells. *J. Power Sources* **2001**;94:189–193.

93. Y. Zhao, L. Yang, D. Liu, J. Hu, L. Han, Z. Wang and F. Pan. A Conductive Binder for High-Performance Sn Electrodes in Lithium- Ion Batteries. *ACS Appl. Mater. Interfaces* **2018**;10:1672–1677.

94. Z. Chen, I. Belharouak, Y. Sun and K. Amine. Titanium-Based Anode Materials for Safe Lithium-Ion Batteries. *Adv. Funct. Mater.* **2013**;23:959–969.

95. M. Wu, X. Xiao, N. Vukmirovic, S. Xun, P. K. Das, X. Song, P. Olalde-velasco, D. Wang, A. Z. Weber, L. Wang, V. S. Battaglia, W. Yang and G. Liu. Toward an Ideal Polymer Binder Design for High-Capacity Battery Anodes. *J. Am. Chem. Soc.* **2013**;135:12048–12056.

96. P. K. Nayak, J. Grinblat, M. Levi, O. Haik, E. Levi, S. Kim, J. W. Choi and D. Aurbach. Multiphase LiNi0.33Mn0.54Co0.13O2 Cathode Material with High Capacity Retention for Li-Ion Batteries. *ChemElectroChem* **2015**;2:1957–1965.

97. A. Purwanto, C. S. Yudha, U. Ubaidillah, H. Widiyandari, T. Ogi and H. Haerudin. NCA cathode material: Synthesis methods and performance

enhancement efforts. *Mater. Res. Express* **2018**;5:122001.

98. V. A. Nguyen and C. Kuss. Review — Conducting Polymer-Based Binders for Lithium-Ion Batteries and Beyond. *J. Electrochem. Soc.* **2020**;167:065501.

99. D. Bresser, D. Buchholz, A. Moretti, A. Varzi and S. Passerini. Alternative binders for sustainable electrochemical energy storage-the transition to aqueous electrode processing and bio-derived polymers. *Energy Environ. Sci.* **2018**;11:3096–3127.

100. J. Zhao, X. Yang, Y. Yao, Y. Gao, Y. Sui, B. Zou, H. Ehrenberg, G. Chen and F. Du. Moving to Aqueous Binder: A Valid Approach to Achieving High-Rate Capability and Long-Term Durability for Sodium-Ion Battery. *Adv. Sci.* **2018**.

101. L. Ling, Y. Bai, Z. Wang, Q. Ni, G. Chen, Z. Zhou and C. Wu. Remarkable Effect of Sodium Alginate Aqueous Binder on Anatase TiO2 as High-Performance Anode in Sodium Ion Batteries. *ACS Appl. Mater. Interfaces* **2018**;10:5560–5568.

102. L. Yue, L. Zhang and H. Zhong. Carboxymethyl chitosan: A new water soluble binder for Si anode of Li-ion batteries. *J. Power Sources* **2014**;247:327–331.

103. A. Wang, W. Zhou, A. Huang, M. Chen, J. Chen and Q. Tian. Modifying the

Zn anode with carbon black coating and nanofibrillated cellulose binder: A strategy to realize dendrite-free Zn-MnO2 batteries. *J. Colloid Interface Sci.* **2020**;577:256–264.

104. P. R. Das and J. E. Soc. PEDOT:PSS as a Functional Binder for Cathodes in Lithium Ion Batteries. *J. Electrochem. Soc.* **2015**;162:A674–A678.

105. J. Pan, G. Xu, Z. Chang, A. Wang, H. Dou and X. Zhang. PAA/PEDOT:PSS as a multifunctional, water-soluble binder to improve the capacity and stability of lithium-sulfur batteries. *RSC Adv.* **2016**;6:40650–40655.

106. T. Kim, L. K. Ono and Y. Qi. Elucidating the Mechanism Involved in the Performance Improvement of Lithium-Ion Transition Metal Oxide Battery by Conducting Polymer. *Adv. Mater. Interfaces* **2019**;6:1801785.

107. C. Sasso, E. Zeno, M. Petit-conil, D. Chaussy, M. N. Belgacem, S. Tapin-lingua and D. Beneventi. Highly Conducting Polypyrrole/Cellulose Nanocomposite Films with Enhanced Mechanical Properties. *Macromol. Journals* **2010**;295:934–941.

108. Y. Xu and Y. Zhang. Synthesis of polypyrrole/sodium carboxymethyl cellulose nanospheres with enhanced supercapacitor performance. *Mater. Lett.* **2015**;139:145–148.

109. N. Su. Improving Electrical Conductivity, Thermal Stability, and Solubility of Polyaniline-Polypyrrole Nanocomposite by Doping with Anionic Spherical

Polyelectrolyte Brushes. *Nanoscale Res. Lett.* **2015**;10:301.

110. U. S. Vogl, P. K. Das, A. Z. Weber, M. Winter, R. Kostecki and S. F. Lux. Mechanism of Interactions between CMC Binder and Si Single Crystal Facets. *Langmuir* **2014**;30:10299–10307.

111. Y. Luo, R. Guo, T. Li, F. Li, Z. Liu and M. Zheng. Application of Polyaniline for Li-Ion Batteries , Lithium-Sulfur Batteries, and Supercapacitors. *ChemSusChem* **2019**;12:1591–1611.

112. W. Kang, N. Deng, J. Ju, Q. Li, D. Wu, X. Ma, L. Li, M. Naebe and B. Cheng. A review of recent developments in rechargeable lithium–sulfur batteries. *Nanoscale* **2016**;8:16541–16588.

113. M. Ling, J. Qiu, S. Li, C. Yan, M. J. Kiefel, G. Liu and S. Zhang. Multifunctional SA-PProDOT Binder for Lithium Ion Batteries. *Nano Lett.* **2015**;15:4440–4447.

114. Y. Shi, X. Zhou, J. Zhang, A. M. Bruck, A. C. Bond, A. C. Marschilok, K. J. Takeuchi, E. S. Takeuchi and G. Yu. Nanostructured Conductive Polymer Gels as a General Framework Material To Improve Electrochemical Performance of Cathode Materials in Li-Ion Batteries. *Nano Lett.* **2017**;17:1906–1914.

115. H. Wu, G. Yu, L. Pan, N. Liu, M. T. Mcdowell, Z. Bao and Y. Cui. Stable Li-ion battery anodes by in-situ polymerization of conducting hydrogel to

conformally coat silicon nanoparticles. *Nat. Commun.* **2013**;4:1943.

116. D. Minudri, D. Mantione, A. Dominguez-Alfaro, S. Moya, E. Maza, C. Bellacanzone, M. R. Antognazza and D. Mecerreyes. Water Soluble Cationic Poly(3,4-Ethylenedioxythiophene) PEDOT-N as a Versatile Conducting Polymer for Bioelectronics. *Adv. Electron. Mater.* **2020**;6:1–10.

Chapter 2. Mixed Ionic and Electronic Binder of PEDOT:PSS and Organic Ionic Plastic Crystals toward Carbon-Free

Chapter 2. Mixed Ionic and Electronic Binder of PEDOT:PSS and Organic Ionic Plastic Crystals toward Carbon-Free

2.1. Introduction

The performance of next-generation solid-state lithium metal batteries (LMB) is intimately related to the ionic-electronic interconnection within the cathode material. In batteries containing liquid electrolytes, the soaking of electrolyte and the addition of carbon provide sufficient ionic and electronic conductivity through the cathode. However, in solid-state systems, cathodes are completely dry and thus, lack mobile Li-ions and good electronic interconnection. Besides, the use of electronic conducting carbon, despite its mature and low cost, results in low density and high porosity cathodes. Therefore, the use of carbon for solid-state batteries needs to be optimized to minimize the contact resistances given by porosity holes.[1] Some strategies to compact the electrodes, apart from calendaring, is the replacement of porous conducting carbon with conducting polymers. Accordingly, organic mixed ionic-electronic conductors (OMIEC) are promising binders to provide that ionic-electronic interconnection through compact carbon-free cathode.

Conducting polymers such as PEDOT, are also intrinsically ionic conductors as they are positively charged in their conducting state and come accompanied by different counter anions, which are able to move within the material, forming organic mixed ionic-electronic conductors (OMIECs) as explained in Chapter 1.[2] Afterwards, the ionic and electronic conductivity can be boosted by a doping effect of solvents, acids and ionic liquids on PEDOT:PSS, which generally leads to 1) stabilization of the polaron states of

PEDOT by interaction with the anions, and 2) phase segregation between isolating PSS and conducting PEDOT.[3,4] Focusing on the strategy of PEDOT:PSS / ionic liquids (ILs) composites, there have been huge efforts in screening a large number of chemical combinations for electronic conductivity, reaching values of 2103 S cm^{-1} for a 1-ethyl-3-methylimidazolium tetracyanoborate (EMIM TCB) composite ($7.5 \cdot 10^{-5}$ mol of IL per gram of PEDOT:PSS, leading to composites of estimated 43 wt.% of PEDOT:PSS).[5] However, the ionic conductivity in conducting polymers is rarely reported and the use of ionic liquids still does not overcome the issues related to the presence of a liquid electrolyte, such as leakage.

In contrast, the emerging organic ionic plastic crystals introduced in Section 1.2.3, provide high ionic conductivity remaining in solid-state. The large dynamism of these salts in combination with their wide electrochemical window make them promising components for energy storage systems as electrolytes for lithium and sodium[6,7] ion batteries but also as electrode additives.[8]

In this chapter, a synergistic approach is proposed combining PEDOT:PSS with two different OIPCs: N-ethyl-N-methylpyrrolidinium bis(trifluoromethylsulfonylimide) (C_2mpyrTFSI) and N-ethyl-N-methylpyrrolidinium bis(fluorosulfonylimide) (C_2mpyrFSI). These OIPCs have been widely studied and applied as electrolytes in energy storage systems.[9–11] The ionic and electronic conductivities of the developed composites have been analyzed demonstrating a synergetic effect of the components. The doping effect of the OIPCs on the structure and morphology of PEDOT:PSS has been studied by XRD and AFM. As a potential application, the OMIEC

composite with the most promising properties has been used as conductive binder in carbon-free solid-state LIB using LFP.

2.2. Composite preparation

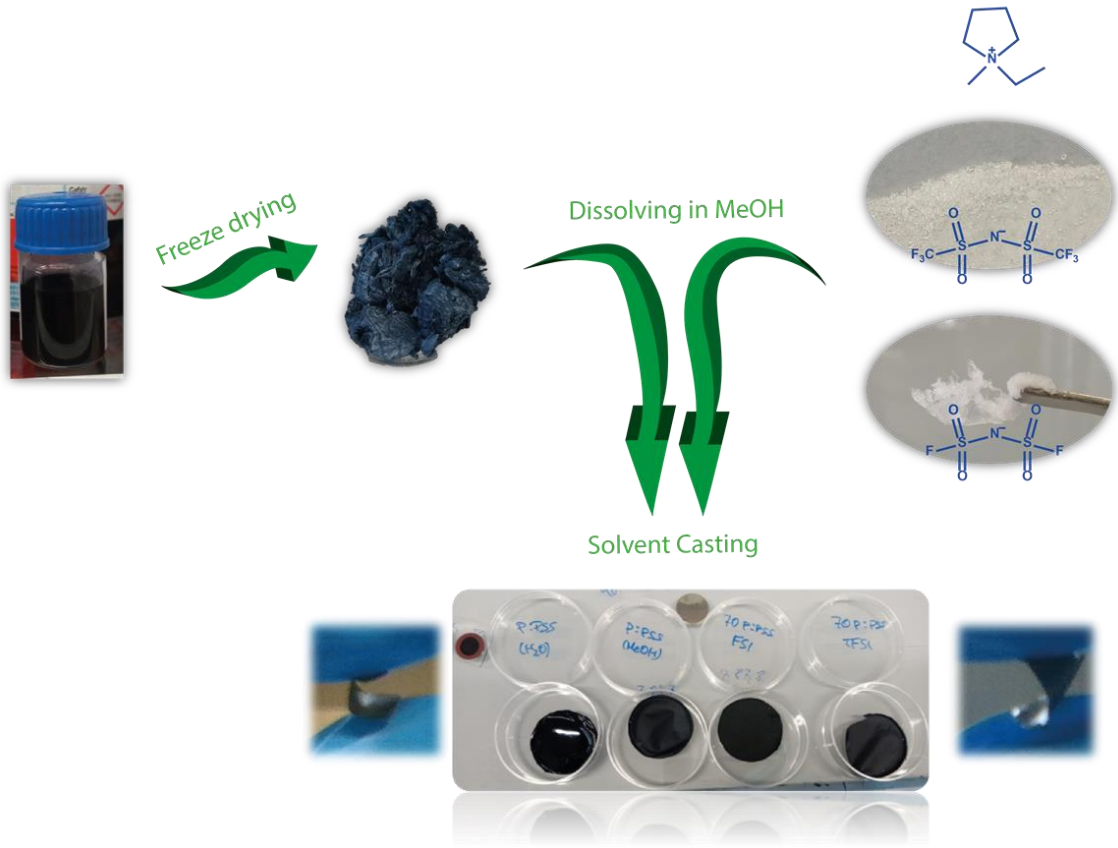

Figure 2.1. Preparation of the P:PSS/OIPC composite films.

The aqueous dispersion of PEDOT:PSS, termed P:PSS(H_2O) in this chapter, was freeze-dried for four days obtaining a sponge-like material. This material was subsequently dispersed in methanol (P:PSS(MeOH)). Various amounts of OIPC (C_2mpyrFSI or C_2mpyrTFSI) were first dissolved in methanol and subsequently added into the P:PSS methanol dispersion to obtain composites of P:PSS/OIPC with weight ratios of 90/10, 80/20 and 70/30. Finally, these materials were drop casted and dried at 130ºC under

vacuum before further characterization to ensure the absence of water, as PEDOT:PSS systems trend to be highly hygroscopic. In this way, highly flexible, homogeneous and robust films were obtained as can be seen in Figure 2.1. The physical and chemical homogeneity of the films was also confirmed until 70/30 wt. % ratio as can be seen from SEM/EDX images in Figure 2.2. When more OIPC was incorporated phase separation occurred observed macroscopically.

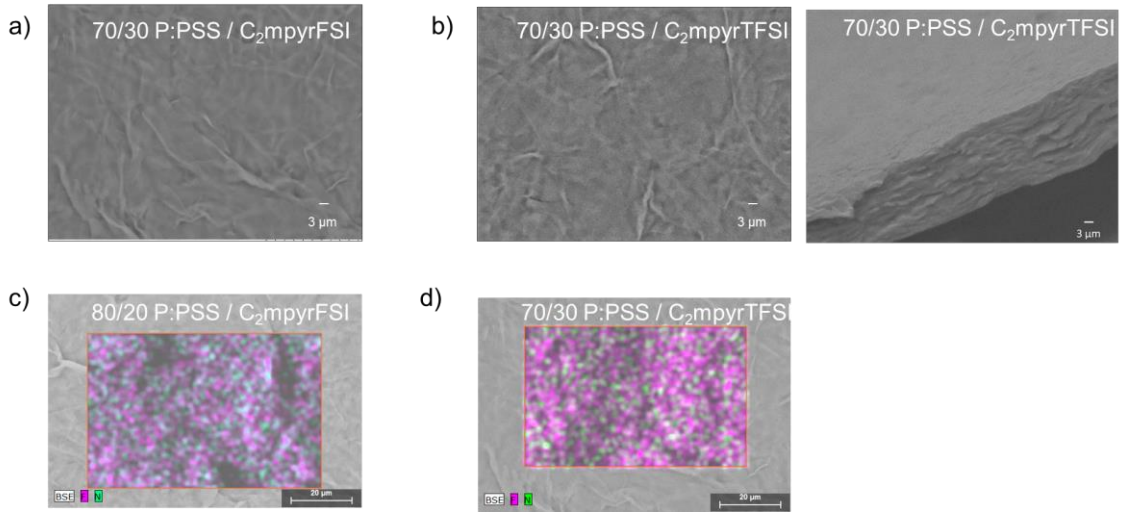

Figure 2.2. SEM images of a) 70/30 P:PSS / C_2mpyrFSI and b) 70/30 P:PSS / C_2mpyrTFSI on the plane and cross-section EDX images of the surface of the composites c) 80/20 P:PSS / C_2mpyrFSI and d) 70/30 P:PSS / C_2mpyrTFSI**.**

2.3. Structural and thermal characterization

Infrared spectroscopy was used to perform the structural characterization of the composites. Figure 2.3 shows the FTIR spectra of neat PEDOT:PSS, the two different OIPCs (C_2mpyrFSI and C_2mpyrTFSI) and their respective 70/30 P:PSS/OIPC composites. On one hand, C_2mpyrFSI exhibits the characteristic peaks of the cation C_2mpyr^+ at 1468 (C-C bending), 1098 (C-N stretching), 1032 and 997 (ring bending) and 935 (C-C stretching) cm^{-1} whereas the peaks at 1377, 1359, 1215, 1170, 822 and 719 cm^{-1} are

attributed to FSI- anion for -SO_2 asymmetric stretching, -SO_2 symmetric stretching, SO_2-N-SO_2 asymmetric stretching, S-N-S asymmetric stretching, S-N-S symmetric stretching respectively. Similarly, C_2mpyrTFSI presents the peaks related to the C_2mpyr^+ cation at 1467, 1050, 998 and 935 cm^{-1} while TFSI anion shows the vibrations at 1404 (-SO_2 stretching), 1349 (-SO_2 stretching), 1333 (C-SO_2-N bending), 1179 (-CF_3 stretching), 1137(C-SO_2-N bending), 780 (C-S and S-N stretching), 760 (CF_3 bending) and 738 (S-N-S stretching). On the other hand, the main peaks of PEDOT:PSS appear at 1042, 1012 (-SO_3) and at 1263, 1129 and 1071 (C-O). Finally, the most intense peaks of both composites, which are related to the PEDOT:PSS, are broader than in the pure PEDOT:PSS and exhibit different relative intensities. These changes suggest an alteration around the environment of the charged PEDOT and the sulfonate group of the PSS, due to the presence and interaction with OIPC ions. When comparing the two 70/30 composites, it is worth noticing that they present significant differences in the peak position and intensity, despite being quite similar chemically, reflecting different interaction degrees between PEDOT:PSS and the distinct salts.

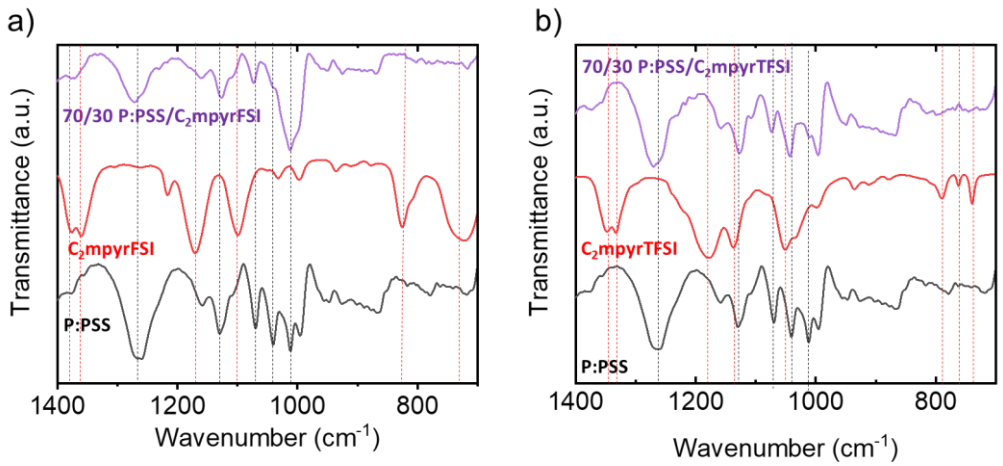

Figure 2.3. FTIR spectra of neat P:PSS (black), OIPCs (red): a) C_2mpyrFSI, b) C_2mpyrTFSI, and their respective 70/30 P:PSS/OIPC composites as shown in the figure legends.

The thermal stability of the materials was determined by thermogravimetric analysis (Figure 2.4). Typically the decomposition of PEDOT:PSS proceeds by a first release of solvent below 100 ºC, generally more than 20 wt. % due to the nature of the highly hygroscopic -SO_3^- groups of PSS, and subsequent decomposition of the polymer chains at around 300 ºC which continues with a gradual decomposition above 400 ºC and ends up in 40 wt.% of residue.[12] In this chapter, even after drying at 130 ºC under vacuum overnight, both P:PSS (MeOH) and all the composites present a weight loss of less than 10 % below 100 ºC; this was attributed to water uptake during the preparation for undertaking the measurement. This effect was accentuated with the addition of OIPC, much more pronounced in the case of C_2mpyrFSI-based composites (Figure 2.4a), which are well known for their hygroscopic behavior. Therefore, for the remaining characterization, in particular the ionic conductivity measurements, materials were handled in a glovebox. The decomposition of C_2mpyrFSI and C_2mpyrTFSI occur in one step starting at 230 and 400 ºC, respectively (Figure 2.4b). The C_2mpyrFSI-

based composites present a first degradation step related to the OIPC prior to PEDOT:PSS degradation, while in the C_2mpyrTFSI this is not observed due to its superior stability. Thus, the thermal stability of these materials is adequate (above 200 ºC) for application in most electronic applications, especially in solid-state batteries where working temperatures might be below 100 ºC.

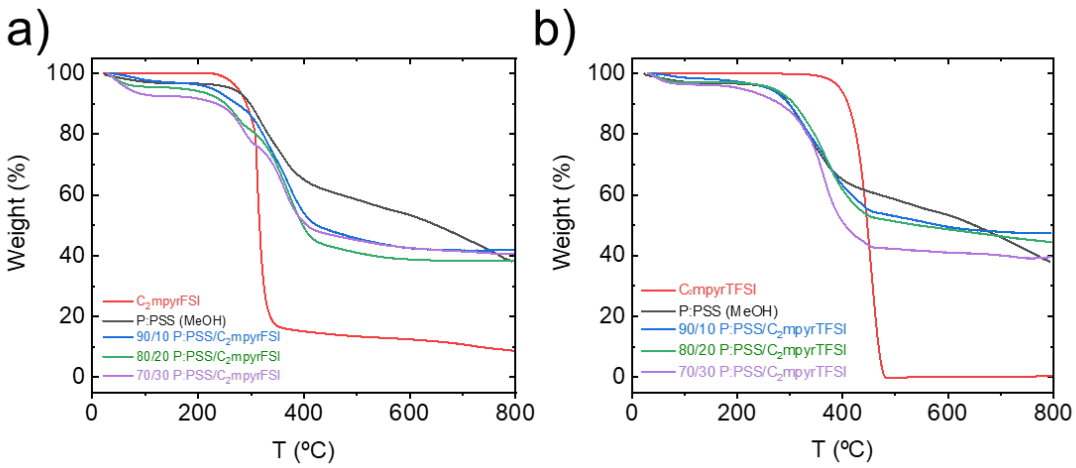

Figure 2.4. Thermogravimetric curves of neat P:PSS (MeOH) (black), OIPCs (red): a) C_2mpyrFSI, b) C_2mpyrTFSI, and their respective composites as follows the legends.

Figure 2.5 presents the XRD patterns of the different PEDOT:PSS materials, as well as the C_2mpyrFSI and C_2mpyrTFSI salts. The commercial dispersion of PEDOT:PSS in water shows only two well-defined peaks at 2θ=18.7º and 25.6º corresponding to the amorphous halo of PSS and the interchain planar π-π stacking distance d_{010} of PEDOT, respectively (related to the lattice spacings d=4.7 Å and 3.5 Å, according to the Bragg's law). After freeze-drying and dispersing it in methanol, the crystalline structure of the material changes notably with an additional two peaks appearing at 2θ=3.9º and 9.3º (d=22,4 Å and 9.5 Å), which are indexed to the alternate ordering

distance of the PEDOT and PSS chains in the plane d_{100} and the second-order reflection d_{200}.[13,14] It is also worth to mention that the two main peaks have sharpened and shifted to higher angles which are related to a better packing of the chains. Regarding the 70/30 P:PSS/C_2mpyrFSI composite, it can be easily seen that there are two sharp peaks related to the crystalline C_2mpyrFSI salt as well as a decrease and broadening in the intensity of the peak related to the d_{010} of PEDOT (~26º). These facts indicate the presence of phase-separated C_2mpyrFSI and a deterioration of the packing of the conducting chains. Interestingly, the crystalline structure of C_2mpyrFSI has apparently changed in comparison with the pristine salt. OIPCs are dynamic salts that present several solid-solid phase transitions, low melting entropy and can be polymorphed depending on the conditions, making the crystalline structure quite complex. In literature, it can be also found metastable phases observed by DSC, features that depend on temperature and heating-cooling rate.[15] Likewise, several authors have already reported modifications in the OIPC crystalline structure when a second component is added.[15,16] Finally, the X-ray spectrum of the 70/30 P:PSS/C_2mpyrTFSI does not show sharp peaks related to the crystalline structure of the OIPC with peaks at 6.2º (d=14.1 Å) and 12.4º (d=7.2 Å) related to the side-by-side packing d_{100} and the d_{200} reflection respectively. Different crystalline structures have been defined for PEDOT:PSS called Type I (non-orientated) and II (orientated lamellar stacking) with specific spacements of 21 and 12 Å respectively.[17] The peak at 6.2° in 70/30 P:PSS/C_2mpyrTFSI is attributed to compact and highly ordered Type II crystals, which improve the charge transport properties and were not observed in neat PEDOT:PSS, nor in C_2mpyrFSI composite.

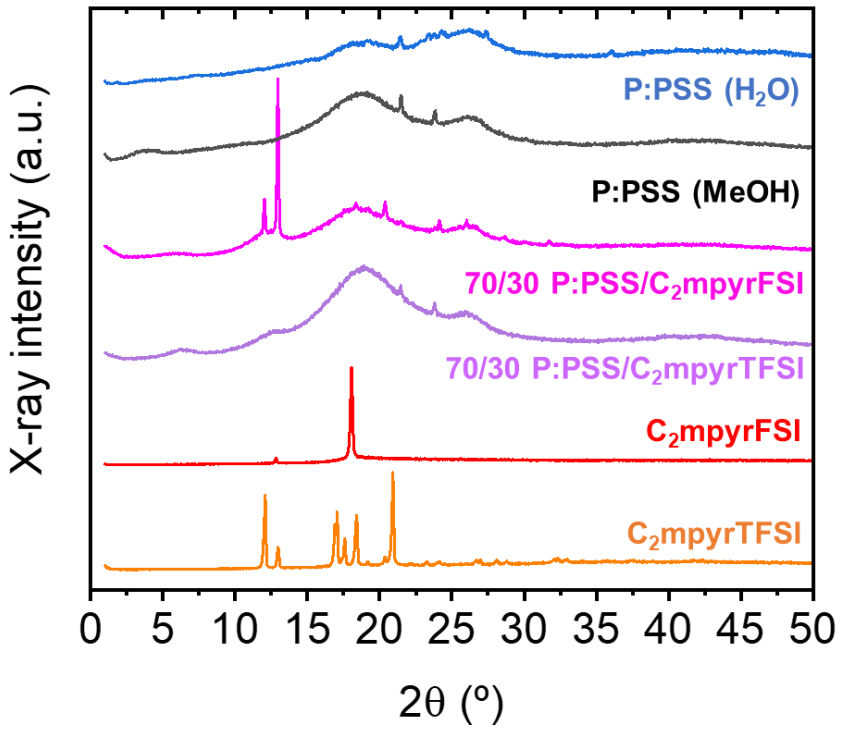

Figure 2.5. XRD patterns of the different pristine PEDOT:PSS, composites and OIPCs as shown in the figure legend

AFM topography images were taken to analyze the surface morphology of the films (Figure 2.6). The P:PSS (H_2O) shows a complete disordering of the PEDOT particles along the film whereas the material dispersed in methanol presents an orientation of the particles, as well as segregation between PEDOT and PSS. It is even more clear with the composites that presented higher electronic conductivity than both P:PSS (H_2O) and P:PSS (MeOH) i.e. 80/20 P:PSS/C_2mpyrFSI and 70/30 P:PSS/C_2mpyrTFSI. In these systems, larger particles and well-defined pathways are observed, which can improve the electron transport, in good agreement with the XRD measurements, especially for the 70/30 P:PSS/C_2mpyrTFSI.

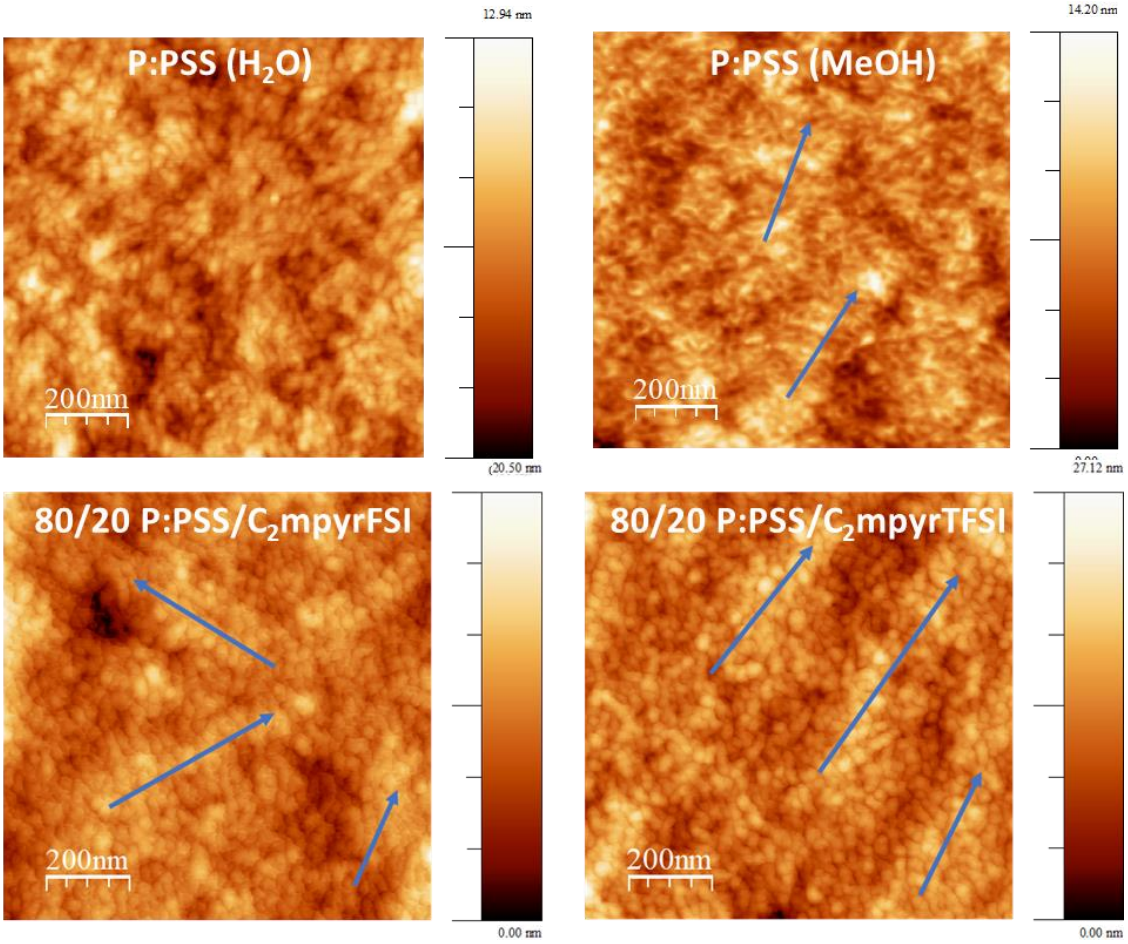

Figure 2.6. Topography AFM images of different PEDOT:PSS and P:PSS/OIPC composites.

Figure 2.7 shows the phase AFM images of the materials where P:PSS (H_2O) reveals a flat and homogeneous structure composed of PEDOT and isolating PSS. When the material is dispersed in methanol, a clear phase separation is observed leading to more continuous PEDOT chains, in agreement with XRD data. Finally, when OIPCs are blended with the conducting polymer in methanol, small circular grains appear as observed by Li et al. with similar ionic salt in addition to an ordered orientation inside the polymer chains.[18] These grains are composed of ordered PEDOT:PSS chains but amorphous OIPC surrounding and doping conducting polymer which leads to an ideal scenario for efficient charge transport.

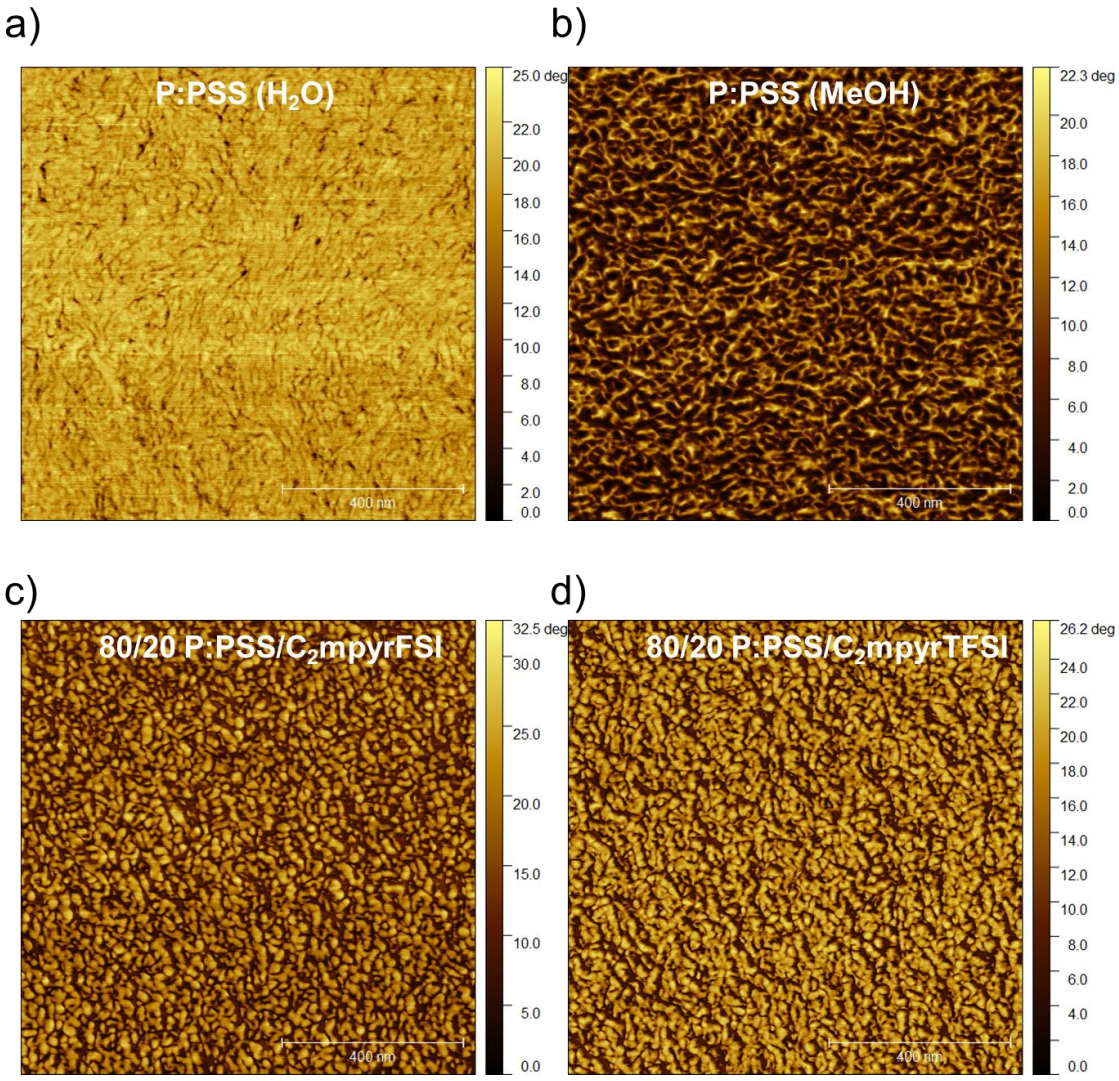

Figure 2.7. Phase AFM images of different a) PEDOT:PSS (H_2O), b) P:PSS (MeOH), c) 80/20 P:PSS/C2mpyrFSI and d) 70/30 P:PSS/C2mpyrTFSI composites.

Given these characterization data, we propose the scheme of Figure 2.8 where, (i) thanks to the interaction of P:PSS with methanol a first phase segregation is obtained and then, (ii) the addition of OIPC leads to an enhancement of this effect, as well as growing of PEDOT particles due to increased ionic interactions until, finally, (iii) an excess of organic salt ends in OIPC precipitation.

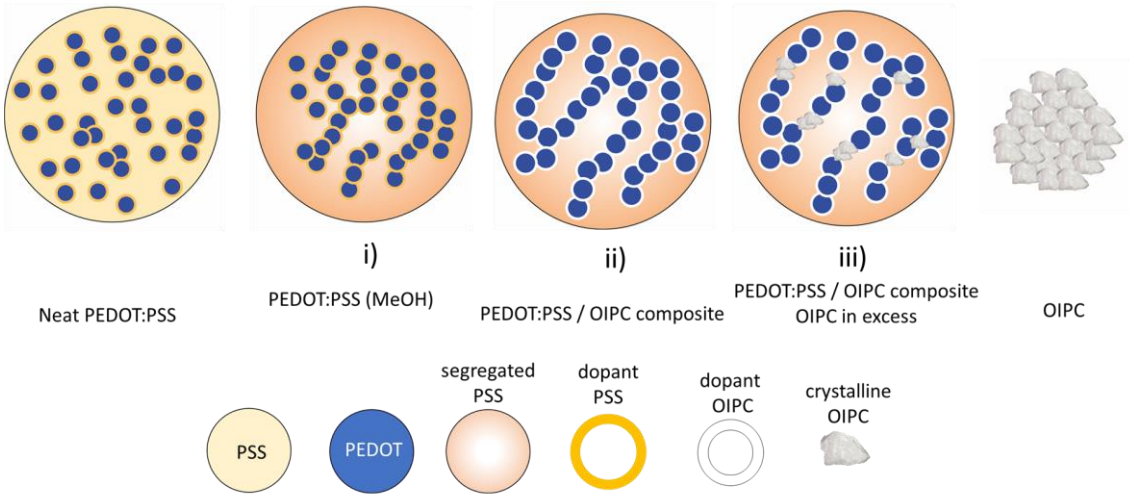

Figure 2.8. Scheme of the evolution of the materials from their neat state: PEDOT:PSS and OIPC to the different composite scenarios.

2.4. Ionic and electronic conductivities

The charge transport within these materials was studied by four-point probe (4PP) to determine the electronic conductivity and electrochemical impedance spectroscopy (EIS) to measure the ionic conductivity.

A significant enhancement of the electronic conductivity for MeOH dispersed P:PSS (416 S cm^{-1}) relative to the commercial PEDOT:PSS (0.2 S cm^{-1}) was observed. A similar effect was also observed when DMSO was used as solvent obtaining similar conductivity values. After adding C_2mpyrFSI to make the composites, the electronic conductivity reaches a value of 515 S cm^{-1} for the 90/10 composite, 469 S cm^{-1} for 80/20 and finally drops to 379 S cm^{-1} (70/30) possibly due to a surpassing of the solvated amount of OIPC which leads to a precipitation of the crystalline salt as seen in the previous section. In the family of the C_2mpyrTFSI composites the values of electronic conductivity are even higher than with C_2mpyrFSI with the 70/30 composite having the highest value (580 S cm^{-1}). Since the calculated ratio of

FSI/PEDOT in the 70/30 composite is 0.85 whereas in the case of TFSI/PEDOT at the same composition is 0.60, it could be reasonable that salt precipitation occurs in the FSI system while not in the TFSI. Besides, the results of the two families are in good agreement with XRD measurements which show highly ordered PEDOT crystals (Type II) when using C_2mpyrTFSI. These conductivity values were obtained after drying the films at 130 ºC under vacuum overnight, as it led to stable and reproducible measurements in comparison to films dried at room temperature, which suffered significant fluctuations due to solvent traces, as can be observed in Figure 2.9a-b. The electronic conductivities obtained are close to the highest conducting composites, which are in the range of 1000-2000 S cm^{-1} but in a completely solid state without the risk of possible leak and associated adverse effects.[5]

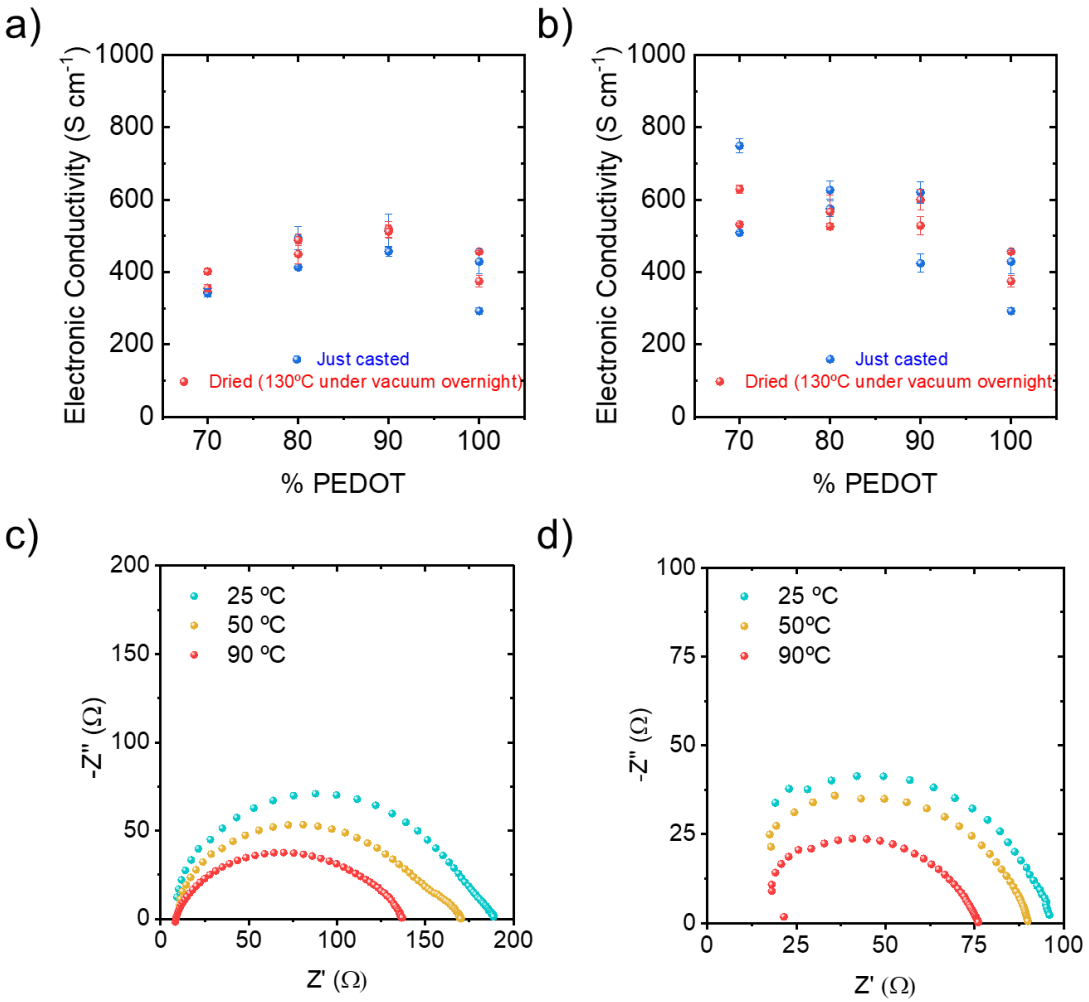

Figure 2.9. Electronic conductivity of P:PSS (MeOH), a) FSI and b) TFSI-based composites dried at room temperature and after drying at 130ºC under vacuum overnight. Nyquist plot of c) 80/20 P:PSS/C_2mpyrFSI and d)70/30 P:PSS/C_2mpyrTFSI at different temperatures.

During the EIS measurements typical closed semicircles of mixed conductors were observed in all temperatures (see Figure 2.9c-d). The electronic resistance, associated with the beginning of the semicircle, which remained constant along the measured temperature range, is negligible relative to contact resistances and more importantly ionic resistances, taking into account the measured electronic conductivities by 4PP (higher than 350 S cm^{-1}). Nonetheless, the ionic contribution manifests as a deformed semicircle involving two time constants that can be associated with the

difference between the ion transport rates along the MIEC material: interphase between PEDOT:PSS and OIPC and neat materials. The overall resistance of the MIEC was estimated considering the whole diameter of the overlapped semicircles.

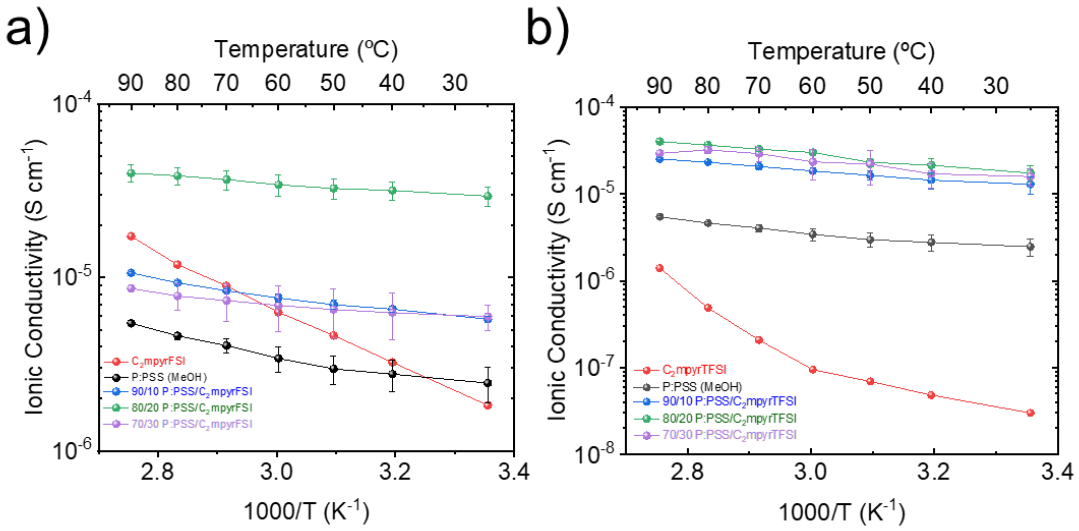

Figure 2.10. Ionic conductivity at different temperatures of a) PEDOT:PSS, C_2mpyrFSI and b) PEDOT:PSS, C_2mpyrTFSI and their respective composites, as follows the legends.

Among the composites based on C_2mpyrFSI, the 80/20 P:PSS/C_2mpyrFSI composite exhibits the highest ionic conductivity (3.7×10^{-5} S cm^{-1} at 70ºC), resulting in higher conductivity compared with neat components, i.e., P:PSS and C_2mpyrFSI (4.0×10^{-6} and 8.9×10^{-6} respectively at 70ºC), as can be observed in Figure 2.10. The ionic conductivities suggest that the optimum composition lies a percolation ratio of high conducting material close to 80/20. Beyond this composition, it is possible that the excess OIPC phase separates and disrupts this conduction pathway resulting in lower ionic conduction. On the other hand, the pure C_2mpyrTFSI salt has an ionic conductivity of 2.1×10^{-7} S cm^{-1} (70 ºC) whereas

its respective composites have conductivity values much higher, with little composition dependence compared with the C_2mpyrFSI systems (2.1×10^{-5} S cm^{-1} for the 90/10 composite and around 3.3×10^{-5} S cm^{-1} for the 80/20 and 70/30). Furthermore, there is no significant decrease in conductivity at high OIPC concentration (70/30) when using C_2mpyrTFSI in contrast to the C_2mpyrFSI system, suggesting better compatibility and continuous ionic percolating pathways for the TFSI containing composites, since OIPC remains amorphous. Such large increases in the ionic conductivity in polymer/OIPC composites have been shown in a related work and is explained by the disordering of the crystalline phase of OIPCs.[16]

Table 2.1. Activation energy of the ionic conductivity of PEDOT:PSS, C_2mpyrFSI, C_2mpyrTFSI and their composites.

Material	Activation Energy [KJ mol^{-1}]
PEDOT:PSS	4.9 ± 0.4
C_2mpyrFSI	12.9 ± 0.1
90/10	3.6 ± 0.2
80/20	1.9 ± 0.1
70/30	1.6 ± 0.3
C_2mpyrTFSI	11.4 ± 0.3
90/10	4.2 ± 0.2
80/20	5.2 ± 0.3
70/30	4.6 ± 0.4

The values of the activation energy for the ionic conductivity are 12.9 KJ mol^{-1} for C_2mpyrFSI, in good agreement with recent studies, and 11.4 KJ mol^{-1} for C_2mpyrTFSI.[19] It is also worth noting the low values of activation energies of the mixed conductors in this chapter (Table 2.1), all of them being below 5 KJ mol^{-1}. The pristine PEDOT:PSS has an activation energy of 4.9 KJ mol^{-1} whereas the composites present values even lower, especially the C_2mpyrFSI-based composites having 1.6 KJ mol^{-1}. Compared with other

similar but electronically insulating polymer-OIPC composites, the activation energies are above 10 KJ mol^{-1} even increasing with the amount of polymer in polystyrene-C_2mpyrFSI and PVDF-C_2mpyrFSI systems.[19] Whilst more work is required to better understand this phenomenon in these OMIEC compounds, this behavior has been previously observed in similar works with values in the same range.[20]

In Figure 2.11 both the electronic and the ionic conductivities at 25ºC of all studied materials are depicted. Taking these values into account, the composites selected with the best compromise between ionic and electronic conduction were the 80/20 P:PSS/C_2mpyrFSI and the 70/30 P:PSS/C_2mpyrTFSI. Indeed, the electronic conductivity of these composites is significantly higher than the neat P:PSS (MeOH) suggesting a doping effect of the OIPCs. In order to study the influence of composition and morphology on charge transport, X-ray diffraction (XRD) and atomic force microscopy (AFM) experiments were carried out in the selected composites.

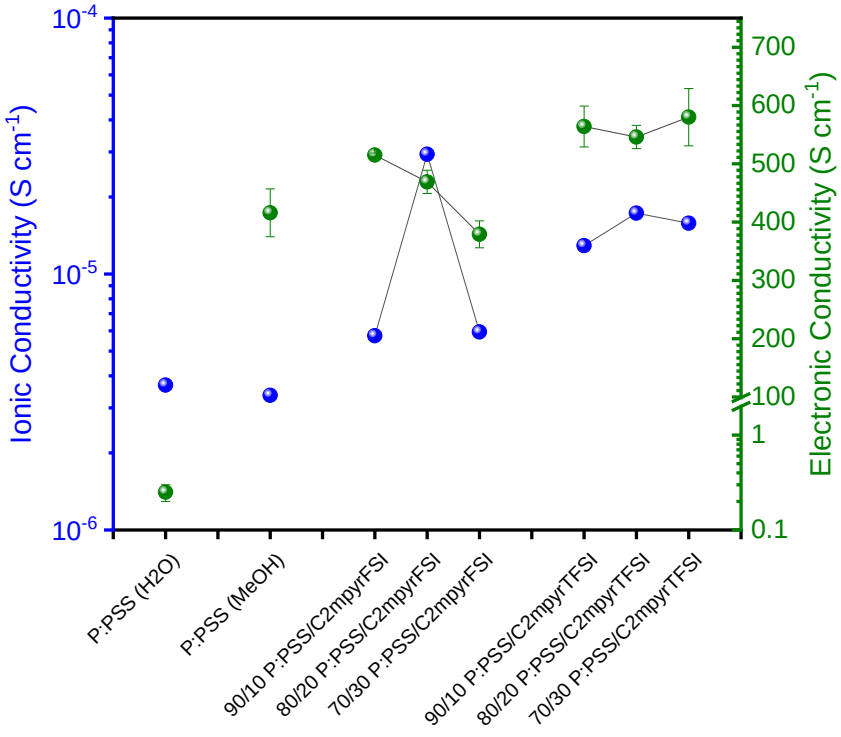

Figure 2.11. Ionic (blue) and electronic (green) conductivities at 70 and 25ºC respectively of the composites and the neat PEDOT:PSS.

2.5. Battery performance

The high electronic and ionic conductivities of the OMIEC composites, together with their good mechanical properties, make them good candidates to apply as a conductive binders in solid-state lithium-ion batteries. First, the electrochemical windows of the best composites were measured by cyclic voltammetry in liquid electrolyte as shown in Figure 2.12 revealing good cycling between 1.0-4.5 V in the case of 80/20 P:PSS/C_2mpyrFSI and 1.7-4.8 V vs Li^0/Li^+ for 70/30 P:PSS/C_2mpyrTFSI indicating good compatibility with most of the active materials used in cathodes.

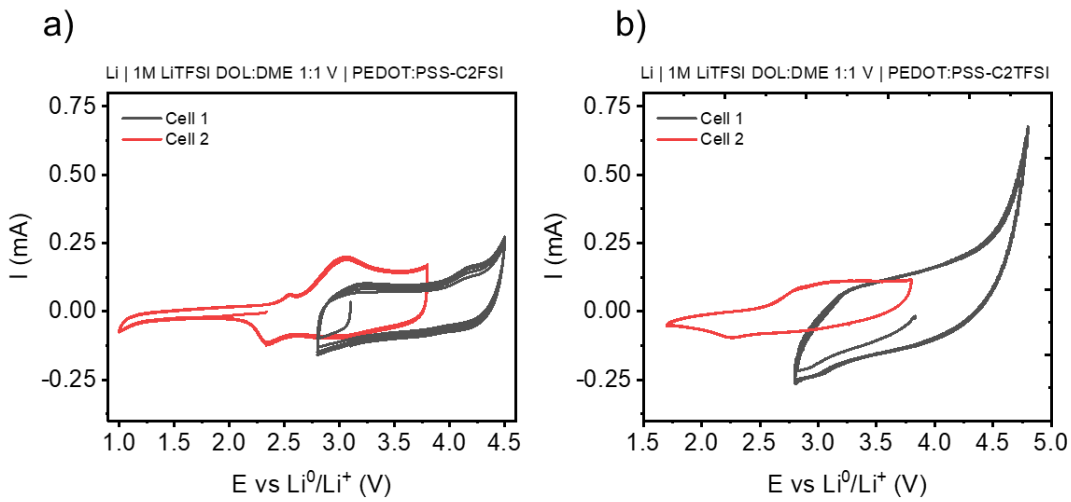

Figure 2.12. Electrochemical window in lithium metal cells of a) 80/20 P:PSS/C_2mpyrFSI and b) 70/30 P:PSS/C_2mpyrTFSI using 1M LiTFSI in DOL:DME 1:1 v at 10 mV s^{-1}.

Then, in a solid-state lithium battery, a source of lithium ions is needed within the electrode to support the electrochemical reactions, being Li intercalation/de-intercalation during battery cycling. Previous work has identified that mixtures of LiFSI salt and C_2mpyrFSI OIPC lead to high ionic conductivity and therefore, LiFSI was incorporated into the 80/20 P:PSS/C_2mpyrFSI composite which was then used as a cathode binder.[21,22] Up to 50 mol % LiFSI in C_2mpyrFSI shows no precipitation of lithium salt and retains high conductivity.[21] This concentration was taken into account for the formulation and considering that solid-state battery electrodes normally contain 60 wt. % of active material, the following electrode formulation was studied in a full cell: 60 % LFP, 35 % of 80/20 P:PSS/C_2mpyrFSI composite and 5 % LiFSI. A previously studied ternary polymer electrolyte system (termed PILBLOC) based on a poly(ionic liquid) di-block copolymer, N-propyl-N-methylpyrrolidinium bis(fluorosulfonyl)imide (C_3mpyrFSI) ionic liquid and LiFSI was used as a solid electrolyte due to its excellent compatibility with lithium metal and stable cycling performance up to 0.20 mA cm^{-2}.[23] Moreover,

the OMIEC-based electrode was compared against a typical cell using this electrolyte as the ionic conducting binder in the electrode containing 60 % LFP, 10 % C65 and 30 % PILBLOC.

The cell performance of the carbon-free OMIEC based electrode is shown in Figure 2.13. It can be observed that a superior specific discharge capacity of LFP is obtained with 80/20 P:PSS/C_2mpyrFSI binder at all rates compared with the di-block binder. The coulombic efficiency remained close to 100 % while values close to the theoretical capacity of LFP were achieved at C/10 (157 mAh g^{-1}) and 145.5 mAh g^{-1} at C/2 rate with a capacity retention of 99.7 % after 500 cycles at C/2.

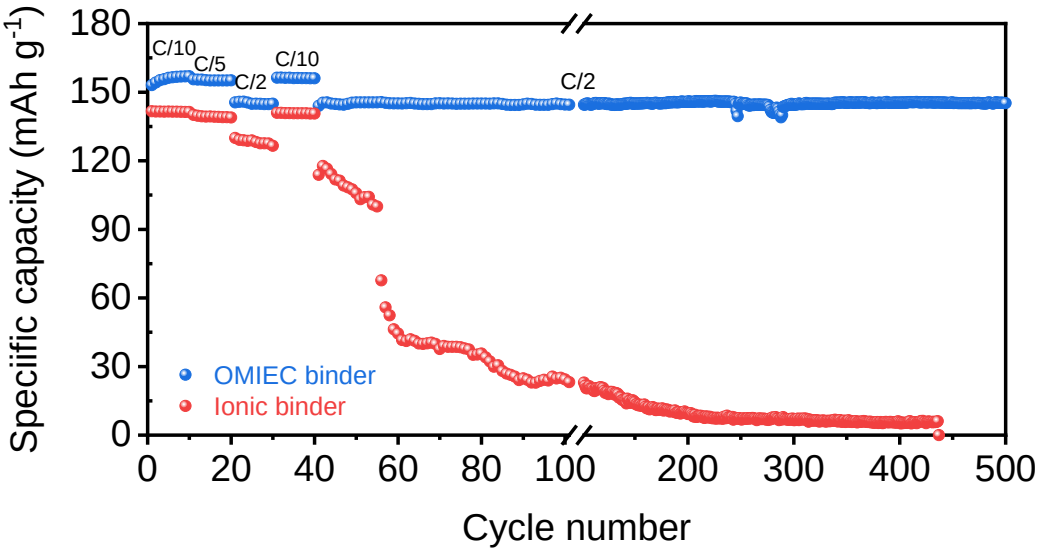

Figure 2.13. Cycling performance at C/10, C/5 and C/2 rates of Li | diblock | LFP cells containing different conducting binders and cycled at 70 ºC.

Figure 2.14a depicts the voltage profile at the beginning of the long-term cycling, in the middle and at the end (500th cycle) of OMIEC-based cell showing a very similar shape with negligible generated resistance and capacity drop. On the other hand, the electrode prepared with the di-block

binder presented a small decay in the first cycles at C/2 that was dramatically accentuated upon longer-term cycling to final failure, reflecting a non-stable cycling at this rate.

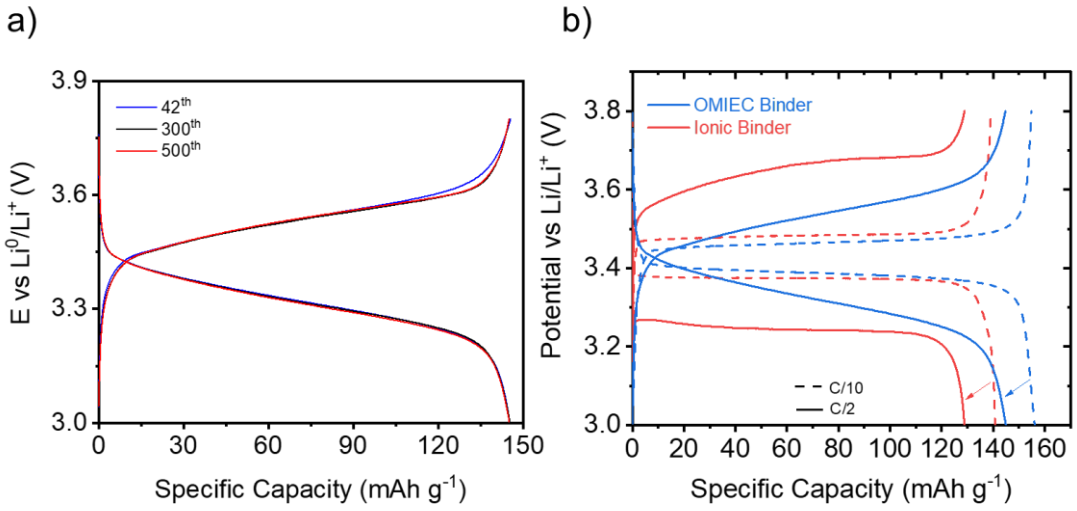

Figure 2.14. a) Voltage profile of Li | diblock | OMIEC binder-based cathode at different cycles of the long-term cycling from the beginning (42nd). b) Voltage profiles at C/10 and C/2 of all-diblock and OMIEC based cells as indicated in the figure legends.

The voltage profiles are depicted in Figure 2.14b, where low overpotentials can be seen at C/10 for both systems, with higher capacity in the case of the OMIEC binder probably due to a better electronic interconnection within the electrode often seen when electronic conducting polymers are used in electrode formulations.[24,25] We note that the measured electronic conductivity of the composites was much higher (469 S cm^{-1}) than the C65 pellet (2.01 ± 0.17 S cm^{-1}, 583 µm). When the C rate is increased up to C/2, as expected, the overpotentials become larger as a consequence of diffusion limitations. This effect is much more evident when the di-block polymer is used both as electrolyte and electrode binder. In this case the electrode contains just 30 % of ionic conductor and 10% of ionically isolating

C65, making the electrode more porous with possible discontinuity of ionic pathways, hence more resistant to ion transport. Whereas, for PEDOT:PSS/OIPC, the entire 40 wt. % of additive can be considered an ion carrier. Moreover, conducting polymers are able to cover the LFP particles, generating a more effective electronic contact between LFP particles than carbon, whose electronic connection is discrete, as represented in Figure 2.15.[24] Furthermore, the sloping profile exhibited by the PEDOT:PSS/OIPC electrode might be due to the pseudocapacitive nature of the binder, leading to additional capacity in addition to the LFP and hence a higher overall capacity value. This effect has been seen in other works when the amount of conducting polymer becomes significant.[26,27] It is worth noting that, simply by changing the binder to the OMIEC whilst using the same solid polymer electrolyte, the device performance went from rapid fading to a stand-out cell with excellent cycling stability at high rate considering the solid-state nature of the device.

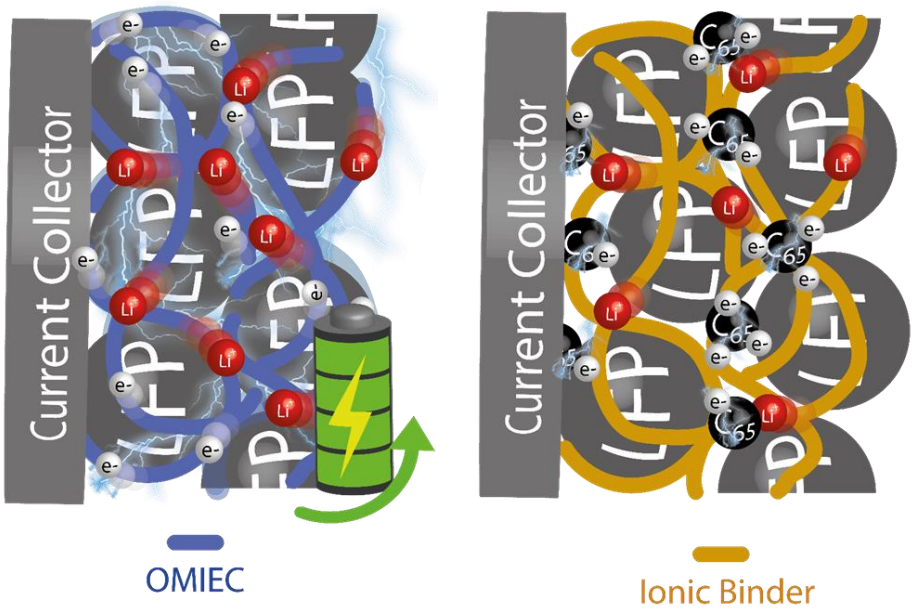

Figure 2.15. Scheme of the electrodes containing P:PSS/OIPC composite (OMIEC) and all-diblock polymer as binders and their conduction pathways.

Table 2.2 summarizes the cell cycling values obtained in this chapter and compares them to the reported performances of similar cells with various electrolyte and binder combinations. Even though ceramic electrolytes (also included as cathode binders) can fulfill the requirements of high ionic conductivity, thermal and electrochemical stability, their rigidity may lead to poor interfacial contact.[28] Despite that, capacities of 120 mAh g^{-1} have been reached for high loading cathodes (8 mg cm^{-2} at C/5) or long-term cycling (400 cycles at C/2 and 1 mg cm^{-2}).[29,30] On the other side, solid polymer electrolytes have provided higher capacity values (159 mAh g^{-1} with 2 mg cm^{-2} at C/10) which might be due to their softer contact.[31] However, they still seem to suffer either when the rate is increased or in long-term cycling. In this respect, P:PSS/C_2mpyrFSI is postulated as an ideal binder with highly promising performance that confirms its ability to behave both as high Li^+ supplier for the active material, in a non-porous configuration, as outstanding

electronic conducting agent and also as electroactive material, contributing to the overall capacity.

Table 2.2. Literature review of solid-state Li|LFP cells based on inorganic and polymer electrolytes.

Electrolyte	Cathode formulation [LFP/C65/ionic binder] Ref.	Current density [mAh cm^{-2}] / LFP loading [mg cm^{-2}]	C rate	Specific capacity [mAh g^{-1}]	Cycling life
Diblock-EC-LiFSI[a]	60/10/30 [32]	0.046 / 2.7	C/10	150	100
PPE-PEO-PPE (LiTFSI)[b]	60/10/30 [33]	0.051 / 3	C/10	112	100
P(EO-co-PO)[c]	70/15/15 [31]	0.034 / 2	C/10	159	50
LAGP[d]	50/5/45 [29]	0.272 / 8	C/5	120	50
Diblock-IL-LiFSI[e]	60/40 P:PSS-OIPC-LiFSI This work	0.1 / 1.2	C/2	145	150
Diblock-IL-LiFSI[e]	60/10/30 PILBLOC-IL-LiFSI This work	0.1 / 1.2	C/2	130	55
PEO (LiTFSI)[f]	60/15/25 [34]	0.128 / 1.5	C/2	122	150
PI/DBDPE/PEO/LiTFSI[g]	60/15/25 [34]	0.128 / 1.5	C/2	143	300
LPO-LLZO[h]	50/5/45 [30]	0.1 / 1	1.5 C	120	400

[a]Poly(ionic liquid) – ethylene carbonate – LiFSI.
[b]Crosslinked poly(ethylene oxide-co-polyphosphoester) – LiTFSI
[c]Poly(ethylene oxide) – LiTFSI
[d]$Li_{1.5}Al_{0.5}Ge_{1.5}(PO_4)_3$
[e]Poly(ionic liquid) – C_3mpyrFSI – LiFSI
[f]Poly(ethylene oxide-co-polypropylene oxide) – LiTFSI
[g]Polyimide – decabromodiphenyl ethane – poly(ethylene oxide) – LiTFSI
[h]Li_3PO_4 – $Li_{6.5}La_3Zr_{1.5}Ta_{0.5}O_{12}$

2.6. Conclusions

In this chapter, a family of solid-state OMIECs with good mechanical properties has been developed by mixing PEDOT:PSS and two different OIPCs (C_2mpyrFSI and C_2mpyrTFSI). Electronic conductivities up to 580 S cm^{-1} were achieved along with increased ionic conductivity values of 3.8×10^{-5} S cm^{-1} at 70 ºC, resulting in a synergistic effect of simultaneously enhancing both electronic and ionic conductivities. The activation energy for the ion transport within the OMIECs remained low (below 5 KJ mol^{-1}) along all the range of compositions as in previous works.[20] The effect of the OIPC addition to PEDOT:PSS on structure and morphology was studied by XRD and AFM. This provided good concordance between both techniques and the

conductivity measurements, and indicated that the composites consisted of highly ordered PEDOT but amorphous OIPC, resulting in facile electron and ion-conducting pathways.

The 80/20 P:PSS/C_2mpyrFSI composite was selected as the optimum OMIEC for application as a binder in carbon-free battery electrodes, given its electronic and ionic conductivity values. These electrodes were tested by galvanostatic charge-discharge using a solid polymer electrolyte based on a poly(ionic liquid) electrolyte. The performance of the cell was superior to that using a typical ionic conducting binder with high specific capacity (145.5 mAh g^{-1} at C/2 and 70 ºC) with a capacity retention of 99.7 % (145.2 mAh g^{-1}) after 500 cycles. Hence, we demonstrate that PEDOT:PSS mixed with OIPC as an OMIEC binder provides an ideal electronic-ionic interconnection within a non-porous battery electrode for all-solid-state batteries driven by its three functionalities: ionic transport, electronic conduction and pseudocapacitive contribution. We highlight that the development of such mixed conductors as binders is a promising way to achieve high-performance solid-state battery technologies in the near future.

2.7. Experimental part

2.7.1. Materials

Poly(3,4-ethylenedioxythiophene):Poly(styrene sulfonate) (Clevios PH 1000), 1.3 wt.% solids in water, was supplied by Heraeus Inc. N-ethyl-N-methylpyrrolidinium bis(trifluoromethylsulfonylimide) (C_2mpyrTFSI) (99%) was purchased from IoLiTec while N-ethyl-N-methylpyrrolidinium

bis(fluorosulfonylimide) (C_2mpyrFSI) was synthesized as previously reported.[35] N-propyl-N-methylpyrrolidinium bis(fluorosulfonyl)imide (C_3mpyrFSI, 99.5 %) was supplied by Solvionic. Lithium iron phosphate ($LiFePO_4$) (ALEEES) and Super C65 (Timcal). 1-Methyl-2-pyrrolidone (NMP) (99.5%) was purchased from Sigma Aldrich. PILBLOC polymer was obtained as in previous work.[23,32]

2.7.2. Synthesis of C_2mpyrFSI

The synthesis of C_2mpyrFSI was carried out following a previously reported, similar procedure [26]. An amount of 9.75 g (0.050 mol) of C_2mpyrBr and 12.53 g (0.057 mol) of KFSI were separately dissolved, each in 40 mL of distilled water. Then, the KFSI solution was added dropwise into the C_2mpyrBr solution with vigorous stirring. C_2mpyrFSI was obtained as a white precipitate that was purified after a liquid-liquid separation with dichloromethane (DCM). After drying under vacuum overnight at 60 °C a waxy solid of C_2mpyrFSI was obtained.

2.7.3. Methods

Fourier Transform Infrared Spectroscopy measurements (FTIR) were conducted on a Nicolet Magna 6700 spectrometer. The samples were analyzed in thin film form. The thermal stability of the composites was investigated with a thermo-gravimetric analysis (TGA) performed on a TGA Q500 from TA Instruments. Measurements were carried out by heating the samples at 10 °C min^{-1} under nitrogen atmosphere from 40 °C to 800 °C.

The crystalline structure of the materials was examined by X-ray diffraction (XRD, D8 Advance) at room temperature using a wavelength of λ=1.5418 Å). The experiments of PEDOT:PSS samples, as well as their composites, were carried out with films (Ø 4 cm), while the fluorinated salts were used as powder. Atomic force microscope (AFM, Dimension ICON) was operated in the tapping mode using a TESP-V2 type silicon tips with a frequency of 320 kHz, a spring constant of 40 N/m and a tip radius of 7nm. The commercially available PEDOT:PSS was spin-coated as received while the composites were dispersed in an approximated concentration of 1 mg/ml.

The electronic conductivity of the composite films was measured with an Ossila Four-Point Probe unit at room temperature. The reported values are the average between different measurements in various directions along the film of 10 mm in diameter. The ionic conductivity of the composites was measured by electrochemical impedance spectroscopy using a VMP-3 potentiostat (Biologic Science Instruments). Films of around 18 μm of thickness were assembled in coin cells under argon atmosphere between two stainless steel spacers. Each composite was studied in heating and cooling ramp from 25 to 90 ºC in a frequency range of 1 MHz to 100 mHz using a voltage amplitude of 10 mV. The samples were equilibrated for 20 minutes before each measurement. The reported values are the average between the heating and cooling measurements.

2.7.4. Electrode preparation, cell assembly and battery characterization

The mixed conducting binder-LFP-based slurry was prepared by first dispersing freeze-dried PEDOT:PSS, C_2mpyrFSI and LiFSI in DMSO and finally the active material powder in a weighted ratio of 60/28/7/5 (LFP/PEDOT:PSS/C_2mpyrFSI/LiFSI). The diblock ionic polymer-LFP electrodes were obtained by mixing an optimized ratio of components (LiFSI/polymer ionic unit: 2 mol; C_3mpyrFSI: 1 mol/polymer ionic unit) similar to a previous work with the corresponding amounts in the weighted ratio: 60 LFP / 10 C65 / 30 DIBLOC in NMP.[23] The diblock copolymer was obtained according to the synthesis reported elsewhere (see Figure 2.16).[23,32]

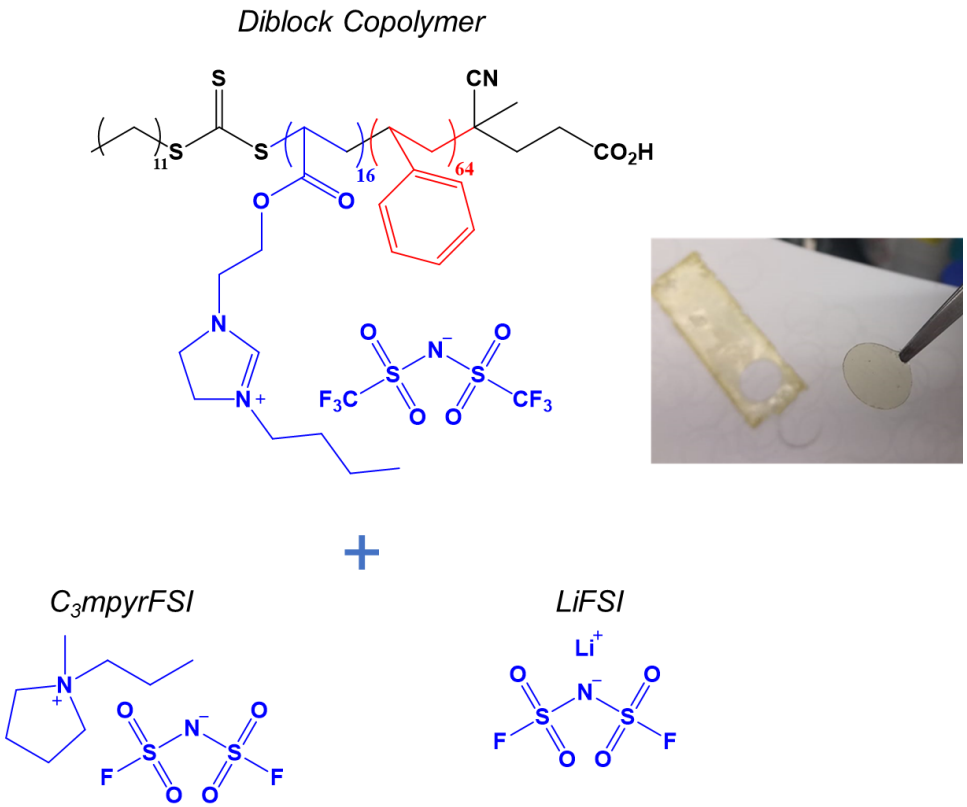

Figure 2.16. Chemical structures of solid electrolyte components: PILBLOC copolymer, C_3mpyrFSI and LiFSI.

The prepared slurries were casted onto carbon-coated aluminum current collector by using a doctor blade, then dried at room temperature and finally dried at 60ºC under vacuum overnight. No liquid electrolyte was used to wet the cathode as the ionic conduction of lithium is ensured by the use of a mixed conductor binder and lithium salt. The resulting mass loading of the electrodes was 1.2 mg cm^{-2} in both systems.

Li|LFP cells (CR2032) were assembled inside an argon glovebox using 50 µm lithium foil. Galvanostatic cycling was performed using a battery tester (Neware) at 70 ºC, which was the optimum temperature for the electrolyte.[32]

2.8. References

1. R. Del Olmo, M. Forsyth and N. Casado. Mixed Ionic-Electronic Conductors Based on Polymer Composites BT - Advances in Nanocomposite Materials for Environmental and Energy Harvesting Applications. eds. A. E. Shalan, A. S. Hamdy Makhlouf and S. Lanceros-Méndez, Springer International Publishing, Cham, **2022**., pp. 493–532.

2. B. D. Paulsen, K. Tybrandt, E. Stavrinidou and J. Rivnay. *Organic mixed ionic – electronic conductorsOrganic mixed ionic – electronic conductors*, Springer US.

3. X. Wu, A. Surendran, J. Ko, O. Filonik, E. M. Herzig, P. Müller-Buschbaum and W. L. Leong. Ionic-Liquid Doping Enables High Transconductance, Fast Response Time, and High Ion Sensitivity in Organic Electrochemical

Transistors. *Adv. Mater.* **2019**;31:1805544.

4. X. Wang, K. Ko, C. Yin, F. Wang, Q. Zhu and T. Tang. Enhancement of thermoelectric performance of PEDOT:PSS films by post-treatment with a superacid. *RSC Adv.* **2018**;8:18334–18340.

5. S. Kee, N. Kim, B. S. Kim, S. Park, Y. H. Jang, S. H. Lee, J. Kim, J. Kim, S. Kwon and K. Lee. Controlling Molecular Ordering in Aqueous Conducting Polymers Using Ionic Liquids. *Adv. Mater.* **2016**;28:8625–8631.

6. F. Makhlooghiazad, F. Nti, J. Sun, T. C. Mendes, S. S. Malunavar, J. M. Pringle and M. Forsyth. Composite electrolytes based on electrospun PVDF and ionic plastic crystal matrices for Na-metal battery applications. *JPhys Mater.* **2021**.

7. S. Malunavar, X. Wang, F. Makhlooghiazad, M. Armand, M. Galceran, P. C. Howlett and M. Forsyth. Highly conductive ionogel electrolytes based on N-ethyl-N-methylpyrrolidinium bis(fluorosulfonyl)imide FSI and NaFSI mixtures and their applications in sodium batteries. *JPhys Mater.* **2021**.

8. H. Ueda, F. Mizuno, R. Kerr, M. Forsyth and P. C. Howlett. Fast Charge and High Stability of Solid-state Graphite Organic Ionic Plastic Crystal Composite Anodes. *Batter. Supercaps* **2022**.

9. A. Gutiérrez-Pardo, F. Aguesse, F. Fernández-Carretero, A. I. Siriwardana,

A. García-Luis and A. Llordés. Improved Electromechanical Stability of the Li Metal/Garnet Ceramic Interface by a Solvent-Free Deposited OIPC Soft Layer. *ACS Appl. Energy Mater.* **2021**;4:2388–2397.

10. X. Wang, H. Zhu, G. W. Greene, Y. Zhou, M. Yoshizawa-fujita, Y. Miyachi, M. Armand, M. Forsyth, J. M. Pringle and P. C. Howlett. Organic Ionic Plastic Crystal-Based Composite Electrolyte with Surface Enhanced Ion Transport and Its Use in All- Solid-State Lithium Batteries. *Adv. Mater. Technol.* **2017**;2:1700046.

11. J. Sunarso, Y. Shekibi, J. Efthimiadis, L. Jin, J. M. Pringle, A. F. Hollenkamp, D. R. MacFarlane, M. Forsyth and P. C. Howlett. Optimising organic ionic plastic crystal electrolyte for all solid-state and higher than ambient temperature lithium batteries. *J. Solid State Electrochem.* **2012**;16:1841–1848.

12. J. Zhou, D. H. Anjum, L. Chen, X. Xu, I. A. Ventura, L. Jiang and G. Lubineau. The temperature-dependent microstructure of PEDOT/PSS fi lms : insights from morphological , mechanical and electrical analyses †. *J. Mater. Chem. C* **2014**;2:9903–9910.

13. N. Kim, S. Kee, S. H. Lee, B. H. Lee, Y. H. Kahng, Y. R. Jo, B. J. Kim and K. Lee. Highly conductive PEDOT:PSS nanofibrils induced by solution-processed crystallization. *Adv. Mater.* **2014**;26:2268–2272.

14. N. Kim, B. H. Lee, D. Choi, G. Kim, H. Kim, J. R. Kim, J. Lee, Y. H. Kahng

and K. Lee. Role of interchain coupling in the metallic state of conducting polymers. *Phys. Rev. Lett.* **2012**;109:1–5.

15. J. Rao, R. Vijayaraghavan, X. Wang, Y. Zhou, P. C. Howlett, D. R. Macfarlane, M. Forsyth and H. Zhu. Influence of Electrospun Poly(vinylidene difluoride) Nanofiber Matrix on the Ion Dynamics of a Protic Organic Ionic Plastic Crystal. *J. Phys. Chem. C* **2018**;122:14546–14553.

16. F. Nti, G. W. Greene, H. Zhu, P. C. Howlett, M. Forsyth and X. Wang. Anion effects on the properties of OIPC/PVDF composites. *Mater. Adv.* **2021**;2:1683–1694.

17. L. Bießmann, N. Saxena, N. Hohn, M. A. Hossain, J. G. C. Veinot and P. Müller-Buschbaum. Highly Conducting, Transparent PEDOT:PSS Polymer Electrodes from Post-Treatment with Weak and Strong Acids. *Adv. Electron. Mater.* **2019**;5:1–10.

18. Q. Li, M. Deng, S. Zhang, D. Zhao, Q. Jiang, C. Guo, Q. Zhou and W. Liu. Synergistic enhancement of thermoelectric and modulated PEDOT flexible films †. *J. Mater. Chem. C* **2019**;7:4374.

19. F. Nti, L. Porcarelli, G. W. Greene, H. Zhu, F. Makhlooghiazad, D. Mecerreyes, P. C. Howlett, M. Forsyth and X. Wang. The influence of interfacial interactions on the conductivity and phase behaviour of organic ionic plastic crystal/polymer nanoparticle composite electrolytes. *J. Mater. Chem. A* **2020**;8:5350–5362.

20. N. Casado, S. Zendegi, R. del Olmo, A. Dominguez-Alfaro and M. Forsyth. Tuning Electronic and Ionic Conductivities in Composite Materials for Electrochemical Devices. *ACS Appl. Polym. Mater.* **2021**.

21. A. Y. Zhou, X. Wang, H. Zhu, M. Yoshizawa-fujita, M. Armand, M. Forsyth, G. W. Greene, M. Jennifer, P. C. Howlett, Y. Zhou, X. Wang, H. Zhu, M. Yoshizawa-fujita and Y. Miyachi. Novel solid state lithium conductors for lithium metal batteries based on electrospun nanofibers and plastic crystal composites. *ChemSusChem* **2017**;10:3135–3145.

22. Y. Zhou, X. Wang, H. Zhu, M. Armand, M. Forsyth, G. W. Greene, J. M. Pringle and P. C. Howlett. N-ethyl-N-methylpyrrolidinium bis(fluorosulfonyl)imide-electrospun polyvinylidene fluoride composite electrolytes: Characterization and lithium cell studies. *Phys. Chem. Chem. Phys.* **2017**;19:2225–2234.

23. N. Goujon, T. Huynh, K. j. Barlow, R. Kerr, K. Vezzù, V. Di Noto, L. A. O'Dell, J. Chiefari, P. C. Howlett and M. Forsyth. Enabling High Lithium Conductivity in Polymerized Ionic Liquid Block Copolymer Electrolytes. *Batter. Supercaps* **2019**;2:132–138.

24. V. A. Nguyen and C. Kuss. Review — Conducting Polymer-Based Binders for Lithium-Ion Batteries and Beyond. *J. Electrochem. Soc.* **2020**;167:065501.

25. P. R. Das and J. E. Soc. PEDOT:PSS as a Functional Binder for Cathodes

in Lithium Ion Batteries. *J. Electrochem. Soc.* **2015**;162:A674–A678.

26. C. Strietzel, K. Oka, M. Strømme, R. Emanuelsson and M. Sjödin. An Alternative to Carbon Additives: The Fabrication of Conductive Layers Enabled by Soluble Conducting Polymer Precursors - A Case Study for Organic Batteries. *ACS Appl. Mater. Interfaces* **2021**;13:5349–5356.

27. P. Ge, S. Li, H. Shuai, W. Xu, Y. Tian, L. Yang, G. Zou, H. Hou and X. Ji. Engineering 1D chain-like architecture with conducting polymer towards ultra-fast and high-capacity energy storage by reinforced pseudo-capacitance. *Nano Energy* **2018**;54:26–38.

28. G. Xi, M. Xiao, S. Wang, D. Han, Y. Li and Y. Meng. Polymer-Based Solid Electrolytes: Material Selection, Design, and Application. *Adv. Funct. Mater.* **2021**;31:1–28.

29. A. Paolella, X. Liu, A. Daali, W. Xu, I. Hwang, S. Savoie, G. Girard, A. G. Nita, A. Perea, H. Demers, W. Zhu, A. Guerfi, A. Vijh, G. Bertoni, G. C. Gazzadi, G. Berti, C. Sun, Y. Ren, K. Zaghib, M. Armand, C. Kim, G. Xu and K. Amine. Enabling High-Performance NASICON-Based Solid-State Lithium Metal Batteries Towards Practical Conditions. *Adv. Funct. Mater.* **2021**;2102765:2102765.

30. T. Deng, X. Ji, Y. Zhao, L. Cao, S. Li, S. Hwang, C. Luo, P. Wang, H. Jia, X. Fan, X. Lu, D. Su, X. Sun, C. Wang and J. G. Zhang. Tuning the Anode–Electrolyte Interface Chemistry for Garnet-Based Solid-State Li Metal

Batteries. *Adv. Mater.* **2020**;32:1–10.

31. S. T. Hsu, B. T. Tran, R. Subramani, H. T. T. Nguyen, A. Rajamani, M. Y. Lee, S. S. Hou, Y. L. Lee and H. Teng. Free-standing polymer electrolyte for all-solid-state lithium batteries operated at room temperature. *J. Power Sources* **2020**;449:227518.

32. T. C. Mendes, N. Goujon, N. Malic, A. Postma, J. Chiefari, H. Zhu, P. C. Howlett and M. Forsyth. Polymerized Ionic Liquid Block Copolymer Electrolytes for All-Solid-State Lithium-Metal Batteries. *J. Electrochem. Soc.* **2020**;167:070525.

33. J. Olmedo, L. Meabe, R. Riva, G. Guzmán-González, L. Porcarelli, M. Forsyth, A. Mugica, I. Calafel, A. Muller, P. Lecomte, C. Jerome and D. Mecerreyes. Flame Retardant Polyphosphoester Copolymers as Solid Polymer Electrolyte for Lithium Batteries. *Polym. Chem.* **2021**.

34. Y. Cui, J. Wan, Y. Ye, K. Liu, L. Y. Chou and Y. Cui. A Fireproof, Lightweight, Polymer-Polymer Solid-State Electrolyte for Safe Lithium Batteries. *Nano Lett.* **2020**;20:1686–1692.

35. M. Yoshizawa-Fujita, E. Kishi, M. Suematsu, T. Takekawa and M. Rikukawa. A Plastic Electrolyte Material in a Highly Desirable Temperature Range: N-Ethyl-N-methylpyrrolidinium Bis(fluorosu lfonyl)amide. *Chem. Lett.* **2014**.1909–1911.

Chapter 3. Mixed Ionic and Electronic Conductors based on PEDOT:PolyDADMA and Organic Ionic Plastic Crystals

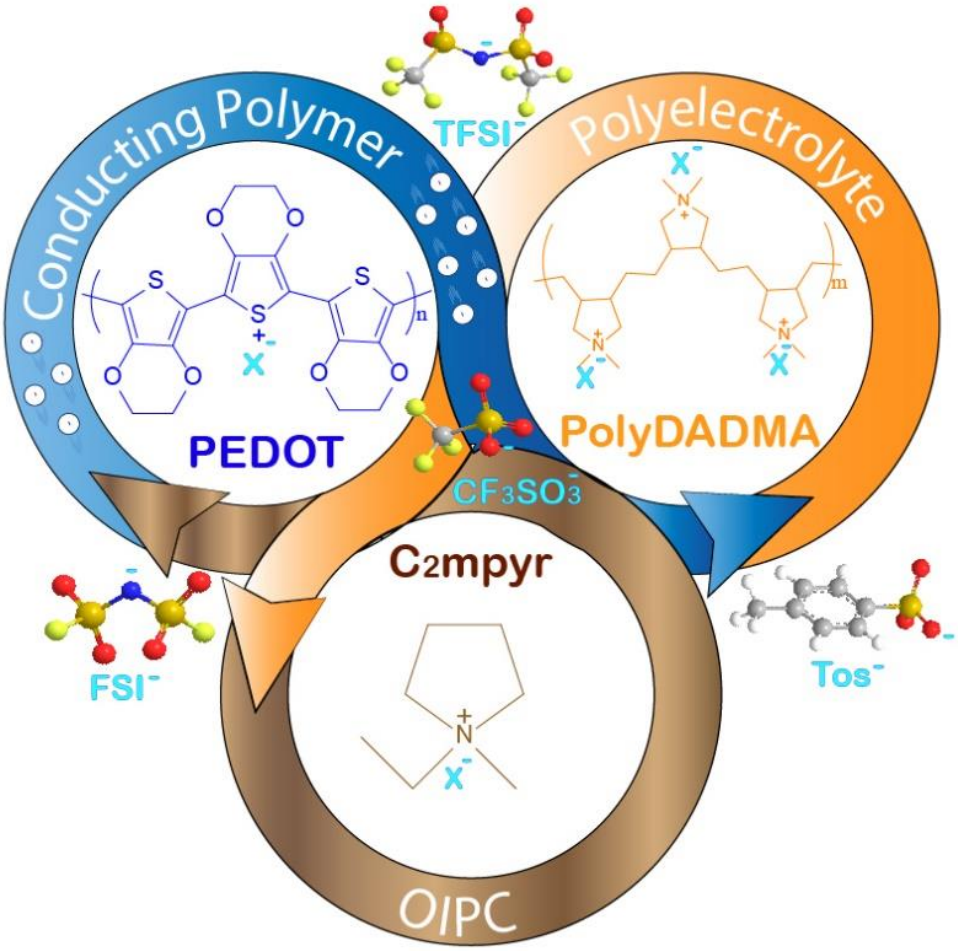

Chapter 3. Mixed Ionic and Electronic Conductors based on PEDOT:PolyDADMA and Organic Ionic Plastic Crystals

3.1. Introduction

In the last few decades, the potential of organic MIECs (OMIECs) has been highlighted because of their high electronic conductivity and flexibility in their synthesis and processability as commented in Chapter 1. These OMIECs are mainly based on π-conjugated polymers that can be functionalized with polyelectrolytes and polymer electrolytes via pendant groups,[1] form copolymers, or blended with other polymers (e.g., polyethylene oxide (PEO)[2] and polystyrene sulfonate (PSS)[3]); improving their properties or the desired application. Among all of the conducting polymers, PEDOT is the most widely studied, being accompanied by anions such as chloride (Cl), tosylate (Tos) or PSS that strongly stabilize the positively charged polarons of $PEDOT^+$ enabling the high efficient electronic conduction.[3–7]

Besides, PSS acts as a dispersing agent to obtain a processable water dispersion. The commercially available PEDOT:PSS dispersion, Clevios PH1000, has an electronic conductivity around 0.2 S cm^{-1}, as can be seen in Chapter 2. This material has been widely employed given its characteristics in a wide variety of applications such as energy storage systems (ESSs),[8] ion pumps,[9] sensors,[10] bioelectronics[11] and thermoelectrics.[12] However, the slight acidity of PSS might be disadvantageous for some of them.[13]

Among the polyelectrolytes successfully employed in those fields, on top of a large number of polyethers, poly(diallyldimethylammonium)-based

(PolyDADMA$^+$) materials have attracted the attention of the scientific community taking advantage of its rich chemistry, being possible to combine with targeted anions; ease to synthesize and film-forming properties. FSI and TFSI anions have been combined with this polycation resulting in robust membranes with high-performance in different types of batteries.[14,15] Triflate anion has been also considered for proton-exchange membranes.[16]

Another promising family of ionic conducting materials for energy storage systems in solid-state is organic ionic plastic crystals (OIPC). They have shown high ionic conductivity and wide electrochemical window, enabling their use in graphite anodes (as electrode additive)[17] as well as lithium- and sodium-ion batteries (as electrolytes).[18,19] Moreover, they have been successfully employed in combination with polymers exhibiting interesting properties given by their interactions (as studied in Chapter 2). [20,21]

In this chapter we investigated the ternary system between PEDOT, PolyDADMA (poly(diallyldimethylammonium)) and C_2mpyr (N-ethyl-N-methylpyrrolidonium OIPC, as illustrated in the graphical abstract, in the presence of four different counter-anions: CF_3SO_3 (triflate), FSI (bis(fluorosulfonyl)imide), TFSI (bis(trifluoromethylsulfonyl)imide) and Tos (tosylate) looking for a synergistic behavior of high ionic-electronic conduction. For this purpose, we first perform the synthesis and characterization of the individual systems (PolyDADMA X). Secondly, the synthesis and characterization of PEDOT:PolyDADMA take place. Thirdly, neat OIPCs (C_2mpyrX) were studied, and finally, the ternary system was investigated in terms of thermal analysis, ionic-electronic conductivity and electrochemical response.

3.2. PolyDADMA X characterization

A series of PolyDADMA X materials were synthesized via anion exchange of PolyDADMAC, where X is either FSI, TFSI, CF_3SO_3 or Tos, as explained in Sections 3.7.3 and 3.7.4, following the scheme of Figure 3.1. The thermal behavior and ionic conductivity of these compounds were tested and are discussed below.

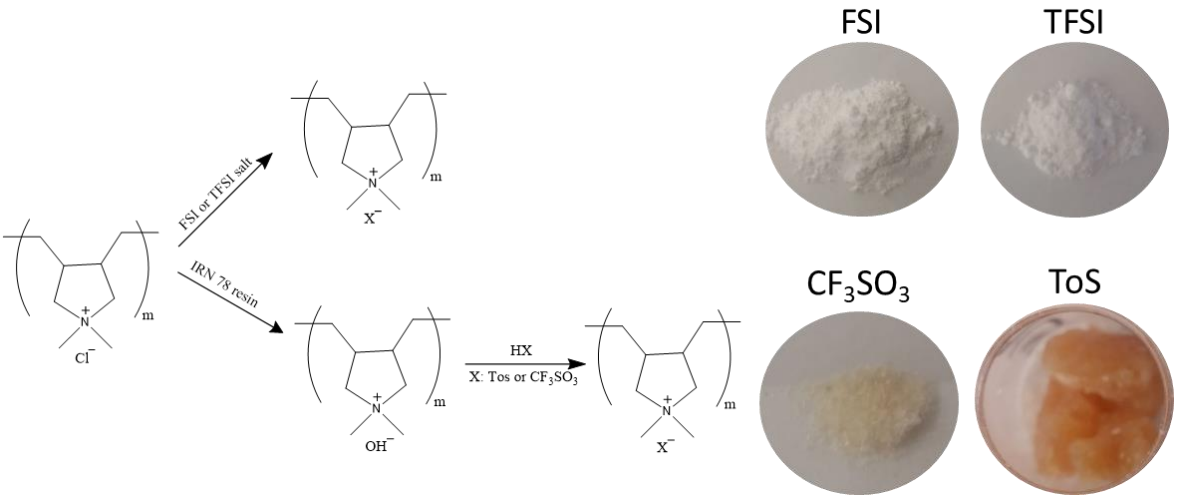

Figure 3.1. Synthesis of different polyelectrolyte poly(diallyldimethylammonium) (PolyDADMA X) materials.

3.2.1. Thermal analysis

Thermogravimetric analysis (TGA) of the PolyDADMA samples was conducted to investigate their thermal stabilities. This technique can result in an overestimate of the long-term thermal stability compared to an isothermal measurement, but it is nevertheless a valuable initial assessment of the relative impact of the different anions on the thermal properties.

PolyDADMA FSI and PolyDADMA TFSI show a decomposition temperature (T_d) of 300 °C and 450 °C, respectively; in agreement with already

reported values.[22] In this study, the thermal behavior of PolyDADMA CF_3SO_3 and PolyDADMA Tos was studied by TGA, as shown in Figure 3.2a. The TGA curves show that the degradation of PolyDADMA CF_3SO_3 and PolyDADMA Tos occur in one step at temperatures higher than 427 °C and 382 °C, respectively. Therefore, the decomposition temperature of the different polyDADMA-X polyelectrolytes follows the trend: FSI < Tos < CF_3SO_3 < TFSI, which shows a huge impact of the anion on the thermal stability as previously observed in ionic liquids with the same tendency.[23] It should be mentioned that a 10% weight loss related to absorbed water was observed for PolyDADMA Tos at around 100 °C, due to its hygroscopic nature.

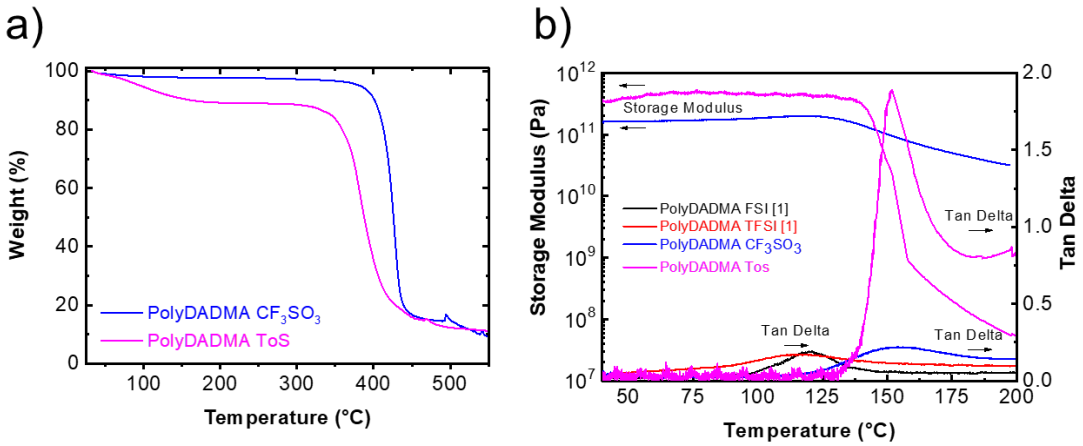

Figure 3.2. a) Thermogravimetric analysis (TGA) curves of the neat PolyDADMA CF_3SO_3 and Tos polyelectrolytes. b) Dynamic mechanical analysis (DMA) curves of the neat PolyDADMA FSI, TFSI, CF_3SO_3 and Tos polyelectrolytes.

As no transition temperatures were observed by differential scanning calorimetry (DSC) in the range of –70 and 200 °C, dynamic mechanical analysis (DMA) was used to study the thermal transitions of PolyDADMA X polyelectrolytes between 40 and 200 °C (Figure 3.2b). During DMA measurements, with increasing temperature, a sharp decay in the storage modulus is usually observed when the material passes through the glass

transition, thus T_g can be determined from the maximum of tan delta and the concomitant decrease in storage modulus. From these DMA data, the T_g measured for PolyDADMA CF_3SO_3 is 154 °C and 152 °C for PolyDADMA Tos. The Tg of PolyDADMA FSI and PolyDADMA TFSI have been previously reported at 121 and 116 °C, respectively.[22]

3.2.2. Ionic conductivity

The ionic conductivity of the PolyDADMA X polyelectrolytes was investigated by EIS between 25 and 90 °C. The values are plotted in Figure 3.3a, which shows that PolyDADMA CF_3SO_3 yields the highest ionic conductivity, 2×10^{-6} S cm^{-1} at room temperature. The value for PolyDADMA FSI (1×10^{-7} S cm^{-1} at 70 °C) is consistent with a previous study (2×10^{-7} S cm^{-1} at 70 °C),[22] as presented in Table 3.1. The ionic conductivity for PolyDADMA TFSI is similar to that of PolyDADMA FSI (1×10^{-7} S cm^{-1} at 70 °C), as reported by Fdz. de Añastro et al. [14] Surprisingly, the conductivity values of PolyDADMA CF_3SO_3 were higher than PolyDADMA FSI and PolyDADMA TFSI in all the ranges of temperatures, despite showing a higher T_g. Static 19F-NMR lineshape analysis was used to study the ion dynamics of PolyDADMA CF_3SO_3 and PolyDADMA TFSI between 20 and 80 °C (see Figure 3.3b), showing $CF_3SO_3^-$ narrower peaks, thus suggesting higher mobility of the anion than that of TFSI.

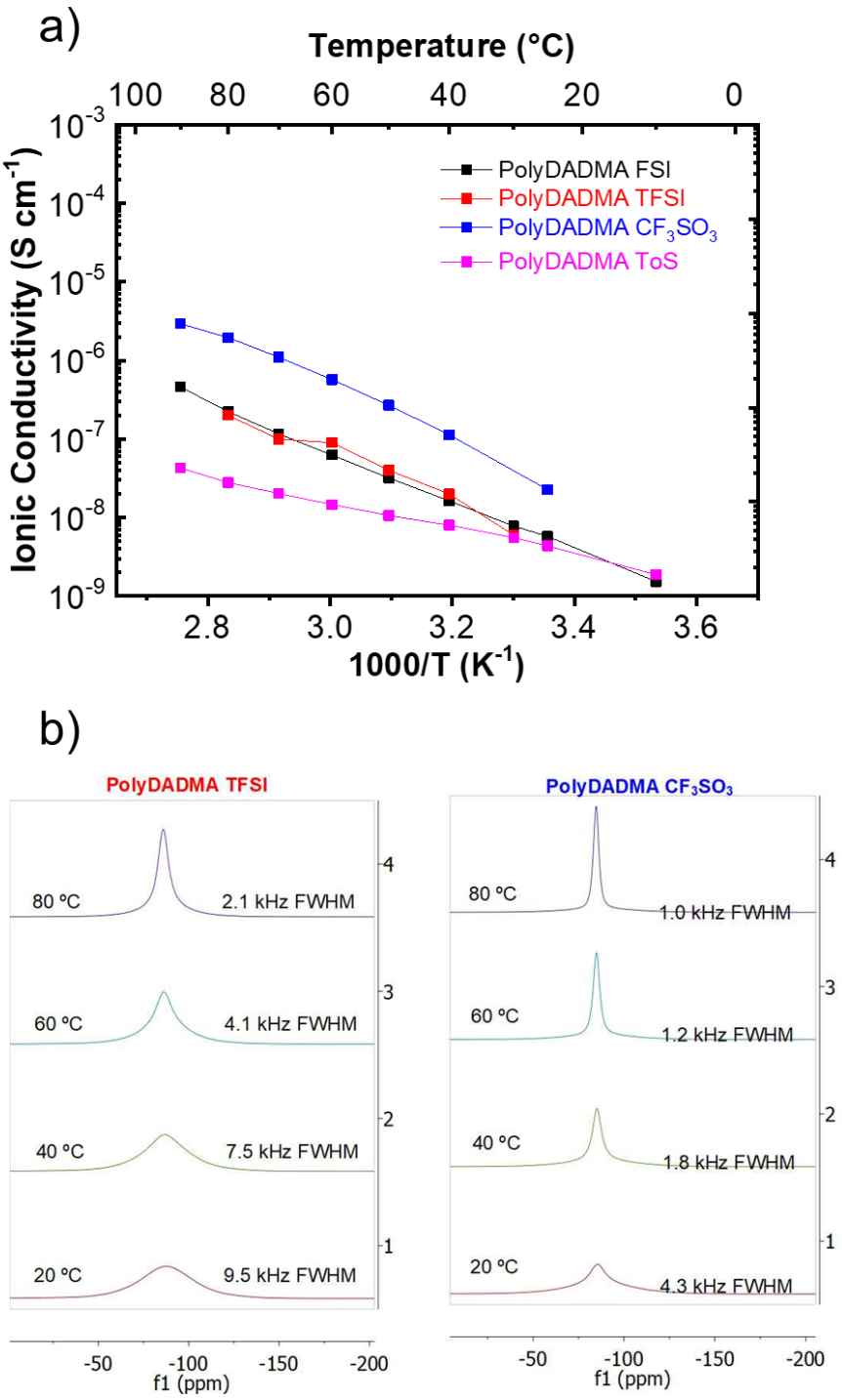

Figure 3.3. a) Ionic conductivity of neat PolyDADMA X (X: FSI, TFSI, CF_3SO_3 and Tos). b) Static 19F-NMR of PolyDADMA TFSI and PolyDADMA CF3SO3 at different temperatures.

Finally, PolyDADMA Tos yielded the lowest ionic conductivity (2×10^{-8} S cm^{-1} at 70 °C), due to the large and rigid nature of the anion, likely resulting in

lower mobility. This material also had the narrowest tan delta in contrast to the other three systems, which showed broad peaks reflecting more dynamic T_g. [24]

Table 3.1. Ionic conductivities (σ_{ionic}) of the PolyDADMA X polyelectrolytes obtained experimentally at 70 °C, compared to literature values and the activation energy (E_a).

Compound	Literature values	Experimental values	
	σ_{ionic} / S cm^{-1}	σ_{ionic} / S cm^{-1}	E_a / KJ mol^{-1}
PolyDADMA FSI	2×10^{-7} [22]	1×10^{-7}	25.9 ± 0.4
PolyDADMA TFSI	1×10^{-7} [14]	-	25.8 ± 2.5 [14]
PolyDADMA CF_3SO_3	-	1×10^{-6}	29.2 ± 1.3
PolyDADMA Tos	-	2×10^{-8}	13.6 ± 0.4

3.3. PEDOT:PolyDADMA X characterization

In order to provide electronic conductivity to PolyDADMAX X systems and obtain new mixed ionic-electronic conductors, EDOT was polymerized in the presence of PolyDADMA X (Figure 3.4), to obtain blends of a conducting polymer (PEDOT) and polyelectrolyte (PolyDADMA X). In the case of FSI and TFSI anions, precipitation of the product was carried out as explained in Section 3.7.5, by the addition of FSI or TFSI salt to the PEDOT:PolyDADMAC. The solubility of these compounds depends totally on the anion, which ranges from non-polar such as acetonitrile, acetone or tetrahydrofuran (in the case of FSI and TFSI), to polar such as methanol or water (Cl, CF_3SO_3 and Tos).

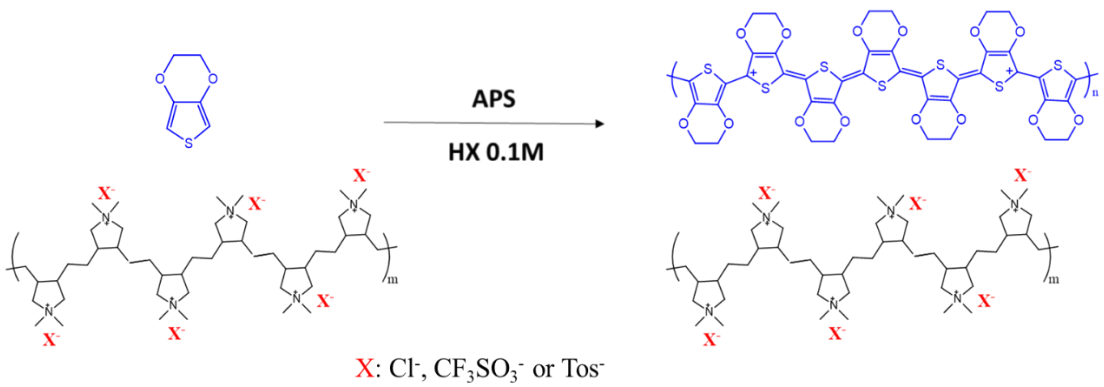

Figure 3.4. Synthesis of PEDOT:PolyDADMA X.

3.3.1. Thermal analysis

The TGA curves of the PEDOT:PolyDADMA X polyelectrolytes, with the anion being either Cl, FSI, TFSI, CF_3SO_3 or Tos, are shown in Figure 3.5. PEDOT:PolyDADMA Cl, PEDOT:PolyDADMA CF_3SO_3 and PEDOT:PolyDADMA Tos show a two-step decomposition profile, while PEDOT:PolyDADMA FSI and PEDOT:PolyDADMA TFSI show a single step decomposition. The lower decomposition step, at around 300 °C, is related to PEDOT, while the step between 350 and 450 °C is attributed to the decomposition of PolyDADMA X. Previous studies have reported that PEDOT:Cl, PEDOT:CF_3SO_3 and PEDOT:Tos decompose below 350 °C,[25,26] while the decomposition of PolyDADMA X occurs around 400 °C. In the case of PEDOT:PolyDADMA Cl, two peaks were observed in the TGA curve with a shoulder in the first peak. This shoulder is due to PolyDADMA Cl, which normally presents a two-step decomposition profile, at 300 °C and 450 °C, the first peak coinciding with the decomposition of PEDOT:Cl.[27]

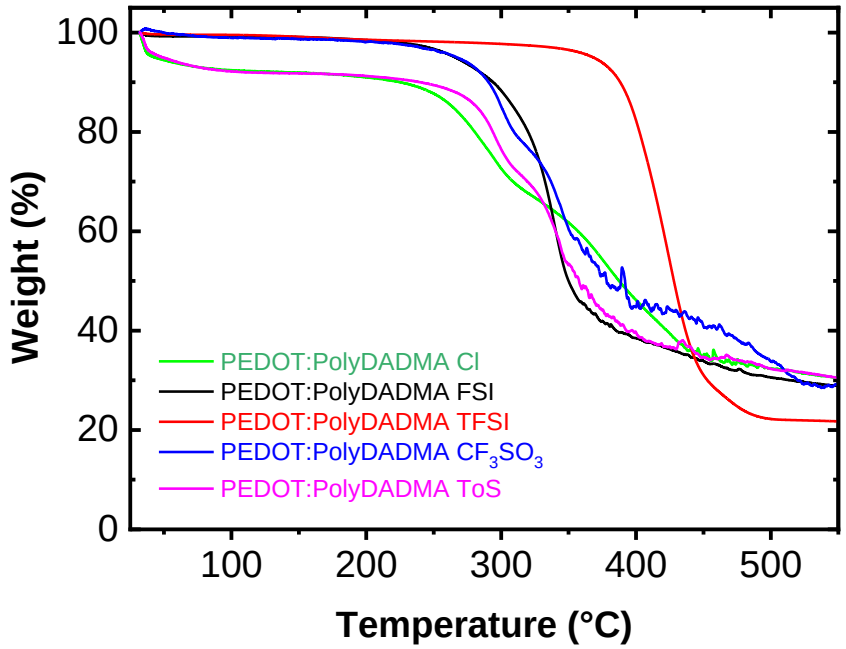

Figure 3.5. TGA curves of PEDOT:PolyDADMA Cl, FSI, TFSI, CF_3SO_3 and Tos.

A comparison of the neat PolyDADMA X and PEDOT X (Table 3.2) shows that the decomposition temperatures have generally diminished in the blends. This is most likely due to the interruption of the interactions within PolyDADMA X by the presence of the other cation ($PEDOT^+$) that can also interact with X^-. The first decomposition temperature of PEDOT:PolyDADMA X is likely related to PEDOT X.

Table 3.2. Decomposition temperature of PEDOT:X, PolyDADMA X and PEDOT:PolyDADMA X, where $T_{1,d}$ means the first step of decomposition and $T_{2,d}$ means the second step of decomposition.

X	T_d *PEDOT:X* / °C	T_d *PolyDADMA X* / °C	$T_{1,d}$ *PEDOT:PolyDADMA X* / °C	$T_{2,d}$ *PEDOT:PolyDADMA X* / °C
Cl	300 [25]	300 and 450 [27]	281, 295	378
FSI	-	300 [22]	-	340
TFSI	-	450 [22]	-	423
CF_3SO_3	360 [26]	427	301	345
Tos	343 [26]	382	296	343

3.3.2. Ionic conductivity

The ionic conductivity of the mixed conductors was investigated by EIS between 25 to 90 °C (Figure 3.6). In all cases, a closed semicircle typical of mixed ionic electronic conductors was observed in the Nyquist plots.[28] Compared to neat PolyDADMA X, the ionic conductivity of PEDOT:PolyDADMA X increased. At 70 °C the highest ionic conductivity value was reached by PEDOT:PolyDADMA TFSI (3×10^{-5} S cm^{-1}) followed by FSI (5×10^{-6} S cm^{-1}), CF_3SO_3 (7×10^{-7} S cm^{-1}), Tos (5×10^{-7} S cm^{-1}) and finally Cl (2×10^{-8} S cm^{-1}). As discussed above, the packing ability of the anion appears to be crucial. The smaller the anion, the stronger the interactions with the polymer, while the bigger anions have lower mobility. The TFSI anion appears to offer the most ideal compromise, in terms of enhancing the ionic conductivity.

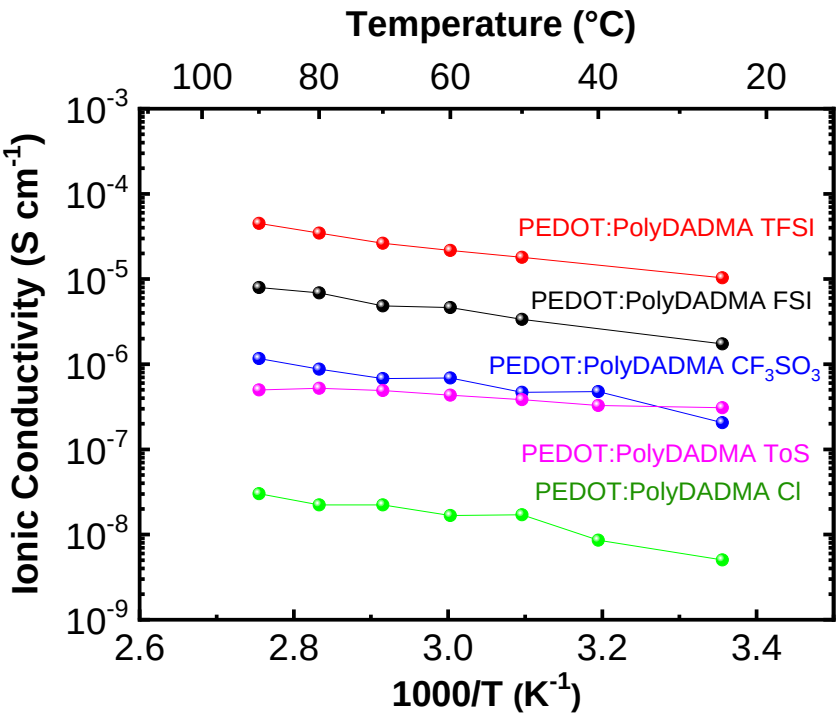

Figure 3.6. Ionic conductivity of PEDOT:PolyDADMA X (X: Cl, FSI, TFSI, CF_3SO_3, Tos)

The activation energies are also influenced by the interactions between the anion and the polymers. The Tos anion resulted in the lowest E_a (4.0 ± 0.4 KJ mol^{-1}) with FSI, TFSI, Cl and CF_3SO_3 having slightly higher values (8.4 ± 0.4, 8.6 ± 0.5, 8.9 ± 1.0 and 7.5 ± 1.0 KJ mol^{-1}, respectively). The activation energies of the mixed conductors are much lower than that of the neat PolyDADMA X, probably because of the interaction of the anion with the other cation (PEDOT), resulting in weaker bonds between X and the cations, as discussed in the thermal stability section. These interactions are also likely to be responsible for the increased ionic conductivity of PEDOT:PolyDADMA X versus the neat PolyDADMA X.

3.3.3. Electronic conductivity

The electronic conductivities of PEDOT:PolyDADMA FSI and PEDOT:PolyDADMA TFSI coatings were measured (Table 3.3), however films of PEDOT:PolyDADMA CF_3SO_3, PEDOT:PolyDADMA Tos and PEDOT:PolyDADMA Cl could not form films.

Higher electronic conductivity values ($\sigma_{electronic}$) were measured for coatings compared with pellets since the coatings are smoother and much thinner than the pellets. The effect of coating thickness is well known in the field of electronic conductors.[29] The conductivity of PEDOT comes from the existence of polarons and bipolarons formed in the chains, where the charges can flow.[30] The FSI system results in higher electronic conductivity than the TFSI system, with conductivity values of 0.60 S cm^{-1} versus 0.25 S cm^{-1}, respectively, which may be the result of a greater formation of polarons in the FSI system.

For the pellets, the highest electronic conductivity was attained by the CF_3SO_3 system (0.3 S cm^{-1}) followed by Cl (0.1 S cm^{-1}) and Tos (0.1 S cm^{-1}), in contrast to FSI (0.04 S cm^{-1}) and TFSI (0.02 S cm^{-1}). PEDOT:Cl and PEDOT:Tos have been previously synthesized by vapor phase polymerization, showing electronic conductivity values of 400 S cm^{-1} and 700 S cm^{-1}, respectively.[7] The tosylate anion can provide π -conjugated electrons where charges of PEDOT can be delocalized. The doping effect of acids on PEDOT has been well studied,[31] and TFMSA, which was involved in the polymerization of PEDOT:PolyDADMA CF_3SO_3, is known as a superacid. These factors make FSI and TFSI poorer dopants in contrast to Cl, CF_3SO_3 and Tos.

Although these electronic conductivity values do not seem high in comparison with the numbers in Chapter 2, even in thick pellet form, the values are close to those of the commercially available Clevios PH1000 (0.2 S cm^{-1}).

Table 3.3. Electronic conductivity ($\sigma_{electronic}$) of coatings and pellets of the PEDOT:PolyDADMA X samples with varying anions.

	Coating		Pellet	
	Thickness / μm	**$\sigma_{electronic}$ / S cm^{-1}**	**Thickness / μm**	**$\sigma_{electronic}$ / S cm^{-1}**
FSI	70	0.60	400	0.04
TFSI	75	0.25	500	0.02
Cl	-	-	250	0.10
CF_3SO_3	-	-	350	0.30
Tos	-	-	250	0.10

3.4. Organic Ionic Plastic Crystals characterization

In order to enhance the mechanical properties and ionic conductivity, OIPCs with the same anions used above were synthesized (see Section 3.7.4) to prepare composites of 80/20 wt% PEDOT:PolyDADMA X/C_2mpyr[X]. Previous studies have indicated that the electronic conductivity can be improved by doping

conducting polymers with ILs.[32,33] In order to understand the effects of the OIPCs on the composite systems, prior thermal and conductivity characterization was performed and is presented and discussed below.

3.4.1. Thermal analysis

The TFSI anion provides the highest thermal stability, with a one-step decomposition observed at 454 °C (Figure 3.7a). The T_d of C_2mpyrFSI was measured to be at 313 °C, which is close to that previously reported by Yamada et al. (300 °C).[34] The decomposition temperature of C_2mpyrTFSI is 150 degrees higher than the corresponding FSI salt, in a similar trend as the PolyDADMA X samples (450 and 300 °C respectively). The thermogram related to the CF_3SO_3 OIPC presents a T_d around 410 °C, which is similar to that previously reported for N-butyl-N-methylpyrrolidinium triflate.[35] Finally, C_2mpyrTos presents a T_d of 357 °C, which is in good agreement with that reported by Dhahri et al. for an imidazolium-tosylate-based salt.[36]

As previously discussed in the section on the thermal stability of PolyDADMA X, the anion has a huge impact on the decomposition behavior. The T_d of these salts follows the same trend observed in PolyDADMA X, that is: Td FSI < Tos < CF_3SO_3 < TFSI. All of them are thermally stable up to at least 300 °C, which enables their use in many electrochemical applications.

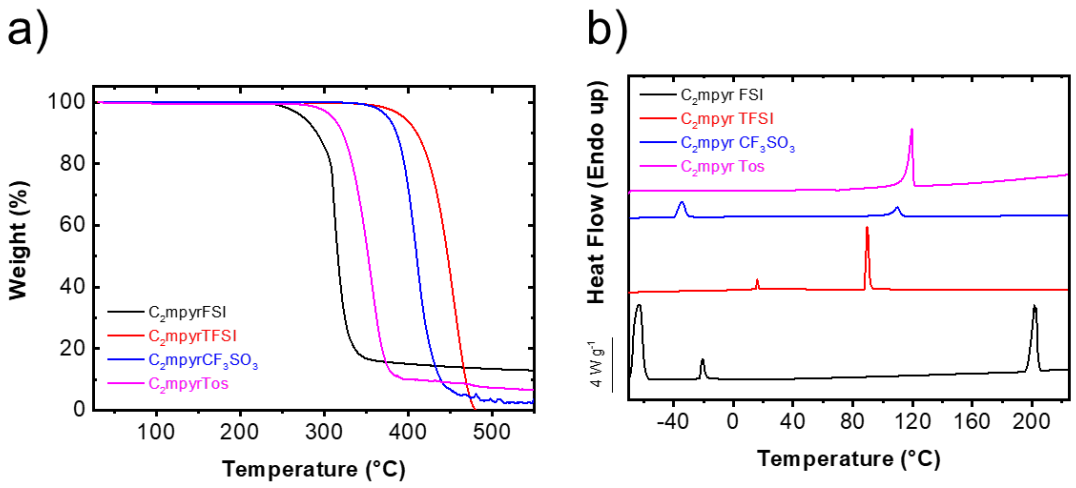

Figure 3.7. a) TGA and b) DSC curves of the organic ionic plastic crystals (OIPCs) with different anions.

Thermal analysis of the OIPCs by DSC showed different thermal behaviors depending on the anion. OIPCs are characterized by having one or more solid-solid transition temperatures prior to melting, a long-range ordered crystalline lattice and entropies of fusion following Timmerman's criterion (<20 J K^{-1} mol^{-1}) as introduced in Section 1.2.3. The existence of solid-solid phase transition temperatures, T_{S-S}, is accompanied by an increase in the mobility of the ions due to rotational motions and/or major structural reorientation of the ions, resulting in a disordered lattice.[37] The solid-solid phase transitions also often result in a small entropy of fusion that gives the material "plastic–crystal" properties.

The DSC curves are presented in Figure 3.7b and summarized in Table 3.4. OIPCs with the FSI and TFSI salts present solid-solid phase transitions with similar values to previous studies.[38,39] In the case of C_2mpyrFSI, there are two T_{S-S} at −64 and −21 °C and a melting point at 201 °C with a low entropy value (10.1 J K^{-1} mol^{-1}). On the other hand, C_2mpyrTFSI presents two T_{S-S} occurring at 16 and 46 °C before the melting point at 90 °C with a higher entropy (29.3 J

K^{-1} mol^{-1}). The higher range of temperatures between the T_{S-S} and melting point and the lower entropy of fusion explains the higher plasticity of C_2mpyrFSI versus C_2mpyrTFSI.[37]

Table 3.4. Thermal properties of the OIPCs from DSC analysis

	III-II / °C	*II-I* / °C	T_m / °C	ΔS / J K^{-1} mol^{-1}
[C_2mpyr][FSI]	-64	-21	201	10.1
[C_2mpyr][TFSI]	16	46	90	29.3
[C_2mpyr][CF_3SO_3]	-	-34.4	110	12.5
[C_2mpyr][Tos]	-	-	120	67.5

The thermal behavior of C_2mpyrCF_3SO_3 is characterized by having one T_{S-S} at −34.4 °C and a melting point at 110 °C. Additionally, the entropy of fusion of this salt satisfies Timmerman's criterion presenting 12.5 J K^{-1} mol^{-1} confirming this material to be an OIPC with a plastic behavior similar to C_2mpyrFSI and over a significant range of temperature. In contrast, C_2mpyrTos does not present any solid-solid phase transitions and has a broad melting point at 120 °C with an entropy of 67.5 J K^{-1} mol^{-1}. These values are close to those previously reported in the literature.[40–42] The high value of entropy and absence of a T_{S-S} means that this salt cannot be considered to have plastic crystal behavior.

3.4.2. Ionic conductivity

Figure 3.8 compares the ionic conductivity of the different salts. In all cases, the conductivity increased with higher temperature, following typical Arrhenius behavior. In the cases of TFSI, CF_3SO_3 and Tos, a dramatic increase in conductivity is observed at high temperatures as the trend is influenced by the melting point of the compounds near 100 °C.

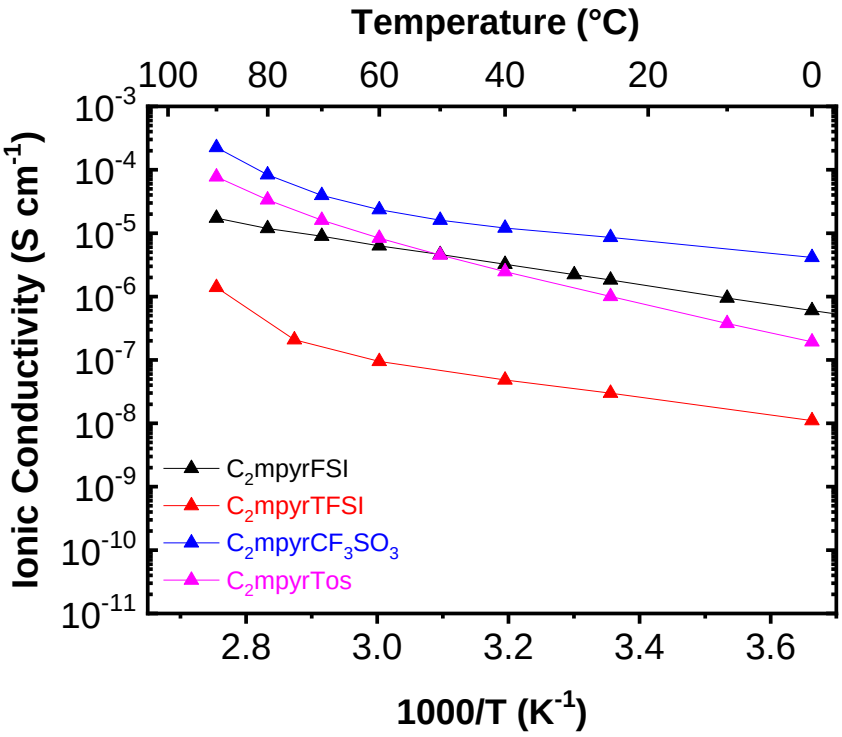

Figure 3.8. Ionic conductivity of OIPCs with different anions (FSI, TFSI, CF_3SO_3 and Tos).

The ionic conductivity values are intimately related to the thermal behavior of the materials. As previously discussed for OIPCs, the existence of a T_{S-S} and melting point with low entropy, are typical of OIPCs with significant ion dynamics. The maximum ionic conductivity value at 70 °C was 4 × 10^{-5} S cm^{-1}, for $C_2mpyrCF_3SO_3$. This can be attributed to the fact that the CF_3SO_3 anion is the smallest of the anion series, along with the thermal behavior discussed above. On the other hand, $C_2mpyrTFSI$ presented the lowest ionic conductivity values (2 × 10^{-7} S cm^{-1} at 70 °C), close to those previously reported in the literature.[41] The $C_2mpyrFSI$ shows an ionic conductivity value of 9 × 10^{-6} S cm^{-1} at 70 °C, which is slightly different from that previously reported (6 × 10^{-6} S cm^{-1} at 70 °C),[43] but the difference could be attributed to different geometries of the EIS cell or differences in the measurement procedure. Surprisingly, given the absence of

OIPC behavior, the values related to C_2mpyrTos (2×10^{-5} S cm^{-1} at 70 °C) are close to C_2mpyrFSI although the latter has a higher conductivity at lower temperatures. Also, very surprisingly, C_2mpyrTos presents higher ionic conductivity values than C_2mpyrTFSI across the entire temperature range in this study. This possibly could be related to the fact that some small impurity is present in the C_2mpyrTos, as suggested by the broad peak onset of the melting point. This is typical of liquidus-like behavior where even a fractional impurity can lead to a liquid eutectic at the grain boundaries of the pure C_2mpyrTos crystals. This liquid phase would increase as the final melt is approached and lead to an increase in high ionic conductivity. Previous studies have shown that even a 1% impurity (or dopant) component can increase the ionic conductivity dramatically.[44,45]

The activation energies for the conductivity of these salts are quite low but this is the case mainly for the ones classified as an OIPC: C_2mpyrFSI (12.9 ± 0.1 KJ mol^{-1}), C_2mpyrTFSI (11.42 ± 0.3 KJ mol^{-1}) and C_2mpyrCF_3SO_3 (8.5 KJ ± 0.2 mol^{-1}). The more disordered a compound is, the lower the activation energy is, and this disorder is connected to the properties of the OIPC, the T_{S-S} and the low entropy of fusion.[46] C_2mpyrCF_3SO_3, which has a large temperature range between the T_{S-S} and the Tm, a low melting point as well as a low melting entropy, was measured to have the lowest activation energy.

3.5. PEDOT:PolyDADMA X + OIPC characterization

Finally, the synthesized OIPCs were added to PEDOT:PolyDADMA X blends, in order to study the doping effect of the OIPCs and improve the transport properties. Composites of 80/20 wt% PEDOT:PolyDADMA X/C_2mpyr[X] were

prepared by dissolving the solids and mixing them in liquid state. Good coatings were formed from the FSI and TFSI system but not with the other anions.

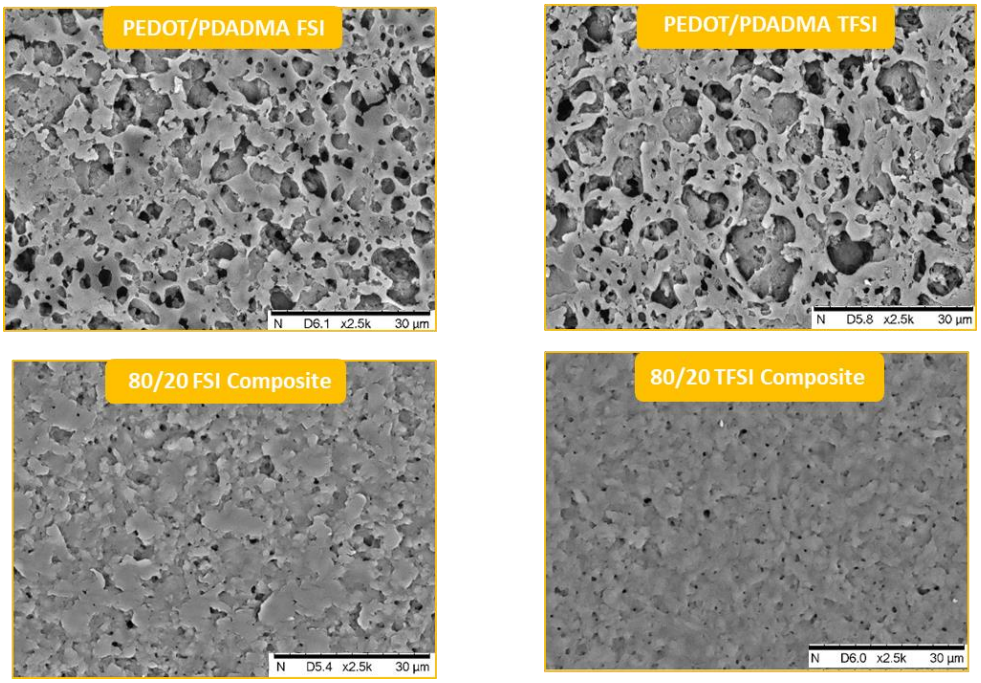

Figure 3.9. SEM images of PEDOT:PolyDADMA FSI, TFSI and their composites with C_2mpyrFSI and C_2mpyrTFSI respectively.

SEM images of the neat PEDOT:PolyDADMA FSI and PEDOT:PolyDADMA TFSI and their composites were taken (Figure 3.9), where it seems the OIPC is able to cover the material forming a more continuous film. Hence, the composites were mixed in solid-state with a mortar and pressed into pellets to compare them under the same conditions (see Figure 3.10).

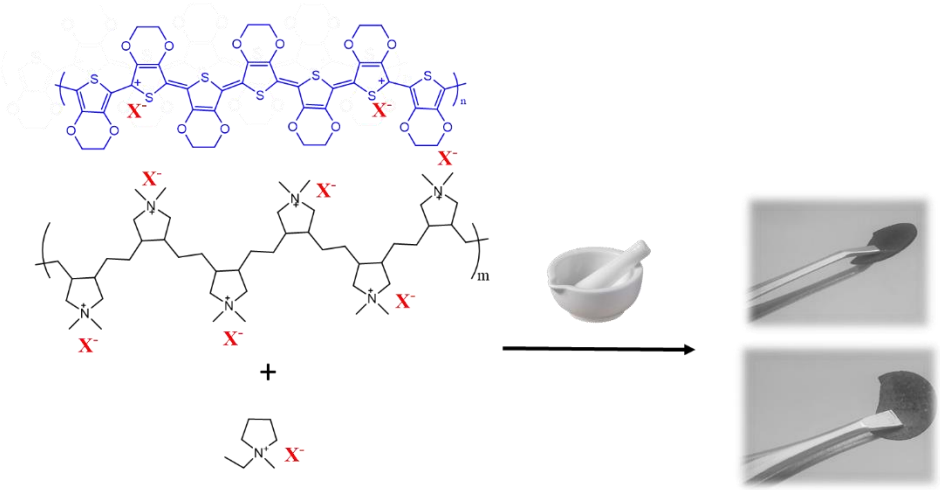

Figure 3.10. Preparation of 80/20 PEDOT:PolyDADMA X / C_2mpyr X composites.

3.5.1. Electronic conductivity

The electronic conductivity of the 80/20 PEDOT:PolyDADMA X / C_2mpyr X pellets of ~500 µm of thickness were measured by 4PP, under the same conditions as PEDOT:PolyDADMA X. C_2mpyrCF_3SO_3 led to a significant enhancement of the electron transport from the pure PEDOT:PolyDADMA CF_3SO_3 (0.3 S cm^{-1}) to the value of 0.73 S cm^{-1}. FSI and TFSI OIPCs slightly enhanced the conductivity from their respective values; for PEDOT:PolyDADMA X conductivity increased from 0.04 S cm^{-1} and 0.02 S cm^{-1} to 0.08 S cm^{-1} and 0.06 S cm^{-1}, respectively. Finally, the electronic conductivity of the 80/20 PEDOT:PolyDADMA Tos/C_2mpyrTos could not be measured, possibly because of the apparent hygroscopic behavior of the material and/or a very low conductivity value.

3.5.2. Ionic conductivity

EIS measurements of the composites were carried out between 30 and 90 °C. The typically closed semicircle of MIECs was observed in all the samples.

Evaluation of the ionic conductivity of the 80/20 wt% PEDOT:PolyDADMA X/C_2mpyr[X] (Figure 3.11) shows there is a significant increase of one order of magnitude for the FSI (2×10^{-5} S cm^{-1} at 70 °C) composite versus PEDOT:PolyDADMA FSI with no OIPC (5×10^{-6} S cm^{-1} at 70 °C). The ionic conductivity value of PEDOT:PolyDADMA CF_3SO_3 at 70 °C was enhanced from 7×10^{-7} S cm^{-1} to 1×10^{-6} S cm^{-1} with the addition of the OIPC. Finally, in the case of TFSI and Tos, the ionic conductivity value decreased from 3×10^{-5} S cm^{-1} and 5×10^{-7} to 4×10^{-6} S cm^{-1} and 2×10^{-8} S cm^{-1}, respectively. The increase of ionic conductivity from the addition of C_2mpyrFSI and C_2mpyrCF_3SO_3 could be because both of these salts have higher intrinsic ion dynamics following Timmerman's criterion (see Section 1.2.3) for plastic crystals, and hence considered as OIPCs, and these higher dynamics are retained in the composites. On the other hand, composites formed with the salts C_2mpyrTFSI and C_2mpyrTos do not fit into this criterion and have intrinsically lower ion dynamics as seen from the conductivity of the pure salts; hence their presence in the composite decreases the overall ionic conductivity.

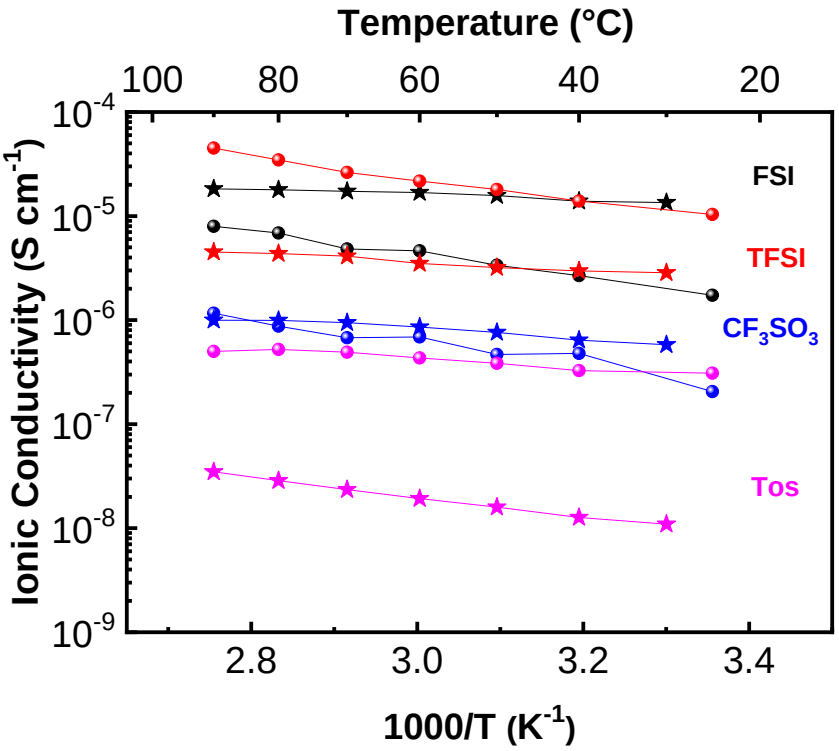

Figure 3.11. Ionic conductivity values of PEDOT:PolyDADMA X (spheres) and 80/20 PEDOT:PolyDADMA X / C_2mpyr[X] composites (stars), where X is FSI (black), TFSI (red), CF_3SO_3 (blue) and Tos (pink).

The Ea of the composites also changed with the addition of the OIPCs. In general, the incorporation of C_2mpyr[X] into the system decreased the activation energy from 8.4 KJ mol^{-1} (PEDOT:PolyDADMA FSI), 8.6 KJ mol^{-1} (PEDOT:PolyDADMA TFSI), 7.5 KJ mol−1 (PEDOT:PolyDADMA CF_3SO_3) to 2.3 KJ mol^{-1}, 3.4 KJ mol^{-1} and 3.6 KJ mol^{-1}, respectively (Table 3.5). Interestingly, the E_a of the Tos composite was increased from 4 KJ mol^{-1} (PEDOT:PolyDADMA Tos) to 8.7 KJ mol^{-1} (80/20 PEDOT:PolyDADMA Tos/C_2mpyrTos). This contrast could be due to the absence of plastic crystal behavior in C_2mpyrTos.

Table 3.5. Ionic conductivity values and E_a of PEDOT:PolyDADMA X and 80/20 wt% composites at 50 °C.

X	PEDOT:PolyDADMA X		80/20 wt% PEDOT:PolyDADMA X/C_2mpyr X	
	σ_{ionic}/S cm^{-1}	E_a/KJ mol^{-1}	σ_{ionic}/S cm^{-1}	E_a/KJ mol^{-1}
FSI	5×10^{-6}	8.4	2×10^{-5}	2.3 ± 0.2
TFSI	3×10^{-5}	8.6	4×10^{-6}	3.4 ± 0.2
Cl	2×10^{-8}	8.9	-	-
CF_3SO_3	7×10^{-7}	7.5	1×10^{-6}	3.6 ± 0.3
Tos	5×10^{-7}	4.0	2×10^{-8}	8.7 ± 0.4

3.5.3. Cyclic voltammetry

The electrochemical behavior was only analyzed for the FSI and TFSI systems since the other systems were unable to form a film, as discussed above. The typical rectangular shape of capacitive behavior was observed, as shown in Figure 3.12.

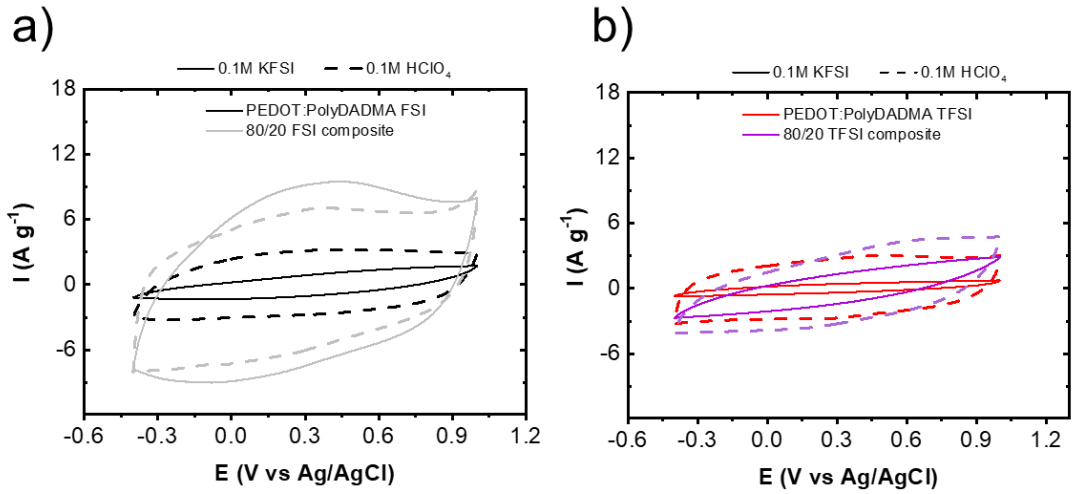

Figure 3.12. Voltammograms at 0.2 V s^{-1} of a) PEDOT:PolyDADMA FSI (black lines) and 80/20 PEDOT:PolyDADMA FSI / C2mpyrFSI composite (grey lines) using 0.1 M KFSI (solid lines) and 0.1 M $HClO_4$ (dashed lines) and b) PEDOT:PolyDADMA TFSI (red lines) and 80/20 PEDOT:PolyDADMA TFSI / C_2mpyrTFSI (purple lines) using 0.1 M KTFSI (solid lines) and 0.1 M $HClO_4$ (dashed lines).

Different aqueous media were used as electrolytes, including 0.1 M KFSI and 0.1 M KTFSI as neutral electrolytes with the same anion as the system to

avoid anion exchange and possible secondary reactions, and 0.1 M $HClO_4$ was used to observe the proton doping effect on PEDOT. The potential window was cycled from −0.4 V to 1 V vs. Ag/AgCl.

In general, the FSI system shows a much higher capacity than TFSI since the electronic conductivity is higher. Focusing on the FSI system, the voltammogram of PEDOT:PolyDADMA FSI in 0.1 M KFSI is quite resistive, unlike when 0.1 M $HClO_4$ was used as the electrolyte, because of the effect of proton doping on PEDOT as discussed above. The capacity was even higher when C_2mpyrFSI was added to obtain 80/20 PEDOT:PolyDADMA FSI / C_2mpyrFSI; indicating a further doping of PEDOT. When the 80/20 FSI composite was cycled using 0.1 M $HClO_4$ as the electrolyte, the capacity was diminished compared to the voltammogram obtained using 0.1 M KFSI as the electrolyte.

Although TFSI is much more resistive than FSI, similar behavior is observed in the voltammograms. PEDOT:PolyDADMA TFSI undergoes doping with protons when $HClO_4$ is used as the electrolyte. The 80/20 TFSI composite also shows an enhanced doping effect when 0.1 M KTFSI was used, compared with the neat PEDOT:PolyDADMA TFSI. However, in this case, the C_2mpyrTFSI is not as effective as C_2mpyrFSI. Finally, when 0.1 M $HClO_4$ was used as the electrolyte, higher current densities were obtained as effect of acid dopping. This doping effect of organic salts has been observed previously.[47]

3.6. Conclusions

Blends of PEDOT and PolyDADMA X were obtained as mixed ionic-electronic conductors, using composites of novel polyelectrolytes and OIPCs. A

series of PolyDADMA X polyelectrolytes were prepared, where X was either chloride (Cl), bis(fluorosulfonyl)imide (FSI), bis(trifluoromethylsulfonyl)imide (TFSI), triflate (CF_3SO_3) or tosylate (Tos). The maximum electronic conductivity was obtained for the PEDOT:PolyDADMA FSI coating (0.60 S cm^{-1}), with an ionic conductivity value of 5 × 10^{-6} S cm^{-1} at 70 °C. The PEDOT:PolyDADMA TFSI coating showed a lower electronic conductivity (0.25 S cm^{-1}) with an ionic conductivity of 4 × 10^{-6} S cm^{-1} at 70 °C. CF_3SO_3 has been postulated as a good anion with promising results, reaching the highest electronic conductivity value (0.3 S cm^{-1}) among the PEDOT:PolyDADMA X pellets, the highest ionic conductivity value among the different OIPCs (4 × 10^{-5} S cm^{-1} at 70 °C) and having a higher ionic conductivity value than the FSI and TFSI samples as a polyelectrolyte (PolyDADMA CF_3SO_3) (1 × 10^{-6} S cm^{-1} at 70 °C).

Finally, 80/20 PEDOT:PolyDADMA X / C_2mpyr[X] composites were prepared and their ionic conductivity and electrochemical capacity were measured. Interestingly, the most promising results were achieved by the authentic OIPCs; C_2mpyrFSI and C_2mpyrCF_3SO_3. The new OIPC C_2mpyrCF_3SO_3 exhibited an important electronic transport boost from the neat PEDOT:PolyDADMA CF_3SO_3 (0.30 S cm^{-1}) to the value of 0.73 S cm^{-1}. Nonetheless, both OIPCs enhanced the ionic conductivity of PEDOT:PolyDADMA X, with a bigger impact in the case of C_2mpyrFSI. A clear doping effect was evident for the FSI OIPC, in terms of the electrochemical performance.

The incorporation of different PolyDADMA X polymers in the PEDOT X blends shows the potential of using such ionic polymers to tune the material's properties concerning ionic and electronic conductivities as well as mechanical

properties. This research also highlights the benefits of incorporating OIPCs as dopants in conducting polymers and mixed ionic-electronic conductors and demonstrates the potential of the new compounds presented herein (PolyDADMA CF_3SO_3, PolyDADMA Tos, C_2mpyrCF_3SO_3 and C_2mpyrTos) for application in electrochemical storage systems.

3.7. Experimental part

3.7.1. Materials

Poly(diallyldimethylammonium chloride) (PolyDADMAC) (M_w = 400,000–500,000 g mol^{-1}) 20 wt% in water, p-toluenesulfonic acid monohydrate (Tosylic acid) (98.5%) and lithium(I) bis(trifluoromethanesulfonyl)imide (LiTFSI) (99.9%) were purchased from Sigma-Aldrich. Potassium bis(fluorosulfonyl)imide (KFSI) (98%) and N-ethyl-N-methylpyrrolidinium bromide (C_2mpyrBr) (99%) were supplied by abcr GmbH. Trifluoromethanesulfonic acid (TFMSA) (98%) was supplied by Alfa Aesar. 3,4-ethylenedioxythiophene (EDOT) (99%) and Amberlite™ IRN-78 ion-exchange resin, OH-form were purchased from Fisher Scientific. 1-ethyl-1-methylpyrrolidinium bis(trifluoromethylsulfonyl)imide, 99% was supplied by IoLiTec. Dialysis tubing of regenerated cellulose, pre-treated, 38 mm MWCO 1 kD and hydrochloric acid (HCl) (37%) were purchased from Scharlab.

3.7.2. Methods

All the compounds were characterized by thermogravimetric analysis (TGA), performed using a TGA Q-500 thermobalance, with a standard furnace

coupling and nitrogen flow of 50 cm^3 min^{-1}. The sample weight was between 1 and 15 mg. Then, the decomposition temperature, T_d, was obtained from the maximum of the first derivate of the thermogram.

The organic salts were characterized by differential scanning calorimetry (DSC). The experiments were performed using a Perkin Elmer 8000 DSC equipped with an Intracooler II and calibrated with indium and tin standards. The heating rate was 10 ˚C min^{-1} in the temperature range of -70 to 225 °C and between 3 and 10 mg of sample was used every time. The measurements were performed by sealing the samples in aluminum pans. The samples were first heated from room temperature to 225 °C to erase thermal history, then cooled and finally, second heating was performed.

Compressive mode dynamic mechanical analysis (DMA, PerkinElmer DMA8000) was used to analyze the thermal behavior of the polymers when nothing was observed by DSC. The polymer was pressed in KBr die and dried at 70 ˚C under vacuum overnight to finally obtain pellets of around 2 mm in thickness and 13 mm in diameter. The temperature range of DMA was from 40 ˚C to 200 ˚C and the frequency was set at 1 Hz. The measurements were performed in a N_2-filled glovebox with a H_2O level lower than 100 ppm.

The ionic conductivities were measured by electrochemical impedance spectroscopy (EIS) using an Autolab 302N potentiostat galvanostat (Metrohm AG, Herisau, Switzerland) with the temperature controlled by a Microcell HC station. PEDOT-based samples were measured making pellets of around 500 μm and 11 mm in diameter. Polyelectrolytes and organic salts were solvent cast on stainless steel electrodes. All the samples were dried at 70 °C under vacuum

overnight. Afterward, the samples were sandwiched between two stainless steel electrodes (with a surface area of 0.5 cm^2). The plots were obtained by applying a 10 mV perturbation to an open circuit potential in the frequency range of 1 MHz to 0.1 Hz. Electronic conductor samples were analyzed considering the resistance of the electronic conduction negligible versus ionic resistance as previously done by McDonald et al.[48] The activation energy (E_a) of the different materials was also studied in the linear region using the Arrhenius Equation (Eq. 3.1):

$$\sigma = \sigma_0 \, exp\left({}^{-E_a}/_{RT}\right) \qquad \text{(Eq. 3.1)}$$

where σ is the ionic conductivity, σ_0 is the pre-exponential factor, E_a is the activation energy, R the universal gas constant and finally T is the absolute temperature.

The electronic sheet resistance was measured using a Jandel 4-Point Probe with the RM3000+ test unit. The samples were pellets with a thickness between 250 and 500 μm and 13 mm in diameter. Coatings with a thickness of around 50 μm were measured when they were possible to form. Electronic conductivity was calculated by taking into account the thickness of the samples as follows Eq. 3.2

$$\sigma_{electronic} = R_S \cdot t \qquad \text{(Eq. 3.2)}$$

where $\sigma_{electronic}$ is the electronic conductivity, R_S is the sheet resistance and t the thickness of the sample.

To evaluate the electrochemical performance of the system, cyclic voltammetry (CV) was carried out with an Autolab PGSTAT204 potentiostat in a conventional three-electrode setup. A platinum wire was used as the counter electrode, Ag/AgCl as the reference electrode and glassy carbon as the working electrode. The samples were dissolved in the relevant solvent to finally drop cast a known quantity of material on top of the carbon electrode. The experiments were performed at 0.2 V s^{-1}.

3.7.3. Synthesis of PolyDADMA FSI and PolyDADMA TFSI

PolyDADMA FSI and PolyDADMA TFSI were synthesized by the anionic exchange reaction of PolyDADMAC in the presence of the fluorinated salt (LiFSI and KTFSI), to synthesize the required polymer as previously reported.[14] In both cases, after filtration of the precipitate, a white solid powder was obtained.

3.7.4. Synthesis of C_2mpyrCF_3SO_3, C_2mpyrTos, PolyDADMA CF_3SO_3 and PolyDADMA Tos

These organic salts and polymers were synthesized via a two-step anion exchange reaction, following a previously reported, similar procedure.[49] Briefly, an aqueous solution of C_2mpyrOH was prepared by passing an aqueous solution of C_2mpyrBr, which has a similar viscosity as water, through a column filled with anion exchange resin (SUPELCO AMBERLITE IRN-78) in the hydroxide form. After that, C_2mpyrOH was neutralized by the dropwise addition of the equimolar acid aqueous solution (TFMSA and Tosylic acid) to obtain the required compound, using an ice bath for cooling. The obtained solutions were stirred at ambient temperature and pressure for 12 h. Excess water was then removed by

rotatory evaporation under vacuum. The same procedure was used for PolyDADMA CF_3SO_3 and PolyDADMA Tos, using the acids TFMSA and tosylic acid. The chemical structures of the prepared OIPCs and polyelectrolytes were confirmed by ^1H and ^9F NMR analysis (see Figures 3.13-18).

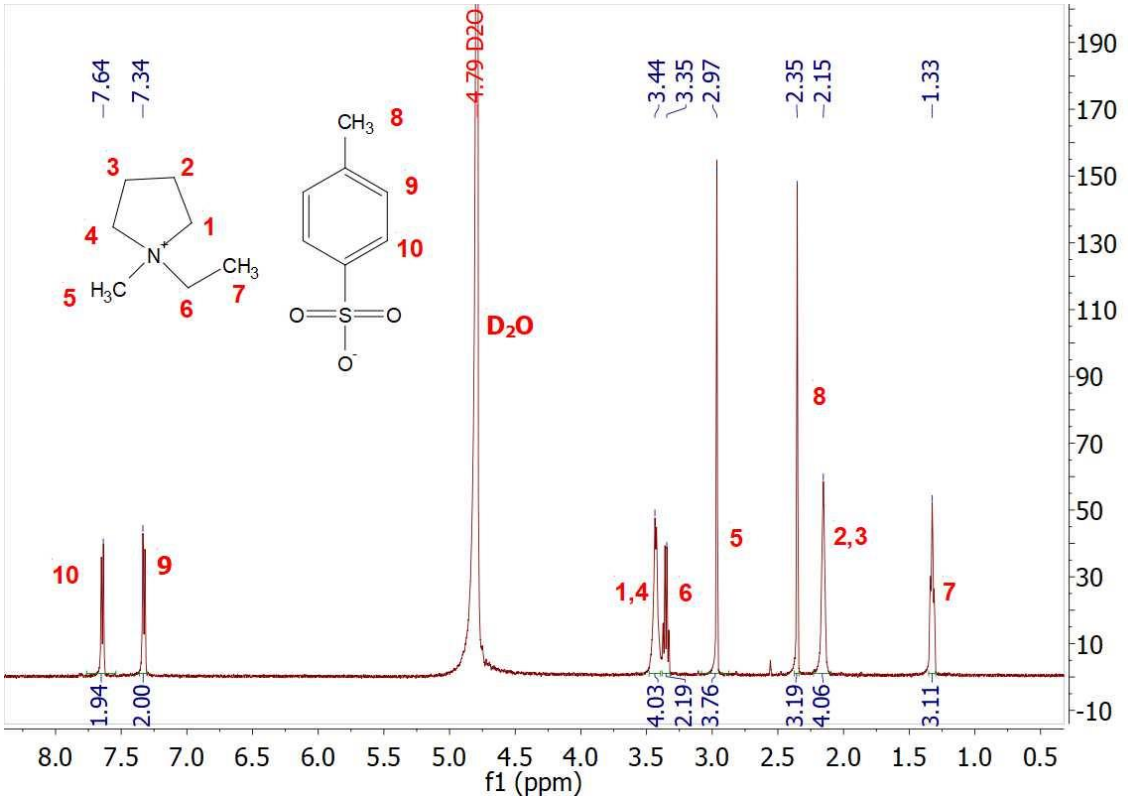

Figure 3.13. ^1H-NMR spectrum of C_2mpyrTos in D_2O.

For $CF_3SO_3^-$ compounds, an equimolar quantity of 4-(trifluoromethyl)benzaldehyde was added as standard to quantify 1H and 19F and thus, see if the ratio between the anion and the cation is one.

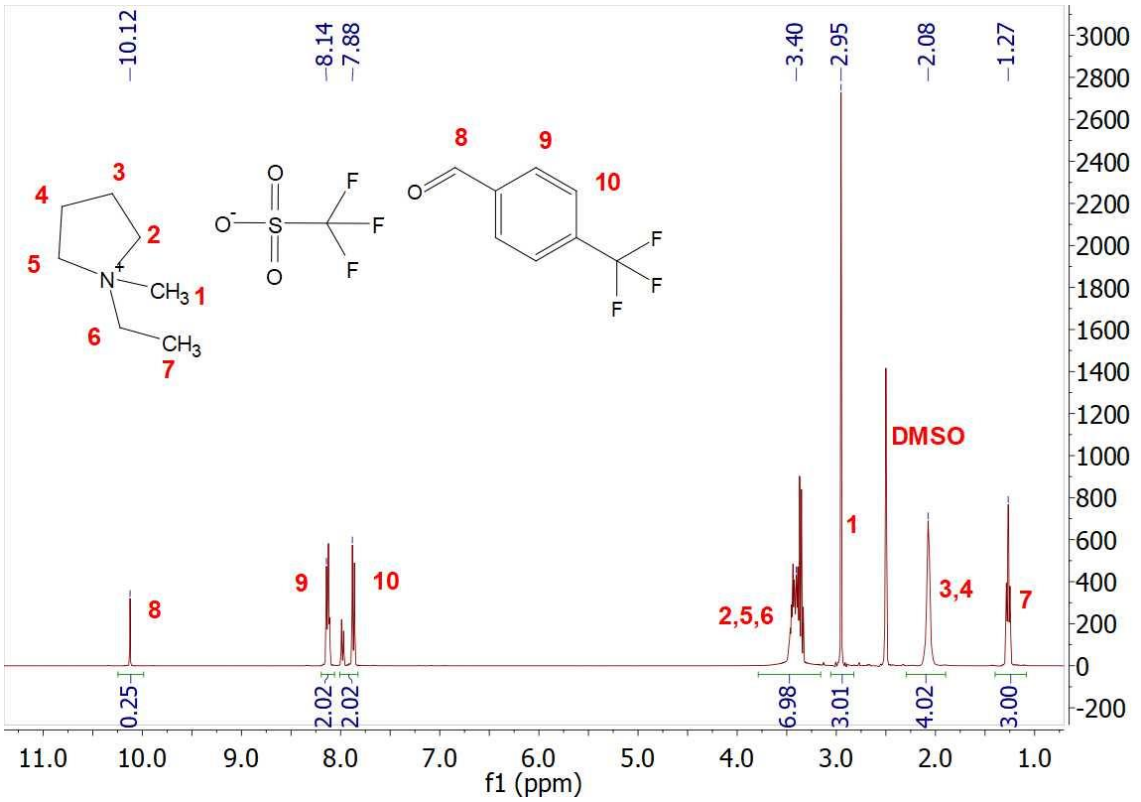

Figure 3.14. 1H-NMR of $C_2mpyrCF_3SO_3$ with 4-(Trifluoromethyl)benzaldehyde in DMSO.

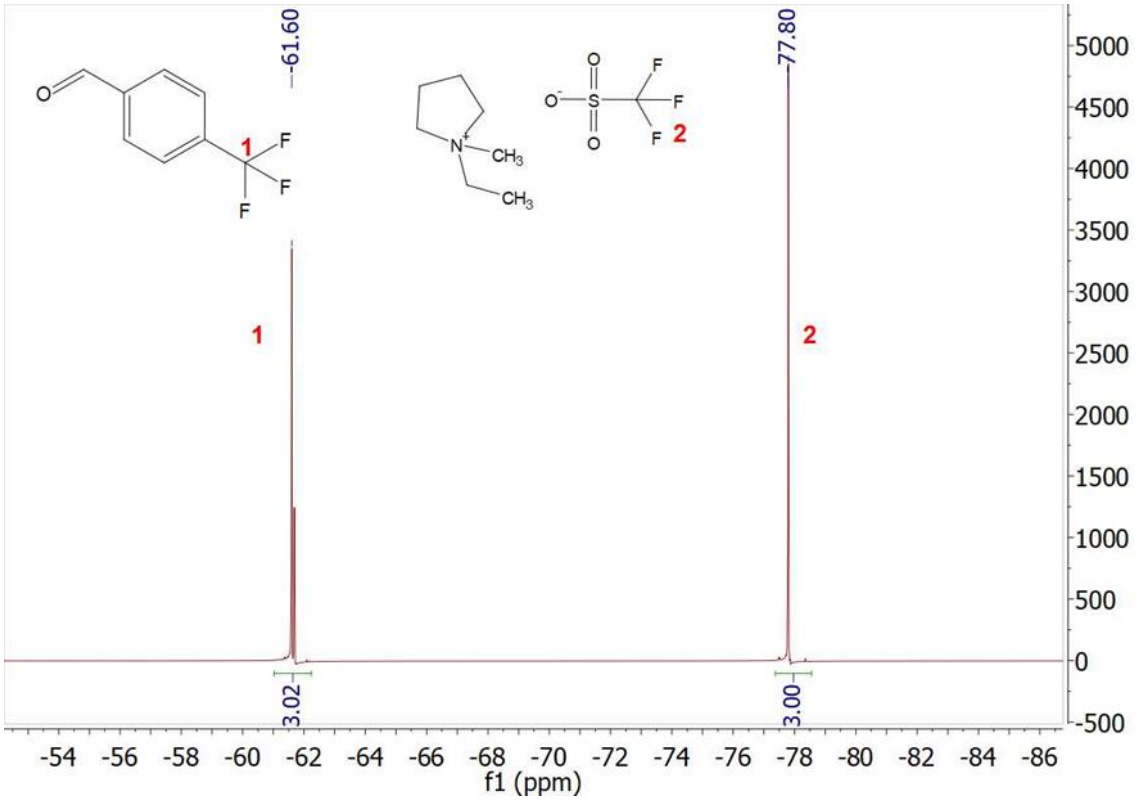

Figure 3.15. ^{19}F-NMR of $C_2mpyrCF_3SO_3$ with 4-(Trifluoromethyl)benzaldehyde in DMSO.

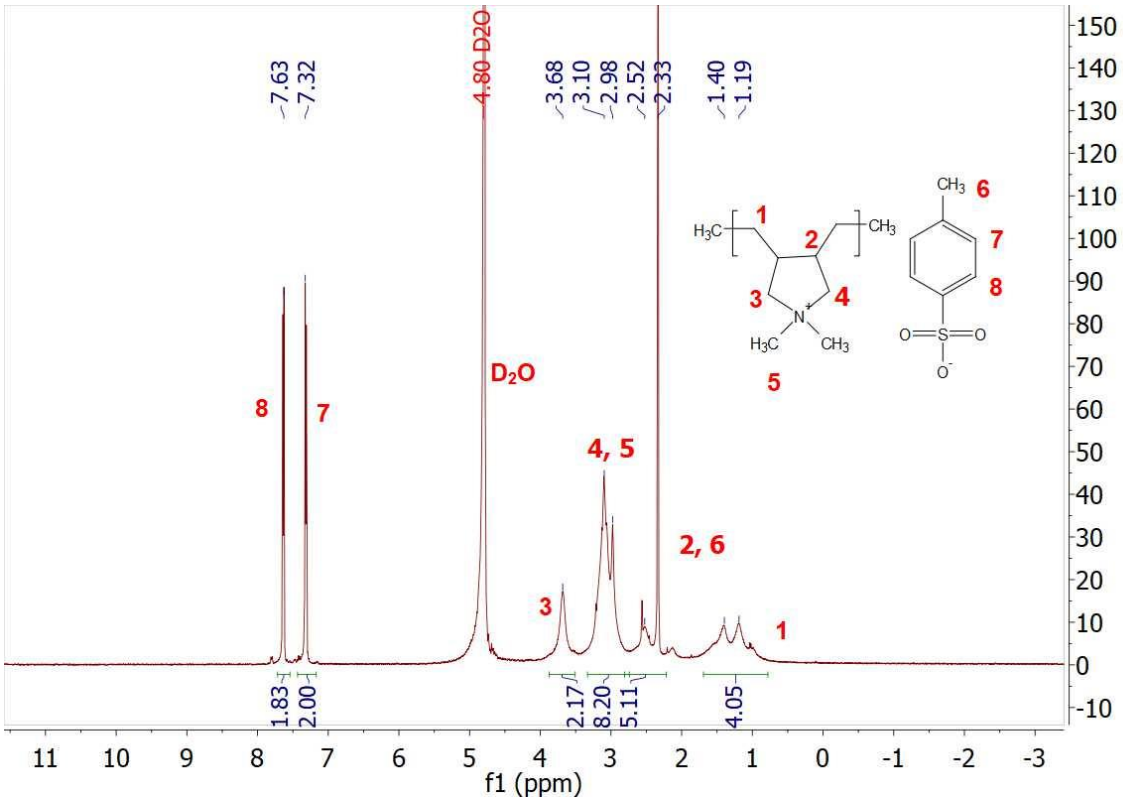

Figure 3.16. 1H- NMR of PolyDADMA Tos in D_2O.

For PolyDADMA CF_3SO_3, 4-(Trifluoromethyl)benzaldehyde was in excess of around 1.2 over the cation and the anion. Traces of water was observed as well.

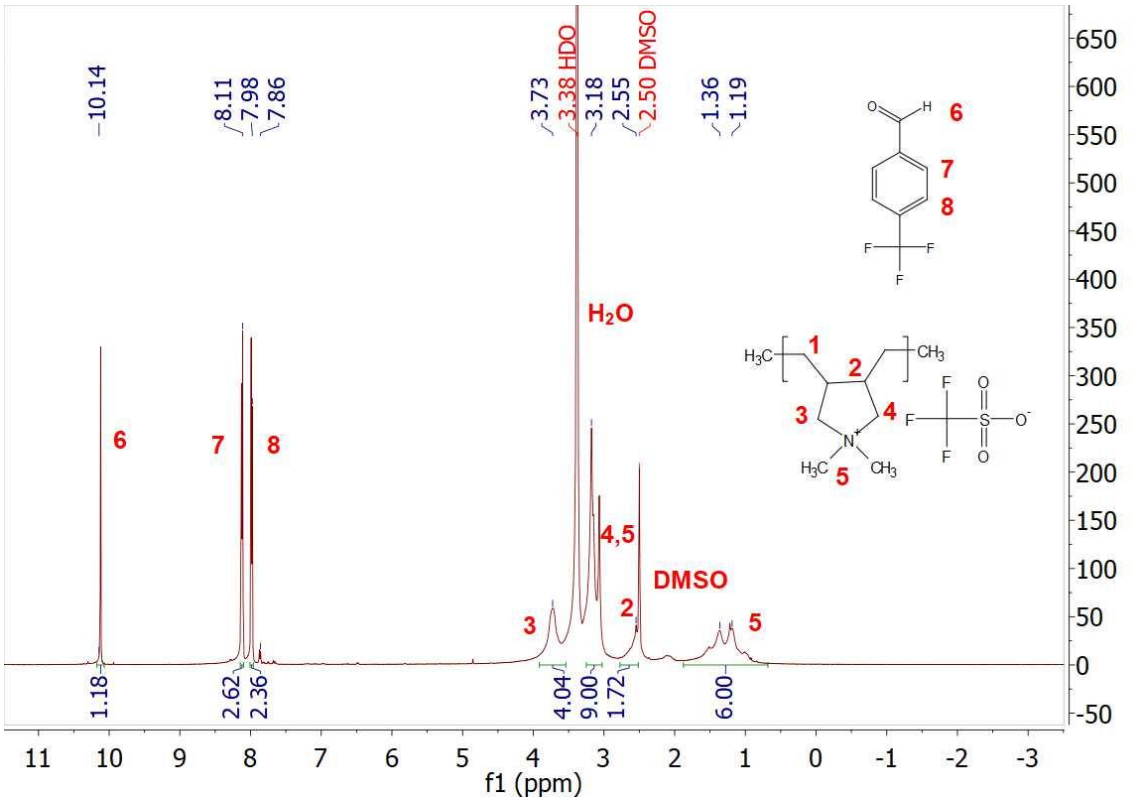

Figure 3.17. 1H-NMR of PolyDADMA CF_3SO_3 with 4-(Trifluoromethyl)benzaldehyde in DMSO.

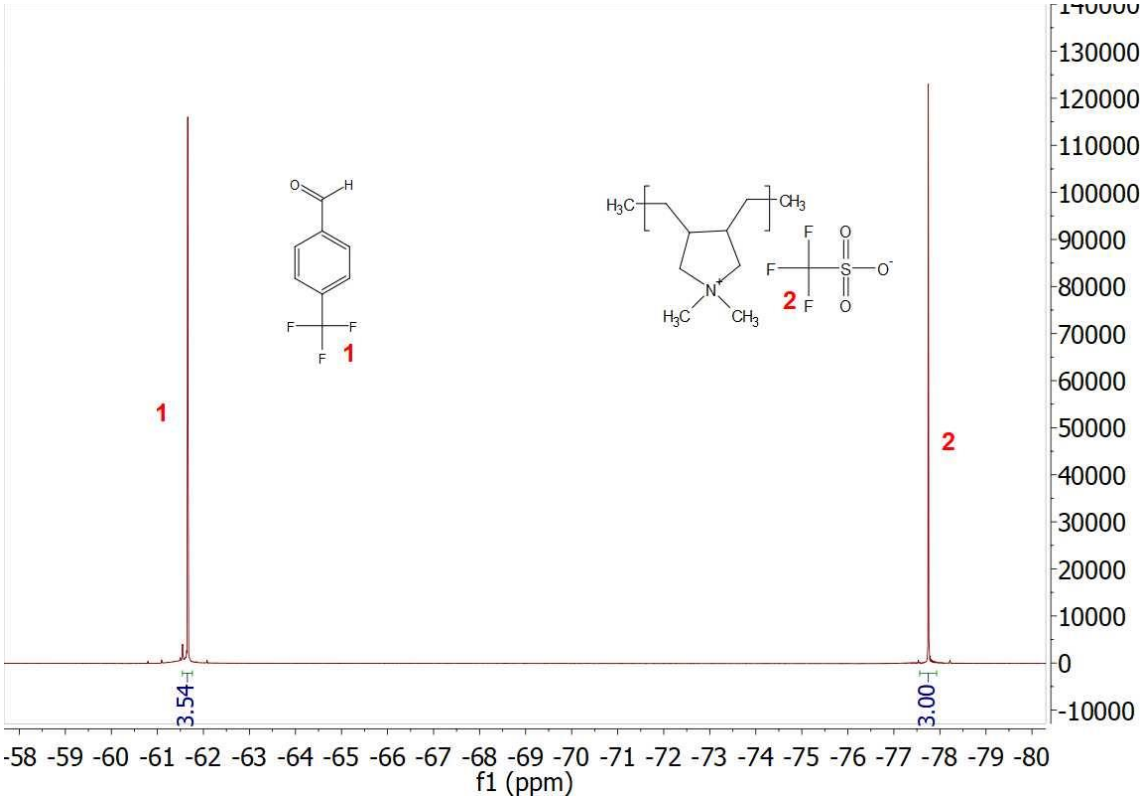

Figure 3.18. 19F-NMR of PolyDADMA CF_3SO_3 with 4-(Trifluoromethyl)benzaldehyde in DMSO.

3.7.5. Synthesis of PEDOT:PolyDADMA FSI PEDOT:PolyDADMA TFSI

The synthesis of PEDOT:PolyDADMA FSI and PEDOT:PolyDADMA TFSI were carried out following a previously reported procedure,[50] by oxidative polymerization in an acidic medium. It was previously reported that using an acidic medium can enhance the doping of PEDOT chains.[51] EDOT (0.3 mL, 2.81 mmol) and 20 wt% PolyDADMAC (1.92 mL, 2.48 mmol) were dispersed in 50 mL of 0.1 M HCl aqueous solution. In a second flask, ammonium persulfate (APS) (0.96 g, 4.22 mmol) was dissolved in 20 mL of 0.1 M HCl. After 20 min of bubbling in an N2 atmosphere to remove oxygen traces, the APS solution was added dropwise over 5 min in an inert atmosphere and the color of the solution changed from clear to white and then to light blue as the reaction was occurring. After 24 h of reaction using an ice bath, the typical dark blue color of PEDOT was observed in the solution.

Subsequently, the fluorinated salt (LiFSI or KTFSI) was added in excess in order to precipitate PolyDADMA as PolyDADMA FSI or PolyDADMA TFSI and dope the PEDOT. PEDOT:PolyDADMA FSI and PEDOT:PolyDADMA TFSI were obtained after filtration and washing with Milli-Q water. In both cases, the molar ratio of PEDOT:PolyDADMAX was 1.14:1.

3.7.6. Synthesis of PEDOT:PolyDADMA Cl, PEDOT:PolyDADMA CF_3SO_3 and PEDOT:PolyDADMA Tos

The synthesis of PEDOT:PolyDADMA Tos was performed by polymerization of the EDOT monomer (0.33 mL, 3.05 mmol) in 30 mL of 0.1 M

tosylic acid in the presence of the previously synthesized PolyDADMA Tos (0.8 g, 2.68 mmol). After adding APS (1.04 g, 4.58 mmol) as the oxidant and after 24 h of reaction under an inert atmosphere as previously explained, a dark blue dispersion was observed. The APS and excess acid were removed over 2 days of dialysis in regenerated cellulose membranes of 1000 Da. After 2 days of freeze-drying, the desired compound was obtained as a dark blue sponge-like solid. The same procedure was followed to obtain PEDOT:PolyDADMA Cl (using hydrochloric acid and the commercially available PolyDADMAC) and PEDOT:PolyDADMA CF_3SO_3 (using TFMSA as the acid, and using the previously synthesized PolyDADMA CF_3SO_3). In the case of the CF_3SO_3 system, it was necessary to first dissolve the PolyDADMA CF_3SO_3 in the minimum quantity of dimethyl sulfoxide (DMSO) prior to adding the acid and EDOT monomer. In all cases, the molar ratio of PEDOT:PolyDADMA X was 1.14:1.

3.8. References

1. S. Inal, J. Rivnay, P. Leleux, M. Ferro, M. Ramuz, J. C. Brendel, M. M. Schmidt, M. Thelakkat and G. G. Malliaras. A High Transconductance Accumulation Mode Electrochemical Transistor. *Adv. Mater.* **2014**;26:7450–7455.

2. D. Moia, A. Giovannitti, A. A. Szumska, I. P. Maria, E. Rezasoltani, M. Sachs, M. Schnurr, P. R. F. Barnes, I. McCulloch and J. Nelson. Design and evaluation of conjugated polymers with polar side chains as electrode materials for electrochemical energy storage in aqueous electrolytes. *Energy Environ. Sci.* **2019**;12:1349–1357.

3. A. Malti, J. Edberg, H. Granberg, Z. U. Khan, J. W. Andreasen, X. Liu, D. Zhao, H. Zhang, Y. Yao, J. W. Brill and I. Engquist. An Organic Mixed Ion – Electron Conductor for Power Electronics. *Adv. Sci.* **2016**;3:1–9.

4. N. Casado, S. Zendegi, R. Del Olmo, A. Dominguez-Alfaro and M. Forsyth. Tuning Electronic and Ionic Conductivities in Composite Materials for Electrochemical Devices. *ACS Appl. Polym. Mater.* **2021**;3:1777–1784.

5. C. Karlsson, J. Nicholas, D. Evans, M. Forsyth, M. Strømme, M. Sjödin, P. C. Howlett and C. Pozo-Gonzalo. Stable deep doping of vapor-phase polymerized poly(3,4-ethylenedioxythiophene)/ionic liquid supercapacitors. *ChemSusChem* **2016**;9:2112–2121.

6. T. Y. Kim, C. M. Park, J. E. Kim and K. S. Suh. Electronic, chemical and structural change induced by organic solvents in tosylate-doped poly(3,4-ethylenedioxythiophene) (PEDOT-OTs). *Synth. Met.* **2005**;149:169–174.

7. H. Kim, K. Jeong, C. J. Yu, H. S. Nam, H. Soh and J. Lee. The effects of the surface morphology of poly(3,4-ethylenedioxythiophene) electrodes on the growth of pentacene, and the electrical performance of the bottom contact pentacene transistor. *Solid. State. Electron.* **2012**;67:70–73.

8. P. R. Das and J. E. Soc. PEDOT:PSS as a Functional Binder for Cathodes in Lithium Ion Batteries. *J. Electrochem. Soc.* **2015**;162:A674–A678.

9. D. Nilsson, N. D. Robinson, J. Isaksson, P. K. J. All, M. Berggren and A.

Richter-dahlfors. Electronic control of Ca2 + signalling in neuronal cells using an organic electronic ion pump. *Nat. Mater.* **2007**;6:673–679.

10. B. J. ** Jang, J. Ha and J. Cho. Fabrication of Water-Dispersible Polyaniline-Poly(4- styrenesulfonate) Nanoparticles For Inkjet-Printed Chemical-Sensor Applications. *Adv. Mater.* **2007**;19:1772–1775.

11. T. J. Zajdel, M. Baruch, G. Méhes, E. Stavrinidou, M. Berggren, M. M. Maharb, D. T. Simon and C. M. Ajo-franklin. PEDOT:PSS-based Multilayer Bacterial-Composite Films for Bioelectronics. *Sci. Rep.* **2018**;8:15293.

12. Y. Zheng, H. Zeng, Q. Zhu and J. Xu. Recent advances in conducting poly(3,4-ethylenedioxythiophene):polystyrene sulfonate hybrids for thermoelectric applications. *J. Mater. Chem. C* **2018**;6:8858–8873.

13. J. Cameron and P. J. Skabara. The damaging effects of the acidity in PEDOT:PSS on semiconductor device performance and solutions based on non-acidic alternatives. *Mater. Horizons* **2020**;7:1759–1772.

14. A. Fdz. de Añastro, N. Casado, X. Wang, J. Rehmen, D. Evans, D. Mecerreyes, M. Forsyth and C. Pozo-gonzalo. Poly(ionic liquid) iongels for all-solid rechargeable zinc/PEDOT batteries. *Electrochim. Acta* **2018**;278:271–278.

15. A. Fdz De Anastro, N. Lago, C. Berlanga, M. Galcerán, M. Hilder, M. Forsyth and D. Mecerreyes. Poly(ionic liquid)iongel membranes for all

solid-state rechargeable sodium battery. *J. Memb. Sci.* **2019**;582:435–441.

16. G. Huang, L. Porcarelli, Y. Liang, M. Forsyth and H. Zhu. Influence of Counteranion on the Properties of Polymerized Ionic Liquids/Ionic Liquids Proton-Exchange Membranes. *ACS Appl. Energy Mater.* **2021**;4:10593–10602.

17. H. Ueda, F. Mizuno, R. Kerr, M. Forsyth and P. C. Howlett. Fast Charge and High Stability of Solid-state Graphite Organic Ionic Plastic Crystal Composite Anodes. *Batter. Supercaps* **2022**.

18. F. Makhlooghiazad, F. Nti, J. Sun, T. C. Mendes, S. S. Malunavar, J. M. Pringle and M. Forsyth. Composite electrolytes based on electrospun PVDF and ionic plastic crystal matrices for Na-metal battery applications. *JPhys Mater.* **2021**.

19. S. Malunavar, X. Wang, F. Makhlooghiazad, M. Armand, M. Galceran, P. C. Howlett and M. Forsyth. Highly conductive ionogel electrolytes based on N-ethyl-N-methylpyrrolidinium bis(fluorosulfonyl)imide FSI and NaFSI mixtures and their applications in sodium batteries. *JPhys Mater.* **2021**.

20. F. Nti, G. W. Greene, H. Zhu, P. C. Howlett, M. Forsyth and X. Wang. Anion effects on the properties of OIPC/PVDF composites. *Mater. Adv.* **2021**;2:1683–1694.

21. F. Nti, L. Porcarelli, G. W. Greene, H. Zhu, F. Makhlooghiazad, D.

Mecerreyes, P. C. Howlett, M. Forsyth and X. Wang. The influence of interfacial interactions on the conductivity and phase behaviour of organic ionic plastic crystal/polymer nanoparticle composite electrolytes. *J. Mater. Chem. A* **2020**;8:5350–5362.

22. R. Yunis, G. M. A. Girard, X. Wang, H. Zhu, A. J. Bhattacharyya, P. Howlett, D. R. Macfarlane and M. Forsyth. The anion effect in ternary electrolyte systems using poly (diallyldimethylammonium) and phosphonium-based ionic liquid with high lithium salt concentration. *Solid State Ionics* **2018**;327:83–92.

23. A. B. Pereiro, S. Martinho, F. Alves, S. Nunes, A. Matias, C. M. M. Duarte, L. P. N. Rebelo and I. M. Marrucho. Fluorinated Ionic Liquids: Properties and Applications. *ACS Sustain. Chem. Eng.* **2013**;1:427–439.

24. S. L. Agrawal and N. Rai. DMA and Conductivity Studies in PVA:NH4SCN:DMSO:MWNT Nanocomposite Polymer Dried Gel Electrolytes. *J. Nanomater.* **2015**.

25. N. Shimogama, M. Uda, K. Oyama, H. Hanochi and T. Hirai. Hydrophobic poly(3,4-ethylenedioxythiophene) particles synthesized by aqueous oxidative coupling polymerization and their use as near-infrared-responsive liquid marble stabilizer. *Polym. J.* **2019**;51:761–770.

26. F. Gonzalez, P. Tiemblo and M. Hoyos. In-Situ Approaches for the Preparation of Polythiophene-Derivative Cellulose Composites with High

Flexibility and Conductivity. *Appl. Sci.* **2019**;9:3371.

27. H. Turhan and N. Bicak. Selective Dinitramide Removal from Aqueous Solution by Crosslinked PolyDADMAC Gels. *Propellants Explos. Pyrotech.* **2020**;45:1–8.

28. S. Wang, M. Yan, Y. Li, C. Vinado and J. Yang. Separating electronic and ionic conductivity in mix-conducting layered lithium transition-metal oxides. *J. Power Sources* **2018**;393:75–82.

29. X. Wang, X. Zhang, L. Sun, D. Lee, S. Lee, M. Wang, J. Zhao, Y. Shao-horn, M. Dinc, T. Palacios and K. K. Gleason. High electrical conductivity and carrier mobility in oCVD PEDOT thin films by engineered crystallization and acid treatment. *Sci. Adv.* **2018**;4:5780.

30. I. Zozoulenko, A. Singh, S. K. Singh, V. Gueskine, X. Crispin and M. Berggren. Polarons, Bipolarons, And Absorption Spectroscopy of PEDOT. *ACS Appl. Polym. Mater.* **2018**;1:83–94.

31. H. Shuzhong, M. Masakazu, K. Kazuhiro, L. Lingyun and W. Qingshuo. Reversible Protonic Doping in Poly(3,4-Ethylenedioxythiophene). *Polymers (Basel).* **2018**;10:1065.

32. M. Y. Teo, N. Ravichandran, N. Kim, S. Kee, L. Stuart, K. C. Aw and J. Stringer. Direct Patterning of Highly Conductive PEDOT:PSS/Ionic Liquid Hydrogel via Microreactive Inkjet Printing. *ACS Appl. Mater. Interfaces*

2019;11:37069–37076.

33. M. Döbbelin, R. Marcilla, M. Salsamendi, C. Pozo-Gonzalo, P. M. Carrasco, J. A. Pomposo and D. Mecerreyes. Influence of ionic liquids on the electrical conductivity and morphology of PEDOT:PSS films. *Chem. Mater.* **2007**;19:2147–2149.

34. H. Yamada, Y. Miyachi, Y. Takeoka, M. Rikukawa and M. Yoshizawa-fujita. Pyrrolidinium-based organic ionic plastic crystals: Relationship between side chain length and properties. *Electrochim. Acta* **2019**;303:293–298.

35. N. V Ignat, P. Barthen, A. Kucheryna, H. Willner and P. Sartori. A Convenient Synthesis of Triflate Anion Ionic Liquids and Their Properties. *Molecules* **2012**;17:5319–5338.

36. A. Dhahri, A. El Ghali and M. H. V Baouab. Synthesis of a new 2,4,5-triphenyl-1H-imidazolium-paratoluenesulfonic acid salt: Thermal and electrochemical stability. *J. Tunis. Chem. Soc.* **2016**;19:139–143.

37. A. Basile, M. Hilder, F. Makhlooghiazad, C. Pozo-gonzalo, D. R. Macfarlane, P. C. Howlett and M. Forsyth. Ionic Liquids and Organic Ionic Plastic Crystals: Advanced Electrolytes for Safer High Performance Sodium Energy Storage Technologies. *Adv. Energy Mater.* **2018**;8:1703491.

38. Y. Zhou, X. Wang, H. Zhu, M. Armand, M. Forsyth and G. W. Greene. N -

ethyl- N -methylpyrrolidinium bis (fluorosulfonyl) imide- electrospun polyvinylidene fluoride composite electrolytes : characterization and lithium cell studies. **2016**.

39. Y. Shekibi, S. J. Pas, N. M. Rocher, B. R. Clare, A. J. Hill, D. R. MacFarlane and M. Forsyth. Surprising effect of nanoparticle inclusion on ion conductivity in a lithium doped organic ionic plastic crystal. *J. Mater. Chem.* **2009**;19:1635–1642.

40. Y. Zhou, X. Wang, H. Zhu, M. Armand, M. Forsyth, G. W. Greene, M. Pringle and P. C. Howlett. N-ethyl-N-methylpyrrolidinium bis(fluorosulfonul)imide-electrospun polyvinylidene fluoride composite electrolytes: characterization and lithium cell studies †. *Phys. Chem. Chem. Phys* **2017**.2225–2234.

41. M. Forsyth, T. Chimdi, A. Seeber, D. Gunzelmann and P. Howlett. Structure and dynamics in an organic ionic plastic crystal, N-ethyl-N-methyl pyrrolidinium bis(trifluoromethanesulfonyl) amide, mixed with a sodium salt. *J. Mater. Chem. A* **2014**;2:3993–4003.

42. J. Golding, S. Forsyth, D. R. Macfarlane, M. Forsyth and G. B. Deacon. Methanesulfonate and p-toluenesulfonate salts of the N-methyl-N-alkylpyrrolidinium and quaternary ammonium cations: novel low cost ionic liquids. *R. Soc. Chem.* **2002**;4:223–229.

43. X. Wang, H. Zhu, G. W. Greene, Y. Zhou, M. Yoshizawa-fujita, Y. Miyachi,

M. Armand, M. Forsyth, J. M. Pringle and P. C. Howlett. Organic Ionic Plastic Crystal-Based Composite Electrolyte with Surface Enhanced Ion Transport and Its Use in All- Solid-State Lithium Batteries. *Adv. Mater. Technol.* **2017**;2:1700046.

44. W. A. Henderson, D. M. Seo, Q. Zhou, P. D. Boyle, J. Shin, H. C. De Long, P. C. Trulove and S. Passerini. An Alternative Ionic Conductivity Mechanism for Plastic Crystalline Salt – Lithium Salt Electrolyte Mixtures. *Adv. Energy Mater.* **2012**;2:1343–1350.

45. D. R. Macfarlane, J. Huang and M. Forsyth. Lithium-doped plastic crystal electrolytes exhibiting fast ion conduction for secondary batteries. *Nature* **1999**;402:792–794.

46. L. Jin, P. Howlett, J. Efthimiadis, M. Kar and M. Forsyth. Lithium doped N,N-dimethyl pyrrolidinium tetrafluoroborate organic ionic plastic crystal electrolytes for solid state lithium batteries. *J. Mater. Chem.* **2011**;21:10171–10178.

47. F. D. Krampa, Y. Aniweh, G. A. Awandare and P. Kanyong. A Disposable Amperometric Sensor Based on High-Performance PEDOT:PSS/Ionic Liquid Nanocomposite Thin Film-Modified Screen-Printed Electrode for the Analysis of Catechol in Natural Water Samples. *Sensors* **2017**;17:1716.

48. M. B. Mcdonald and P. T. Hammond. Efficient Transport Networks in a Dual Electron/Lithium-Conducting Polymeric Composite for Electrochemical

Applications. *ACS Appl. Mater. Interfaces* **2018**;10:15681–15690.

49. A. S. L. Gouveia, L. C. Tome and I. M. Marrucho. Density, Viscosity, and Refractive Index of Ionic Liquid Mixtures Containing Cyano and Amino Acid-Based Anions. *J. Chem. Eng. Data* **2015**;61:83–93.

50. C. Pozo-Gonzalo, R. Marcilla, M. Salsamendi, D. Mecerreyes, J. A. Pomposo, J. Rodriguez and H. J. Bolink. PEDOT:Poly(1-vinyl-3-ethylimidazolium) Dispersions as Alternative Materials for Optoelectronic Devices. *J. Polym. Sci. A Polym. Chem* **2008**;46:3150.

51. H. Yano, K. Kudo, K. Marumo and H. Okuzaki. Fully soluble self-doped an electrical conductivity greater than 1000 S cm-1. *Sci. Adv.* **2019**;5:1–10.

Chapter 4. Unraveling the influence of Li^+-cation (PMTFSI-Li) and $TFSI^-$-anion (PDADMA-TFSI) in poly(ionic liquid) binders for lithium-ion batteries

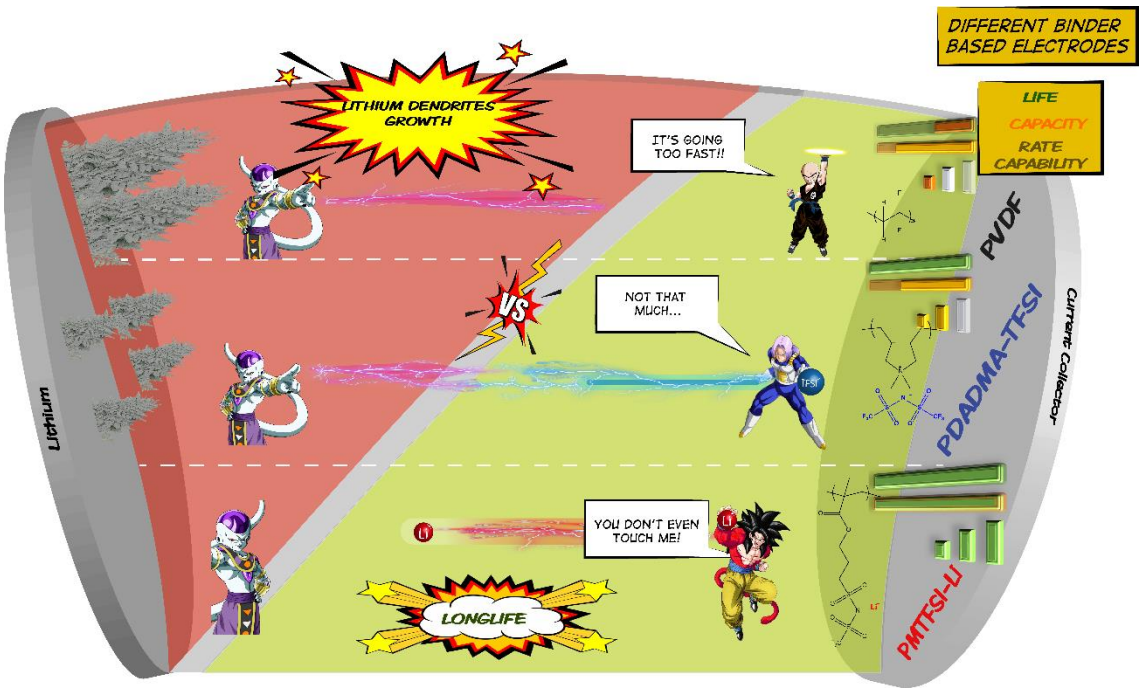

Chapter 4. Unraveling the influence of Li^+-cation (PMTFSI-Li) and $TFSI^-$-anion (PDADMA-TFSI) in poly(ionic liquid) binders for lithium-ion batteries

4.1. Introduction

Due to the exponential increase in world's energy demand during the last decades and the transition to a climate-neutral society, research on energy storage has focused on improving the performance of actual devices to increase the efficiency and range of power electronics and electric vehicles.[1,2] Among the electrochemical energy storage technologies, batteries, supercapacitors, and pseudo-capacitors stand out, in particular lithium-ion batteries (LIB) which offer high energy density and light-weight devices.[3,4] As introduced in Chapter 1 cathodes in LIBs are composed of a redox-active material, responsible for the charge storage in the electrodes, electronic conducting agents (i.e. carbon or electronic conducting polymers), and a polymer that acts as binder (commonly poly(vinylidene fluoride), PVDF).[5] Today, one of the main challenges facing this type of battery is to obtain the maximum real specific capacity and capacity retention during long-term cycling tests where parameters such as active material particle size, electronic conductivity, porosity, electrolyte, and ionic conductivity play an important role in the electrochemical performance of composite electrodes.

It has been demonstrated that the interaction of the carbon coating and the binder has a considerable impact on the mechanism of charge transfer, which could be a determining factor in the performance of lithium batteries, mainly at high charge/discharge rates.[6,7] In this regard, the choice of the binder can be crucial to determine the performance of composite electrodes and in general

lithium-based batteries.[6,8] Trends in the development of polymeric materials as binder include water-processable polymers and biopolymers,[1,9,10] as well as the use of ionic polymers, such as single-ion conducting polymers (SICP) and poly(ionic liquid)s (PIL)s. As an example, Xu et al. found that the use of CMC-Li polyelectrolyte as binder for NMC/C-based cathodes diminished the overpotential in comparison with standard PVDF, which was critical for long-term cyclability.[11] In addition to that, some works have reported the benefits of using functionalized binders that have electronic conductive properties, providing a more intimate electronic contact between redox-active compounds and the current collector.[12,13] On the other hand, the use of single-ion conduction polymers as binders has been suggested to overcome ion transport limitations and therefore, improve cell performances.[11,14–17] Some PILs based on mobile $TFSI^-$ have also been employed as binders, looking for facilitating Li^+ conduction pathways, observing a more stable cycling and higher specific capacities in LFP/C cathodes.[17] However, the role of the type of mobile ion (cationic or anionic) in polymeric binders and their behavior in contact with conventional liquid electrolytes has not been investigated in detail so far.

In this chapter, LFP/C based cathodes were prepared using two different type of poly(ionic liquid) polymers: poly(diallyldimethylammonium bis(trifluoromethanesulfonyl)imide (PDADMA-TFSI) and poly(lithium 1-[3-(methacryloyloxy) propylsulfonyl]-1-(trifluoromethanesulfonyl) (PMTFSI-Li) as binders (see Figure 4.1) and labeled as C-PMTFSI-Li and C-PDADMA-TFSI, respectively. These polymers were chosen as ionic conducting binders for LFP/C cathodes to provide suitable conditions to elucidate the role of $TFSI^-$ and Li^+ ions transport within the composite electrode on the overall electrochemical

performance of the cells. The electrodes were cycled using 1M LiTFSI in DOL: DME (1:1 v/v) as electrolyte and compared with conventional LFP/C/PVDF electrodes in terms of cyclic voltammetry, cyclability, cycle life, and electrochemical impedance spectroscopy (EIS).

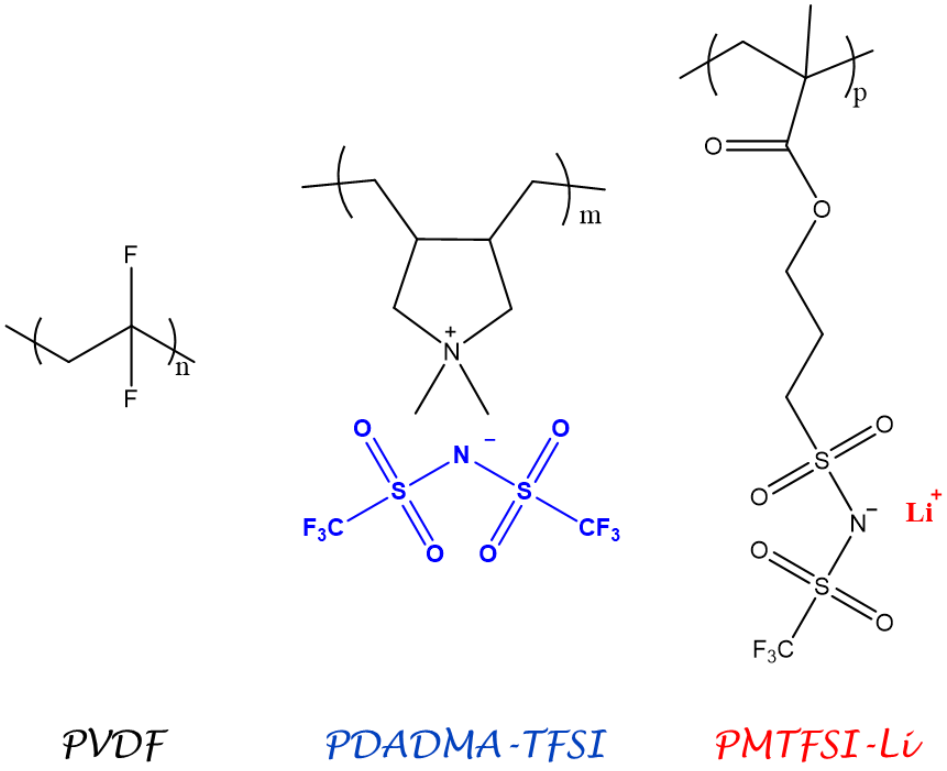

Figure 4.1. Chemical structure of the studied binders: a) Polyvinylidene fluoride (PVDF, Solef® 5130), poly(diallyldimethylammonium bis(trifluoromethanesulfonyl)imide (PDADMA-TFSI), and poly(lithium 1-[3-(methacryloyloxy) propylsulfonyl]-1-(trifluoromethanesulfonyl) (PMTFSI-Li).

4.2. Application in Lithium-ion batteries

LFP electrodes were obtained using a slurry composed of 80 wt.% active material (LFP), 10 wt.% conducting carbon and 10 wt.% binder. Moreover, 1M LiTFSI DOL:DME (1:1 v/v ratio) was chosen as electrolyte to maintain an ionic homogeneity in the system.

4.3. Electrolyte uptake

PDADMA-TFSI and PMTFSI-Li were used as binders in $LiFePO_4$/C-based cathodes to assess the importance of ion transport (TFSI- in PDADMA-TFSI and Li^+ in PMTFSI-Li) within the cathode structure. The electrochemical performances were compared to a cell containing the commonly used non-conductive PVDF binder. In traditional lithium-ion batteries with non-conductive binders, liquid electrolyte penetrates into the pores of the cathode providing ionic conduction through the electrode. To evaluate possible wettability variations in the electrodes, generated by changes in the intrinsic properties of the binders and their compatibility with the rest of the electrode components, electrolyte absorption tests were carried out (Figure 4.2). For this purpose, pristine electrodes (LFP/C65/binder 80/10/10 wt. %) were soaked separately in fresh electrolyte (0.5 mL) for short (5 seconds) and long (48 h) immersion times in closed vials independently and subsequently weighted. Noteworthy, 48 h was considered to ensure a thermodynamic equilibrium of the system in terms of electrolyte saturation and chemical equilibrium of the ionic species.

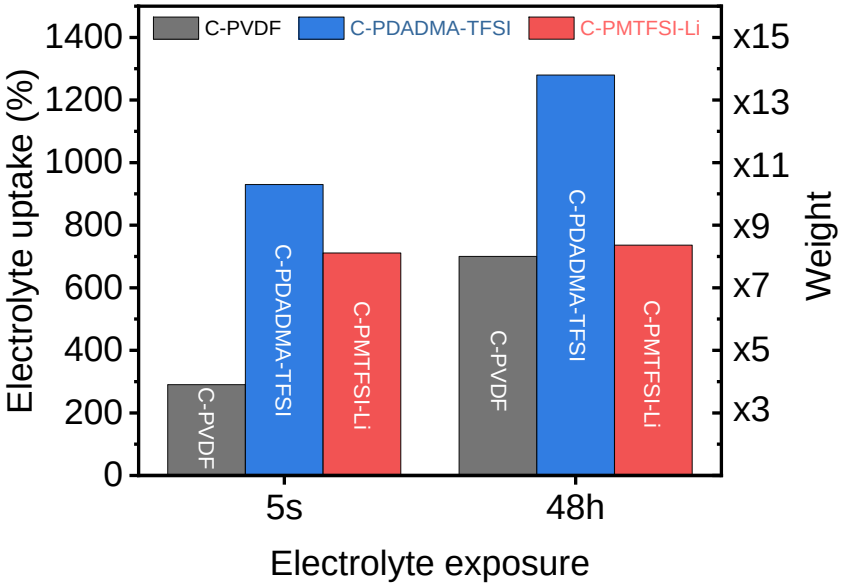

Figure 4.2. Electrolyte uptake of LFP/C65/binder 80/10/10 wt. % electrodes using PVDF, PDADMA-TFSI and PMTFSI-Li binders after 5s and 48 h of immersion time in 1M LiTFSI in DOL: DME (1:1 v/v) fresh electrolyte.

The results of immersing the electrodes in the electrolyte for short periods revealed that ionic binders have a higher electrolyte uptake (C-PDADMA-TFSI: 930 %, C-PMTFSI-Li: 711 %) than C-PVDF (290 %). These values are associated with the low polarity and poor wettability of C-PVDF, which limit the diffusion of the electrolyte along the electrode, in comparison with ionic binders. This behavior has been already reported by several authors, indicating a dependence between the amount of electrolyte absorbed by the electrode and the electrolyte-binder affinity, where polar binders improve wettability and overall ionic mobility across the electrode.[18,19]

Once the thermodynamic equilibrium was reached, the results after 48 h revealed that C-PDADMA-TFSI (1280 %), C-PMTFSI-Li (736 %) and C-PVDF (700 %), electrodes had adsorbed respectively 40, 74, and 97 % of their total electrolyte adsorption capacity in the first 5 s of wetting. Interestingly, C-PMTFSI-

Li led to much faster absorption of electrolyte. Despite C-PVDF and C-PMTFSI-Li showed a similar electrolyte uptake capacity after 48 h, C-PDADMA-TFSI demonstrated a capacity to hold significantly higher amounts of liquid electrolyte (580 % more compared to PVDF), which will have an impact on the battery performance as discussed in the following sections by facilitating ion transport through the electrode.

4.4. Electrochemical response

To assess the effect of electrolyte uptake and free ions (either TFSI- or Li+) on the redox reaction kinetics of the cathode, Li||LFP cells with the three different binders were studied by cyclic voltammetry. In the first cycle, broad peaks related to $LiFePO_4/FePO_4$ redox reaction are observed in the range of 2.8-3.8 V (see Figure 4.3a). Nonetheless, the oxidation-reduction peak positions vary among different binders and it can be seen that PMTFSI-Li binder offers the best environment for the redox reaction to occur showing the sharpest and highest peaks, particularly in the anodic side.

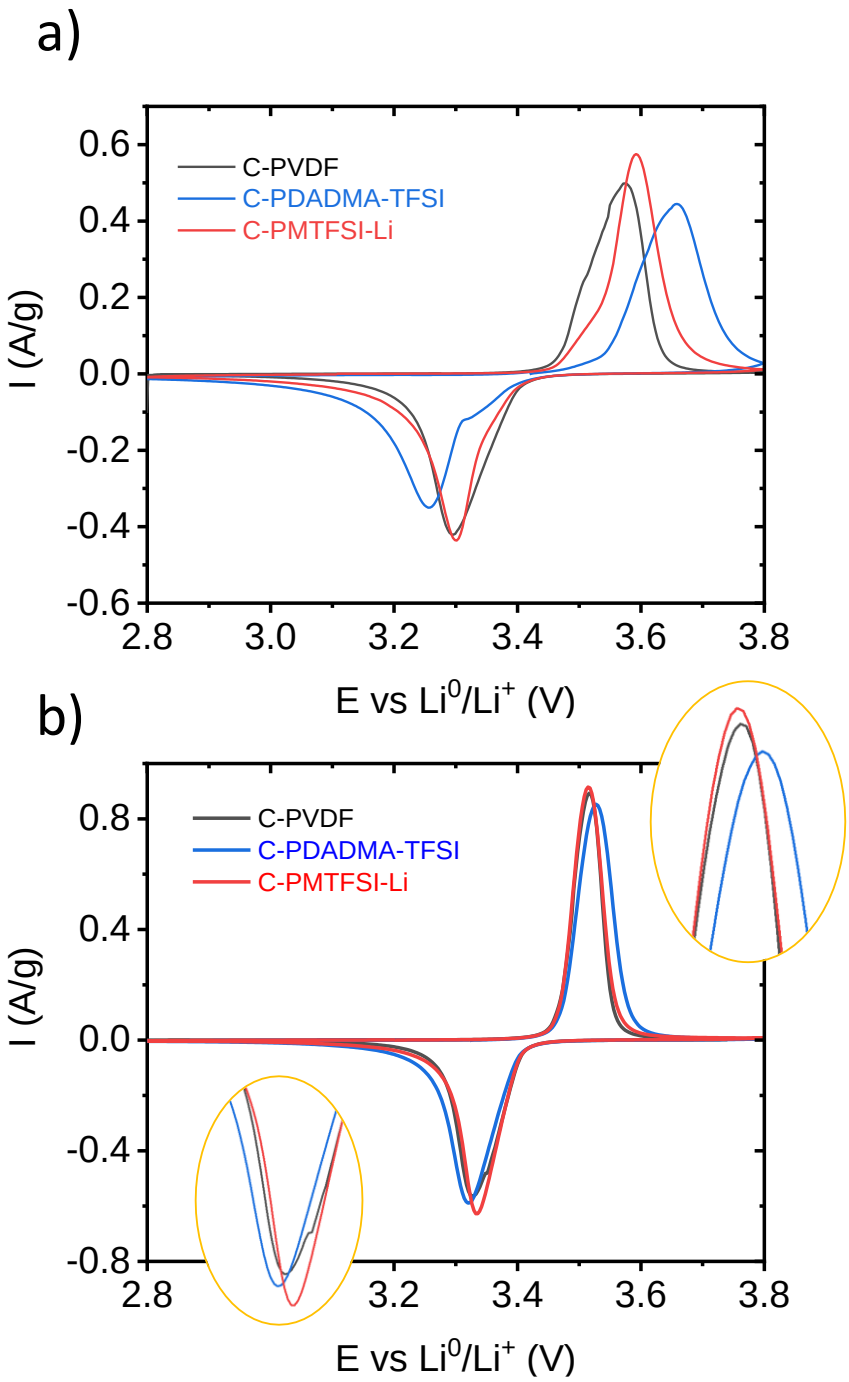

Figure 4.3. Cyclic voltammograms of Li||LFP cells of cycle number a) 1 and b) 6; with different cathode binders at 0.1 mV s^{-1}.

It has been reported that cell stabilization occurs during the first five cycles of potentiostatic cycling.[20] For this reason, voltammograms collected from the sixth cycle were compared and shown in Figure 4.3b. As a result, the observed difference between reduction and oxidation peak potentials, called peak-to-peak

separation, were 179, 189, and 209 mV for C-PMTFSI-Li, C-PVDF, and C-PDADMA-TFSI, respectively. Similar behavior was observed for other Li+ conducting polymer electrolytes.[15,21] These results evidence the kinetic limitation for C-PDADMA-TFSI hindering the reaction by the ionic interactions of free $TFSI^-$ ions with available Li^+ cations, while the redox reaction is more favored and reversible with for C-PMTFSI-Li since it represents a Li^+ source for the active material; the PVDF binder is in the middle of both scenarios. Furthermore, higher oxidation current densities were reached with C-PMTFSI-Li (0.91 A g^{-1}) in comparison with C-PVDF and C-PDADMA-TFSI (0.89 and 0.85 A g^{-1}). A smoother covering of LFP particles was observed when using PMTFSI-Li binder than PVDF or PDADMA-TFSI (see Figure 4.4), where sharp white LFP particles remain immersed into the polymer matrix, which may improve the contact and hence, current signal.

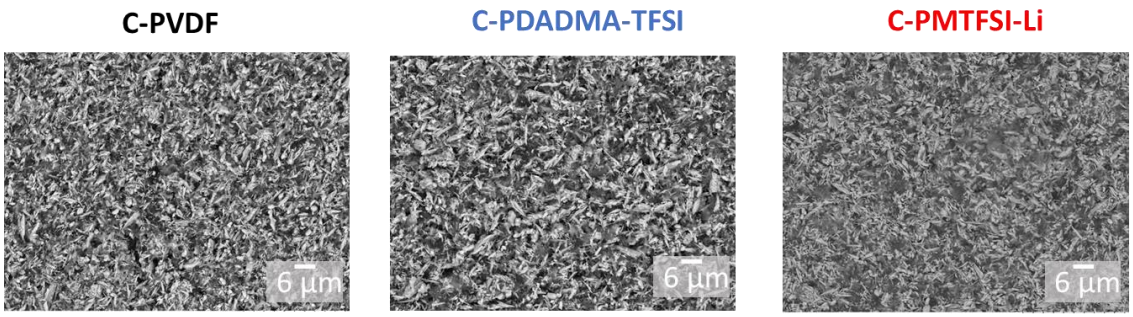

Figure 4.4. SEM images of pristine LFP-based cathodes (LFP/C65/binder, 80/10/10 wt. %) using different binders as labelled.

4.5. Galvanostatic cycling

After 10h of OCV to guarantee the equilibrium of the cells, fresh cells were cycled at current densities and subsequently at 1C for 500 cycles (Figure 4.5a). C-PMTFSI-Li electrodes provided higher capacity values than C-PDADMA-TFSI and C-PVDF, in all the studied C-rates, reaching the theoretical capacity density

(170.3 ± 0.8 mAh g^{-1}) at C/10 and outstanding values at 10C (100.6 ± 0.5 mAh g^{-1}). In accordance with the electrochemical response study, C-PVDF remained in second place providing a capacity density of 156.1 ± 1.5 mAh g^{-1} at low rate (C/10), followed by PDADMA-TFSI (146.7 ± 1.2 mAh g^{-1} at C/10). Nonetheless, at high C-rates (10 C) C-PDADMA-TFSI reached values of 87.7 ± 0.2 mAh g^{-1} slightly surpassing C-PVDF (87.2 ± 0.3 mAh g^{-1}). This phenomenon, even if close values of capacities are implied, becomes significant when observing the voltage profiles. When the cells were cycled at C/10 (see Figure 4.5b) low and almost indistinguishable overpotentials were observed. At this rate, the charge/discharge process is governed by reaction kinetics offered by the different ionic environments, proceeding following cyclic voltammetry study: C-PMTFSI-Li > C-PVDF > C-PDADMA-TFSI. However, when the C-rate was increased, large overpotentials were observed due to mass transfer limitations (Figure 4.5c), specially for C-PVDF. C-PMTFSI-Li exhibited a smaller polarization, due to its structural characteristics that promote Li^+ transport, as described for other polymeric systems with single lithium-ion conducting properties.[15,16,21] C-PDADMA-TFSI can also slightly mitigate this effect by facilitating the Li^+ mobility since more electrolyte uptake was observed for this electrode, but also by interaction with free $TFSI^-$ ions of the binder. Similar works have already demonstrated the benefits of free anions in terms of polarization.[17,22] Finally, C-PVDF shows the worst scenario.

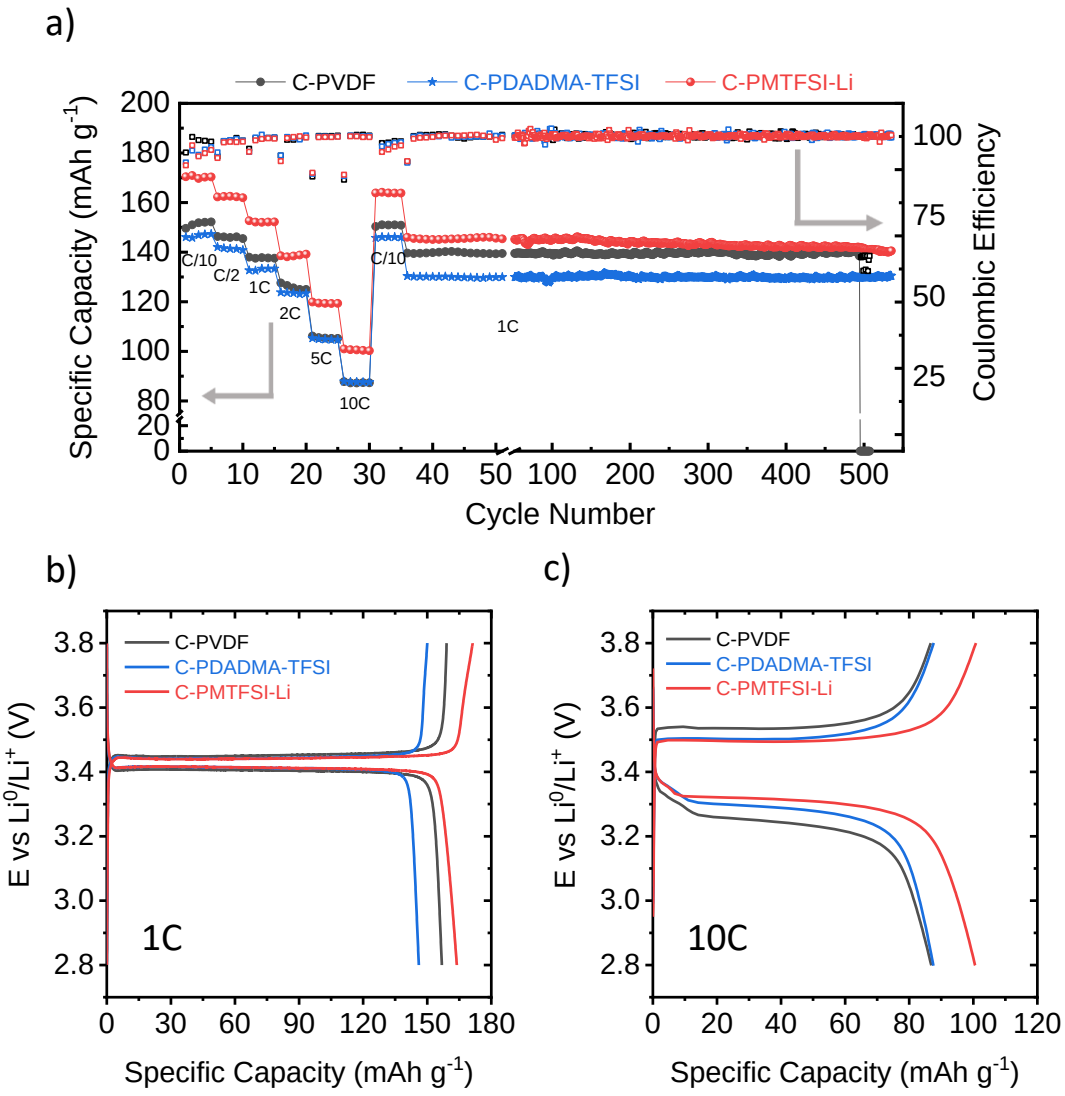

Figure 4.5. a) Rate capability and long-term cycling of Li||LFP cells using different binders: C-PVDF, C-PDADMA-TFSI, C-PMTFSI-Li as shown in figure legend. Voltage profiles of the cells at b) 0.1C and c) 10C rates at room temperature.

In the long-term cycling, after 535 cycles C-PMTFSI-Li and C-PDADMA-TFSI showed stable cycling and high capacity retention (140.5 mAh g^{-1}, 96%, and 130.5 mAh g^{-1}, 99% respectively), while C-PVDF delivered 138.5 mAh g^{-1}, 99% in cycle number 494 before fading. Subsequently, cells were opened to evaluate electrode deterioration after rinsing the cycled electrodes with DOL/DME (1/1) to remove the adsorbed salt excess. Figure 4.6, shows cross-sectional SEM images of the cathodes before and after cycling, where C-PVDF based cathode showed

a more damaged structure than the ones based on C-PDADMA-TFSI and C-PMTFSI-Li.

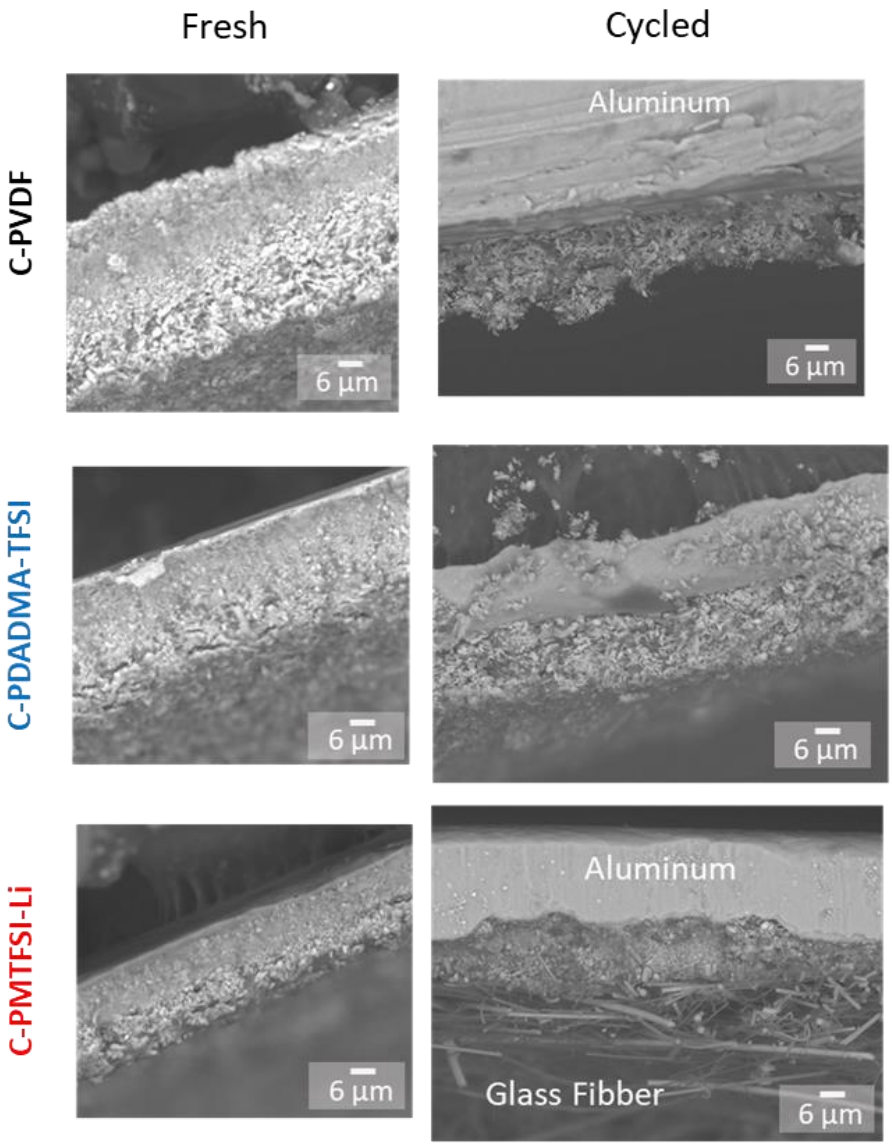

Figure 4.6. Cross-sectional SEM images of fresh electrodes and after 500 cycles of LFP-based cathodes using different binders as labelled.

In order to gain insight into the potential application of these polymer binders, electrodes with higher loadings (4 mg_{LFP} cm^{-2}) were prepared and analyzed. After cycling under the same conditions of rate capability (Figure 4.7), C-PMTFSI-Li and C-PDADMA-TFSI electrodes were able to cycle stably at high current density of 10C, while C-PVDF started to fail at that current density. A

similar trend was observed for the low loading electrodes in the long cycling at 1C current density (Figure 4.3a), highlighting the superior performance of C-PMTFSI-Li based electrode. Further characterization was carried out using the lower-loading electrodes to avoid the influence of resistances and diffusion limitations present in the 4 mg cm^{-2} electrodes.

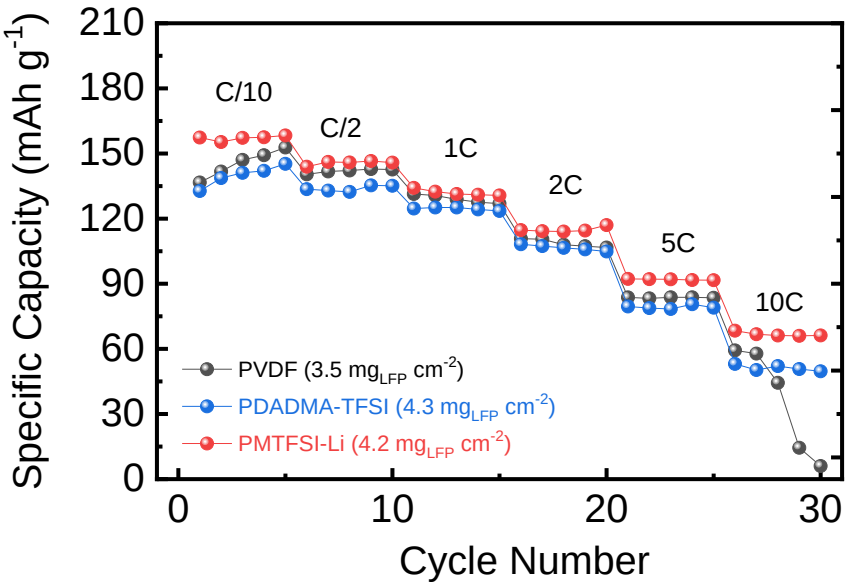

Figure 4.7. Rate capability of Li||LFP cells with different binders: PVDF, PDADMA-TFSI, PMTFSI-Li as shown in figure legend (~ 4 mg_{LFP} cm^{-2}).

4.6. Electrochemical Impedance Spectroscopy and post mortem analysis

In order to get a deeper understanding of the systems, EIS was performed to elucidate different resistances and capacitive contributions involved in the electrode composite. However, as explained by Suarez-Hernandez et al., the EIS spectrum of a battery is influenced by several factors (potential, additives, state of charge (SOC), etc.).[16] For this reason, EIS spectra were collected at the same voltage and SOC=50% to see the effect of the different binders under the same conditions. Firstly, fresh cells were assembled and exposed to 18h of OCV,

observing different voltage evolutions. Secondly, the cells were galvanostatically cycled by applying a low current density, corresponding to a C-rate of C/10 and 5 min of OCV before EIS measurement to ensure steady-state conditions at SOC=50% when charging and discharging in the third cycle.

The effect of the voltage on EIS spectrum has been studied addressing the changes in the concentration of the ionic species.[23] In this chapter, even if all the cells started at the same potential (3.4 V), different OCV profiles were obtained for each binder and hence, a comparison between cells in a specific time would be influenced by its potential (see Figure 4.8a). In this step, EIS spectra were taken every two hours to observe the evolution of the Nyquist plot to larger semicircles and more capacitive shape at low frequencies given by the accumulation of charged species inside the electrode as can be observed from Figure 4.8b. From these results it can be concluded a faster stabilization occurred in the cells based on ionic binder, obtaining capacitive EIS spectra at low frequencies and reaching the voltage plateau at shorter times, specially for C-PMTFSI-Li being almost instantaneous, in good agreement with the wettability test.

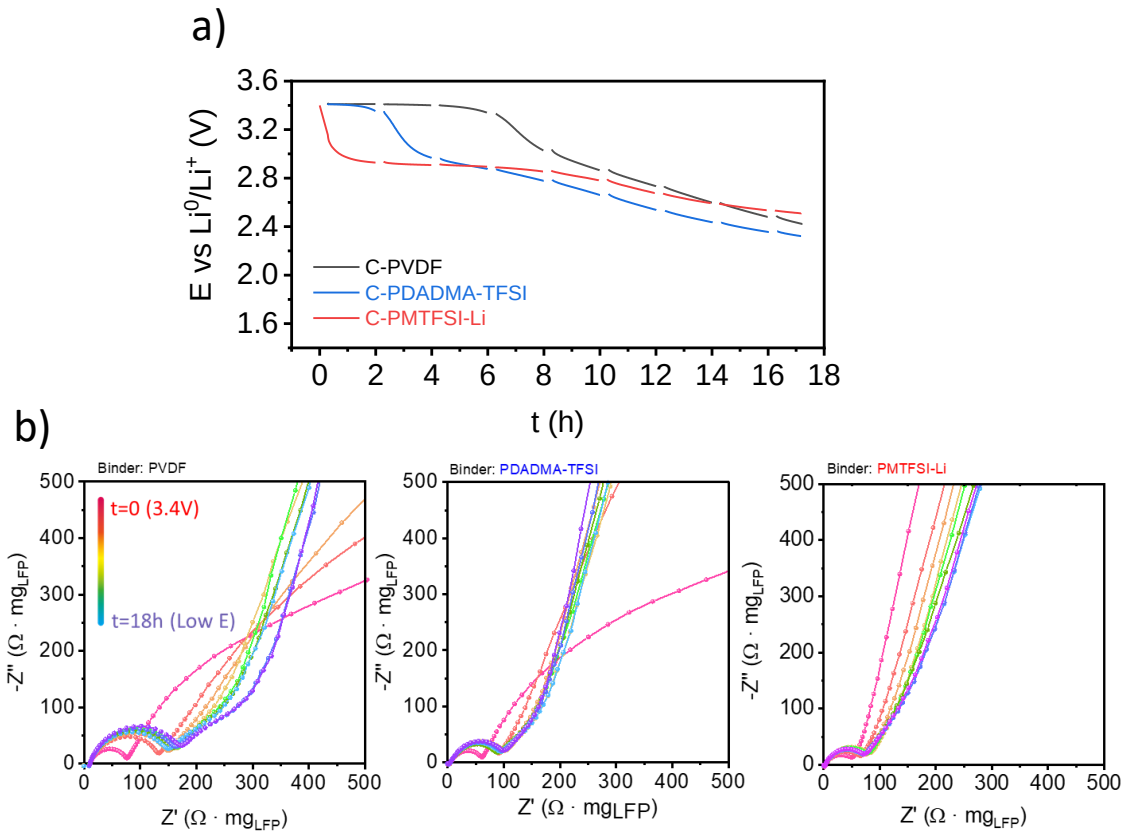

Figure 4.8. a) OCV profiles and b) Nyquist plot evolution along the time of fresh cells using different binders as the legend indicates.

Subsequently, (EIS at SOC=50% of charge and discharge) is depicted in Figure 4.9. The used equivalent circuit (*ecc)* (Figure 4.9a) was proposed by similar previous works to fit the data because of its confirmed accuracy in LFP-based cells and quality of extracted information. In these Nyquist plots, firstly the solution electrolyte resistance remained relatively constant in all the cases R_s≈4 Ω. Subsequently, at high frequencies, can be found a depressed semicircle that corresponds mostly to the interfacial charge transfer resistance (R_{ct}), in parallel with the double-layer capacitance (C_{dl}), together with a small contribution of the contact between particles resistance (R_c) and respective capacitance (C_c). At intermediate frequencies we observe the resistance related to the lithiation process of the active material (R_{lr}) and its associated lithiation capacitance (C_{Li^+}),

which is related to the amount of Li^+ out of the active material particle (in this case LFP). Finally, at very low frequencies a capacitive shape appears as a consequence of Li^+ intercalation in the phosphate matrix quantified by its chemical capacitance (C_μ). This parameter counts the ease for Li^+ to reach the active material.

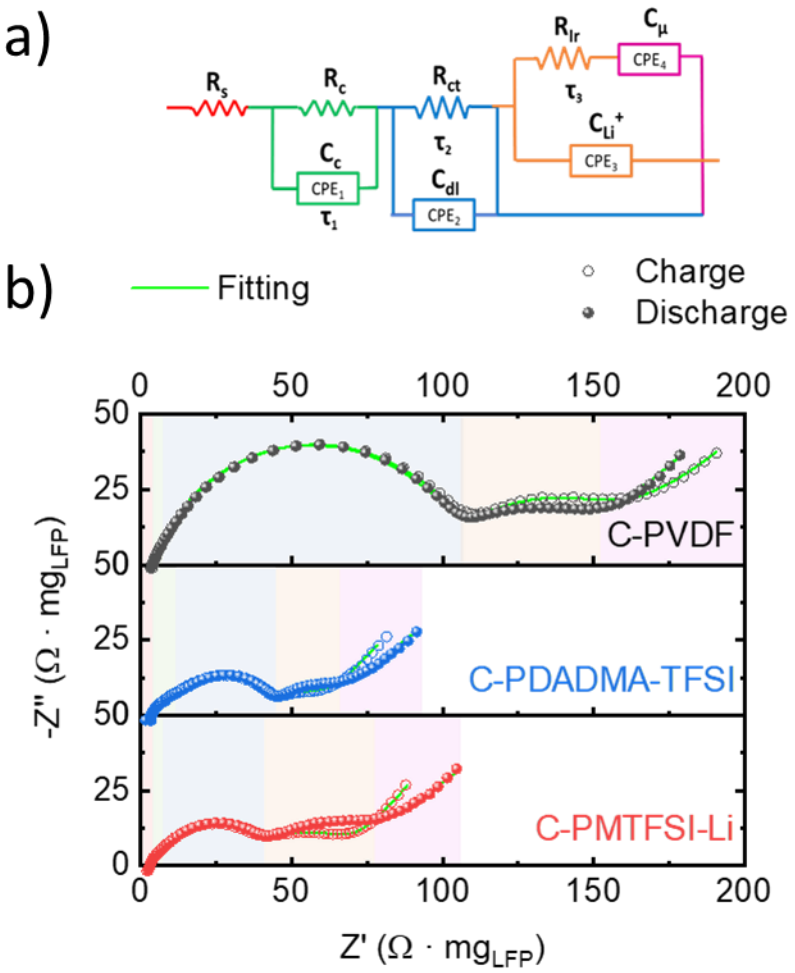

Figure 4.9. a) Proposed equivalent circuit and b) EIS spectra of Li||LFP cells with different binders at SOC=50%; obtained for charge and discharge processes are identified by empty circles and filled spheres respectively, and green lines correspond to obtained fitting.

The cells containing the three different binders presented significantly different Nyquist plots, while the impedance spectra at charged and discharged states were also different (Figure 4.9b). Even if an identical shape was observed

during charge and discharge until medium frequencies in the three cells, more capacitive spectra were exhibited at low frequencies when cells were discharging since they were accumulating Li^+. Table 4.1 summarizes the extracted data from the equivalent circuit for these parameters. If we consider the behavior upon discharging at high frequencies, a higher R_c (8.1 Ω·mg) was observed when C-PDADMA-TFSI was used according to the higher porosity observed by SEM while the use of PMTFSI-Li binder led to lower R_c (3.5 Ω·mg). Subsequently, R_{ct} was remarkably lower in the case of C-PDADMA-TFSI (34.2 Ω·mg) and C-PMTFSI-Li (36.2 Ω·mg) compared with C-PVDF (102.5 Ω·mg) which enabled a faster ion delivery from the electrolyte corroborating lower charge transfer limitations when PDADMA-TFSI and PMTFSI-Li binders were used. Apart from, C-PMTFSI-Li and C-PDADMA-TFSI showing very low charge transfer resistances, they also exhibit the highest C_{dl} (4.8×10^{-3} and 3.7×10^{-3} F g_{LFP}^{-1}), meaning a higher amount of charged species in the double layer as expected, whereas C-PVDF has a lower C_{dl} 1.6×10^{-3} F g_{LFP}^{-1}.

Table 4.1. Extracted fitting data from Nyquist plots of Li||LFP cells using different binders at SOC=50% when charging (shaded in orange) and discharging (shaded in blue). The units of resistances (R) are $\Omega \cdot mg_{LFP}$ and capacitances (C) are $F\ g_{LFP}^{-1}$.

Cathode	R_C	C_C	R_{ct}	C_{dl}	R_{lr}	C_{Li^+}	C_μ
C-PVDF	4.2	3.2×10^{-3}	98.7	1.7×10^{-3}	45.4	0.46	32.2
C-PVDF	2.6	4.2×10^{-3}	102.5	1.6×10^{-3}	48.5	0.45	27.7
C-PDADMA-TFSI	7.5	$1.1\ 10^{-3}$	33.7	3.9×10^{-3}	15.9	0.79	20.6
C-PDADMA-TFSI	8.1	0.8×10^{-3}	34.2	3.7×10^{-3}	18.1	0.71	15.4
C-PMTFSI-Li	3.4	3.5×10^{-3}	34.1	4.9×10^{-3}	29.6	0.40	41.1
C-PMTFSI-Li	3.5	3.0×10^{-3}	36.2	4.8×10^{-3}	35.5	0.47	27.2

At low frequencies, C-PDADMA-TFSI based cell showed the lowest R_{lr} (18.1 Ω·mg) indicating the fastest medium for the Li^+ ion to reach the active center, followed by C-PMTFSI-Li and finally C-PVDF. However, the values of C_μ parameter is aligned with the CV experiments, showing a more hindered reaction

for C-PDADMA-TFSI (15.4 F g_{LFP}^{-1}) in comparison with C-PVDF and C-PMTFSI-Li, (27.7 and 27.2 F g_{LFP}^{-1}, respectively). Even if C-PVDF and C-PMTFSI-Li presented very similar C_μ when they were discharging, C-PMTFSI-Li exhibited a higher value when it was charging (41.1 F g_{LFP}^{-1}) in comparison with C-PVDF (32.2 F g_{LFP}^{-1}) meaning a more effective galvanostatic charge storage (Figure 4.10iii). These values are in agreement with C_{Li^+} in each case, where in C-PDADMA-TFSI the cell accumulates more Li^+ ions that did not reach the active material (0.71 F g_{LFP}^{-1}), while C-PVDF and C-PMTFSI-Li presented lower capacitance values (0.45 and 0.47 F g_{LFP}^{-1}, respectively). These values at low frequencies can be understood if we consider the interactions that may occur between Li^+ ions and free $TFSI^-$ counterions of C-PDADMA-TFSI, which may increase Li^+ mobility and retain its entrance to active centers as proposed by the scheme (Figure 4.10i-ii). Nonetheless, once again C-PMTFSI-Li exhibited a more effective galvanostatic charge with a lower amount of accumulated Li^+ (0.40 F g_{LFP}^{-1}) in comparison with C-PVDF (0.46 F g_{LFP}^{-1}) since the release of Li^+ from the active material might be boosted by repulsion with mobile Li^+ associated with the PMTFSI-Li binder (see Figure 4.10iv). Overall, EIS results suggested a favored medium for mass transport when PDADMA-TFSI binder was used but at the same time, the Li^+-$TFSI^-$ interactions hinder the redox reaction. Moreover, the use PMTFSI-Li binder provided the ideal scenario with low charge transference resistance and efficient galvanostatic charge and discharge.

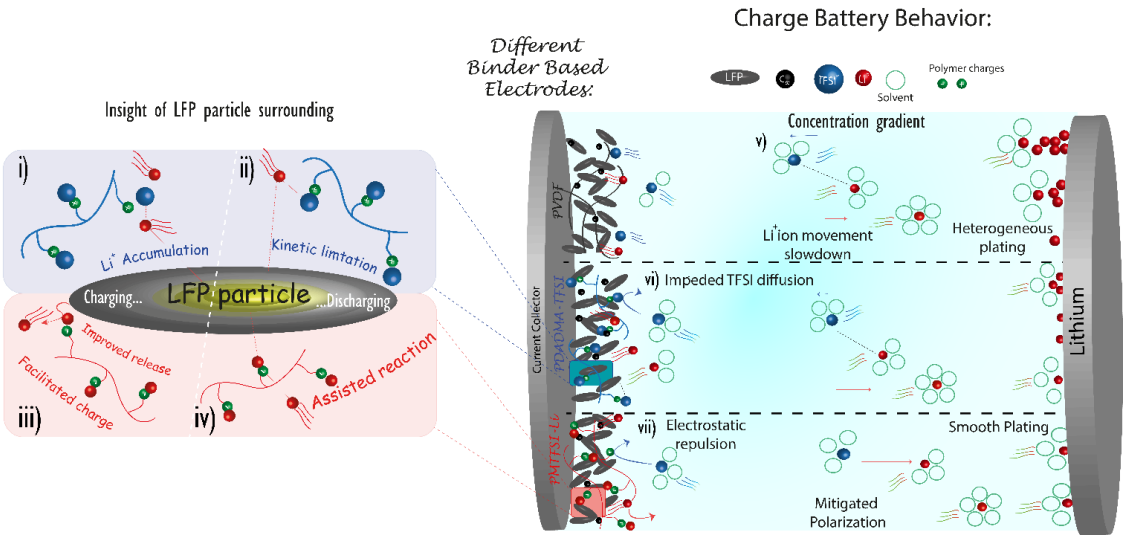

Figure 4.10. Proposed scheme of the ionic interactions between charged species for C-PVDF, C-PDADMA-TFSI, and C-PMTFSI-Li cells.

After EIS measurements, the same cells were cycled at 2C for 40 cycles to promote cell polarization and subsequently opened inside an argon-filled glovebox. SEM images of cross-sectional lithium were taken to observe anode deterioration. As is shown in Figure 4.11, a huge amount of mossy lithium layer was formed onto the anode in C-PVDF cell which could shorten its cycle life while C-PDADMA-TFSI cell, because of its enhanced mass transport during cycling, mitigated that growth. Interestingly, no mossy lithium was observed in the C-PMTFSI-Li cell, which apparently, limited the deterioration of the anode preventing potential lithium metal failure. Therefore, similarly to what occurs in the field of electrolytes, the single lithium-ion polymer used as binder seems to prevent concentration gradients by regulating ion concentration in the electrode and hence, inhibiting non-homogeneous lithium plating. In a PVDF scenario, typical concentration gradients lead to a slowdown of the Li^+ mobility in the electrolyte producing heterogeneous plating onto the lithium metal anode as represented in Figure 4.10v. Unlike, PDADMA-TFSI and PMTFSI-Li based electrodes limited this problem by acting as ion buffers by restraining the

polarization of the $TFSI^-$ counterion. PDADMA-TFSI system already contains a high population of $TFSI^-$ anions impeding its diffusion (Figure 4.10vi), whereas PMTFSI-Li may repulse TFSI anions electrostatically by interaction with negatively charged polymer chain (Figure 4.10vii).

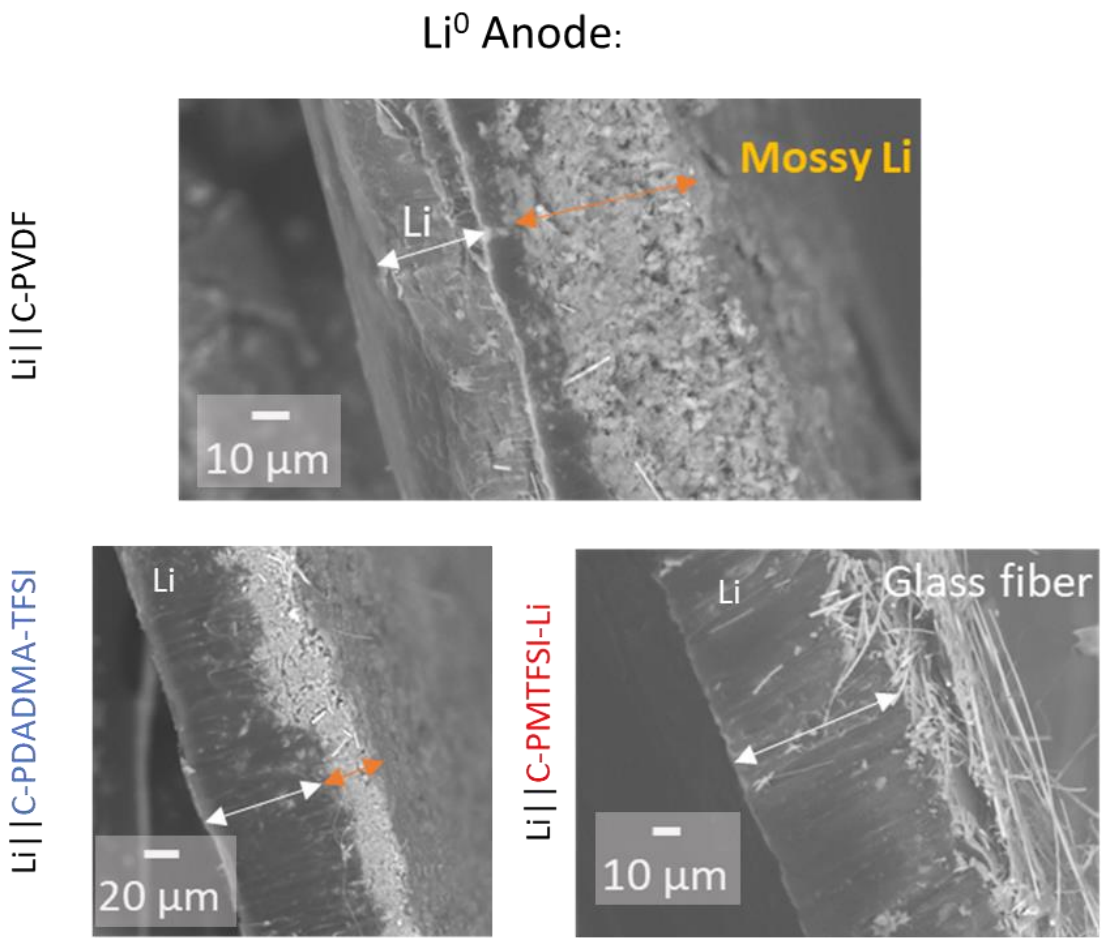

Figure 4.11. Cross-sectional SEM images of lithium metal anode from different Li||LFP cells (as labelled in the figure) after being cycled at 2C for 40 cycles.

4.7. Optimization of PMTFSI-Li

Effect of molecular weight

In the previous sections, PMTFSI-Li of a molecular weight of 50 KDa has been employed for the comparison against PDADMA-TFSI and PVDF with similar

low loadings (1-4 mg cm^{-2}). However, the molecular weight has an impact on the mechanical properties and we observed that when preparing electrodes with higher mass loadings of active material, the slurries containing PMTFSI-Li resulted in cracked electrodes. In order to investigate the effect of the molecular weight on binding properties, two new polymers of higher molecular weights (250 KDa and 2,000 KDa) were synthesized and employed in LFP formulations.

With 250 KDa electrodes of 10-12 mg_{LFP} cm^{-2} were obtained, while when using 50 and 2,000 KDa the electrodes started cracking at 6.6 and 4.3 mg_{LFP} cm^{-2} respectively (see Figure 4.12a). SEM pictures of electrodes with the same mass loading (~ 4 mg_{LFP} cm^{-2}) were taken proving deeper and more critical fissures for 50 and 2,000 KDa (Figure 4.12b). These results indicate that, either PMTFSI-Li (> 2,000 KDa) forms too rigid coatings or the presence of residual emulsifiers from the polymerization is affecting the properties of the polymer.

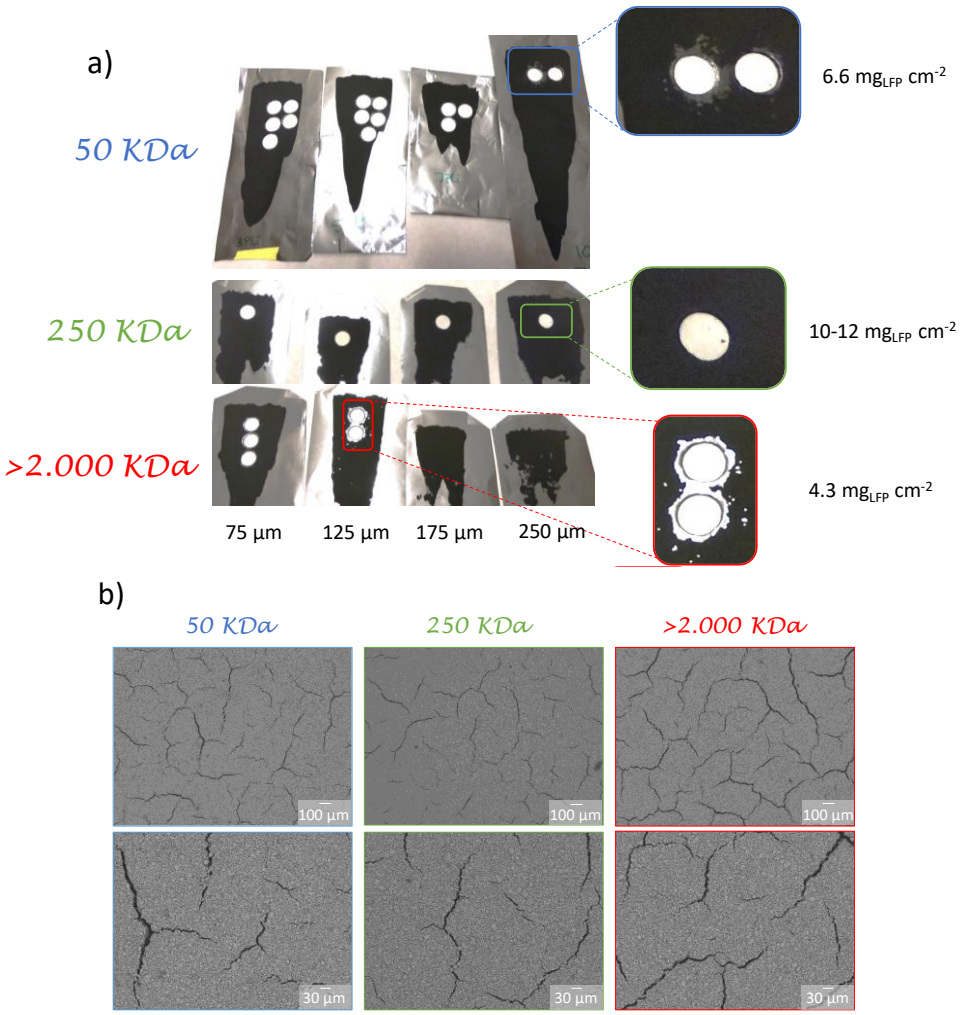

Figure 4.12. a) Pictures of LFP electrodes containing PMTFSI-Li of different molecular weights as binder coated at different thicknesses 75-250 µm. b) SEM surface pictures of 4 mg_{LFP} cm^{-2} electrodes using PMTFSI-Li binder of 50, 250 and >2,000 KDa.

The enhanced mechanical properties by increasing the M_w of PMTFSI-Li were confirmed by DMA obtaining storage modulus values at 40 ºC of 2.1×10^7, 3.4×10^7 and 4.7×10^7 Pa for 50, 250 and >2,000 KDa respectively (see Figure 4.13).

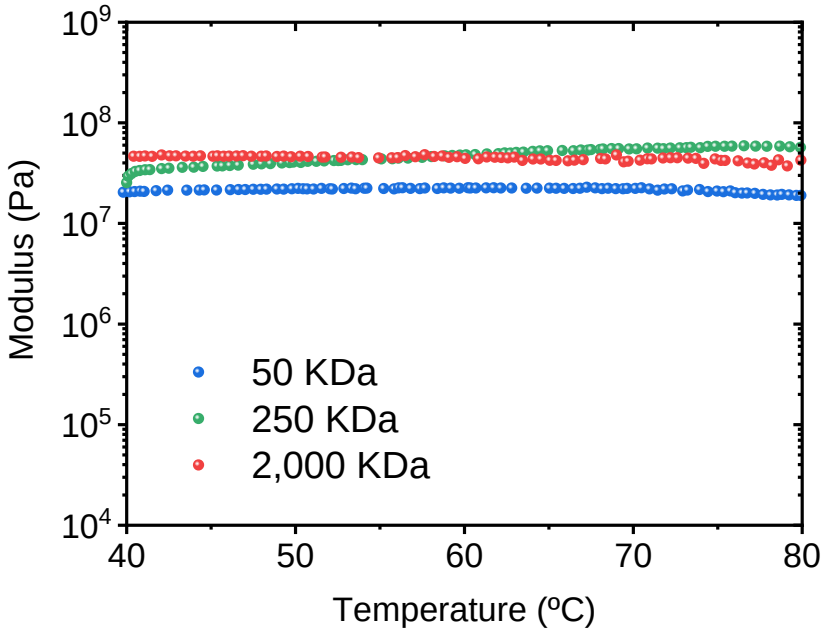

Figure 4.13. Storage modulus as function of temperature of PMTFSI-Li with different molecular weight.

Subsequently, the cathodes based on PMTFSI-Li of different molecular weights (termed C-50, C-250 and C-2,000) were subsequently cycled using 1M LiTFSI (DOL/DME 1:1 v/v) against lithium metal in a rate capability test (Figure 4.14a). From Figure 4.14b can be seen the specific capacity delivered by the different PMTFSI-Li-based cells at 1C and different mass loadings. The results reveal that the three cathodes deliver roughly the same specific capacity at 1C when using low loadings (138 mAh g^{-1} with 3-3.7 mg_{LFP} cm^{-2}), but it rapidly decreases with higher mass loadings (117.4 mAh g^{-1} with 11 mg_{LFP} cm^{-2}). In agreement with the quality of the slurries observed before, C-250 still provides higher specific capacities in all the range measured. Figure 4.14c depicts the specific capacity of ~ 4.5 mg_{LFP} cm^{-2} cells at different C-rates, reflecting a similar performance for different molecular weights of PMTFSI-Li at low C-rate (161 mAh g^{-1} at C/10). However, when the electrodes are pushed to cycle at higher C-rates, C-250 remains as the best electrode reaching values of 78.6 mAh g^{-1} cm^{-2} at 10C.

Accordingly, the quality of the electrode seems not only to affect the capacity obtained at high mass loadings, when the fissures are evident; but also the rate capability.

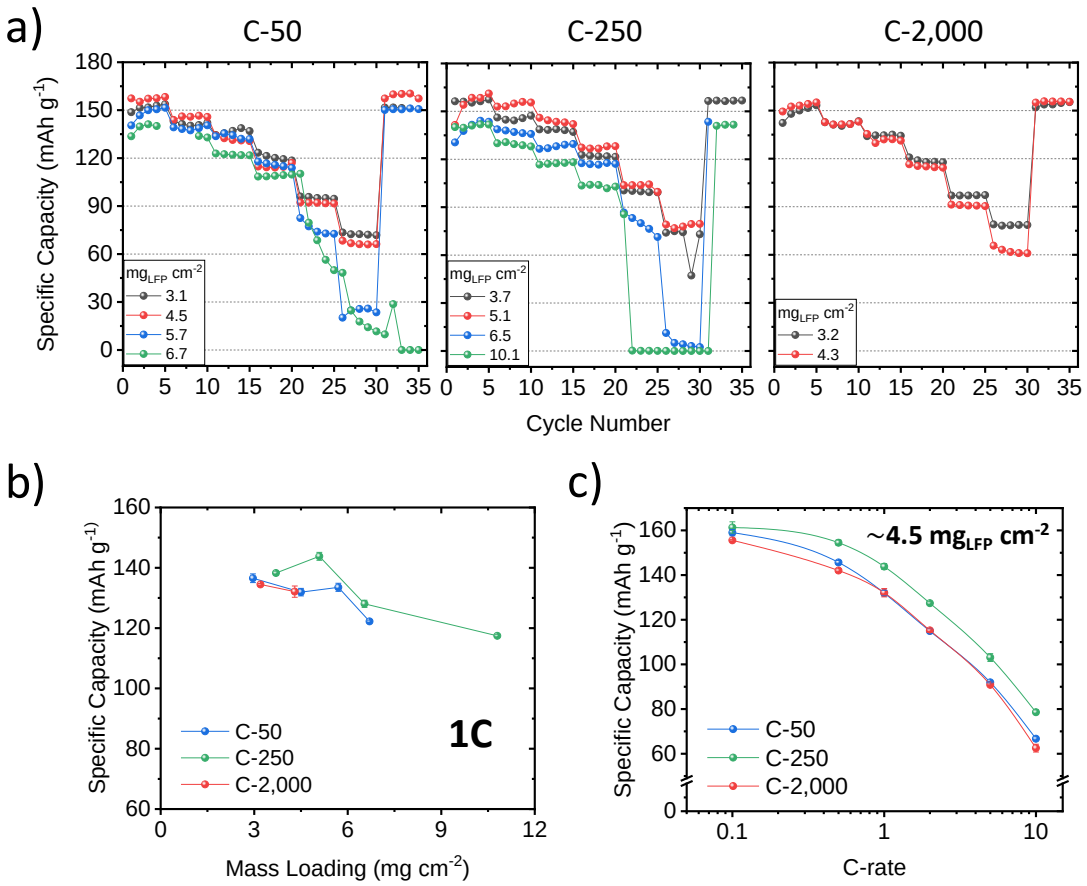

Figure 4.14. a) Cycling of Li|1M LiTFSI (DOL/DME)|LFP cells using PMTFSI-Li of different M_w as binders at different mass loadings. b) Specific capacity at 1 C versus loading of electrode; and c) Specific capacity of 4.5 mg LFP cm^{-2} as function of C-rate.

Effect of the electrolyte

An ideal electrolyte should provide high ionic conductivity that leads to low overpotentials during cycling, but also be stable at high current densities, which are required for fast charge-discharge cyclings and high-loading devices. These properties are key for the lifespan, energy and power density of the devices. In order to obtain a stable cycling for high loading electrodes, different electrolytes

were tested in Li||LFP cells: 1M LiTFSI DOL/DME (1:1 v/v), 1M LiTFSI EC/DEC (1:1 v/v) and 1M $LiPF_6$ EC/DEC (1:1 v/v) at 1 C (Figure 4.14). The results show slightly higher capacities delivered when using 1M LiTFSI DOL/DME (1:1 v/v), but rapid fade after 20 cycles. In contrast, the electrolytes containing EC/DEC solvent present much more stable cycling (100 cycles) delivering ~ 113 mAh g^{-1} at 1C (1.2 mAh cm^{-2}), revealing a big impact of the solvent on the cell performance and not so much the nature of these salts (LiTFSI and $LiPF_6$).

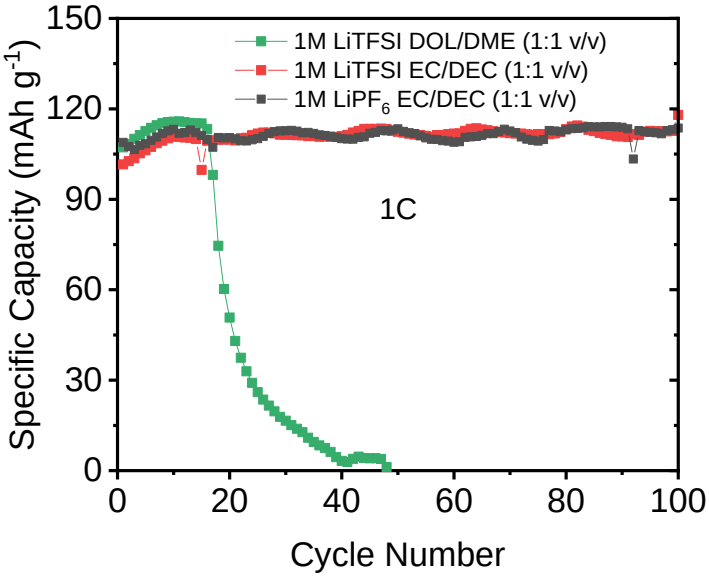

Figure 4.15. Cycling of Li||LFP cells using PMTFSI-Li 250 KDa as binder and different electrolytes at 1C. Mass loading electrodes ~ 10 mg_{LFP} cm^{-2}.

1M $LiPF_6$ EC/DEC (1:1 v/v) was selected as electrolyte to compare against conventional PVDF for the exhibited stability and wide use in LIBs.[24] Figure 4.16 shows the cycling of Li||LFP cells containing PVDF and PMTFSI-Li of 250 KDa as binders for the cathodes (C-250) at 1C. PVDF-based cell faded after 100 cycles delivering 119.5 ± 1.9 mAh g^{-1} (0.95 mAh cm^{-2}) while C-250 exhibits very stable cycling of 130.4 ± 1.4 mAh g^{-1} (0.98 mAh cm^{-2}), in good agreement with the observed results in Sections 4.5-4.6.

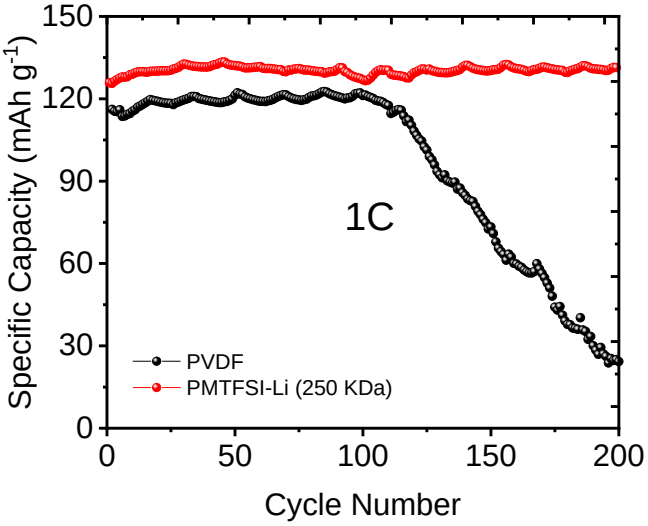

Figure 4.16. Cycling of Li|1M $LiPF_6$ EC/DEC (1/1 v:v)|LFP cells at 1C using PVDF and PMTFSI-Li (250 KDa) as binders. Mass loading electrodes ~ 7.5 mg_{LFP} cm^{-2}.

4.8. Conclusions

In this chapter, we studied the impact of using different types of poly(ionic liquid) polymers as binders in LFP cathodes for LIB and compared their performances with conventional PVDF binder. The cells containing the innovative PMTFSI-Li binder exhibited optimum conditions for the LFP redox reaction and consequently the best discharge capacity (170.3 ± 0.8 mAh g^{-1}) at C/10. An outstanding capacity at 10C (100.6 ± 0.5 mAh g^{-1}) and stable cyclability with a capacity retention of 96% (140.5 mAh g^{-1}) after >500 cycles at 1C were obtained. When comparing C-PDADMA-TFSI and C-PVDF, at low C-rate C-PVDF had higher capacities than C-PDADMA-TFSI, but as the C-rate was increased, mass transport limitations limited the performance of C-PVDF, particularly with high loading electrodes, producing large overpotentials. Transport limitations were identified by EIS through significant charge transfer resistances. Moreover, C-PVDF cell showed a more deteriorated cathode after long-term cycling in contrast

to the stable cycling of C-PDADMA-TFSI as a consequence of an efficient charge transfer through Li^+ interaction with mobile free TFSI anions. Furthermore, when fresh cells were cycled at 2C for 40 cycles after EIS measurements to promote cell polarization, no mossy lithium was observed in the anode in the C-PMTFSI-Li cell, while a small layer was found in C-PDADMA-TFSI cell and a large amount of mossy lithium was observed for C-PVDF cells, being probably the cause of the fade. Interestingly, the ionic binders showed a more homogeneous plating, particularly the single-ion conducting polymer PMTFSI-Li. Therefore, the use of ionic binders is proposed for enhanced and longer-life batteries and greener processing since PDADMA-TFSI and PMTFSI-Li are also soluble in acetone and water respectively, potentially avoiding the use of toxic NMP. Finally, PMTFSI-Li was synthesized with higher M_w to reach mass loadings in the range of 10-12 mg_{LFP} cm^{-2}; and still obtaining higher specific capacities (130.4 ± 1.4 mAh g^{-1} with PMTFSI-Li M_w=250 KDa) in comparison with conventional PVDF (119. ± 1.9 mAh g^{-1}).

4.9. Experimental part

4.9.1. Materials

PVDF Solef® 5130 (1,000-1,100 Kg mol^{-1}) was used as a reference binder. The synthesis of PDADMA-TFSI was proceeded by ion exchange using poly(dyallyldimethylammonium chloride) (400-500 kg mol^{-1}) and KTFSI as reported in literature.[25] For the N-methyl-2-pyrrolidinone (NMP, 99%, Sigma-Aldrich), anhydrous 1,3-dioxolane (99.8%, Sigma-Aldrich), anhydrous dimethoxy ethane (99.5%, Sigma-Aldrich), lithium bis(trifluoromethanesulfonyl)imide

(LiTFSI, 99%, Iolitec), conductive carbon (Super C65, Timcal), lithium iron phosphate ($LiFePO_4$, Aleees) were used without further treatment.

4.9.2. Synthesis of PMTFSI-Li

PMTFSI-Li was synthesized by using reversible addition-fragmentation chain transfer (RAFT) polymerization of commercial lithium 1-[3-methacryloyloxy) propylsulfonyl]-1-(trifluoromethansesulfonyl) imide monomer (LiMTFSI) (Specific Polymers) targeting 50 KDa; and by inverse emulsion polymerization (IEP) for >2,000 KDa according to already reported procedures.[26] For the synthesis of PMTFSI-Li of 250 KDa, free radical polymerization (FRP) was employed. A degassed solution of LiMTFSI (1.5 g 4.31 mmol) and AIBN (1 mg, 0.061 mmol) in 5 g DMF was polymerized in a Schlenk tube vigorously stirring at 90 ºC under argon atmosphere for 8h. The obtained polymer was purified by precipitation in cold diethyl ether and subsequently dried at 60ºC under high vacuum overnight. Table 4.2 summarizes the data obtained by size exclusion chromatography (SEC) in comparison with the reported procedure. The highest M_w polymer was out of the range of the SEC columns available and a M_w of >2,000 is stimated.

Table 4.2. SEC of the synthesized polymers at 25 ºC, 0.1 M LiCl in water

Label	M_n (kg mol^{-1})	M_w (kg mol^{-1})	Đ	Ref.
50	44.9	59.2	1.32	[26]
250	88.3	259	2.934	This work
>2,000	-	-	-	[26]

4.9.3. Electrode preparation

The slurries were prepared by dissolving the binder first in NMP in a small beaker and subsequently addition of C65 and LFP. After one day stirring, the

viscous slurry was coated onto carbon-coated aluminum foil (current collector) with the aid of an automatic doctor blade (NEURTEK Instruments) and it was left drying at room temperature for 12 h. Finally, disks of 11 mm diameter were punched and further dried at 60ºC under vacuum for 24h prior characterization. To evaluate the intrinsic properties of binders, thin electrodes were prepared (between 1.0-2.3 mg_{LFP} cm^{-2}).

4.9.4. Electrolyte uptake

Pristine electrodes (LFP/C65/binder 80/10/10 wt. %, 11 mm diameter) of 1-2.3 mg_{LFP} cm^{-2} were soaked separately in fresh electrolyte (0.5 mL) for short (5 seconds) and long (48 h) immersion times in closed vials independently and subsequently weighted. Noteworthy, 48 h was considered to ensure a thermodynamic equilibrium of the system in terms of electrolyte saturation and chemical equilibrium of the ionic species.

4.9.5. Cell assembly

To evaluate the intrinsic properties of binders, thin electrodes (between 1.0-2.3 mg_{LFP} cm^{-2}) were prepared based on PVDF, PDADMA and PMTFS-Li (50 KDa) to reduce transport problems associated with mechanical properties of the electrodes. Another group of electrodes with higher loadings (4 mg_{LFP} cm^{-2}) was prepared to evaluate the processability of the binders during the preparation of thicker electrodes and the identification of the potential for high loading electrodes. In the last step, much viscous slurries based on PMTFSI-Li with different molecular weights were prepared similarly, and subsequently coated at different thicknesses 75-250 µm to find the critical loadings.

Li||LFP cells were assembled in CR2032 coin cells inside Ar glovebox, by firstly cleaning Li ribbons with cyclohexane and a nylon brush prior punching 12 mm disks and using 120 µL of electrolyte in glass microfiber separators.

4.9.6. Electrochemical characterization

Rate capability for assembled cell was performed constant current at (0.1C, 0.5C, 1C, 2C, 5C and 10C) on a Neware battery cycles, whereas VMP-3 potentiostat (Biologic) was used to carry out further electrochemical characterization Cyclic voltammetry (CV) was used in the range of 2.8-3.8V at 0.1 mV s^{-1}. Electrochemical impedance spectroscopy (EIS) was employed to determine processes resistances and capacitances involved in Li||LFP cells with a perturbation of 10 mV and a frequency range from 1MHz-0.1Hz with a VMP-3 potentiostat (Biologic). Afterward, data were fitted in frequency, Z and -Z'' by using Zview software obtaining Chi-Squared values below 1×10^{-4}.

4.9.7. Dynamic mechanical analysis

Compressive mode dynamic mechanical analysis (DMA, PerkinElmer DMA8000) was used to analyze the mechanical properties of the polymers. The polymer was pressed in KBr die and dried at 70 ˚C under vacuum overnight to finally obtain pellets of around 1-4 mm in thickness and 0.5 cm^{-2}. The temperature range of DMA was 40-80 ˚C and the frequency was set at 1 Hz. The measurements were performed in open air.

4.10. References

1. H. Chen, M. Ling, L. Hencz, H. Y. Ling, G. Li, Z. Lin, G. Liu and S. Zhang. Exploring Chemical, Mechanical, and Electrical Functionalities of Binders for Advanced Energy-Storage Devices. *Chem. Rev.* **2018**;118:8936–8982.

2. C. Liu, Z. G. Neale and G. Cao. Understanding electrochemical potentials of cathode materials in rechargeable batteries. *Mater. Today* **2016**;19:109–123.

3. H. D. Abruña, Y. Kiya and J. C. Henderson. Batteries and electrochemical capacitors. *Phys. Today* **2008**;61:43–47.

4. T. Placke, R. Kloepsch, S. Dühnen and M. Winter. Lithium ion, lithium metal, and alternative rechargeable battery technologies: the odyssey for high energy density. *J. Solid State Electrochem.* **2017**;21:1939–1964.

5. D. Mecerreyes, L. Porcarelli and N. Casado. Innovative Polymers for Next-Generation Batteries. *Macromol. Chem. Phys.* **2020**;221:1–7.

6. K. A. Seid, J. C. Badot, O. Dubrunfaut, S. Levasseur, D. Guyomard and B. Lestriez. Influence of the carboxymethyl cellulose binder on the multiscale electronic transport in carbon-LiFePO 4 nanocomposites. *J. Mater. Chem.* **2012**;22:24057–24066.

7. D. Xu, X. Chu, Y. B. He, Z. Ding, B. Li, W. Han, H. Du and F. Kang.

Enhanced performance of interconnected LiFePO4/C microspheres with excellent multiple conductive network and subtle mesoporous structure. *Electrochim. Acta* **2015**;152:398–407.

8. A. Eftekhari. LiFePO4/C nanocomposites for lithium-ion batteries. *J. Power Sources* **2017**;343:395–411.

9. J. Zhao, X. Yang, Y. Yao, Y. Gao, Y. Sui, B. Zou, H. Ehrenberg, G. Chen and F. Du. Moving to Aqueous Binder: A Valid Approach to Achieving High-Rate Capability and Long-Term Durability for Sodium-Ion Battery. *Adv. Sci.* **2018**.

10. D. Bresser, D. Buchholz, A. Moretti, A. Varzi and S. Passerini. Alternative binders for sustainable electrochemical energy storage-the transition to aqueous electrode processing and bio-derived polymers. *Energy Environ. Sci.* **2018**;11:3096–3127.

11. J. Xu, S. L. Chou, Q. F. Gu, H. K. Liu and S. X. Dou. The effect of different binders on electrochemical properties of LiNi 1/3Mn1/3Co1/3O2 cathode material in lithium ion batteries. *J. Power Sources* **2013**;225:172–178.

12. V. A. Nguyen and C. Kuss. Review — Conducting Polymer-Based Binders for Lithium-Ion Batteries and Beyond. *J. Electrochem. Soc.* **2020**;167:065501.

13. P. R. Das and J. E. Soc. PEDOT:PSS as a Functional Binder for Cathodes

in Lithium Ion Batteries. *J. Electrochem. Soc.* **2015**;162:A674–A678.

14. G. Guzmán-González, G. Ramos-Sánchez, L. E. Camacho-Forero and I. González. Charge Delocalization on BO 4- Centers to Improve Conductivity on Single Lithium Ion Conducting Polymer Electrolytes: A Computational/Experimental Approach. *J. Phys. Chem. C* **2019**;123:17686–17694.

15. L. Qiu, Z. Shao, D. Wang, F. Wang, W. Wang and J. Wang. Novel polymer Li-ion binder carboxymethyl cellulose derivative enhanced electrochemical performance for Li-ion batteries. *Carbohydr. Polym.* **2014**;112:532–538.

16. R. Suarez-Hernandez, G. Ramos-Sánchez, I. O. Santos-Mendoza, G. Guzmán-González and I. González. A Graphical Approach for Identifying the Limiting Processes in Lithium-Ion Battery Cathode Using Electrochemical Impedance Spectroscopy. *J. Electrochem. Soc.* **2020**;167:100529.

17. J. S. Lee, K. Sakaushi, M. Antonietti and J. Yuan. Poly(ionic liquid) binders as Li+ conducting mediators for enhanced electrochemical performance. *RSC Adv.* **2015**;5:85517–85522.

18. N. S. Choi, Y. G. Lee and J. K. Park. Effect of cathode binder on electrochemical properties of lithium rechargeable polymer batteries. *J. Power Sources* **2002**;112:61–66.

19. B. Lestriez. Functions of polymers in composite electrodes of lithium ion batteries. *Comptes Rendus Chim.* **2010**;13:1341–1350.

20. G. Guzmán, J. Vazquez-Arenas, G. Ramos-Sánchez, M. Bautista-Ramírez and I. González. Improved performance of LiFePO4 cathode for Li-ion batteries through percolation studies. *Electrochim. Acta* **2017**;247:451–459.

21. L. Xie, L. Zhao, J. Wan, Z. Shao, F. Wang and S. Lv. The Electrochemical Performance of Carboxymethyl Cellulose Lithium as a Binding Material for Anthraquinone Cathodes in Lithium Batteries. *J. Electrochem. Soc.* **2012**;159:A499–A505.

22. Y. Y. Lin, Y. M. Chen, S. S. Hou, J. S. Jan, Y. L. Lee and H. Teng. Diode-like gel polymer electrolytes for full-cell lithium ion batteries. *J. Mater. Chem. A* **2017**;5:17476–17481.

23. N. Vicente, M. Haro, D. Cíntora-Juárez, C. Pérez-Vicente, J. L. Tirado, S. Ahmad and G. Garcia-Belmonte. LiFePO4 particle conductive composite strategies for improving cathode rate capability. *Electrochim. Acta* **2015**;163:323–329.

24. Q. Li, J. Chen, L. Fan, X. Kong and Y. Lu. Progress in electrolytes for rechargeable Li-based batteries and beyond. *Green Energy Environ.* **2016**;1:18–42.

25. A. Fdz. de Añastro, N. Casado, X. Wang, J. Rehmen, D. Evans, D. Mecerreyes, M. Forsyth and C. Pozo-gonzalo. Poly(ionic liquid) iongels for all-solid rechargeable zinc/PEDOT batteries. *Electrochim. Acta* **2018**;278:271–278.

26. J. L. Olmedo-Martinez, L. Porcarelli, A. Alegria, D. Mecerreyes and A. J. Mu. High Lithium Conductivity of Miscible Poly (ethylene oxide)/ Methacrylic Sulfonamide Anionic Polyelectrolyte Polymer Blends. *Macromolecules* **2020**;53:4442–4453.

Chapter 5. Improving LFP cathode performance through mixed ionic-electronic conducting binders for high energy and power density

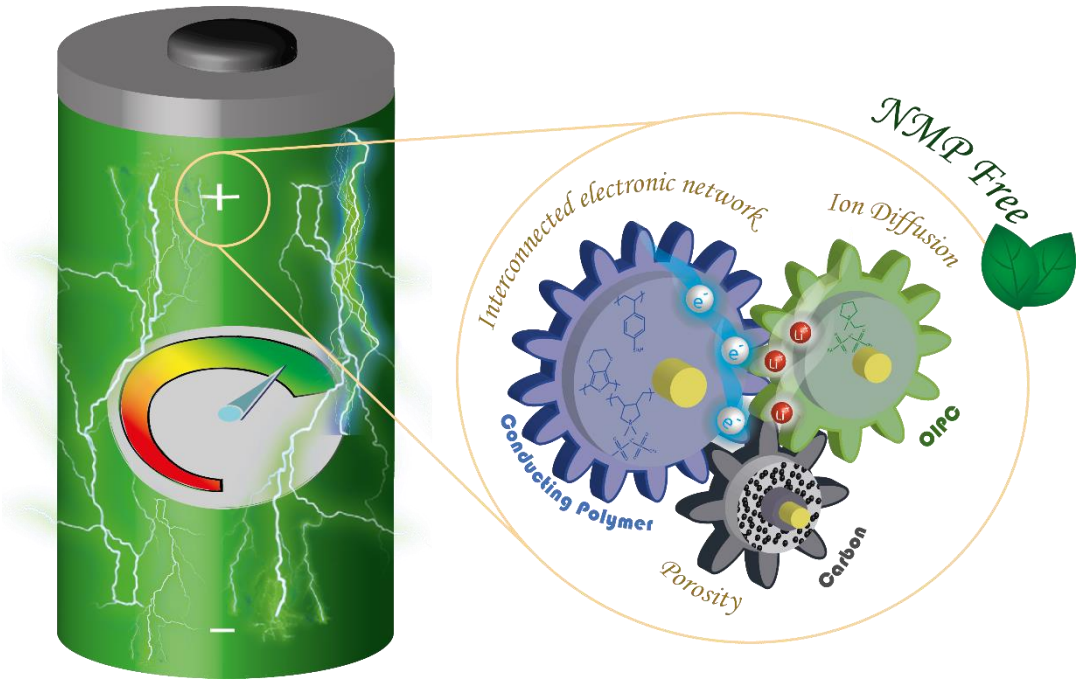

Chapter 5. Improving LFP cathode performance through mixed ionic-electronic conducting binders for high energy and power density

5.1. Introduction

The wide use of Lithium Ion Batteries (LIBs) over the world requires more optimization on the devices to extract their maximum real specific capacity. Since the commercialization of the first LIB in 1991 by Sony, it has been largely improved to satisfy daily needs in portable electronics such as laptops and smartphones.[1] However, the energy demand for these electronics has increased with the tools and performance they can offer to us, as well as the demand for powering electric vehicles. Therefore, there is an interest in the optimization of LIB to supply most of the energy as possible at higher rates and extend the cycle life.[2] In the field of the optimization of LIB, there are multiple factors to consider, from the chemistry and formulation of the electrolyte that allows the stable long-term cycling at high current densities, to the active material for electrodes development, as well as the optimization of their additives amount, manufacturing, and cycling conditions.[3]

Specifically, on the cathode side, where nowadays the lithium iron phosphate ($LiFePO_4$, LFP) active material is one of the most widely used, it is generally accompanied by redox inactive materials such as conducting carbon and a polymeric binder (typically electronically isolating poly(vinylidene fluoride), PVDF). Today, one of the main challenges that faces this technology is to obtain the maximum real specific capacity and capacity retention during long-term cycling tests. As discussed in Chapter 4, the choice of type of binder can be key for this purpose.[4]

Indeed, multiple works have shown the benefits of conducting polymer-(CP) coatings on active material particles or even using them as functionalized binders.[5,6] Despite the conducting carbon particles included in the electrode formulation, CPs have shown a better electronic interconnection contact and, therefore, better electrochemical responses.[6] The use of CPs enables stable cyclability and capacity values closer to the theoretic, even in electrodes with a high active material load (92 wt. %).[7] In addition to that, it has been also shown the first carbon-free solid-state battery employing this kind of material in Chapter 2, which takes the advantage of the reduced porosity, which is highly beneficial for solid-state devices. Furthermore, those conducting polymers can even contribute their pseudo-capacity increasing the obtained total capacity of the cell.[8] Nonetheless, in liquid state batteries, the porosity of the final electrode must be also optimized to control the electrolyte absorption and facilitate the Li^+ transport through the cell. Therefore, the use of CP in carbon-free formulations is restricted to the porosity generated in the cathode morphology.

Single-ion conducting polymers or poly(ionic liquids) have been also employed to overcome ion transport limitations in LFP composites cathodes and improve the cell performance, specially at high C-rates.[9–11] Recently, organic ionic plastic crystals (OIPCs) emerged as solid-state alternative electrolytes with high ionic conductivity and wide electrochemical window, being applied in lithium- and sodium-ion technologies.[12,13] Moreover, OIPCs have been also incorporated into electrode formulation in solid-state graphite cells to promote the ion transport resulting in promising results comparable to liquid state.[14] OIPC demonstrated as well an enhancement of electrolyte/electrode and electrode/current collector contacts.[14,15]

In this chapter, the mixed ionic and electronic conductors (MIECs) studied in Chapters 2 and 3 based on CP and OIPC are evaluated as binders for high-performance cathodes in terms of energy and power density. The selected MIECs are depicted in depicted in Figure 5.1: PEDOT:PSS (termed PPSS) and PEDOT:PolyDADMA TFSI (namely PPTFSI) in combination with the optimum amount of N-ethyl-N-methylpyrrolidinium bis(trifluoromethanesulfonyl)imide (C_2mpyrTFSI) OIPC (in this chapter also referred as O). Different LFP cathodes were prepared without carbon and in presence of carbon C65, C. Afterward, the carbon-free formulations of neat CP and CP-O composites, as well as their carbon-based version CP-C and CP-O-C were evaluated in Li||LFP cells through potentiostatic and galvanostatic cycling, as well as impedance tests. The results of the electrochemical performance of the different cells were correlated with the intrinsic properties of the additives, such as: porosity, electrolyte uptake, electronic conductivity and impedance.

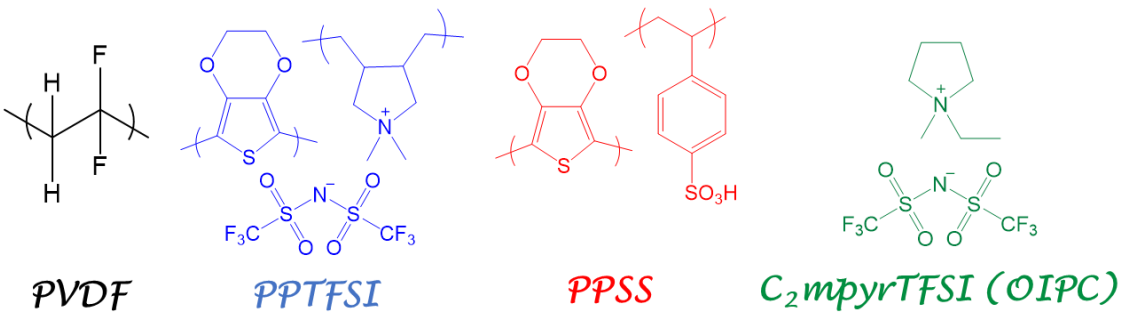

Figure 5.1. Chemical structure of the used binders: PVDF, PEDOT:PDADMA-TFSI (PPTFSI), PEDOT:PSS (PPSS) and C_2mpyrTFSI (OIPC).

5.2. Application in Lithium-ion batteries

To investigate the performance of MIEC materials as binders in LIB, cathode formulations were prepared containing 80 wt.% of LFP in all the cases and varying the binder/conductive additive composition, as listed in Table 5.1.

PEDOT:PSS-OIPC and PEDOT:PolyDADMA TFSI-OIPC composites were formulated according to the optimum ratios already reported in Chapters 2-3. Moreover, C_2mpyrTFSI was chosen as OIPC since 1M LiTFSI DOL:DME (1:1 v/v ratio) was chosen as electrolyte to maintain an ionic homogeneity in the system.

Table 5.1. Slurry composition of each electrode maintaining 80 wt. % of LFP. -O is referred as the addition of C_2mpyrTFSI OIPC to form a polymer-OIPC composite in the indicated weighted ratio according to Chapters 2-3. The averaged loading units are mg_{LFP} cm^{-2}.

Binder, %	C65 (%)	Solvent	Averaged Loading
PVDF, 10	10	NMP	2.5
PPTFSI, 20	-	NMP	2.0
PPTFSI, 10	10	NMP	2.0
PPTFSI-O (80-20), 20	-	NMP	3.4
PPTFSI-O (80-20), 10	10	NMP	1.8
PPSS, 20	-	DMSO	1.3
PPSS, 10	10	DMSO	1.4
PPSS-O (70-30), 20	-	DMSO	1.6
PPSS-O (70-30), 10	10	DMSO	1.1

5.3. Electronic conductivity

The electronic conductivity properties of the different additives were studied by four-point probe (4PP) in composites without active material (see Table 5.2). Since PVDF is an isolating polymer, a PVDF-C slurry was prepared with the same ratio as utilized in LFP cathodes (50/50 wt. %). Even if neat PPTFSI MIEC polymer or PPTFSI-O composite were not able to surpass the electronic conductivity of standard PVDF-C (1.5 S cm^{-1}), the addition of C65 boosted the values, especially for the OIPC based composite leading to 5.1 S cm^{-1} (PPTFSI-O-C). Contrary, PPSS and particularly PPSS-O (580 S cm^{-1}) exceed ×300 times the value of standard PVDF-C. However, the addition of C65 drop the electronic conduction down in both cases, remaining higher the OIPC-based MIEC (94.4 S cm^{-1}). Those values can be understood if we consider the electronic conductivity

of C65 (2.0 S cm^{-1} measured in a pellet of 580 µm), which leads to an increase of PPTFSI values, but a decrease PPSS-based ones. Interestingly, the electronic conductivity of the combination of C65 and PPTFSI materials leads to higher values than the neat compounds. In addition to that, the interaction of OIPC with the rest of the additives leads systematically to higher electronic conductivity values, because of possible smoother integration of C65 particles as a result of its plastic properties.

Table 5.2. Electronic conductivity values of the different additives used in this chapter.

Composite	Polymer (wt. %)	OIPC (wt. %)	C65 (wt.%)	σ_e (S cm^{-1})
C65 (pellet)	-	-	100	2.00 ± 0.10
PVDF-C	50	-	50	1.50 ± 0.20
PPTFSI	100	-	-	0.25 ± 0.05
PPTFSI-C	50	-	50	2.90 ± 0.30
PPTFSI-O	80	20	-	0.13 ± 0.01
PPTFSI-O-C	40	10	50	5.10 ± 1.00
PPSS	100	-	-	416 ± 41
PPSS-C	50	-	50	87.8 ± 0.8
PPSS-O	70	30	-	580 ± 49
PPSS-O-C	40	10	50	94.4 ± 5.2

5.4. Porosity and electrolyte uptake

It is well known that the incorporation of carbon particles into electrode formulations inevitably brings porosity changes in the morphology, which is key for ionic and electronic transport in electrodes for energy storage devices with liquid electrolyte.[16] In this sense, the porosity of the electrodes, prepared with different additives was analyzed following a standardized protocol of physisorption (see experimental Section 5.9.4).[17] The results of this analysis are reported in Table 5.3.

Table 5.3. Porosity parameters extracted from physorption experiments. S_{BET}: specific surface area; V_{pore}: pore volume; Dpore: pore diameter; and ϕ: porosity. Percent of porosity was stimated considering the pore volume and apparent densities.

Cathode	S_{BET} ($m^2\ g^{-1}$)	V_{pore} ($cm^3\ g^{-1}$)	D_{pore} (nm)	ϕ (%)
ePVDF-C	12.1	0.088	29.4	10.0
ePPTFSI	4.2	0.039	35.0	4.3
ePPTFSI-C	8.0	0.064	32.1	7.1
ePPTFSI-O	2.6	0.018	28.0	1.9
ePPTFSI-O-C	9.3	0.064	27.7	7.0
ePPSS	3.1	0.025	32.6	2.4
ePPSS-C	5.1	0.055	42.7	5.7
ePPSS-O	5.2	0.042	32.0	4.0
ePPSS-O-C	8.9	0.074	33.2	7.7

Generally, the porosity of the cathode composite decreases when increasing the amount of binder, obtaining the lowest values for carbon-free electrodes. Since the density of PEDOT:PSS is much lower than that of LFP, an increase in the PEDOT:PSS mass fraction leads to a strong increase in the binder volume fraction.[7] Thus, the polymer can fill the spaces between the LFP particles, decreasing the ratio of the void volume and thereby the porosity of the composite cathode.[18]

The pore diameter remains in the range of 30 to 40 nm for all the cases. However, the incorporation of C65 leads consistently to larger S_{BET} and V_{pore}, as expected. OIPC incorporation modifies the porosity of ePPTFSI cathode leading to a highly dense formulation (ePPTFSI, 4.2 $m^2\ g^{-1}$, 4.3 %; and ePPTFSI-O, 2.6 $m^2\ g^{-1}$, 1.9 %), but remaining practically with not changes in the carbon-based formulation (ePPTFSI-C, 8.0 $m^2\ g^{-1}$, 7.1 %; and ePPTFSI-O-C, 9.3 $m^2\ g^{-1}$ and 7.0 %). Nonetheless, when OIPC is present in any PPSS-based formulation more porous cathodes are obtained (ePPSS, 3.1 $m^2\ g^{-1}$, 2.4 %; ePPSS-O, 5.2 $m^2\ g^{-1}$, 4.0 %; ePPSS-C, 5.1 $m^2\ g^{-1}$, 5.7 %; and ePPSS-O-C, 8.9 $m^2\ g^{-1}$, 7.7 %). ePVDF-

C remains as the most porous electrode with 12.1 m^2 g^{-1} surface area and 10.0 % of porosity. The porosity is a key parameter to control for a smooth ionic diffusion into the whole electrode when they are in contact with liquid electrolyte, too dense electrodes may suffer from diffusion limitations.

The porosity of the electrode will affect the electrolyte uptake, which is also an important parameter to consider since it will influence the total cell impedance. To investigate the swelling of the electrode composite in contact with electrolyte, fresh electrodes were immersed in fresh 1M LiTFSI DOL:DME (1:1 v/v) separately for 48 h to ensure the electrode saturation of solvent and ionic species diffusion reaching the steady-state. Overall, the carbon addition to the formulation leads to notably higher electrolyte uptake, in comparison to the electrodes based on just LFP-MIEC without carbon, as expected considering the higher measured porosities (Figure 5.2). Interestingly, the electrolyte uptake does not change with the addition of OIPC, unlike the porosity. Lastly, comparing the different families, ePVDF-C showed a value of around 700 % of electrolyte uptake while PPTFSI-based electrodes remained much lower (around 545 % for PPTFSI-C and PPTFSI-O-C) and PPSS-based electrodes reached values of around 1250 % for ePPSS-C and ePPSS-O-C showing a higher affinity with the studied electrolyte.This phenomenon can be given by the different PEDOT:Polymer composition in each family. Although both families were prepared with the same 1:2.5 w/w ratio, due to different polyelectrolyte molecular weights, the compositions result in 1:1.91 and 1:0.87 molar ratios for PEDOT:PSS and PEDOT:PolyDADMA TFSI, respectively, consequently PEDOT:PSS contains a higher molar ratio of polyelectrolyte, which favours the wettability of the electrode.

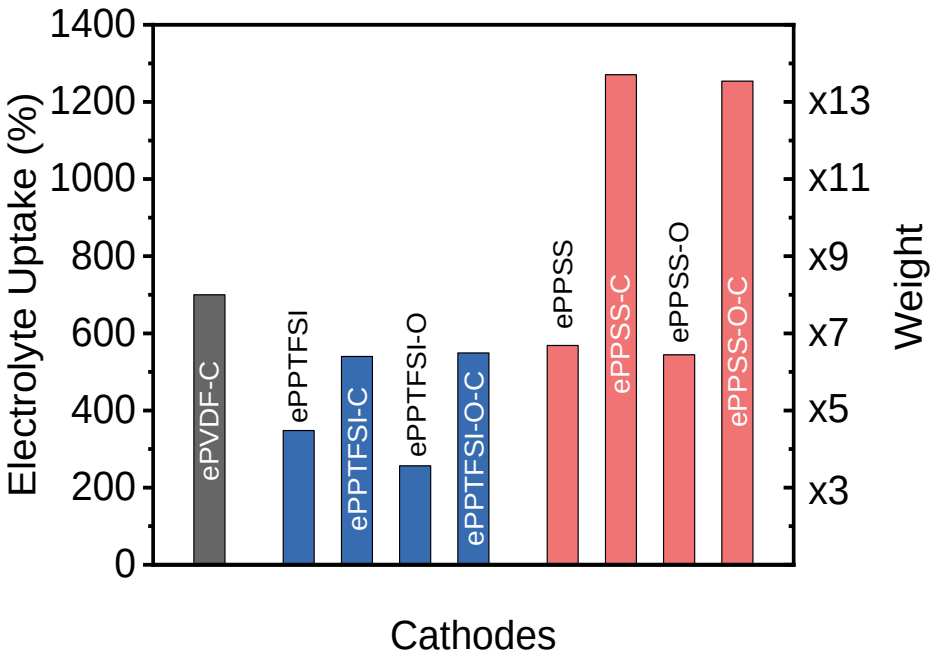

Figure 5.2. Weight increment of LFP electrodes with different additives after 48 h of immersion time in 1M LiTFSI DOL:DME (1:1 v/v) fresh electrolyte.

5.5. Electrochemical response and morphology

To evaluate the electrochemical window of the proposed MIEC materials, LFP-free electrode formulations were assembled in Li||MIEC-O-C cells and subsequently studied by cyclic voltammetry (see Figure 5.3a-b). Two fresh cells were assembled for each material for going to upper and lower potentials. PPTFSI-O-C and PPSS-O-C were nicely cycled in the range of 2.3-4.2 and 1.7-4.8 V vs Li^0/Li^+ respectively. Even if the shape of the voltammograms suggests a non-conducting state of PEDOT from 2.5 V vs Li^0/Li^+ to lower potentials, its potential use in high voltage cathode such as NMC is confirmed with such a wide stability window. Interestingly, in spite of presenting much higher electronic conductivity, the electrochemical response of PPSS-O is much resistive than PPTFSI-O, which can be attributed to a less favorable doping/dedoping

(oxidation/reduction) of PEDOT through less porous PPSS-O surface, compared to PPTFSI-O as can be seen from Figure 5.3c-d.

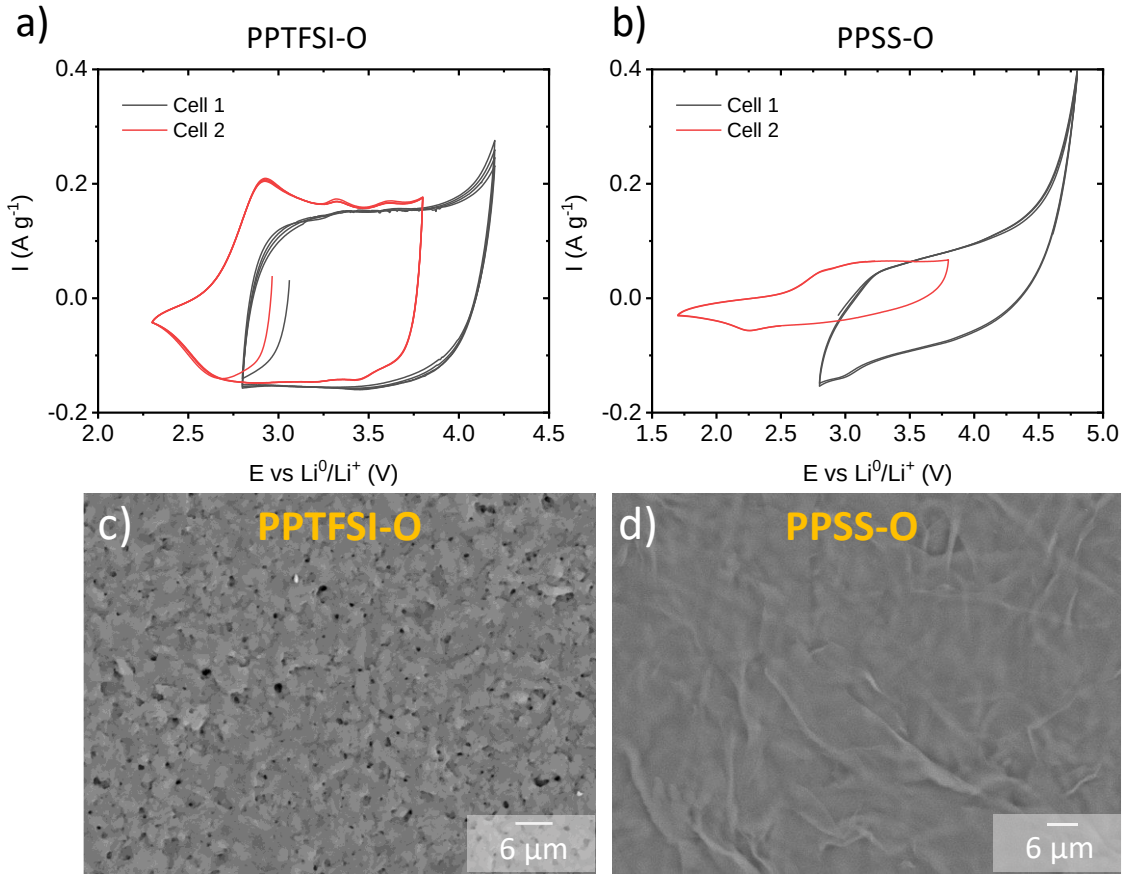

Figure 5.3. Electrochemical window of a) PPTFSI-O-C and b) PPSS-O-C measured in Li|1M LiTFSI DOL/DME (1/1 v/v)|MIEC composite without LFP at 10 mV s^{-1}. SEM pictures of c) PPSS-O and d) PPTFSI-O electrode surfaces.

To evaluate the role of the different binders on the redox reaction kinetics of LFP, Li||LFP cells were assembled and several cyclic voltammograms were recorded. Figure 5.4a-b shows the stabilized voltammograms for PPTFSI and PPSS-based LFP electrodes.

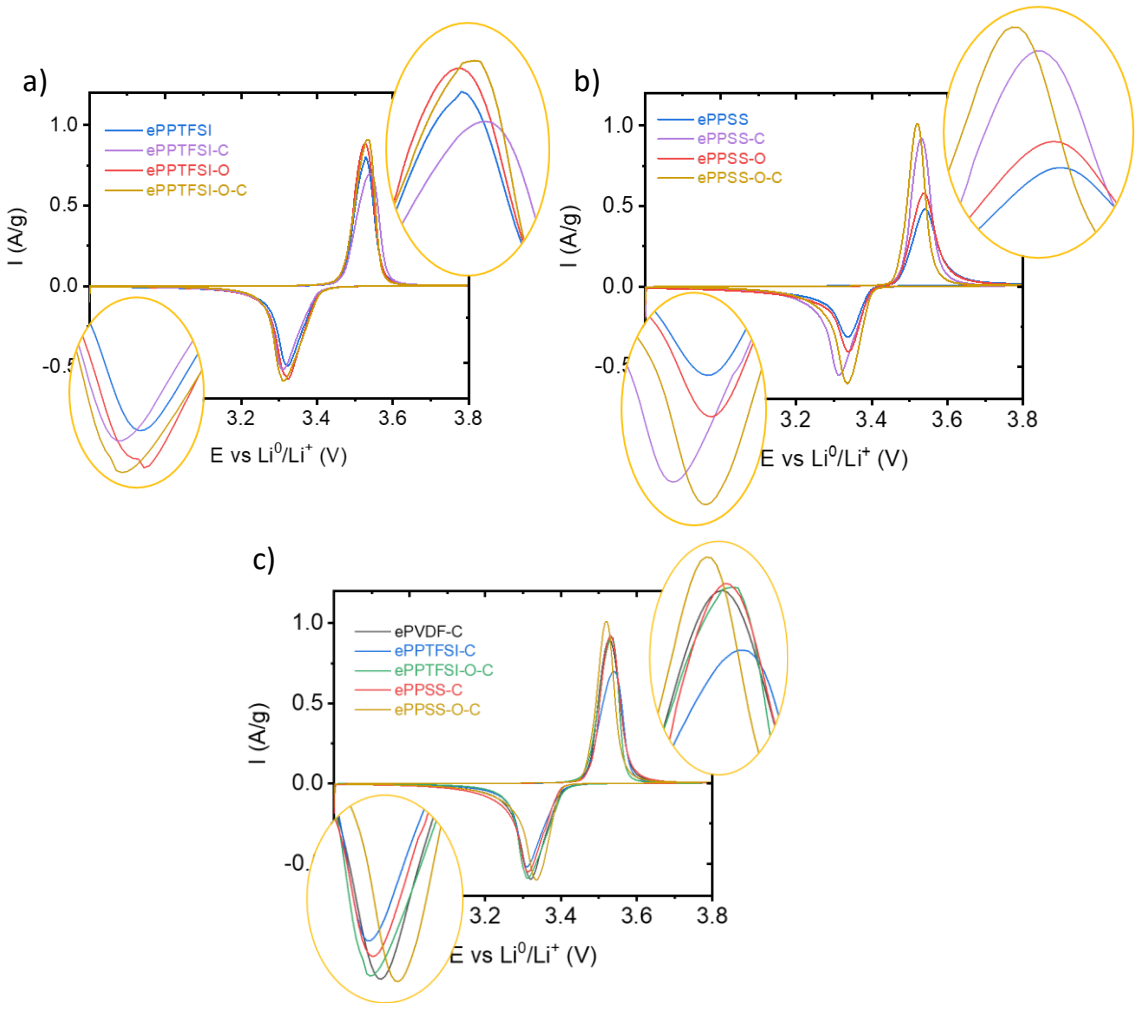

Figure 5.4. Cyclic voltammograms at 0.1mV s^{-1} of Li||LFP based cells using 1M LiTFSI DOL:DME (1:1 v/v) containing different additives: a) PPTFSI-, b) PPSS-based binders and c) comparison of cathodes containing MIEC polymers and C65, with standard PVDF-C cathode.

Generally, it can be seen from these graphs that OIPC incorporation promotes the redox reaction of LFP, obtaining sharper redox peaks and smaller potential differences (ΔE) between the oxidation and reduction peaks, suggesting an improvement in the kinetics and reversibility of the redox reactions, respectively. Interestingly, despite having a much lower electronic conductivity the ePPTFSI and ePPTFSI-O electrodes delivered much higher currents compared to ePPSS and ePPSS-O in agreement with the higher electrochemical response observed during electrochemical window evaluation, also probably as

a consequence of a more homogeneous coating forming as can be seen from SEM images in Figure 5.5. Upon addition of C65 to ePPTFSI (Figure 5.5b-c) or ePPTFSI-O (Figure 5.5d-e), more porous surfaces are formed in accordance with physisorption results. For the PPSS family, only ePPSS-O-C (Figure 5.5i) resulted in quite homogeneous coating, whereas ePPSS-C (Figure 5.5g), and specially ePPSS (Figure 5.5f) and ePPSS-O (Figure 5.5h), exhibit large plasticized areas leaving the bright LFP particle areas segregated, maybe as a consequence of the high ability of PPSS for film formation, but at the same time, difficult to disperse with low volume of solvent in the slurries preparation. In conclusion, in both families, eMIEC-O-C electrodes offer the highest currents in comparison with carbon and OIPC free versions, agreeing with the best scenario of electrolyte uptake, porosity and electronic conductivity experiments.

The carbon-based electrodes, which generally have shown the best intrinsic properties for composite electrodes, are depicted with ePVDF-C in Figure 5.4c. ePPSS-O-C electrode shows an outstanding performance, offering 1.01 A g^{-1} as oxidation current density and ΔE of 183 mV, which surpasses ePVDF-C (0.90 A g^{-1} and 208 mV) performance. The current intensities of ePPSS-C and ePPTFSI-O-C are slightly above ePVDF-C (0.92 and 0.91 A g^{-1}), but the ΔE are larger (217 and 224 mV respectively). Lastly, ePPTFSI-C remains as the worse scenario with values of 0.7 A g^{-1} and 233 mV, for current density and ΔE, respectively. Two conclusions are derived from these values: 1) the use of MIECs helps the current delivery, and 2) the presence of OIPC seems to diminish the ΔE enabling faster kinetics of redox reaction (also observed for the carbon-free formulations), which is key to improve the electrochemical performance of electrodes for LIBs.

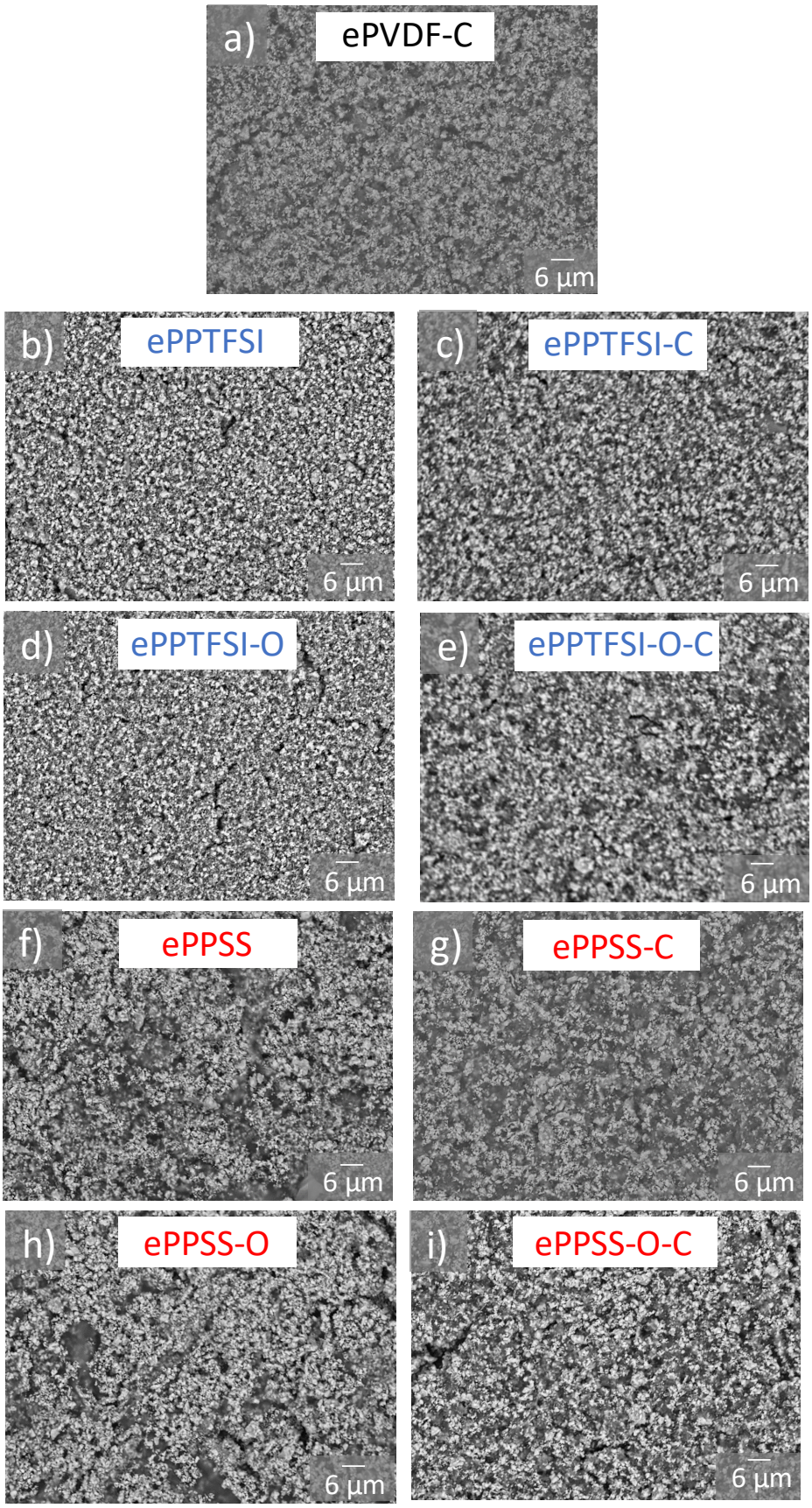

Figure 5.5. SEM images of LFP based electrodes containing distinct additives as labelled in the figure: a) PVDF-C, b) PPTFSI, c) PPTFSI-C, d) PPTFSI-O, e) PPTFSI-O-C, f) PPSS, g) PPSS-C, h) PPSS-O and i) PPSS-O-C.

5.6. Galvanostatic cycling

Fresh cells were galvanostatically cycled after 10h of OCV conditions, to guarantee the thermodynamic equilibrium of the cells, at different rates and subsequently long-term at 1C. From Figure 5.6a-b it can be seen the cycling of PPTFSI and PPSS families, where the best scenarios are offered by the formulations that contain carbon, even if carbon-free cathodes cycle relatively stable. For the family of PPTFSI, ePPTFSI-O shows a similar behavior as ePPTFSI-O-C until is cycled at high rates, where large overpotential is observed (Figure 5.6d); until finally fade after 400 cycles in the long term cycling at 1C. For the PPSS family, ePPSS and ePPSS-O remain quite low in capacity compared to the carbon based formulations in all the range of rates measured, in accordance to the cyclic voltammetries.

It is important to notice the large overpotentials exhibited by the less porous cathodes (ePPTFSI-O: 392, ePPSS: 294, ePPSS-O: 322 and ePPSS-C: 394 mV), which have an impact in lowering the capacities, but also to the detriment of the battery lifespan (Figure 5.6d,f). It is worth to mention the lowest overpotentials are obtained with the mixure of ePolymer-O-C (ePPTFSI-O-C: 226 and ePPSS-O-C: 244 mV). Zhong et al., have reported the best performances of LFP cathodes are given by the ratio acetylene black/PEDOT:PSS = 1:1 obtaining the lowest overpotentials and rate capabilities, in good agreement with the obtained results in this chapter.[19]

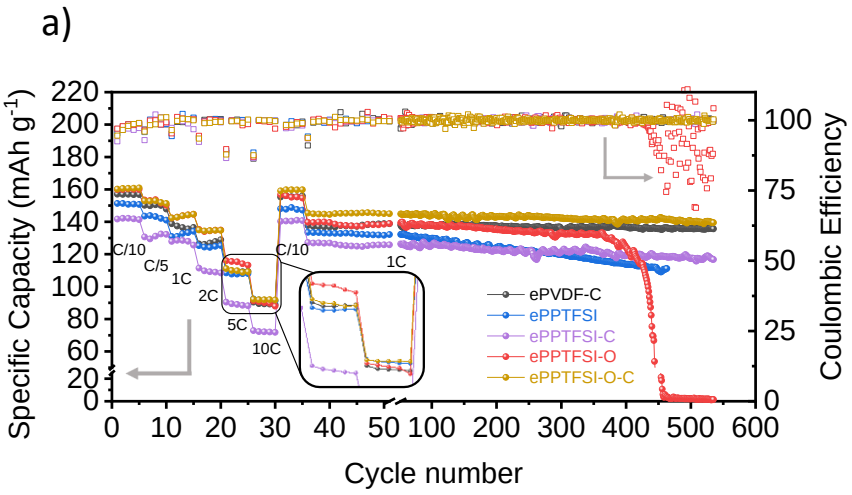
a)
Specific Capacity (mAh g-1)
Coulombic Efficiency
Cycle number
C/10
C/5
1C
2C
5C
10C
ePVDF-C
ePPTFSI
ePPTFSI-C
ePPTFSI-O
ePPTFSI-O-C

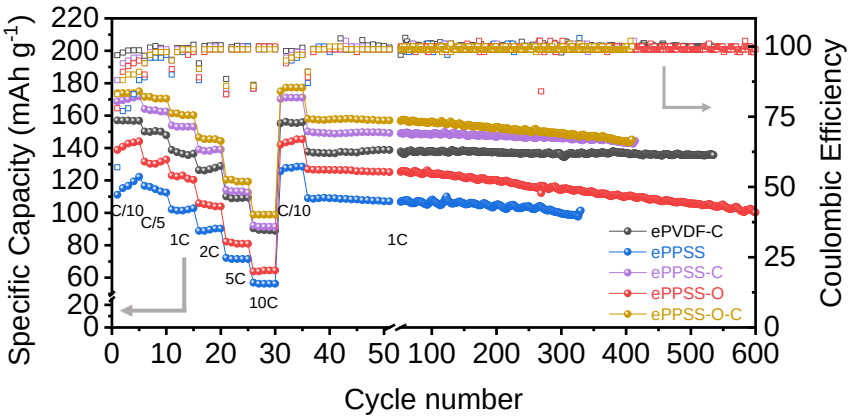
b)
Specific Capacity (mAh g-1)
Coulombic Efficiency
Cycle number
C/10
C/5
1C
2C
5C
10C
ePVDF-C
ePPSS
ePPSS-C
ePPSS-O
ePPSS-O-C

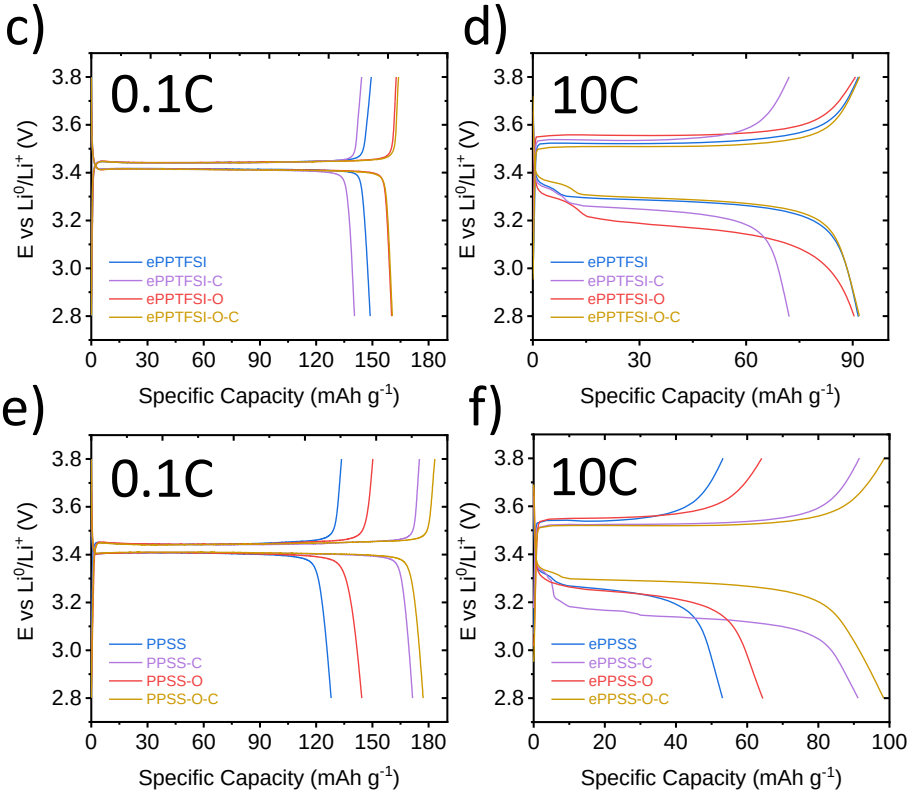
c)
0.1C
E vs Li0/Li+ (V)
Specific Capacity (mAh g-1)
ePPTFSI
ePPTFSI-C
ePPTFSI-O
ePPTFSI-O-C
d)
10C
e)
0.1C
PPSS
PPSS-C
PPSS-O
PPSS-O-C
f)
10C
ePPSS
ePPSS-C
ePPSS-O
ePPSS-O-C

Figure 5.6. Rate capability and long-term cycling of the different Li||LFP cells: a) PPTFSI- and b) PEDOT:PSS-based additives. Voltage profiles of (c-d) PPTFSI- and (e-f) PPSS-based cells at C/10 and 10C as it is shown in the figure legend.

The cyclings of carbon-based electrodes are depicted together with ePVDF-C in Figure 5.7a. At low C-rates of 0.1 C, ePPTFSI-O-C, ePPSS-C and ePPSS-O-C offer higher capacity values (159.8, 171.1 and 177.3 mAh g^{-1} respectively) in comparison with ePVDF-C (155.5 mAh g^{-1}). Surprasingly, ePPSS-C and particularly ePPSS-O-C exceed the theoretical capacity of LFP (170 mAh g^{-1}), probably due to the pseudocapacitive response of the highly conducting polymer PEDOT. However, when the C-rate is increasing, ePPSS-O-C is again very far from standard ePVDF-C (89.4 mAh g^{-1} at 10C and an overpotential of 371 mV) offering 98.9 mAh g^{-1}. ePPTFSI-O-C and ePPSS-C are still slightly above ePVDF-C (91.9 and 91.4 mAh g^{-1}). Interestingly, even if ePPSS-C offers much higher capacities than ePPTFSI-O-C at low C-rates as a consequence of the higher electronic conductivity, ePPTFSI-O-C performs better at higher C-rates, more notably when looking at the voltage regions in the charge profiles. At low C-rate (0.1C), the observed overpotentials are low and indistinguishable (see Figure 5.7b). Nonetheless, at 10C Figure 5.7c reflects a similar shape for ePPSS-O-C and ePPTFSI-O-C with very low polarization, as discussed below, but longer slope for ePPSS-O-C (blue shaded area), which is attributed to a higher pseudo capacitive response of PEDOT according to the higher electronic conductivity, once the porosity is high enough to permit the smooth entrance of ions. These results show the benefits of using mixed conductors, obtaining capacity values close to the theoretical but also improved performance at high current densities taking advantage of their ionic-electronic conducting properties.

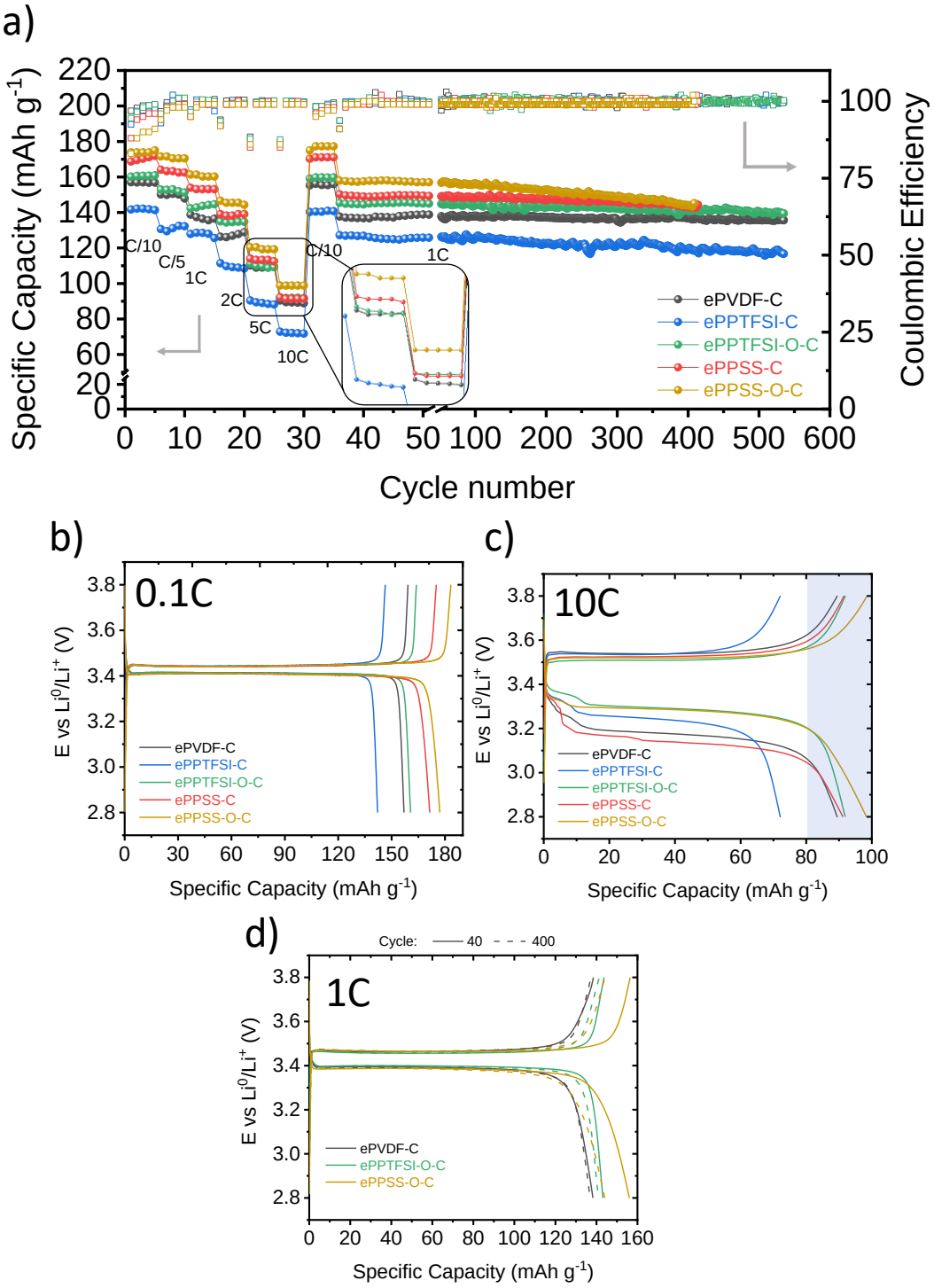

Figure 5.7. a) Rate capability and long-term cycling of Binder-C-based cathodes in Li||LFP cells as shown in figure legend. Voltage profiles of carbon-based electrodes at b) C/10 and c) 10C. d) Voltage profiles at 1C of cycle number 40 (continuous lines) and 400 (dashed lines).

Finally, in the long-term cycling at 1C after 400 cycles, ePPSS-O-C and ePPSS-C deliver the highest capacities (144.1 and 143.3 mAh g^{-1}, respectively) followed by ePPTFSI-O-C (140.9 mAh g^{-1}) and e-PVDF-C (136.8 mAh g^{-1}). However, the capacity of ePPSS-O-C and ePPSS-C is dropping leaving capacity retentions of 91 and 95 %, respectively, whereas ePPTFSI and ePVDF-C remain stable offering 97 and 99 % of capacity retention. The reason of the different capacity retentions between PPSS and PPTFSI could be addressed in the stability of the polyelectrolyte. It has been already reported a very stable cycling of PDADMA-TFSI binder-based electrode in Chapter 4, in agreement with the results obtained with ePPTFSI. Figure 5.7d shows the voltage profiles of ePVDF-C, ePPTFSI-O-C and ePPSS-O-C in cycle number 50 and 400. Even if ePPSS-O-C exhibits a higher capacity in cycle number 40, after 400 cycles there is a significant shift to lower capacity being very close to the ePPTFSI-O-C electrode. In contrast, ePVDF-C and ePPTFSI-O-C present very similar profiles given by the high capacity retention. This fact highlight the importance of the selected polyelectrolyte surrounding the conducting polymer to form the mixed conductor in the long term performance.

Moreover, to avoid the use of toxic NMP solvent PPSS family has already shown a good performance when it is used processed with DMSO. However, PPTFSI has been processed still with NMP. Therefore, taking advantage of the processability of PPTFSI in acetonitrile, same formulation of ePPTFSI-O-C was prepared using acetonitrile obtaining similar performance (Figure 5.8) obtaining similar performance with similar loading (2.0 ± 0.2 mg_{LFP} cm^{-2}).

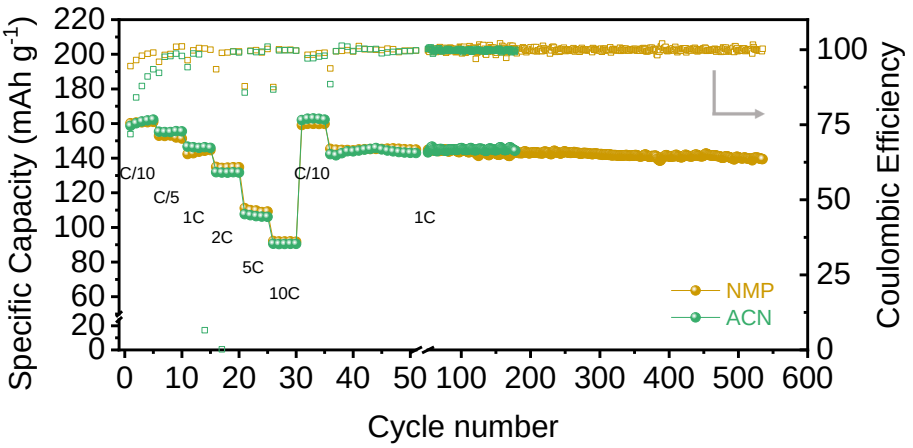

Figure 5.8. Cycling performance of ePPTFSI cathode processed with different solvents (2.0 ± 0.2 mg_{LFP} cm^{-2}).

5.7. Electrochemical Impedance Spectroscopy

To further understand the differences between the additives, EIS at a state of charge=50% (at 0.1C) when discharging was performed for fresh cells after several cycles of stabilization. The used equivalent circuit (see Figure 5.9a) was proposed by similar previous works to fit the data because of its proven accuracy in LFP-based cells.[20] In the Nyquist plots performed in this chapter (Figure 5.9b), the solution electrolyte resistance remained relatively constant in all the cases R_s≈3-4 Ω. Subsequently, at high frequencies can be found a depressed semicircle that corresponds mostly to the interfacial charge transfer resistance (R_{ct}), in parallel with the double layer capacitance (C_{dl}), together with a small contribution of the contact between particles resistance (R_c) and respective capacitance (C_c).

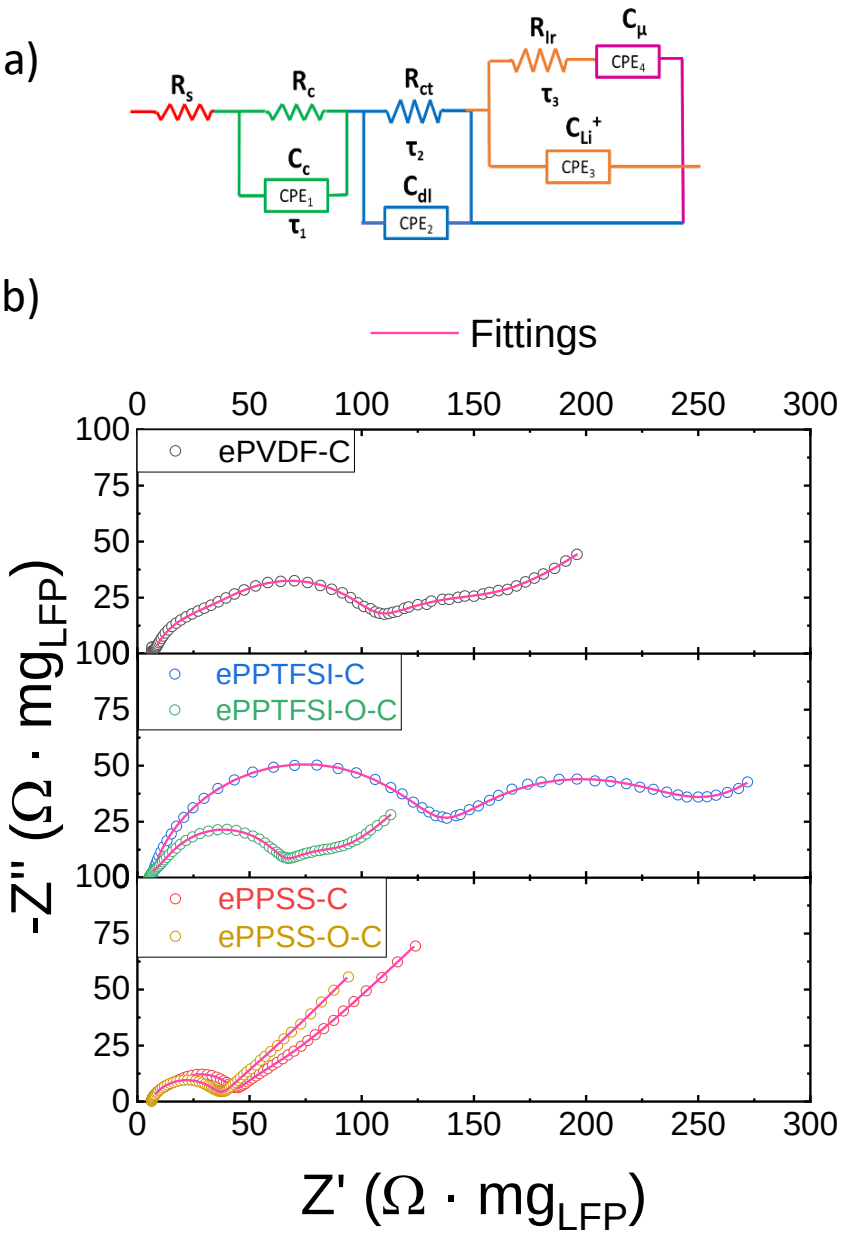

Figure 5.9. a) Proposed equivalent circuit and b) EIS spectra of Li||LFP cells with different binders at SOC=50 %. Pink Lines correspond to the obtained fitting

At intermediate frequencies we observe the resistance related to the lithiation process of the active material (R_{lr}) and its associated lithiation capacitance (C_{Li^+}), which is related to the amount of Li^+ out of the active material particle (in this case LFP). Finally, at very low frequencies a capacitive shape appears as a consequence of Li^+ intercalation in the phosphate matrix quantified by its chemical capacitance (C_μ). This parameter counts the ease for Li^+ to reach

the active material. Table 5.4 summarizes the extracted parameters from the EIS fitting.

Table 5.4. Extracted fitting data from Nyquist plots of Li||LFP cells using different binders at SOC=50%. The units of resistances (R) are $\Omega \cdot mg_{LFP}$ and capacitances (C) are $F\ g_{LFP}^{-1}$.

Electrode	R_c	C_c	R_{ct}	C_{dl}	R_{lr}	C_{Li^+}	C_μ
ePVDF-C	28.30	1.20×10^{-3}	72.89	6.20×10^{-3}	49.31	0.70	17.6
ePPTFSI-C	16.57	6.40×10^{-3}	114.20	2.90×10^{-3}	113.80	0.45	79.4
ePPTFSI-O-C	5.03	1.23×10^{-3}	56.08	3.58×10^{-3}	25.60	1.20	27.4
ePPSS-C	9.14	1.28×10^{-3}	29.04	5.16×10^{-3}	18.48	0.83	2.1
ePPSS-O-C	4.20	1.61×10^{-4}	21.41	3.33×10^{-3}	16.45	0.70	0.9

In the range of high frequencies, it can be observed a remarkable contact resistance in ePVDF (28.3 ± 1.2 $\Omega \cdot \mathrm{mg_{LFP}}$) in good agreement with the highest porosity obtained among the different cathodes, followed by ePPTFSI-C (16.6 ± 8.8 $\Omega \cdot \mathrm{mg_{LFP}}$). It is interesting to notice the plasticizing effect of the OIPC lowering this resistance (5.0 ± 0.3 $\Omega \cdot \mathrm{mg_{LFP}}$), similarly as what occurs for ePPSS-C, passing from 9.1 ± 0.3 $\Omega \cdot \mathrm{mg_{LFP}}$ to 4.2 ± 0.5 $\Omega \cdot \mathrm{mg_{LFP}}$ for ePPSS-O-C. In terms of R_{ct}, ePPTFSI-C, ePVDF-C and ePPTFSI-O-C showed the highest resistances (114.2 ± 25.7, 72.9 ± 2.8 and 56.1 ± 0.4 $\Omega \cdot \mathrm{mg_{LFP}}$ respectively) in comparison with ePPSS-C and ePPSS-O-C (29.0 ± 0.5 and 21.4 ± 6.2 $\Omega \cdot \mathrm{mg_{LFP}}$) coinciding with the superior electrolyte uptake observed. Finally, in the low-frequency region, PPTFSI-C presents the highest R_{lr} 113.8 ± 5.4 $\Omega \cdot \mathrm{mg_{LFP}}$). Interestingly, the OIPC leads to a decrease in this resistance up to 25.6 ± 1.3 $\Omega \cdot \mathrm{mg_{LFP}}$. ePVDF-C remains in an intermediate state with 49.3 ± 5.8 $\Omega \cdot \mathrm{mg_{LFP}}$of R_{lr}. Finally, the PPSS system offers the lowest lithiation resistance (18.5 ± 3.4 $\Omega \cdot \mathrm{mg_{LFP}}$ for ePPSS-C), observing again positive impact of OIPC by decreasing this parameter (16.5 ± 3.7 $\Omega \cdot \mathrm{mg_{LFP}}$ for ePPSS-O-C).

5.8. Conclusions

In summary, we demonstrated a promising impact of OMIECs composed of OIPCs (C_2mpyrTFSI) and conducting polymers as binders on lithium-ion batteries. Two different conducting polymers were used (PEDOT:PSS and PEDOT:PolyDADMA TFSI) with very different electronic conductivities (reaching 580 S cm^{-1} and 5 S cm^{-1} respectively), which are higher than the PVDF-Carbon composite (1.5 S cm^{-1}). Furthermore, the addition of conducting carbon not only modified the electronic conductivity, but also brought porosity to the electrodes, which is key to avoid impeded diffusion of ions into the electrode. This effect was observed in electrolyte uptake experiments, with significantly lower uptakes for carbon-free electrodes; and cyclic voltammetry, where higher and sharper redox peaks were observed for the most porous electrodes. Despite the large difference in electronic conductivity between the two families of OMIECs, they both delivered much higher capacities (i.e. 177.3 and 159.8 mAh g^{-1} for ePPSS-O-C and ePPTFSI-O-C respectively at C/10) than conventional formulation based on PVDF-C (155.5 mAh g^{-1}) in all the range of current densities measured due to the more intimate contact between redox-active particles and conducting agent. It is worth noting that in some of the OMIEC-based electrodes the theoretical capacity of LFP was exceeded due to the pseudocapacitive contribution of PEDOT. Moreover, the PDADMA-TFSI family presented really stable cycling over time (97 % of capacity retention for ePPTFSI-O-C after 400 cycles at 1C) in contrast to the widely used PEDOT:PSS (95 % of capacity retention under same conditions). Finally, EIS experiments revealed lower contact, charge transference and lithiation resistances for OMIEC-based electrodes than for PVDF-based ones. OIPC incorporation consistently led to enhanced specific capacities and capacity

retention in good agreement with EIS measurements. Finally, it is worth to mention that the MIEC binders proposed can be processed using less toxic solvents than NMP, which is used for PVDF based electrodes (PPSS in DMSO and PPTFSI in acetonitrile), opening the door to a more sustainable battery manufacturing processes.

5.9. Experimental part

5.9.1. Materials

PVDF Solef® 5130 (1,000-1,100 kg mol-1) was used as a reference binder. Poly(3,4-ethylenedioxythiophene):poly(styrene sulfonate) (Clevios PH 1000), 1.3 wt.% solids in water, was supplied by Heraeus Inc. N-ethyl-N-methylpyrrolidinium bis(trifluoromethylsulfonylimide) (C_2mpyrTFSI) (99%) was purchased from IoLiTec. PEDOT:PolyDADMA TFSI was obtained as in detailed in Chapter 3. N-methyl-2-pyrrolidinone (NMP, 99%, Sigma-Aldrich), anhydrous 1,3-dioxolane (99.8%, Sigma-Aldrich), anhydrous dimethoxy ethane (99.5%, Sigma-Aldrich), lithium bis(trifluoromethanesulfonyl)imide (LiTFSI, 99%, Iolitec), conductive carbon (Super C65, Timcal), lithium iron phosphate ($LiFePO_4$, Aleees) were used without further treatment.

5.9.2. Electronic conductivity

Slurries with no active material were prepared similarly to the detailed description in Section 5.2. After casting onto PET isolating substrates and subsequently drying for 24 h at 60 ºC under high vacuum, Four-Point Probe

technique was employed to measure the electronic conductivity values of additives utilized in each cathode formulation.

5.9.3. Electrode preparation

The slurries were prepared by dissolving first the binder in NMP or DMSO in a small beaker and subsequently C65 and LFP were added. Afterwards, the viscous slurry was coated onto carbon coated aluminum foil (current collector) with the aid of an automatic doctor blade (NEURTEK Instruments) and it was left drying at room temperature for 12 h. Finally, disks of 11 mm diameter were punched and further dried at 60ºC under vacuum for 24h prior characterization.

5.9.4. Porosity characterization

LFP-based slurries were prepared as detailed in SI and subsequently dried at 60 ºC for several days. The porosity of collected powder was characterized by nitrogen physisorption at 77 K using a Micromeritics ASAP 2020. All samples were degassed at 25 °C at a pressure of 10 mmHg for 100 h, and helium was applied as backfilling gas between the degassing and analysis step. The total surface area was determined according to the multipoint Brunauer−Emmert−Teller (BET) method in the range $0.1 \leq p/p0 \leq 0.25$, and the total pore volume of the samples was determined at a relative pressure (p/p0) of ~0.985). Moreover, t-plot method was used for estimating the micropore volume. Finally, the pore size distribution (PSD) was calculated using the method proposed by Barrett–Joyner–Halenda (BJH method).

5.9.5. Electrolyte uptake

Pristine electrodes (11 mm diameter) were soaked separately in fresh electrolyte (0.5 mL) for 48 h in closed vials independently and subsequently weighted. Noteworthy, 48 h was considered to ensure a thermodynamic equilibrium of the system in terms of electrolyte saturation and chemical equilibrium of the ionic species.

5.9.6. Cell Assembly

Cathode disks (11 mm diameter) of LFP with an active material loading between 1.1-3.4 mg_{LFP} cm^{-2} were prepared according to Section 5.9.2. Li||LFP cells were assembled in CR2032 coin cells inside Ar glovebox, by firstly cleaning Li ribbons with cyclohexane and a nylon brush prior punching 12 mm disks and using 120 µL of 1M LiTFSI DOL:DME (1:1 v/v) as electrolyte, to maintain the same mobile anion used in the cathode, in glass microfiber separators. For cycling batteries, Neware battery cycler was used whereas VMP-3 potentiostat (Biologic) was used to carry out further electrochemical characterization.

5.9.7. Electrochemical measurements

Cyclic voltammetry was used in the range of 2.8-3.8V at 0.1 mV s^{-1} for 6 cycles to obtain stabilized voltammograms since broad peaks were observed in the first cycle. Electrochemical impedance spectroscopy (EIS) was employed to determine processes resistances and capacitances involved in Li||LFP cells with a perturbation of 10 mV and a frequency range from 1MHz-0.1Hz. Afterward, data

were fitted in frequency, Z and -Z'' by using Zview software obtaining Chi-Squared values below 1×10^{-4}.

5.10. References

1. T. Placke, R. Kloepsch, S. Dühnen and M. Winter. Lithium ion, lithium metal, and alternative rechargeable battery technologies: the odyssey for high energy density. *J. Solid State Electrochem.* **2017**;21:1939–1964.

2. I. O. Santos-Mendoza, J. Vázquez-Arenas, I. González, G. Ramos-Sánchez and C. O. Castillo-Araiza. Revisiting Electrochemical Techniques to Characterize the Solid-State Diffusion Mechanism in Lithium-Ion Batteries. *Int. J. Chem. React. Eng.* **2019**.

3. G. Guzmán, J. Vazquez-Arenas, G. Ramos-Sánchez, M. Bautista-Ramírez and I. González. Improved performance of LiFePO4 cathode for Li-ion batteries through percolation studies. *Electrochim. Acta* **2017**;247:451–459.

4. A. Eftekhari. LiFePO4/C nanocomposites for lithium-ion batteries. *J. Power Sources* **2017**;343:395–411.

5. P. Sengodu and A. D. Deshmukh. Conducting polymers and their inorganic composites for advanced Li-ion batteries: A review. *RSC Adv.* **2015**;5:42109–42130.

6. V. A. Nguyen and C. Kuss. Review — Conducting Polymer-Based Binders for Lithium-Ion Batteries and Beyond. *J. Electrochem. Soc.* **2020**;167:065501.

7. P. R. Das and J. E. Soc. PEDOT:PSS as a Functional Binder for Cathodes in Lithium Ion Batteries. *J. Electrochem. Soc.* **2015**;162:A674–A678.

8. L. Zhan, Z. Song, J. Zhang, J. Tang, H. Zhan, Y. Zhou and C. Zhan. PEDOT : Cathode active material with high specific capacity in novel electrolyte system. *Electrochim. Acta* **2008**;53:8319–8323.

9. J. Xu, S. L. Chou, Q. F. Gu, H. K. Liu and S. X. Dou. The effect of different binders on electrochemical properties of LiNi 1/3Mn1/3Co1/3O2 cathode material in lithium ion batteries. *J. Power Sources* **2013**;225:172–178.

10. G. Guzmán-González, G. Ramos-Sánchez, L. E. Camacho-Forero and I. González. Charge Delocalization on BO 4- Centers to Improve Conductivity on Single Lithium Ion Conducting Polymer Electrolytes: A Computational/Experimental Approach. *J. Phys. Chem. C* **2019**;123:17686–17694.

11. J. S. Lee, K. Sakaushi, M. Antonietti and J. Yuan. Poly(ionic liquid) binders as Li+ conducting mediators for enhanced electrochemical performance. *RSC Adv.* **2015**;5:85517–85522.

12. X. Wang, H. Zhu, G. W. Greene, Y. Zhou, M. Yoshizawa-fujita, Y. Miyachi,

M. Armand, M. Forsyth, J. M. Pringle and P. C. Howlett. Organic Ionic Plastic Crystal-Based Composite Electrolyte with Surface Enhanced Ion Transport and Its Use in All- Solid-State Lithium Batteries. *Adv. Mater. Technol.* **2017**;2:1700046.

13. S. Malunavar, X. Wang, F. Makhlooghiazad, M. Armand, M. Galceran, P. C. Howlett and M. Forsyth. Highly conductive ionogel electrolytes based on N-ethyl-N-methylpyrrolidinium bis(fluorosulfonyl)imide FSI and NaFSI mixtures and their applications in sodium batteries. *JPhys Mater.* **2021**.

14. H. Ueda, F. Mizuno, R. Kerr, M. Forsyth and P. C. Howlett. Fast Charge and High Stability of Solid-state Graphite Organic Ionic Plastic Crystal Composite Anodes. *Batter. Supercaps* **2022**.

15. F. Nti, G. W. Greene, H. Zhu, P. C. Howlett, M. Forsyth and X. Wang. Anion effects on the properties of OIPC/PVDF composites. *Mater. Adv.* **2021**;2:1683–1694.

16. A. Vu, Y. Qian and A. Stein. Porous electrode materials for lithium-ion batteries-how to prepare them and what makes them special. *Adv. Energy Mater.* **2012**;2:1056–1085.

17. M. J. Lacey, F. Jeschull, K. Edström and D. Brandell. Porosity Blocking in Highly Porous Carbon Black by PVdF Binder and Its Implications for the Li-S System. *J. Phys. Chem. C* **2014**;118:25890–25898.

18. S. Xun, X. Song, V. Battaglia and G. Liu. Conductive Polymer Binder-Enabled Cycling of Pure Tin Nanoparticle Composite Anode Electrodes for a Lithium-Ion Battery. *J. Electrochem. Soc.* **2013**;160:A849–A855.

19. H. Zhong, A. He, J. Lu, M. Sun, J. He and L. Zhang. Carboxymethyl chitosan/conducting polymer as water-soluble composite binder for LiFePO4 cathode in lithium ion batteries. *J. Power Sources* **2016**;336:107–114.

20. N. Vicente, M. Haro, D. Cíntora-Juárez, C. Pérez-Vicente, J. L. Tirado, S. Ahmad and G. Garcia-Belmonte. LiFePO4 particle conductive composite strategies for improving cathode rate capability. *Electrochim. Acta* **2015**;163:323–329.

Chapter 6. Conclusions

In this Ph.D. thesis, we developed innovative Organic Mixed Ionic-Electronic Conductors (OMIECs) based on conducting polymers and Organic Ionic Plastic Crystals (OIPCs) for the area of electrochemical energy storage systems. Overall, we demonstrated the doping effect of OIPCs on conducting polymers improving both the electronic and ionic conductivities, which influenced the electrochemical performance of OMIEC composites.

In the first part of this thesis, a novel strategy to prepare all-solid-state mixed conductors based on PEDOT:PSS and OIPCs was presented. Both ionic and electronic conductivities were evaluated for two different OIPCs (C_2mpyrFSI and C_2mpyrTFSI), as well as their nanostructure. The observed results reflects the importance of having the OIPC amorphous by interaction with PEDOT:PSS, while ordered PEDOT chains, for optimum charge transport in a synergistic manner. Taking advantage of the particular properties of these materials, PEDOT:PSS-C_2mpyrFSI was employed in the first carbon-free solid-state battery (in presence of a certain amount of LiFSI) as unique additive for LFP active material replacing conventional formulation based on C65+catholyte. The exhibited performance of OMIEC-based cell reveals a much higher specific capacity than conventional formulation, as well as more stable cycling in long term.

In the second part of the thesis, new PEDOT-based OMIECs were developed by using $PDADMA^+$ as stabilizer in replacement of PSS. Several anions were evaluated (FSI, TFSI, tosylate, triflate) in terms of electronic-ionic conductivity and thermal properties. Subsequently, the effect of OIPC

incorporation (maintaining C_2mpyr^+ as cation and the homologue anions) on charge transport was investigated as well as their impact on the electrochemical response of PEDOT. The exhibited PEDOT pseudocapacity resulted notably higher when it was accompanied by OIPC than pristine, in good agreement with the measured conductivities.

In the third part of this work, the implications of using different kinds of poly(ionic liquid)s as binders, having ($TFSI^-$) and cationic (Li^+) counter-ions; are evaluated against conventional PVDF in Li||LFP cells. This strategy permits to elucidate the role of each mobile ion ($TFSI^-$ and Li^+) in the electrochemical performance of lithium batteries when they are present in the electrode formulation. Potentiostatic and galvanostatic analysis showed significantly improved performances for ionic binder-based cells, especially PMTFSI-Li, in comparison with PVDF, resulting also in higher rate capabilities and longer battery lifespan. EIS analysis and post-mortem analysis revealed the differences between the different binder-based cells, such as a clear mitigation of mossy lithium growth when using poly(ionic liquid) binders. Afterward, the promising PMTFSI-Li binder was successfully optimized with the objective of increasing the areal capacity.

In the last work, the materials developed in the first two experimental parts: PEDOT:PSS and PEDOT:PDADMA-TFSI were evaluated in Li||LFP cells. The addition of OIPC (C_2mpyrTFSI) and C65 in the formulation were evaluated in terms of electronic conductivity, porosity and electrolyte uptake which revealed a clear impact on the electrochemical performance. The best scenarios were found for the materials that contain mixed conductor, OIPC and carbon, where even if PEDOT:PSS-OIPC-C delivered higher capacities, PEDOT:PDADMATFSI-OIPC-

C exhibited a more stably cycling. This fact highlights the importance of the ionic polymer that stabilizes PEDOT for a high energy and power density, but also for the long-term cycling.

In order to have a comparison between the materials developed in this thesis and the reported in the literature in terms of charge transport, the obtained conductivity values for PEDOT:PSS-OIPC (Chapter 2) and PEDOT:PolyDADMA X-OIPC (Chapter 3) are depicted in Figure 6.1. In this thesis PEDOT:PSS in combination with either C_2mpyrFSI or C_2mpyrTFSI showed the highest values for electronic (~ 580 S cm^{-1}) and ionic conductivities (3.7 × 10^{-5} S cm^{-1} at 70 ºC), but they are also among the highest values reported so far as can be seen in Figure 6.1. Moreover, PEDOT:PolyDADMA-X/OIPC materials reached values of 0.73 S cm^{-1} for electronic and 3 × 10^{-5} S cm^{-1} for ionic conductivities respectively, staying in the middle of the area of conductive polymers (Figure 6.1).

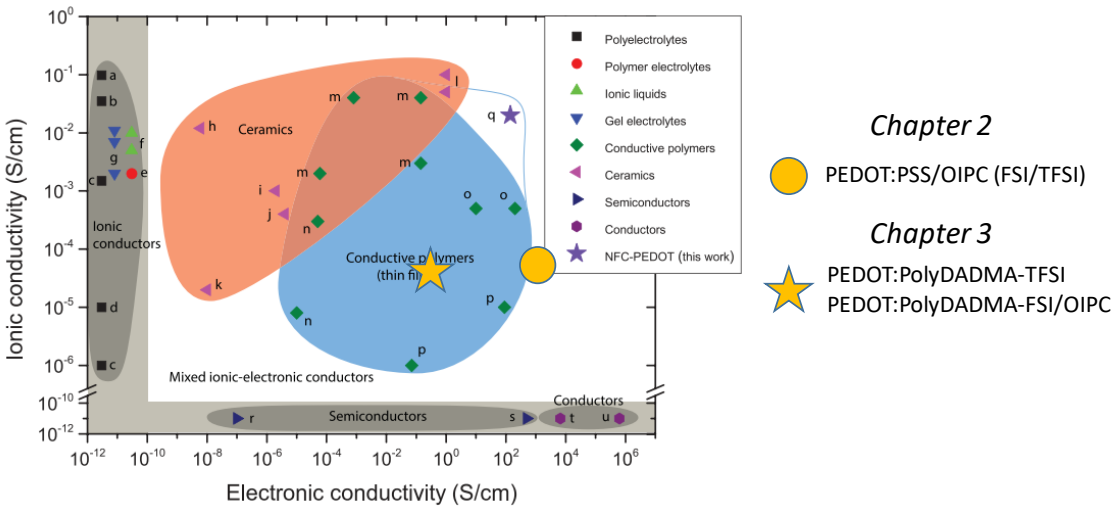

Figure 6.1. Electronic and ionic conductivity values of the materials developed in this work in comparison with the reported values in literature.

The performance of the batteries with liquid electrolyte assembled in this thesis are also compared in the Ragone plot of Figure 6.2a. As result, the highest

energy and power densities follow the trend PPTFSI-O-C < PMTFSI-Li < PPSS-O-C, surpassing all the values obtained with conventional PVDF. Figure 6.2b collects these results and evaluate some other features such as the capacity retention after >400 cycles (PPSS-O-C, 91 % < PMTFSI-Li, 96% < PPTFSI-O-C, 97 % < PVDF, 99 %). Moreover, the processing of the slurries was also evaluated considering PMTFSI-Li and PPTFSI-O-C are instantaneously dissolved by the solvent (NMP, H_2O or acetonitrile), whereas usually PVDF takes longer and in the other extreme PPSS-O-C needs more than a week to be completely dissolved before casting. Finally, sustainability was also considered as key parameter since PMTFSI-Li is water soluble, and therefore potentially enabling a greener processing and recyclability. PPTFSI-O-C and PPSS-O-C are not soluble in water but they can still avoid the use of toxic NMP, by using acetonitrile or DMSO respectively.

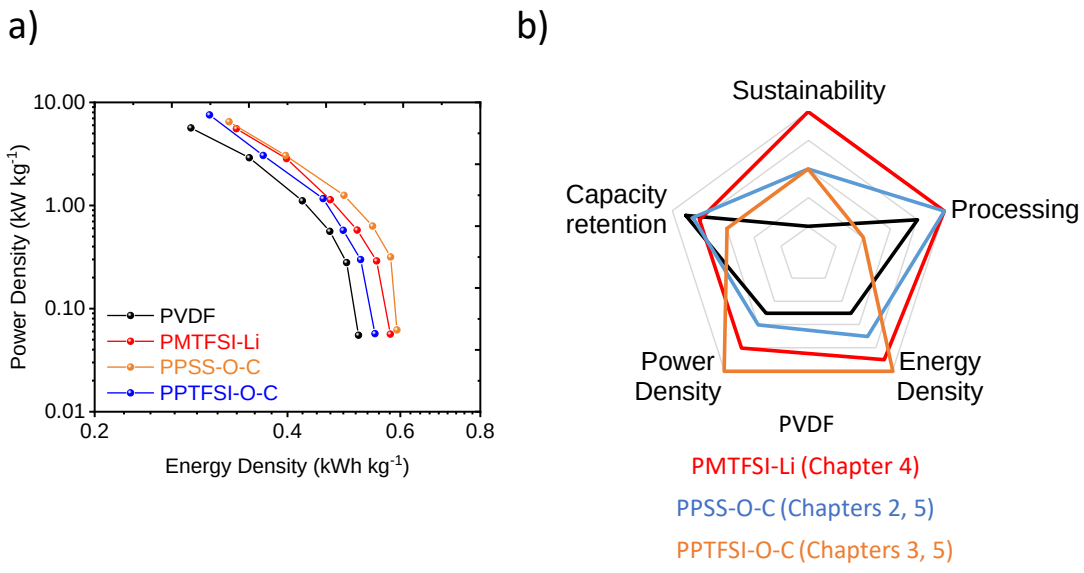

Figure 6.2. a) Ragone plot of the best additives developed in this thesis in comparison with conventional PVDF under the same mass loadings. The values are calculated considering only the mass of the active material, time of discharge and voltage in the discharge plateau. b) Radar chart of different features for different cathode additives.

As overall conclusion, the proposed materials exhibited ionic and electronic transport properties that enabled high-performance batteries for high energy and power density. The comparison has shown the crucial importance of the ionic polymer that accompanies the conducting polymer PEDOT, affecting the conductivities and more importantly the cell performance. On the other hand, PMTFSI-Li have exhibited a very interesting compromise between cell performance, processing and sustainability, which results in a promising candidate for binder applications and for future OMIEC materials development.

Resumen

La sostenibilidad energética y medioambiental son a día de hoy dos de los mayores retos de nuestra sociedad, recogidos en la agenda 2030. Por ello, en las últimas décadas se ha intensificado el desarrollo y optimización de baterías recargables para reemplazar el uso de combustibles fósiles en el sector automotor y, por ende, sus problemas asociados con la contaminación. También es necesario satisfacer nuestras necesidades como sociedad en el uso de dispositivos móviles, cada vez con mayores energías de consumo; y en estaciones de almacenamiento de energía. El objetivo de los avances en este sector pasa por dispositivos con mayores energías y potencias, pero también más seguros y ligeros.

En este sentido, materiales capaces de transportar carga a través de iones y electrones se postulan como candidatos ideales para implementarlos en dispositivos de almacenamiento de energía. Idealmente, deben de ser fácilmente procesables, con altas conductividades (de electrones e iones), ligeros y con buenas propiedades electroquímicas (respuestas reversibles). Este tipo de materiales se han empleado tanto como aglutinantes funcionalizados como directamente electrodos. En este campo de materiales, se distinguen los orgánicos e inorgánicos, destacando estos primeros por sus altas conductividades electrónicas, procesado y potencial funcionalización. Los materiales orgánicos de conductividad mixta (electrónica e iónica), generalmente se basan en polímeros conductores dopados con materiales de alta conductividad iónica. Específicamente, poli(etilendioxitiofeno) (PEDOT) es uno de los más utilizados debido a su alta conductividad electrónica y estabilidad. Por

ello, en esta tesis se desarrollaron nuevos materiales basados en PEDOT para el área de almacenamiento de energía electroquímica.

Además, en las últimas décadas los cristales plásticos orgánicos iónicos (*Organic Ionic Plastic Crystals,* OIPCs) han destacado como materiales conductores iónicos para electrolitos en este tipo de dispositivos. Estas sales se consideran la versión en estado sólido de los líquidos iónicos, evitando los posibles problemas asociados a la fuga de líquidos pero presentando aún altas conductividades iónicas, alta estabilidad electroquímica y procesabilidad.

En la primera parte de esta tesis, se han desarrollado y caracterizado nuevos materiales de conductividad mixta combinando el polímero comercial PEDOT:PSS (Clevios PH1000) con dos OIPCs diferentes basados en un derivado del catión pirrolidinio (N-etil-N-metilpirrolidinio) y aniones fluorados (bis(fluorosulfonil)imida y bis(trifluorometilosulfonil)imida): C_2mpyrFSI y C_2mpyrTFSI. Como resultado, se obtuvieron materiales de altas conductividades, lo que resulta de especial interés particularmente como aglutinante para baterías de litio metal en estado sólido. En presencia de sal de litio, los materiales se emplearon como aglutinantes de cátodo (con $LiFePO_4$), libre de carbón conductor por primera vez en estado sólido; y utilizando un polímero dibloque ya optimizado y reportado como electrolito. Este proyecto demostró las ventajas de usar este tipo de materiales para baterías de estado sólido gracias a su adecuada conductividad iónica, alta conductividad electrónica y reducida porosidad (al no tener carbón), conllevando a mayores energías volumétricas. Además, mostró que un rendimiento deficiente de una batería con formulación catódica convencional, basada en la adición de electrolito en el cátodo (catolito), no necesariamente implica un electrolito deficiente. La

formulación del electrodo puede ser optimizada para, con el mismo electrolito, obtener dispositivos de alto rendimiento.

En la segunda parte de la tesis, se han desarrollado y caracterizado novedosos materiales de conductividad mixta mediante la polimerización oxidativa de EDOT en presencia PDADMAs (poli(dialildimetilamina)) con diferentes aniones: FSI, TFSI, tosilato y triflato, formando mezclas PEDOT:PDADMA X (donde X son los distintos aniones). La familia de materiales basados en PDADMA han sido ampliamente utilizados como electrolitos en diversos tipos de baterías ofreciendo altos rendimientos. Los materiales se han caracterizado en térmicamente y electroquímicamente tanto puros (PEDOT:PDADMA X) como en presencia de un 20 % en peso de los OIPCs homólogos (C_2mpyr X). Estos OIPCs fueron también caracterizados previamente de manera similar. Los resultados demostraron una mayor respuesta electroquímica por parte de los composites que contenían OIPCs en consonancia con las conductividades medidas.

En la tercera parte de la tesis, dos polielectrolitos (PDADMA-TFSI y PMTFSI-Li) fueron seleccionados como aglutinantes catódicos funcionalizados para celdas Li||$LiFePO_4$ para evaluar el rol de las distintas especies móviles ($TFSI^-$ y Li^+ respectivamente) en el cátodo, en comparación con PVDF convencional. Para valorar las diferencias entre los tres tipos de aglutinantes, 1M LiTFSI DOL/DME (1:1 v/v) fue utilizado como electrolito líquido manteniendo la homogeneidad de las especies móviles. Los resultados demostraron una deposición de litio más homogénea durante el ciclado por parte de los aglutinantes iónicos, conllevando a un ciclado mucho más estable; y una notable mayor capacidad en todas las densidades de corriente medidas para las celdas

basadas en PMTFSI-Li. Este polielectrolito, debido a su alto rendimiento, fue optimizado en términos de peso molecular y selección de electrolito para el desarrollo de dispositivos más próximos a las capacidades superficiales obtenidas industrialmente. En este último paso, PMTFSI-Li demostró todavía un rendimiento superior a PVDF en dispositivos de 1.2 mAh cm^{-2}. Como valor añadido de este polímero es totalmente procesable usando agua como solvente, evitando el uso de NMP tóxico.

Por último, los materiales conductores mixtos desarrollados en las dos primeras partes de esta tesis doctoral (PEDOT:PSS y PEDOT:PDADMA-TFSI en combinación con C_2mpyrTFSI) fueron evaluados en celdas Li||LiFePO4. De nuevo, el electrolito líquido 1M LiTFSI DOL/DME (1:1 v/v) fue utilizado para mantener la homogeneidad iónica de los distintos sistemas. Los resultados mostraron una fuerte dependencia de las celdas con la porosidad, obteniendo los mejores escenarios en las celdas que contenían aglutinante de conducción mixta en combinación con carbón conductor, que incrementa notablemente la porosidad hasta niveles óptimos. Además, la adición de OIPC resultó clave para obtener mayores densidades de capacidad, en total sintonía con los capítulos iniciales de esta tesis. Finalmente, si bien los aditivos basados en PEDOT:PSS ofrecían mayores capacidades, de acuerdo a sus superiores conductividades, los basados en PEDOT:PDADMA-TFSI mostraron una alta estabilidad en el ciclado a largo plazo, tal y como se observó para PDADMA-TFSI en el tercer proyecto. Además, estos materiales son procesables en solventes menos tóxicos que NMP como DMSO o acetonitrilo. Este estudió abre nuevas posibilidades para la optimización de baterías de litio para la obtención dispositivos con mayores densidades de capacidad y estables a largo plazo.

Como conclusión, en esta tesis doctoral se han desarrollado distintos materiales orgánicos de conductividad mixta basados en PEDOT y distintos polielectrolitos y OIPCs para dispositivos de almacenamiento de energía. En general, se ha mostrado que pueden ser utilizados para estado sólido en formulaciones libres de carbón, mientras que para estado líquido es necesaria una cierta porosidad para el buen funcionamiento del dispositivo (conseguida a través de carbón conductor). También, se ha observado una fuerte dependencia del rendimiento de las baterías con el polielectrolito acompañante de PEDOT. Finalmente, se ha demostrado el beneficioso impacto de la presencia de OIPCs en las propiedades de los materiales (conductividades) y en el dispositivo final (capacidades específicas).

List of acronyms

4PP	Four-Point-Probes
AFM	Atomic Force Microscopy
AIBN	2,2‘-azobis-isobutyronitrile
AM	Active Material
C_2mpyr	N-ethyl-N-methylpyrrolidinium
CCTS	Carboxymethyl chitosan
CMC	Carboxymethyl cellulose
CP	Conducting Polymer
CV	Cyclic Voltammetry
DEC	Diethyl carbonate
DFT	Density Functional Theory
DMA	Dynamic Mechanical Analysis
DME	1,2-dimetoxiethane
DMF	Dimethylformamide
DOL	Dioxolane
DSC	Differential Scanning Calorimetry
EC	Ethyl carbonate

EDLC	Electric Double Layer Capacitor
EDOT	3,4-Ethylenedioxythiophene
EIS	Electrochemical Impedance Spectroscopy
EMIM TCB	1-Ethyl-3-methylimidazolium tetracyanoborate
ESS	Energy Storage System
FRP	Free-Radical Polymerization
FSI	Bis(fluorosulfonyl)imide
FTIR	Fourier-transform Infrared Spectroscopy
IEP	Inverse Emulsion Polymerization
IL	Ionic Liquid
LFP, $LiFePO_4$	Lithium iron phosphate
LIB	Lithium-ion Battery
LMB	Lithium-metal battery
$LiPF_6$	Lithium hexafluorophosphate
MIEC	Mixed Ionic-Electronic Conductor
NCA	Lithium nickel cobalt aluminum oxide
NFC	Nanofibrillated cellulose
NMC	Lithium nickel manganese cobalt oxide

NMP	N-Methyl-2-pyrrolidone
NMR	Nuclear Magnetic Resonance
OIPC	Organic Ionic Plastic Crystal
P3HT	Poly(3-hexylthiophene)
PA	Polyacetylene
PANI	Polyaniline
PolyDADMA, PDADMA	Polydiallyldimethylammonium
PEDOT	Poly(3,4-ethylenedioxythiophene)
PEO	Poly(ethylene oxide)
PIL	Poly(ionic liquid)
PMTFSI-Li	Poly(lithium 1-[3-(methacryloyloxy) propylsulfonyl]-1-(trifluoromethanesulfonyl)
PPy	Poly(pyrrol)
PSS	Poly(styrene sulfonate)
PTSA	p-Toluene sulphonic acid
PVDF	Poly(vinylidene fluoride)
RAFT	Reversible addition-fragmentation chain transfer
RH	Relative humidity

SA	Sodium Alginate
SAXS	Small-angle X-ray scattering
SEC	Size exclusion chromatography
SEM	Scanning electron microscope
SICP	Single-ion conducting polymer
SOC	State of charge
SPE	Solid Polymer Electrolyte
TEMPO	(2,2,6,6-tetramethylpiperidin-1-yl)oxidanyl
TFSI	Bis(trifluoromethanesulfonyl)imide
TGA	Thermogravimetric analysis
UV	Ultraviolet-visible spectroscopy
VPP	Vapor phase polymerization
WAXS	Wide Angle X-ray Scattering
XPS	X-ray Photoelectron Spectroscopy
XRD	X-ray Diffraction

List of publications, conference presentations and collaborations

PUBLICATIONS

1. Mixed Ionic-Electronic Conductors Based on PEDOT:PolyDADMA and Organic Ionic Plastic Crystals. **R. Del Olmo**, N. Casado, J. L. Olmedo-Martinez, X. Wang and M. Forsyth. Polymers. 2020;12:1981.

2. Tuning Electronic and Ionic Conductivities in Composite Materials for Electrochemical Devices. N. Casado, S. Zendegi, **R. Del Olmo**, A. Dominguez-Alfaro and M. Forsyth. ACS Appl. Polym. Mater. 2021;3:1777–1784.

3. Mixed Ionic-Electronic Conductors Based on Polymer Composites. **R. Del Olmo**, M. Forsyth, N. Casado (2022). In: Shalan, A.E., Hamdy Makhlouf, A.S., Lanceros-Méndez, S. (eds) Advances in Nanocomposite Materials for Environmental and Energy Harvesting Applications. Engineering Materials. Springer, Cham.

4. Mixed Ionic and Electronic Conducting Binder of PEDOT:PSS and Organic Ionic Plastic Crystals toward Carbon-Free Solid-State Battery Cathodes **R. del Olmo**, T. C. Mendes, M. Forsyth and N. Casado. J. Mater. Chem. A 2022.

5. Unraveling the influence of Li^+-cation (PMTFSI-Li) and $TFSI^-$-anion (PDADMA-TFSI) in poly(ionic liquid) binders for lithium-ion batteries. **R. Del Olmo**, G. Guzman-Gonzalez, I. O. Santos-Mendoza, D. Mecerreyes, M. Forsyth and N. Casado. *Under Revision (J. Power Sources)*. 2022.

6. Improving LFP cathode performance through mixed ionic-electronic binders for high energy and power density. **R. Del Olmo**, G. Guzman-Gonzalez, M. Forsyth, O. Sanz, D. Mecerreyes and N. Casado. *Under preparation*. 2022.

7. PEDOT:PSS-based Screen-printable Inks for H_2O_2 Electrochemical Detection. L. Campos-Arias, **R. Del Olmo**, N. Peřinka, N. Casado, J. L. Vilas-Vilela, D. Mecerreyes, F. J. del Campo and Lanceros-Méndez. Submitted. 2022.

CONFERENCE PRESENTATIONS

1. PEDOT - OIPC composites as organic mixed ionic-electronic binders for solid state Li-ion batteries. **R. del Olmo**, T. C. Mendes, M. Forsyth and N. Casado. Polymat Students Seminar 2021. San Sebastián, Spain (oral presentation).

2. PEDOT - OIPC composites as organic mixed ionic-electronic binders for solid state Li-ion batteries. **R. del Olmo**, T. C. Mendes, M. Forsyth and N. Casado. SEJIPOL2020-21 5th Young Polymer Scientist Seminar 2021. CSIC. Madrid, (oral presentation).

3. PEDOT - OIPC composites as organic mixed ionic-electronic binders for solid state Li-ion batteries. **R. del Olmo**, T. C. Mendes, M. Forsyth and N. Casado. CNMat2022 XVI National Congress of Materials 2022. Ciudad Real, Spain (oral presentation).

COLLABORATIONS

The electrochemical characterization of the solid-state battery of Chapter 2 was carried out in collaboration with Deakin University (Melbourne, Australia). I did a secondment of 5 months under IONBIKE RISE programme (Marie Sklodowska-Curie) at the Institute for the Frontier Materials under the supervision of Prof. Maria Forsyth.